FROM GIANTS TO DWARFS: PROBING THE EDGES OF GALAXIES

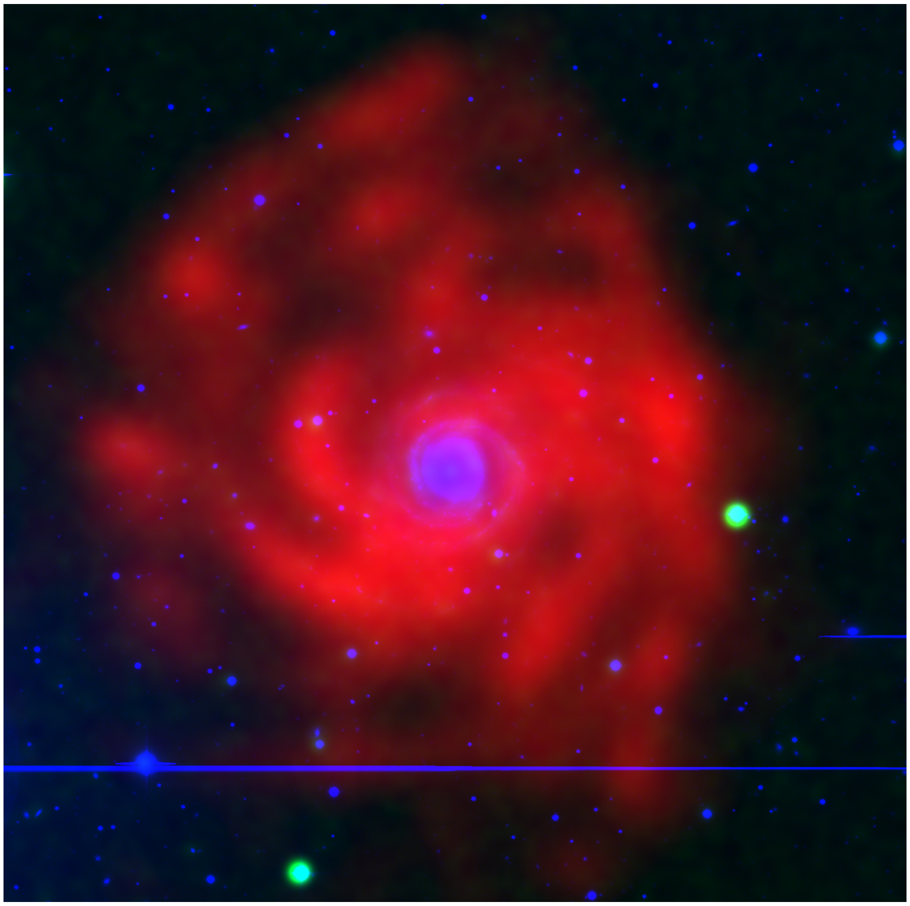

ANTÓNIO MIGUEL PEREIRA PORTAS

submitted to the University of Hertfordshire in partial
fulfilment of the requirements of the degree of PhD.

April 2010

Front cover image is a RGB composition of NGC 765: blue represents the optical R–band emission, red is the 21-cm emission of the neutral hydrogen disc and green is the far–UV emission of the field.

“ It was the best of times, it was the worst of times, it was the age of wisdom, it was the age of foolishness, it was the epoch of belief, it was the epoch of incredulity, it was the season of Light, it was the season of Darkness, it was the spring of hope, it was the winter of despair, we had everything before us, we had nothing before us ...”

Charles Dickens, “A Tale of Two Cities”

When I first stumbled upon the opening paragraph of Dickens’ “A Tale of Two Cities”, I was mesmerised by the fact that this 19th century literary work captured the essence of my personal experience of achieving a PhD in Astrophysics. Naively I did not foresee the enormous emotional demand of such a colossal experience. We are challenged on a daily basis, forced to think by ourselves, ripped outside of our safety zone. It is uncomfortable, crude, nonetheless enjoyable and addictive!

At the end of this journey, my personal balance is utterly positive. Looking back, I now realise that the tools learned and polished along the path, are as fundamental as the object of study *per se*. I will take with me the intellectual maturation acquired, hoping to preserve it and nurture it in the years to come. I could not finish without sharing one single word which invades my thoughts every time I think about my PhD experience: enlightenment!

Acknowledgements

Research is not a solitary action. It heavily relies on a network of collaborations. I would like here to acknowledge people that crossed my path during the elaboration of this project.

Many, many thanks to my PhD supervisor team: Professor Elias Brinks, Doutora Mercedes Filho and Dr. Antonio Usero. Because I was blessed enough for my professional relations to migrate into my personal sphere, I am also grateful to my dearest Dutch friend, Elias Brinks, who never stopped believing in me: *you are a true inspiration!* To an amazing Portuguese woman, Mercedes Filho and to the coolest Spanish man, Antonio Usero, many many thanks! Thank you all for the fun and the laughs over the last years! *Dank u wel! Muito obrigado! Muchas gracias!*

I am grateful to the studentship from the University of Hertfordshire and to all the staff and colleagues from the Centre for Astrophysics Research. I also acknowledge the Centro de Astrofísica da Univerdade do Porto, for hosting me during several periods of time during the elaboration of this project. I am also thankful to all my collaborators, especially the members of the THINGS project.

To all my friends in the UK, Portugal, and across the world, a deep and sincere *thank you* for being a fundamental part of my life.

E como os últimos serão sempre os primeiros, um muitíssimo obrigado à minha mãe e ao meu pai, vocês são os melhores pais do Universo! Obrigado ao meu irmão e cunhada, e por último obrigado as minhas três Marias: Maria Francisca, Maria Margarida e Maria João por encherem o meu céu de estrelas.

Abstract

In this thesis we address fundamental questions about what constitutes and limits an H I disc, probing the distribution of neutral gas in the outer parts of galaxies. We use a subsample of galaxies observed as part of the THINGS survey to investigate the H I extent of spiral galaxy discs. We revisit previous work on the extent of H I discs, showing the limitations set by insufficient linear resolution. We then exploit the high spatial and velocity resolution combined with good sensitivity of THINGS to investigate where the atomic gas discs end and what might shape their edges. We find that the atomic gas surface density across most of the disc is constant at $5 - 10 \times 10^{20}$ atoms cm^{-2} and drops sharply at large radius. The general shape of the H I distribution is well described by a Sérsic–type function with a slope index, $n = 0.14 - 0.22$ and characteristic radius r_i. We propose a new column density threshold of 5×10^{19} atoms cm^{-2} to define the extent of the gas disc. This limit is well within reach of modern instruments and is at the level where disc gas becomes susceptible to ionisation by an extragalactic radiation field. We argue that at this level the H I column density has decreased to 1/10th of that across the inner disc and that by going to yet lower column density the disc is unlikely to grow by more than 10% in radius. The H I column density at which the radial profiles turn over is too high for it to be caused by ionisation by an extragalactic UV field and we postulate that the H I extent is set by how galaxy discs form. Ionisation by extragalactic radiation will only play a rôle at column densities below 5×10^{19} atoms cm^{-2}, if any.

To study the crucial relation between observed edges and how closely these reproduce the intrinsic distribution of gas through our interferometric measurements, we created an ensemble of models based on four radial density distributions. We conclude that the observed edges in spiral galaxies faithfully reflect their intrinsic shape. Only in very specific cases of highly inclined (>75°) and/or large vertical scaleheight discs do we see strong deviations from the intrinsic surface density of the observed shape of the edges in spiral galaxies.

In the case of NGC 3198 we concluded that there is no significant difference in the radial profiles obtained with either constant or exponentially increasing vertical gas distributions, when scaleheights are not higher than 1 kpc at the outskirts of the disc. We infer an upper limit to the scaleheight of NGC 3198 of 2 kpc.

To address the distribution of neutral gas at larger scales, we study an H I rich, giant LSB galaxy, NGC 765. We present H I spectral line and radio–continuum VLA data, complemented by optical and *Chandra* X-ray maps. NGC 765 has the largest H I-to-optical ratio known to date of any spiral galaxy and one of the largest known H I discs in absolute size with a diameter of 240 kpc measured at a surface density of 2×10^{19} atoms cm $^{-2}$. We derive a total H I mass of $\mathrm{M}_{\mathrm{H\,I}} = 4.7\times10^{10}\ \mathcal{M}_{\odot}$, a dynamical mass of $\mathrm{M}_{\mathrm{dyn}} \sim 5.1\times10^{11}\ \mathcal{M}_{\odot}$ and an H I mass to luminosity ratio of $\mathrm{M}_{\mathrm{H\,I}}/\mathrm{L}_{\mathrm{B}} = 1.6$, making it the nearest and largest 'crouching giant'. Optical images reveal evidence of a central bar with tightly wound low-surface brightness spiral arms extending from it. Radio–continuum ($\mathrm{L}_{1.4\,\mathrm{GHz}} = 1.3\times10^{21}$ W Hz^{-1}) and X–ray ($\mathrm{L}_{\mathrm{X}} \approx 1.7\times10^{40}$ erg s^{-1}) emission is found to coincide with the optical core of the galaxy, compatible with nuclear activity powered by a low-luminosity AGN. We may be dealing with a galaxy that has retained in its current morphology traces of its formation history. In fact, it may still be undergoing some accretion, as evidenced by the presence of H I clumps the size (< 10 kpc) and mass (10^{8}–$10^{9}\ \mathcal{M}_{\odot}$) of small (dIrr) galaxies in the outskirts of its H I disc and by the presence of two similarly sized companions. In an exploration of future work, we engaged in a study of the edges in the H I discs of dwarf irregular galaxies, their parameterisation and simulation. A collection of simulations were created based on the dwarf galaxy NGC 2366, similar to what was done for the larger spiral galaxies, showing that line–of–sight column densities are affected for discs with inclinations higher than 60° . Five out of eleven of the dwarfs from THINGS which are less inclined than 60° were analysed and parameterised with our Sérsic–type function. Their discs have average central column densities spread evenly from $\log_{10}$ NH I = 20.7 atoms cm^{-2} to $\log_{10}$ NH I = 21.3 atoms cm^{-2}. Their radial decline is shallower (slope index peaks around $n \approx 0.3$) than for spirals. The up–coming Local Irregular That Trace Local Extremes (LITTLE) THINGS project, will likely enlarge the number of local dwarf irregular (dIm) galaxies to which this type of analysis can be applied and for which these preliminary results verified.

Contents

List of Figures

List of Tables

Chapter 1

Introduction

1.1 Galaxies in the Universe

Galaxies are *par excellence* the most complex, most diversified and most fascinating structures in the Universe. They populate the Universe spanning a range of sizes and masses: on the one hand there are gas–rich systems, ranging from small, amorphous dwarfs to grand–design spirals. On the other, we find gas–poor objects, from dwarf spheroidals and ellipticals to massive cD galaxies. To talk about their origin and evolution is to talk about the origin and evolution of the Universe itself.

From an observational point of view, The Wilkinson Microwave Anisotropy Probe (hereafter WMAP; Bennett *et al.* 2003), was instrumental in helping to provide the widely accepted ΛCDM standard model for cosmology (Spergel *et al.* 2007). In this world view the gaussian density fluctuations constrained by WMAP are thought to be the relic seeds that were at the origin of the distribution of large scale structure of the Universe as seen today (Hinshaw *et al.* 2009).

Even if it is well beyond the purpose of this project to discuss cosmological models or evolutionary mechanisms of galaxies, the concept of all the known galaxies, in their rich diversity, evolving from small density fluctuations of the cosmic microwave background in a very early and very uniform Universe is yet to be fully understood and is quite daunting.

The exact moment when the first galaxies were assembled, still remains unknown, although deep imaging surveys like the Hubble Deep Field (Williams *et al.* 1996) and

The Great Observatories Origins Deep Survey (GOODS; Giavalisco *et al.* (2004)) have shown that star–forming galaxies were already quite common structures when looking back to a redshift of $z \sim 5 - 7$ when the Universe was only about 1 Gyr old.

In this project we focus our attention on a specific class of objects: *spiral galaxies.* The two main baryonic components residing in spiral galaxies are stars and gas, both distributed in thin rotating discs. In addition, stars are found in central bulges. Embedded in the discs we find spiral arms, structures characterized by larger numbers of stars, and accumulations of gas and dust, leading to conditions favourable to subsequent star formation.

Accretion of small clumps of both baryonic and dark matter, falling towards more massive dark matter haloes, is now a well accepted scenario for the assembly of late–type galaxies (Navarro *et al.* 1995; Springel *et al.* 2005). Discs form by cooling and the dissipative collapse of baryonic matter (e.g., Fall & Efstathiou 1980). During this process, infalling gas should preserve a large fraction of its angular momentum whilst settling into a disc. It has lately become clear that a realistic description of star formation and feedback are indispensable ingredients in numerical models if they are to match the observed properties of galaxies (Sommer-Larsen *et al.* 1999, 2003; Governato *et al.* 2004, 2007, 2010; Scannapieco *et al.* 2008).

Quite often, galaxies are spatially concentrated in groups or clusters of galaxies, within which all elements are gravitationally bound. Clusters of galaxies are in turn distributed to form superclusters of galaxies. At even larger scales, numerical simulations of structure formation predict a Universe made up of filamentary structures, the Cosmic Web, in which galaxies and most of the baryonic mass are concentrated, surrounding large regions known as voids (see Davé *et al.* 1999, for details) .

1.2 Neutral hydrogen

The Universe is filled with large amounts of neutral hydrogen, detectable via its 21--cm emission line. The 21-cm emission occurs when the spin of a hydrogen atom spontaneously decays from the $\mathbf{F} = 1$ level to the $\mathbf{F} = 0$ level (hyperfine transition), $\mathbf{F}$ being the total angular momentum of the hydrogen atom. This decay corresponds to a radiated energy that in turn corresponds to a frequency of 1420.46 MHz, which is equivalent to a wavelength of 21 cm.

Neutral hydrogen can either be detected in emission or absorption depending mainly on the balance between temperature of the background T_{bg}, and the spin temperature T_S of the H I cloud itself. H I emission will be present when $T_{bg} < T_S$ and assuming an optically thin medium. An example of H I in emission are the H I integrated maps and respective column densities that are measured in the course of this thesis. When there is a strong background source, the H I spectrum will present an absorption feature as in that case we will have $T_{bg} > T_S$. Often the non-thermal emission from an active galactic nucleus (AGN) in a galaxy will show an absorption profile along the line of sight towards the nucleus.

1.3 Contextualization of the project

Deep observations of the neutral hydrogen 21–cm emission line down to surface brightnesses as low as $\sim 10^{19}$ atoms cm^{-2} and obtained either with single dishes or arrays of radio telescopes, have shown galaxies to be individual entities with sharply defined boundaries (excluding those which are obviously interacting). Until recently it was not obvious if this surface brightness was simply set by the sensitivity limit of our instruments or if this represents a true edge, and even less if this edge is due to the galaxy running out of baryonic matter, or if the sharp edge is caused by an external ionising radiation field, as proposed by several authors (e.g. Sunyaev 1969; Maloney 1993), much like an inverted Strömgren sphere.

However, deeper H I surveys have started to reveal low level filaments apparently linking galaxies. An example is the work by Braun & Thilker (2005) who published an H I map showing that M31 and M33 are connected by a faint stream of material. Their maps reach sensitivities of 4×10^{16} atoms cm^{-2}.

We also know that at high redshift and much lower neutral column densities of $< 10^{15}$ atoms cm^{-2}, the Universe is full of detectable structure, in the form of Ly-α forest clouds (e.g. Telfer *et al.* 2002). So, one expects a transition from the mainly neutral galaxy disc to the mainly ionised Cosmic Web.

We contextualise this project in the above mentioned framework aiming to push the detection of H I in galaxy discs to lower limits and to investigate what limits the size of H I discs in different classes of objects: from ordinary high surface brightness (HSB) spirals to low surface brightness (LSB) giant H I discs. We choose these on the basis of their high content of neutral gas. As mentioned by Roberts & Haynes (1994), spiral galaxies are more gas rich, having on average 11% of their baryonic mass in neutral hydrogen. In Chapter 2, we revisit the H I distribution in the outer parts of a subsample of spiral galaxies from the The H I Nearby Galaxy Survey (THINGS) survey (Walter *et al.* 2008), characterising the conditions at large radii. We investigate correlations with the distribution of other components contributing to the (baryonic) mass distribution, and address the question what limits the extent of the neutral gas distribution, establishing that the rapid decline of neutral hydrogen at the outer parts of H I discs is an intrinsic property of the disc. In order to shed light on the complex question of how the observed (through interferometry) gas distribution relates with the true distribution of gas, we simulate some models of H I discs in Chapter 3.

Since we are studying gas–rich galaxies, in Chapter 4 we present NGC 765, a galaxy which resembles the classical LSB galaxy Malin 1. Malin 1 remains the prototype of a class of objects often called “crouching giants” or “Malin 1 cousins”, consisting of large ($\sim$ 200 kpc) LSB H I discs. This sub–class of spiral galaxies are extremely rich in gas (Impey & Bothun 1989). NGC 765 provides us with an opportunity to study such an extraordinary system in more detail, probing the distribution of H I out to lower levels and to large galactic radii. To round off this project we draw our conclusions in Chapter 5 and outline future work by showing preliminary results of the parameterisation and analysis of the outer regions of the dwarf galaxies of the THINGS survey.

1.4 Literature review

1.4.1 The extent of spiral galaxies

At optical wavelengths, the radial stellar light profile is well described by an exponential function, the surface brightness decreasing with radius with a characteristic scale length, h. As reviewed by Pohlen & Trujillo (2006), radial stellar profiles come in three different types distinguished by the presence, or lack of a break in the surface brightness profile. Classical Freeman Type I profiles show no break whereas Type II and the more recently identified Type III profiles present a “knee” at which the exponential becomes steeper or flatter, respectively. Recently, Bournaud *et al.* (2007)

proposed that these profiles originate from the way galaxies assemble during the early stages of galaxy formation, from the dynamical evolution of clump cluster and chain galaxies. As for Type II and III, Pohlen & Trujillo (2006) suggest bar resonances and star formation thresholds might be associated with the observed breaks in the profiles.

About 60% of disc galaxies show a clearly truncated disc with the truncation radius, R_{max} varying between 4 to 5 radial scale lengths, h (e.g. van der Kruit 2007). Beyond the truncation radius the surface brightness drops much more rapidly than the extrapolated exponential disc profile. Although this is most clearly observed in edge–on systems, the same holds true for less inclined galaxies. It is common to quote the extent of the stellar disc in terms of the Holmberg radius or more commonly nowadays, R_{25}, corresponding to the radius at a surface brightness of 25 B–mag arcsec^{-2}. Also used is R_{e}, or effective radius, which is the radius confining half the light emitted by a galaxy. We refer the reader to the work of van der Kruit (2007), for a review of the definition of the Holmberg radius.

In contrast, when observing neutral hydrogen discs of spiral galaxies, there are no similar conventions for characterising the size of the H I disc, or for describing the run of surface density as a function of radius. Several definitions have been proposed, quoting the radius at a set column density level. For instance Bosma (1981), chose $R_{1.82}$, corresponding to the radius at a column density of 1.82×10^{20} atoms cm^{-2} (or $100\,\mathrm{K\,km\,s^{-1}}$). Others like Broeils & Rhee (1997), define the H I diameter at a level of $1\,\mathcal{M}_{\odot}$ pc^{-2}, which is approximately 1.25×10^{20} atoms cm^{-2} . Both limits have more to do with being convenient numbers, much like R_{25}, rather than defining a physical extent.

Radial H I surface brightness profiles, more usually presented as H I column density profiles, remain flat out to radii well beyond R_{25}. Broeils & Rhee (1997) derive a diameter ratio between the H I and optical diameter of 1.7 ± 0.5. There does not seem to be any signature that coincides with the location of the "knee" found in Freeman Type II or III profiles, nor does there seem to be a change in properties near $1.1R_{\mathrm{max}}$ which is where generally a warp sets in (van der Kruit 2007).

Spiral galaxies do show a finite extent in deep H I images which means that either i) the column density drops below the detection limit; ii) galaxies are running out of material (so the H I extent is a consequence of the process of galaxy formation);

iii) there is a tidal radius beyond which material can be easily removed through interactions (Chung *et al.* 2007); iv) H I turns very cold and becomes H_2 (Combes & Pfenniger 1997; Bournaud *et al.* 2007); v) the H I becomes ionised, for example by an isotropic extragalactic radiation field. These conditions are not mutually exclusive and a combination of some of the above might actually define the shape of the H I distribution at the galaxy edge.

If edges are being caused by a mere instrumental detection threshold it would imply that the H I would continue to gradually extend to larger radii. This would be exciting as it would allow the kinematics of galaxies to be probed to much larger radii than possible today, tracing in detail their dark matter (DM) distribution. It would also imply that it should be straightforward to trace the transition from galaxy disk to the material forming the Cosmic Web.

In contrast, if galaxies simply run out of material, the study of edges becomes relevant in terms of the baryonic fraction and how much this contributes at large galactic radius, and compare this with λCDM predictions. As mentioned, H I could very cold and become H_2,undergoing a phase transition to metallic H_2.

Another aspect of the study of edges is environmental related. Hostile environments like those found in a cluster of galaxies will affect the shape of the edges, e.g. through tidal interactions and ram pressure effects, and in extreme cases cause a misalignment of the gas from its optical counterpart. A comparison between edges of galaxies embedded in clusters and those that are relatively isolated should provide us with some valuable clues as to the importance of the effects of environment.

Previous papers that focussed on the possibility of atomic hydrogen in the outskirts of galaxies being ionised due to an isotropic extragalactic radiation field are, among others, by Sunyaev (1969), van Gorkom (1991), Maloney (1993), and Dove & Shull (1994a). In addition, dynamical interactions, internal sources of ionisation (Dove & Shull 1994b; Bland-Hawthorn & Maloney 1999), or global properties of the intergalactic medium in the vicinities of galaxies (Linder *et al.* 2003) might affect the way edges of H I discs are shaped. To date, only few objects have been studied in detail. Some examples of previous studies are: NGC 3198 (Maloney 1993; Dove & Shull 1994a; Corbelli *et al.* 1989), M31 (Sunyaev 1969) and M33 (Corbelli *et al.* 1989).

NGC 891 is an example of an edge–on galaxy with a large amount of anomalous extra–planar gas in the halo which has been mapped several times, the most sensitive data obtained by Oosterloo *et al.* (2007a). According to the authors the new deep H I image did not increase the radius of this object from previous images, but only the amount of gas present in the halo (which can make up to 15% of the total H I mass). In fact, the authors fairly question why would an isotropic radiation field preferentially act in the plane of the disc, oblivious of the low density gas in the halo region.

There is ample observational evidence that sporadic episodes of minor mergers and cold accretion of gas not only can enlarge the size of H I discs but also replenish gas used in star formation. Sancisi *et al.* (2008) review cold gas accretion in galaxies where the authors collected observational evidence on gas-rich dwarf companions and/or other morphological structures in both halo or outskirts of H I discs, acting as a gas reservoir for future star formation. In fact, the process of cold accretion seems to dominate galaxy evolution at intermediate redshift as shown by clumpy galaxies obtained by several cosmological simulations. We refer the reader to Elmegreen *et al.* (2009) and references therein.

How large can an H I disc grow and what are the physical conditions of the gas at large galactic radii remain open questions. For instance could the maximum size of a disc be Hubble–type dependent? What are the typical dimensions of an H I disc? We know that the local Universe is populated with H I discs ranging from radial sizes of $\sim$ 10 up to 50 kpc, as shown in the THINGS survey (Walter et al. 2008), which provides a homogeneously observed sample of local galaxies.

In addition, observations of edge–on spiral galaxies indicate that H I discs are thin and also present a well delimited boundary in the vertical direction. Although there is no golden rule as to the ratio of gas scaleheight to radial extent, in our own Galaxy Nakanishi & Sofue (2003) state that the H I gas reaches 1.5 kpc above the Galactic plane in the northern hemisphere, in comparison to the 17 kpc radius measured at a column density of 1 $\mathcal{M}_\odot\,\mathrm{pc}^{-2}$ of the H I disc. This yields a ratio of 1:11 which could be an underestimate since the disc of the Galaxy is shown to be significantly lopsided. Other galaxies such as the super thin edge–on UGC 7321 (Uson & Matthews 2003) yield an axial ratio of 1:29; NGC 6503 (Greisen *et al.* 2009) presents a ratio of 1:30, NGC 2997 (Hess *et al.* 2009) has a ratio of 1:43, just to quote some values.

There are also examples of large H I discs in early-type galaxies as studied by Oosterloo *et al.* (2007b). The author refers to the morphology of H I discs around a sample of 30 early type southern gas-rich galaxies. Two of these objects, both classified as SA0, present large H I discs: NGC 6799 with a disc diameter of ∼240 kpc and NGC 5266 with 200 kpc. However both are lenticular galaxies and the gas disc might be a transient feature, the result of a recent merger or the infall of dwarf companions (see Roberts & Haynes 1994; Morganti *et al.* 1997, and references therein).

1.4.2 Crouching giants

To probe H I up to large galactic radii it pays to turn our attention to a special class of under luminous galaxies: low surface brightness (LSB) galaxies. Although initially this category was thought to consist predominantly of late–type spirals and dwarf irregular (dIrr) galaxies, we now know that they span the entire range of galaxy mass (Bothun *et al.* 1997). They are thought to evolve more slowly, as suggested by their low surface brightness, low metallicities and low star formation rates when compared with high surface brightness (HSB) galaxies (see Impey & Bothun 1997; Mihos *et al.* 1999; Rahman *et al.* 2007, and references therein). This also means that LSB discs have consumed less of their gas and are therefore gas–richer systems when compared with HSB discs (McGaugh & de Blok 1997; O'Neil *et al.* 2004).

An extreme category of LSBs is collectively known as that of 'crouching giants' (Disney & Phillipps 1987) or 'Malin 1 cousins' after the giant LSB galaxy Malin 1, discovered serendipitously by Bothun *et al.* (1987). It has one of the largest radial extents known for a spiral galaxy, out to a radius of $\sim$ 100 kpc (Impey & Bothun 1989; Barth 2007) with an extrapolated disc central surface brightness of μ_0 (V) = 25.5 mag arcsec^{-2}. It is one of the most gas–rich galaxies known with an H I mass of $\sim 5 \times 10^{10} \mathcal{M}_\odot$ (Barth 2007) and the neutral gas extending out to $\sim$ 120 kpc radius (Pickering *et al.* 1997). The discovery of Malin 1 prompted searches for more of these giant LSB systems. GP 1444 was discovered by Davies *et al.* (1988). This was followed by F568–6 or Malin 2, found by Bothun *et al.* (1990) and 1226+0105 by Sprayberry *et al.* (1993). All these 'Malin 1 cousins' were found to be gas rich and have discs characterised by large scale lengths and low central surface brightness as reported by Sprayberry *et al.* (1995), who increased the number of known LSB giant discs by a further eight objects. More recently, O'Neil *et al.* (2004) detected 38 of these 'crouching giants' (Disney & Phillipps 1987) raising to roughly 55 the number of massive LSB galaxies with H I mass higher than $10^{10}\mathcal{M}_\odot$. It should be noted, though, that spatially resolved imaging, in H I as well as in the optical, is needed to confirm which of these giant LSB candidates are indeed Malin 1–type objects.

The formation and evolution of LSB giants remains puzzling and several explanations have been put forward. Hoffman *et al.* (1992) propose that objects with the characteristics of a Malin 1, i.e. a rather normal bulge and a low surface brightness, can be due to rare 3σ density fluctuations in a primordial Gaussian random field. Dalcanton *et al.* (1997) postulate that the initial mass and angular momentum of a protogalaxy determine the luminosity and surface brightness of today's systems, high angular momentum protogalaxies leading naturally to giant LSBs. Rather than their characteristics being due to their initial conditions, some authors like Noguchi (2001) suggest that the formation and strength of a bar in the disc of an HSB galaxy could result in the redistribution of matter, lowering the central brightness of the object and converting it into a giant LSB galaxy. More recently, Mapelli *et al.* (2008) propose that giant LSBs might be the late stage evolution of a head–on collision, i.e. the late stage of a ring galaxy at ~ 1.5 Gyr after impact.

Giant LSB discs, provide an unique opportunity to study alternative formation and evolution histories to HSB galaxies, undoubtedly contributing to probe the Dark Matter halo out to an unprecedented large galactocentric distances.

1.5 The THINGS survey

The H I Nearby Galaxy Survey (THINGS) (Walter *et al.* 2008) is one of the largest surveys, having obtained almost 500 hours of observations with the NRAO[1] Very Large Array (VLA) in B, C and D configurations, that resulted in 21–cm H I observations of a sample of 34 objects of the local Universe. The survey's unique characteristics allowed the creation of a database of high spatial ($\sim 6''$) and velocity (≤ 5 km s^{-1}) H I maps, as well as the velocity fields, velocity dispersion maps and individual channel maps of each THINGS target, all available to the community.[2]

The THINGS sample overlaps with other surveys such the *Spitzer* Infrared Nearby

---

[1] The National Radio Astronomy Observatory is a facility of the National Science Foundation operated under cooperative agreement by Associated Universities, Inc.

[2] available at http://www.mpia.de/THINGS/Data.html

Galaxies Survey (SINGS; Kennicutt *et al.* 2003) or the Heterodyne Receiver Array CO Line Extragalactic Survey (HERACLES; Leroy *et al.* 2009), allowing a more complete multiwavelength coverage of some of the targets. Data from THINGS were used to investigate a large range of issues such as the star formation at sub–kpc scales (Bigiel *et al.* 2008; Leroy *et al.* 2008), dynamics and distribution of dark matter through the study of rotation curves and mass models (de Blok *et al.* 2008; Tamburro *et al.* 2008) and H I holes, bubbles that permeate the disc (Bagetakos *et al.* 2010, submitted). These are only a few examples of the first scientific results originated by THINGS during the elaboration of this project.

In this thesis we make use of the high resolution maps from the THINGS survey to probe the rapid decline of H I densities at the peripheries of spiral galaxies. All objects studied in this project are THINGS targets with the exception of the giant LSB disc of NGC 765 in Chapter4.

For the edges analysis of Chapter 2, we preselected those 24 candidates which according to their Hubble type are classified as spiral galaxies. After a first inspection of the available integrated H I maps, we rejected those galaxies which are larger than the VLA primary beam ($\sim 32'$ in diameter) and, therefore, have not been mapped completely. This reduced the sample to 9 objects: NGC 925, NGC 3184, NGC 3198, NGC 3351, NGC3521, NGC 3627, NGC5194, NGC 7331 and NGC 7773. Table 1.1 summarizes the properties of the sub–sample of THINGS spiral galaxies.

In Chapter 5, the dwarf galaxies were selected from the THINGS database based on a criteria of their B–band magnitude being fainter than -18.5 which is generally agreed to be the transition between late spirals and dwarf irregular galaxies. It is known, though, that galaxies cover a continuum of magnitudes and morphologies and it remains fairly subjective where to draw the line as to what constitutes a dwarf. This results in a subsample of THINGS of 11 objects: DDO 53, DDO 154, Ho I, Ho II, IC 2574, M 81 DwA, M 81 DwB, NGC 1569, NGC 2366, NGC 2976 and NGC 4214. All galaxies were classified as Irr with the exception of IC 2574 (Sm) and NGC 2976 (SAc). Two objects were discarded from the B–magnitude criteria. NGC 3077 although fainter then -18.5 is in active interaction with M 81. NGC 4449 presents a counter–rotating outer envelope which implies a recent capture of a (dwarf) companion, and is, therefore, disturbed. In Table 1.2 we present basic properties of our dwarf targets. All values are taken from Walter *et al.* (2008). Specific details

Table 1.1: General properties of the THINGS subsample

Galaxy	Type	α J2000	δ J2000	Distance Mpc	incl °	PA °	noise mJy beam^{-1}	noise Kelvin
NGC 925	Scd	$02^h\,27^m\,16.5^s$	$+33^\circ\;34'\;43.5''$	9.16	66.0	286.6	0.76	4.6
NGC 3184	SABc	$10^h\,18^m\,17.0^s$	$+41^\circ\;25'\;28.0''$	11.1	16.0	179.0	0.42	2.5
NGC 3198	Sc	$10^h\,19^m\,55.0^s$	$+45^\circ\;32'\;58.9''$	13.8	71.5	215.0	0.40	2.5
NGC 3351	Sb	$10^h\,43^m\,57.7^s$	$+11^\circ\;42'\;14.0''$	9.33	41.0	192.0	0.35	4.2
NGC 3521	SABb	$11^h\,05^m\,48.6^s$	$-00^\circ\;02'\;09.2''$	10.05	72.7	192.0	0.50	3.0
NGC 3627	SBb	$11^h\,20^m\,15.0^s$	$+12^\circ\;59'\;29.0''$	9.25	61.8	173.0	0.36	2.2
NGC 5194	Sbc	$13^h\,29^m\,52.7^s$	$+47^\circ\;11'\;43.0''$	7.77	42.0	172.0	0.54	3.3
NGC 7331	Sbc	$22^h\,37^m\,4.10^s$	$+34^\circ\;24'\;56.5''$	3.82	75.8	167.7	0.57	5.0
NGC 7793	Scd	$23^h\,57^m\,49.7^s$	$-32^\circ\;35'\;27.9''$	9.16	49.3	290.0	1.09	6.6

Notes: **column 1:** galaxy name; **column 2:** Hubble type; **columns 3 & 4:** right ascension and declination; **column 5:** distance; **columns 6 & 7:** inclination and position angle; **columns 8 & 9:** rms noise in a single channel map at $10''$ resolution in mJy beam^{-1} and Kelvin respectively. All properties, except for the noise in columns 8 & 9 were taken from Walter *et al.* (2008).

about the data reduction are given in the respective chapters.

Table 1.2: General properties of the THINGS dwarfs subsample

Galaxy	Type	α J2000	δ J2000	M$_B$ mag	Distance Mpc	incl °	PA °	noise mJy beam^{-1}	noise Kelvin
DDO 154	Irr	$12^h\,54^m\,05.9^s$	27° 09′ 09.9″	−14.23	4.3	66.0	229.7	0.74	4.48
DDO 53	Irr	$8^h\,34^m\,07.2^s$	66° 10′ 54.0″	−13.45	3.6	31.0	132.0	0.73	4.42
HO I	Irr	$9^h\,40^m\,32.3^s$	71° 10′ 56.0″	−14.80	3.8	12.0	50.0	1.24	7.52
HO II	Irr	$8^h\,19^m\,05.0^s$	70° 43′ 12.0″	−16.84	3.4	41.0	177.0	1.52	9.21
IC 2574	Sm	$10^h\,28^m\,27.7^s$	68° 24′ 59.4″	−18.11	4.0	53.4	55.7	1.19	7.21
M 81 DwA	Irr	$8^h\,23^m\,56.0^s$	71° 01′ 45.0″	−11.49	3.6	23.0	49.0	0.69	4.18
M 81 DwB	Irr	$10^h\,05^m\,30.6^s$	70° 21′ 52.0″	−14.23	5.3	44.0	321.0	0.63	3.82
NGC 1569	Irr	$04^h\,30^m\,49.0^s$	64° 50′ 53.0″	−18.12	2.0	63.0	112.0	0.89	5.39
NGC 2366	Irr	$07^h\,28^m\,53.4^s$	69° 12′ 51.1″	−17.17	3.4	63.8	39.8	1.11	6.73
NGC 2976	SAc	$09^h\,47^m\,15.3^s$	67° 55′ 00.0″	−17.78	3.6	64.5	334.5	0.46	2.79
NGC 4214	Irr	$12^h\,15^m\,39.2^s$	36° 19′ 37.0″	−17.43	2.9	43.7	65.0	1.14	6.91

Notes: **column 1:** galaxy name; **column 2:** Hubble type; **columns 3 & 4:** right ascension and declination; **column 5:** B–magnitude; **column 6:** distance; **columns 7 & 8:** inclination and position angle; **columns 9 & 10:** rms noise in a single channel map at 10″ resolution in mJy beam^{-1} and Kelvin respectively. All properties, except for the noise in columns 9 & 10 were taken from Walter *et al.* (2008).

Chapter 2

The edges of THINGS: H I in the outer parts of spiral galaxies

This chapter is based on a paper being prepared for submission to The Astronomical Journal

In this Chapter, we address the distribution of neutral hydrogen in the outer parts of spiral galaxies, as well as a parameterisation of the typical edges present in radial profiles of column densities. We start with a re–analysis of almost 100 hr of archival NRAO Very Large Array data of NGC 3198, the galaxy which has become the prototype for this kind of analysis. These data have formed the basis of several papers interpreting the extent of the neutral, atomic gas disc as being set by the extragalactic radiation field (Maloney 1993; Dove & Shull 1994a). These ultra–deep VLA data will be used as a benchmark against which the THINGS data will be measured.

In Sect. 2.1 we describe how we selected a subsample of 9 galaxies from THINGS, among those NGC 3198, the idea being to investigate the outer H I edges of a sample of galaxies at much improved spatial resolution. Although the spatial resolution is much higher, the surface brightness sensitivity of THINGS in a single beam is lower and quite some effort has gone into devising the best way to analyse the data (Sect. 2.3). In Sect. 2.4 we study the truncation of the H I disc in a single object, followed by a parameterisation of the column density decline of the H I discs using a Sérsic–like $r^{1/n}$ power law (Sect. 2.5.1). A detailed description of the edges of individual objects and the fitting results are presented in Sect. 2.5.2. In Sect. 2.5.3 we search for common trends between objects. We finish with an analysis and discussion of our results in Sect. 2.6.

2.1 H I observations

The observations and data reduction pertaining to the THINGS survey are presented by Walter *et al.* (2008). The observations took place over 2.5 years. All galaxies were observed in VLA B, C, and D configuration. Data reduction followed standard procedures using AIPS (Astronomical Image Processing System) software. The AIPS task IMAGR was used to produce natural and robust weighted H I data cubes. Natural weighted cubes are obtained to achieve highest signal-to-noise at a cost of spatial resolution. Robust weighted cubes offer the best compromise of spatial resolution and sensitivity. We investigated a large range of robust parameter values settling for a value of 0.5.

In all maps presented here the residual flux in the cleaned cubes was properly taken into account as mentioned by (Walter *et al.* 2008). The authors refer to a poorly known problem in obtaining the correct H I flux of cleaned maps, since these are a combination of two maps: one containing the restored clean components (convolved with a clean beam) and the other the residual map, which is related to the dirty beam. For a correct flux derivation of the multi-array combined data of the extended objects of the THINGS project, one should take into account that, in the residual map the flux is overestimated by a factor of the ratio between dirty and clean beam sizes. Please see (Walter *et al.* 2008) for further details on this topic.

The original data cubes were convolved to a $10''$ circular beam to avoid any bias due to an elliptical beam with a set beam position angle sampling differently sized areas depending on the azimuth within the galaxy under study. Besides, smoothing the maps improves the signal–to–noise for faint, extended emission. The $10''$ beam was judged to be a good compromise between improving the signal–to–noise while maintaining sufficient resolution to resolve any sharp H I edge. At the distance of our targets, $10''$ corresponds to a linear resolution ranging from 190 to 710 pc. Table 2.1 lists the effective linear resolution for our targets along the major and minor axes.

All analysis in this chapter is based on integrated H I maps obtained via the AIPS task XMOM after having first blanked those regions in each cube deemed to be devoid of line emission (the blanking is based on a mask derived from a data cube convolved to 30″ resolution; see Walter *et al.* 2008, for details). The integrated maps were all corrected for primary beam attenuation.

Table 2.1: Linear sizes of a 10″ circular beam as measured along the major and minor axis

Galaxy	major axis pc	minor axis pc
NGC 925	444	1092
NGC 3184	538	560
NGC 3198	669	2108
NGC 3351	487	646
NGC 3521	488	1641
NGC 3627	448	949
NGC 5194	388	522
NGC 7331	713	2909
NGC 7793	190	292

2.1.1 NGC 3198 archive data: observations

NGC 3198 was observed in H I with the Westerbork Synthesis Radio Telescope (WSRT) by van Albada *et al.* (1985); Begeman (1989) in order to determine the distribution of its dark matter. The paper by Begeman (1989) presents an overlay of H I contours on a III-aJ photograph, this being the only H I data thus far published on this galaxy in full, and shows that the H I disc extends up to 11 disc scale lengths. This galaxy was observed for ∼ 100 hr with the VLA in D–array configuration by van Gorkom (1991). Maloney (1993) and Dove & Shull (1994a) published H I column density profiles based on the van Gorkom (1991) data but no full account of these observations has ever been published. We decided to retrieve the data from the VLA archive in order to use this object as a benchmark.

The VLA D–array observations of NGC 3198 reside in the public domain (VLA project ID: AS0283). The galaxy was observed over a set of 9 runs using three pointing

Table 2.2: Observational setup for NGC 3198 archive data

Parameter	Value	
Object	NGC 3198	
Instrument	VLA	
Configuration	D–array	
Project ID	AS0283	
Primary calibrators	3C48, 3C286	
Secondary calibrator	1031+567	
Central velocity	650 km s^{-1}	
FWHM of primary beam	32′	
Total bandwidth	6.250 MHz	
Number of channels	32 (out of 64 available)	
FWHP of synthesised beam	60.4″ × 54.0″	
Channel spacing	0.098 MHz	20 km s^{-1}
rms noise	0.22 mJy beam^{-1}	0.041 K

Table 2.3: Observational setup for NGC 3198 archive data - cont.

Field	α (1950)	δ (1950)	Observing dates (1987)	Time on source (min)
North	$10^h17^m34^s$	45 ° 57′ 45″	29 Mar	568
			24 Apr	572
			30 Apr	567
Centre	$10^h16^m52^s$	45 ° 47′ 60″	20 Apr	568
			28 Apr	572
			7 May	567
South	$10^h16^m10^s$	45 ° 38′ 15″	30 Mar	572
			25 Apr	574
			1 May	569

centres. Data were only taken in one polarisation (right hand circular). A total of 85.4 hr was spent on target. Table 2.2 and 2.3 summarises the observations. A standard observational setup was used, including two primary (3C48 and 3C286) and one secondary calibrator, 1031+567. The latter was found to have a flux density of 1.85 Jy. Only the central 32 velocity channels out of a maximum of 64 (after Hanning smoothing) spanning a bandwidth of 6.25 MHz were recorded.

All data reduction was performed using the 31DEC06 version of Classic AIPS using standard techniques. Channels 27 to 31 were used to determine the continuum background which was subtracted (using UVLIN), leaving only line emission. Final continuum subtracted *uv*–data sets were created for each of the three runs for each field and merged using the task DBCON.

Three data cubes were created with IMAGR, one for each field, using robust weighting and a robust parameter of 2. This was considered to be a good compromise between the sensitivity one would obtain with natural weighting and resolution obtainable with uniform weighting. This results in a beam size of $\sim 60.4\,'' \times 54\,''$. The maps were cleaned down to a level of 2.5σ. No residual scaling was applied to these maps (see Walter *et al.* 2008, for details).

We used a simple mosaicking to combine the fields. Taking the centre field as reference image we calculated the offsets of the the northern and southern fields in arcsec and projected them onto the same grid as the central field using the AIPS task LGEOM. We derived the rms noise in each of the fields so as to be able to assign proper weights to areas of overlap. We follow Brinks & Shane (1984) for combining the fields:

$$S^E = \frac{\sum_{i=1}^{n} S_i f_i}{\sum_{i=1}^{n} f_i^2} \tag{2.1}$$

where S^E is the optimum signal-to-noise map, S_i is the intensity at a grid point in a channel map of field i and f_i is the primary beam attenuation at a grid point of field i. After combining the three fields, we find an rms noise of 0.22 mJy beam^{-1} or 0.04 K. This corresponds to a sensitivity level of $4.5 \times 10^{18}\,\mathrm{cm}^{-2}$ ($3\,\sigma$ in a single $20\,\mathrm{km\,s}^{-1}$ channel). This is in good agreement with the $3\,\sigma$ rms noise level in a single channel of $4 \times 10^{18}\,\mathrm{cm}^{-2}$ quoted by Maloney (1993), assuming that he based his analysis on natural weighted data. Note that the quoted noise level applies to the area covered by the optical outline of NGC 3198. It increases with increasing distance from the galaxy due to the correction for attenuation by the primary beam.

We applied a similar blanking technique as Walter *et al.* (2008) to produce the final data cube. First, we convolved the data cube to a circular 75″ Gaussian beam. Individual channel maps were clipped at the 2σ level. We used as our criterion that genuine emission should be visible in at least 3 consecutive channels at or above the 2σ level. Once identified, all pixels outside these areas were blanked in the production of subsequent maps and their analysis. Finally we used the task XMOM to combine the individual velocity channels into an integrated H I map.

2.2 NGC 3198: comparing THINGS with archival D–array data

Figure 2.1 presents the integrated H I map of NGC 3198 based on the VLA D–array archive data, the same H I map overlaid as contours on a DSS image, and its velocity field. The lower right panel shows the THINGS map on the same scale. The H I extends well beyond the optical image on the DSS. Despite having served as the prototype for studying the edge of the neutral gas disc, the H I distribution is in fact far from regular. Towards the North some warping is evident while in the South the gas seems to break up in individual clouds, and spreads over a larger area. This is also reflected by the difference in extent: approximately 11.7′ (47 kpc) to the North and 8.8′ (35 kpc) to the South.

The velocity field shows a steep rise in the inner part reflecting solid body rotation, and a flat rotation in the outer regions at $\sim 150\,\mathrm{km\,s^{-1}}$. A rotation curve for NGC 3198 was derived by de Blok *et al.* (2008). They find a slight twist in position angle of 20 ° over the inner 200″ and an increase from 70 ° to 75 ° in inclination beyond 300″, indicative of a modest warp; de Blok *et al.* (2008) determined a systemic velocity of 660.7± 2.6 km $\mathrm{s^{-1}}$. All parameters are in good agreement with the rotation curve analysis by Begeman (1989). An independent check by us on the archival VLA data gave values in agreement with the above.

In Figure 2.2 we tried to reproduce as closely as possible the NE and SW major axis cross cuts featured by Maloney (1993). We read off the values from his Figure 8 and

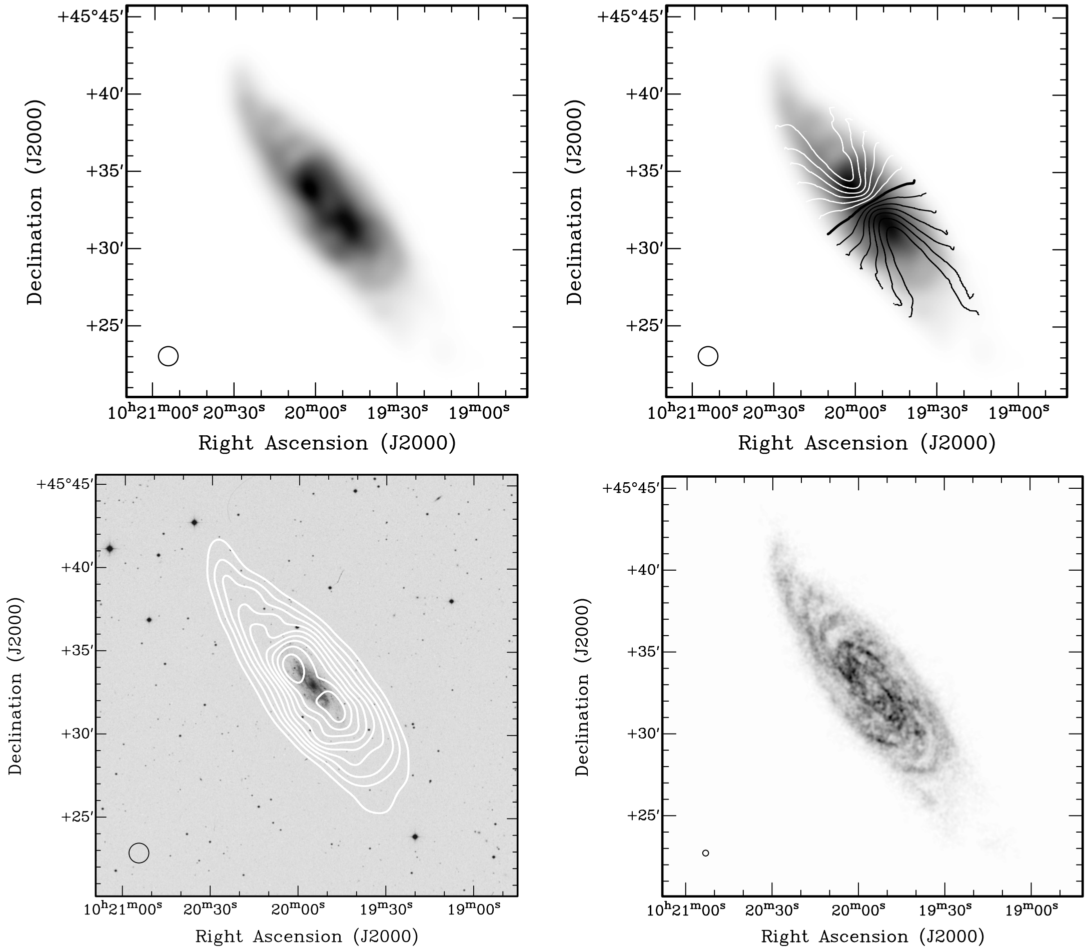

Figure 2.1: *Top left panel:* D-array H I surface brightness map of NGC 3198. The beam size is 60″ × 54″; *Top right panel:* velocity contours superimposed on the H I image. The contours are separated by 20 km s^{-1} . The thicker contour falls at 660 km s^{-1} , approximately the systematic velocity. The NE side (white contours) is receding; *Bottom left panel:* contours of the H I map superimposed on an optical image from the Digital Sky Survey. The contours range from 5 % to 95 % of a maximum intensity of 5 × 10^{21} cm^{-2}. *Bottom right panel:* THINGS H I surface density map of NGC 3198 created at a resolution of 10″. The size of the synthesised beam is indicated in each frame in the bottom left hand corner.

converted them to our adopted distance for NGC 3198 of 13.8 Mpc. At this distance $1'$ corresponds to ~ 4 kpc. We overplot Maloney's values on the cross cuts through the H I column density map we produced, choosing to show the entire major axis rather than a region near the supposed H I edge. The profiles, as expected, show a very similar behavior. The slight offset between his values and our H I profiles can be due to differences in the calibration and to Maloney having used slightly different values for the position angle and inclination. Small changes in the orientation parameters have quite a noticeable effect on the profiles.

There are a few issues with the data Maloney used in his paper. As already mentioned by him, the NE and SW halves of NGC 3198 look quite different. In fact, asymmetries and lopsidedness are characteristics shared by many presumably isolated galaxies, something we will return to below. In the case of NGC 3198, the H I map shows a lopsided distribution towards the NE, and what seems to be a cloud or clump at 50 kpc distance from the centre. The NE major axis cut appears the better behaved one, except that the sharp drop in column density might in fact be accentuated by the modest warp mentioned above.

Second, it merits pointing out that the drop in surface density seen in the data on which Maloney based his analysis, occurs over a single beam and therefore is basically unresolved. One therefore should not lend too much weight to the detailed shape of the decline and how this matches the observed H I profile because this profile merely reflects the beam shape. This is not to say that Maloney's conclusion that the edges to the H I discs of spiral galaxies are defined by an extragalactic radiation field is necessarily invalid.

Lastly, we should like to point out that no error bars are drawn given in Maloney (1993). We provide these in Figure 2.2 from where it is clear that any measurements below 10^{19} atoms cm^{-2}, despite showing a believable trend, are dominated by noise.

Maloney was well aware of the limitations of the data he used and suitably careful in their interpretation. What this does imply is that there is a need for observations at much higher resolution but with sufficient sensitivity to trace the edges of a sample of spiral galaxies. The idea is that at higher resolution, the edge of a galaxy can be resolved, adding another constraint to models trying to explain its detailed shape. Also, at higher resolution edges can be traced as a function of azimuth within the plane of the galaxy under investigation, and effects of lopsidedness and warps can be

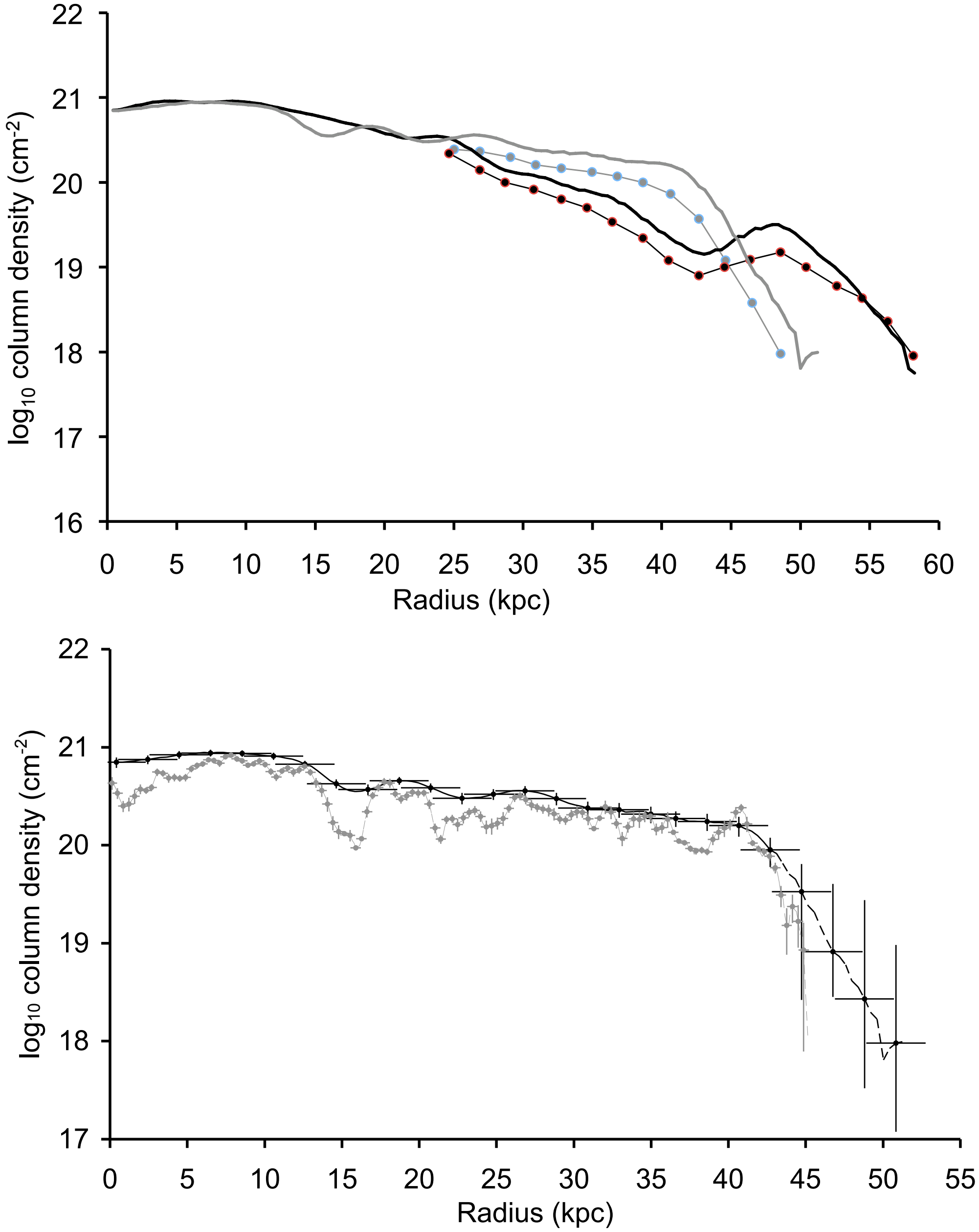

Figure 2.2: *Top panel:* Cross cut along the semi–major axis of NGC 3198 D–array archive data. The black thick line corresponds to the receding (NE) semi–major axis, the grey thick line, to the SW semi–najor axis. The dots connected by the thin solid lines (red for the NE and blue for the SW) reproduce the profiles presented by Maloney (1993). *Bottom panel:* Cross cut along receding semi-major axis with typical associated error bars. The black dashed line is based on the NGC 3198 D–array H I map; the grey dashed line is derived from the THINGS H I map. The vertical error bars are formal 1σ errors, the horizontal bars reflect the spatial resolution.

taken into account.

The THINGS survey has the potential to address the shortcomings of earlier observations. As can be seen in Figure 2.1, bottom right panel, at this resolution the integrated map reveals a wealth of fine–scale structure in NGC 3198 and shows much better any asymmetries, and their origins, in the H I radial distribution described above. In Figure 2.2 (top panel) we overplot radial H I profiles through the residual flux and primary beam corrected THINGS H I surface brightness map, along the same principal axes as shown in Fig. 2.2 (bottom panel) but this time we provide error bars to our data points. The radial profile is sampled at 10″ intervals. The profiles match closely, the THINGS profile showing, of course, more substructure. The slight offset in flux level is due to the fact that the residual flux correction was applied to the THINGS data and not to the archive data. The surface density drop at the H I edge is now resolved, extending across 9 beams. The sensitivity, taken again as a $3\,\sigma$ detection in a single channel (of $5\,\mathrm{km\,s^{-1}}$ rather than $20\,\mathrm{km\,s^{-1}}$) is a respectable 2.5×10^{19} atoms $\mathrm{cm^{-2}}$. Although this sensitivity level, as we will see in the following, probes column densities corresponding to radii where the H I has set in its precipitous drop, some processing is required in order to follow this drop further in radius.

2.3 Potential biases in the analysis of H I edges

2.3.1 The impact of blanking THINGS data cubes

Having demonstrated the need for high sensitivity, high resolution data, we will argue that the THINGS sample is eminently suited for a study of the edge of the atomic gas disc in spirals. At this point it is important to note that all analysis on integrated H I maps is usually performed on maps which were created from data cubes which have undergone considerable processing before collapsing the data along the velocity axis. This processing is often based on some conditional blanking (e.g., the task MOMNT in AIPS). This blanking introduces a subtle bias and the process could conceivably create an edge. In the particular case of THINGS, we used a cube convolved to a resolution of 30″ as a mask for conditional blanking of the 10″ resolution data analysed here (with the additional requirement that emission needs to be present in

3 consecutive channels above the 2σ level in the $30''$ cube; see Walter *et al.* (2008) for details). We subsequently used AIPS task XMOM to integrate the cube along the velocity axis. In the next few paragraphs we will assess what the effect this blanking has, if any, on the radial profiles.

We decided to run these tests on NGC 3351, chosen for its fairly symmetrical H I distribution. As a first test we took a $10''$ data cube created without the residual flux scaling correction (Walter *et al.* 2008) and used the AIPS task SQASH to create an integrated H I map without any blanking applied, simply adding the emission from all channels which were found to contain line emission. The result is shown in Fig. 2.3 which compares the integrated H I map thus produced with the THINGS $10''$ map. The noise in the former is much higher (by a factor of 5 on average). This can be understood as follows. The noise in neighboring channels is virtually uncorrelated (note that the spectral line data were Hanning smoothed online and that the VLA online system only stores every other channel). In the map created by SQASH, the noise therefore increases according to $\sqrt{n}$ where n is the number of channels added. In those channels where emission is present, the signal adds linearly. In a map created using conditional blanking, for each pixel only channels containing emission are added, greatly reducing the number of channels involved and hence reducing the noise. Calculating the noise as a function of position becomes a bit more involved but is facilitated by a map, provided as part of the output from XMOM which keeps track of the number of channels, n, which contribute to the sum produced at each pixel. The noise in each pixel can then again be calculated by taking $\sigma\sqrt{n}$. In all maps and profiles shown, we corrected for primary beam attenuation which is a simple multiplicative factor increasing outwards from the pointing centre. This factor affects all maps of NGC 3351 in a similar manner.

Fig. 2.4 compares a radial profile taken through both maps, along the receding major axis. The grey band shows the profile and associated uncertainty through the conditionally blanked data. The dots correspond to the SQASH map. In the latter only a few error bars at representative radii are plotted, for clarity. Both profiles present the same global behavior, pointing towards a decline when moving to larger radial distances. In the case of the SQASH map, the rapidly increasing noise contribution severely limits a study of the peripheral region, though.

The problem with using SQASH is that along each line of sight only few, of order

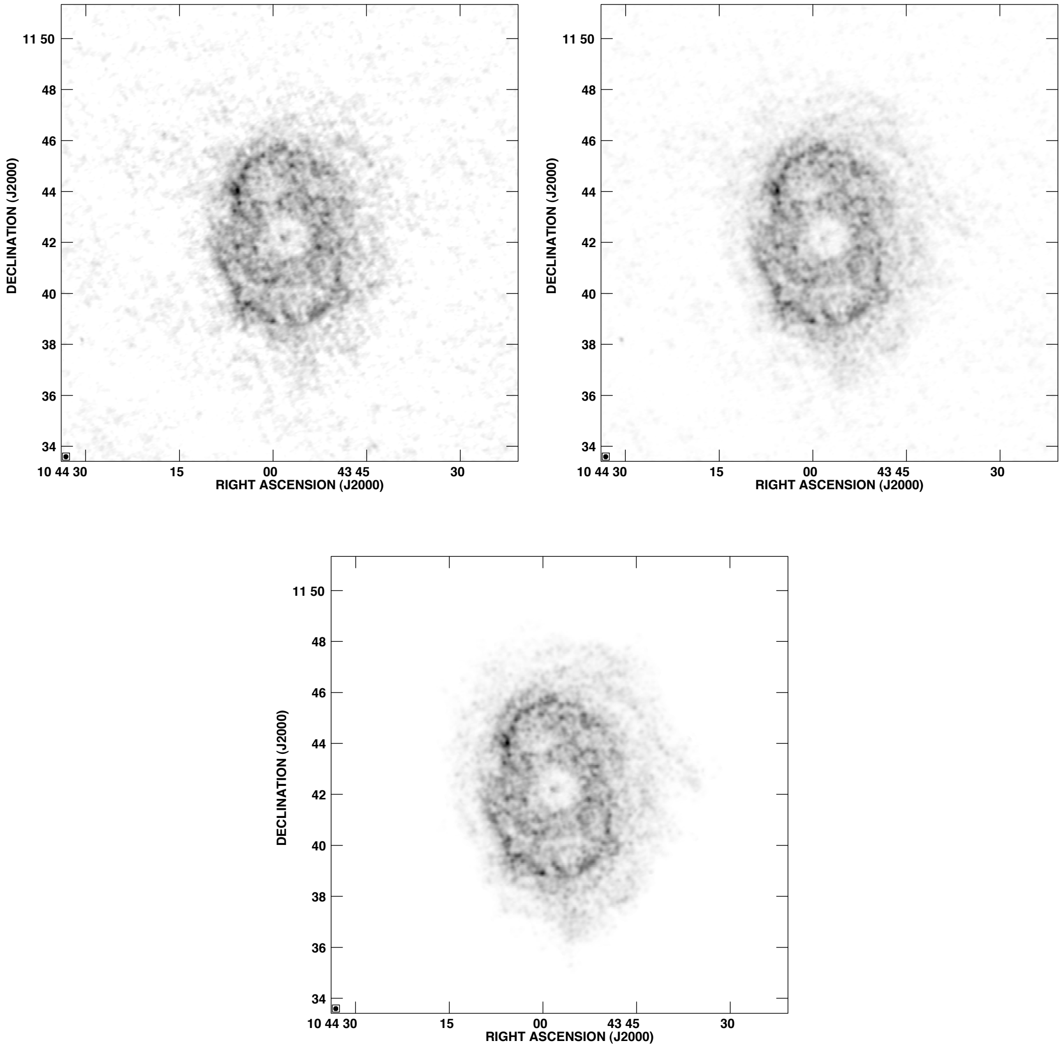

Figure 2.3: *left panel:* A non-blanked H i map of NGC 3351 obtained by brute summing the emission channels, using AIPS task SQASH; *middle panel:* A non-blanked H i map of NGC 3351 obtained via the GIPSY task SHUFFLE; *right panel:* The moment zero integrated H i map of NGC 3351 as derived by the AIPS task XMOM after applying the blanking as described in the text.

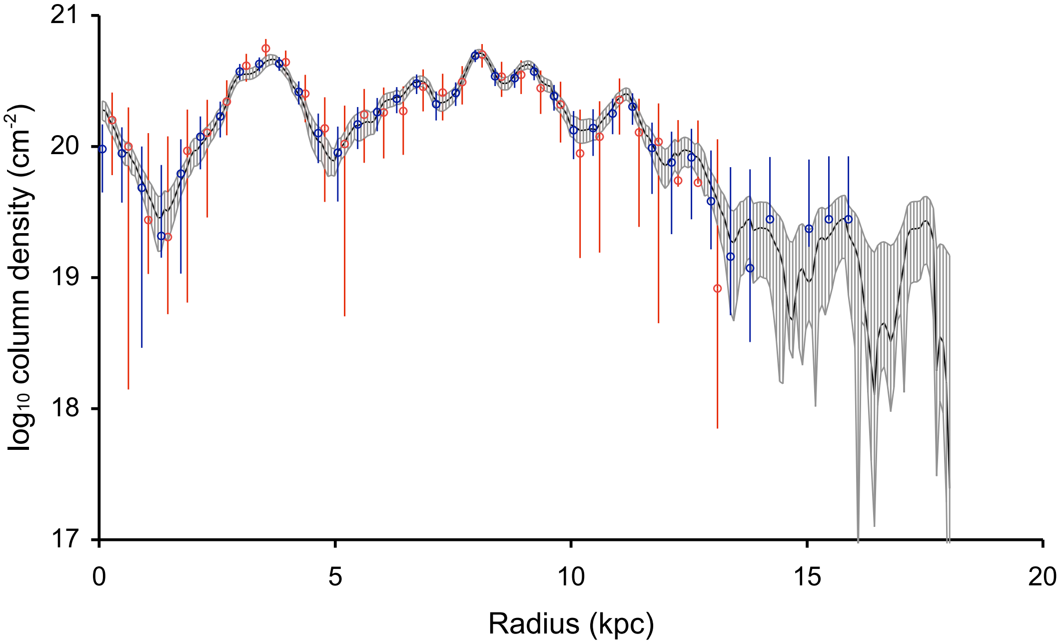

Figure 2.4: Radial H I surface density profiles based on maps of NGC 3351 made in three different ways. The thin black line correspond to the map based on the blanked H I data cube. The vertical grey lines represent the corresponding 1σ uncertainty. The blue open circles plus error bars represent the radial profile obtained after using the GIPSY task SHUFFLE. The radial profile based on a simple SQASH is represented by the the open red circles, again plus error bars.

10 channels contribute to the total H I column density while another 60 or so only contribute noise. The channels contributing emission change with location on the sky, their centroid being given by the mean velocity of the H I at a particular location and the range of channels set mainly by the velocity dispersion of the gas. The Groningen Image Processing SYstem (GIPSY) reduction package (van der Hulst *et al.* 1992) contains a task called SHUFFLE which takes out the overall velocity field across the galaxy by shifting the velocity centroid of each spectrum to make it coincide with the systemic velocity. After applying SHUFFLE we proceeded with another SQASH but this time adding emission across 16 SHUFFLEd channels only, greatly reducing the noise compared to the map produced with SQASH. In order to be able to shift (shuffle) the spectra, one needs a velocity field for SHUFFLE to work with. We used the GIPSY task ROTCUR to find the rotational velocity and geometrical parameters for our target (see de Blok *et al.* (2008) for details). We then produced a model velocity field using the GIPSY task VELFI. This has the benefit that small deviations from circular rotation and regions where the observed velocity contains blanked values, are replaced by a sensible expected value. An added advantage is that we can extrapolate the map created by VELFI to extend beyond where the H I in individual channels fades to below the detection threshold.

The result of this exercise is also shown in Fig. 2.3 where we use the same grey scale as for the other two maps we already discussed. There is a notable improvement in the sense that the rms noise has decreased with respect to the SQASH map. We add in Fig. 2.4 a radial profile taken through this SHUFFLEd map to compare it with the conditionally blanked result. The profile closely follows that of the conditionally blanked version and there is no evidence, in any of the maps, that blanking introduces any artifacts, nor limits the apparent extent of the H I disc.

2.3.2 Other biases

As explained previously, the THINGS maps are residual flux corrected, so for completeness we compared our results against an integrated map created without residual flux correction but which has undergone otherwise exactly the same treatment (conditional blanking, primary beam correction, etc.). The difference is negligible. This can be understood as any correction *locally* is very small, at the $1 - 2\sigma$ level and any effect only becomes appreciable when integrating over a substantial area. On a related note, the noise characteristics of the residual flux corrected maps becomes a hybrid (we refer the reader to Usero *et al.* (2010), for a detailed account of the subtle effects involved). Those areas which contain emission, however, preserve the noise characteristics of the clean components, i.e. the noise before scaling. Throughout the chapter we quote this slightly higher, but more correct value.

Finally some comments regarding another effect which might be influencing our results which is the absence of short spacings in our data. Structures larger than a set size will not be seen by an interferometer like the VLA. The full synthesis observations obtained by THINGS should recover emission at scales of up to $15'$. Even in the unlikely event of less than ideal *uv*–coverage of the shorter spacings, emission at spatial scales half this extent should definitely be recovered. The high quality of the final THINGS data cubes and absence of a depression or "negative bowl" surrounding emission attest to this. Scales of several to 10 arcmin are much larger than the typical scale length of the observed edges (less than $1'$) which is why we feel confident that they are not affected, and even less so caused by this effect.

2.4 Analysing radial profiles: NGC 3351

Although the THINGS data reach down to surface densities as low as 2.5×10^{19} atoms cm^{-2}, ideally one would like to reach sensitivities nearer to that achieved on NGC 3198 (van Gorkom 1991) in order to be able not only to determine where the edge sets in, but to determine its shape as a function of radius. Naively, to increase the sensitivity one might suggest to simply produce a radial profile integrating in annuli in the plane of the galaxy (ellipses in the plane of the sky with orientation parameters derived, for example, on the basis of a fit to the velocity field). This does not work, however. Figure 2.5 show a version of the H I distribution of NGC 3351 corrected to face–on. This was achieved by first rotating the $10''$ resolution H I map by an angle of $-(PA + 90)$ degrees so as to put the major axis of the galaxy East–West. The next step was to stretch this map along the minor axis direction by a factor of $(\cos\, i)^{-1}$. As can be seen, the gas in the outskirts is far from symmetric, showing distinct morphological lopsidedness. Lopsidedness is quite a common phenomenon and significant asymmetries are routinely found in galaxies (Richter & Sancisi 1994;

Haynes *et al.* 1998; Noordermeer *et al.* 2001).

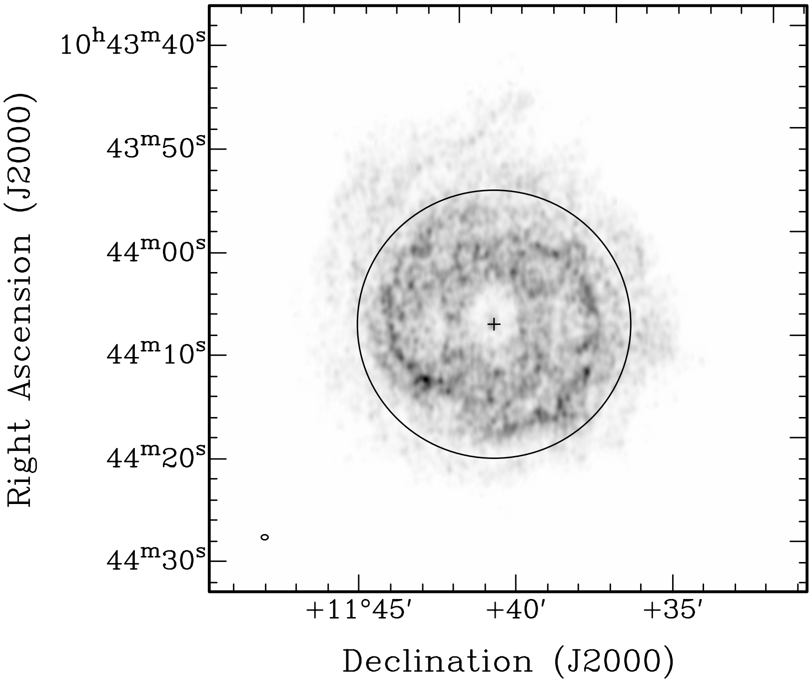

Figure 2.5: De–projected integrated H I map of NGC 3351. The major axis is oriented East–West. The circle represents a radius of 15 kpc.

If we were to average the H I surface density map in rings over 360 ° in azimuth we would in the outskirts lump together areas without emission with parts that have, leading at best to a washing out of the signature of a sharp edge, but more likely to a decrease which is not a reflection of the intrinsic shape of the surface density profile. Instead of averaging along the entire circumference, we chose a 30 ° sector centered on the major axis and averaged along a 30 ° wide arc in 10″ radial bins. We plot the resulting radial profile for NGC 3351 in Fig. 2.6 (top panel) produced with the GIPSY routine ELLINT. The decrease in signal–to–noise ratio when moving outwards is compensated for by the effect of averaging over larger arcs at the edge of the galaxy, increasing the number of independent beams contributing to the average. A segment with an opening angle of 30 ° was considered to be a good compromise, reducing the noise substantially without artificially smoothing any sharp edge. The task ELLINT requires as input parameters the position angle of the receding major axis, PA, inclination, i, and central position. We used the average values reported by de Blok *et al.* (2008), and listed in Table 1.1.

Map units are corrected to face–on surface densities by ELLINT. The units (Jy beam^{-1} m s^{-1}) are converted to column densities according to:

$$N_{\mathrm{HI}} = 1.8224 \times 10^{18} \times \sum_i T_B(V_i)\Delta V \tag{2.2}$$

where $T_B(V)$ is the surface brightness temperature (in K) in velocity channel i, and ΔV is the channel width (in km s^{-1}). The relation between brightness temperature and source flux density S (Jy beam^{-1}) is in turn given by:

$$T_B = S \times \lambda^2 \times (2k \times 1.133 \times \theta_B^2)^{-1} \tag{2.3}$$

where λ is the wavelength, k the Boltzmann constant, and θ_B the FWHM of our circular $10''$ beam. We find that 1 mJy beam^{-1} corresponds to a T_B of 6.1 K.

In order to calculate the rms noise in the radial profile, we evaluate at each point in the map the noise depending on the number of channels contributing to the integrated H I map as explained above. After applying ELLINT we evaluate how many independent beams, n_B (the number of pixels divided by the number of pixels beam^{-1}), contribute to each $10''$-wide arc in a 30 ° sector and divide the noise by $\sqrt{n_B}$.

Figure 2.6 (top panel) presents the ELLINT averaged profile for a 30 ° sector of NGC 3351 along the receding major axis. In addition to the profile being overall smoother and less noisy than a simple 1–pixel wide cut along the major axis, we can now follow the N_{HI} profile reliably down to levels of 2.0×10^{18} atoms cm^{-2} , well below what could be reached in a simple radial profile. The profile can be traced to even lower surface brightness levels, but at lower significance. We confirm that the edge of NGC 3351 is sharp, N_{HI} dropping steeply from 18 kpc onwards.

Obviously, if a single cause lies behind the observed steep drop, there should not be any difference with where we choose a particular 30 ° sector. To investigate this we divided NGC 3351, into twelve 30 ° sectors and calculated a radial profile for each. The bottom panel of Fig. 2.6 presents the individual sector profiles. Although the angular resolution is the same at $10''$, the linear resolution in the plane of the galaxy

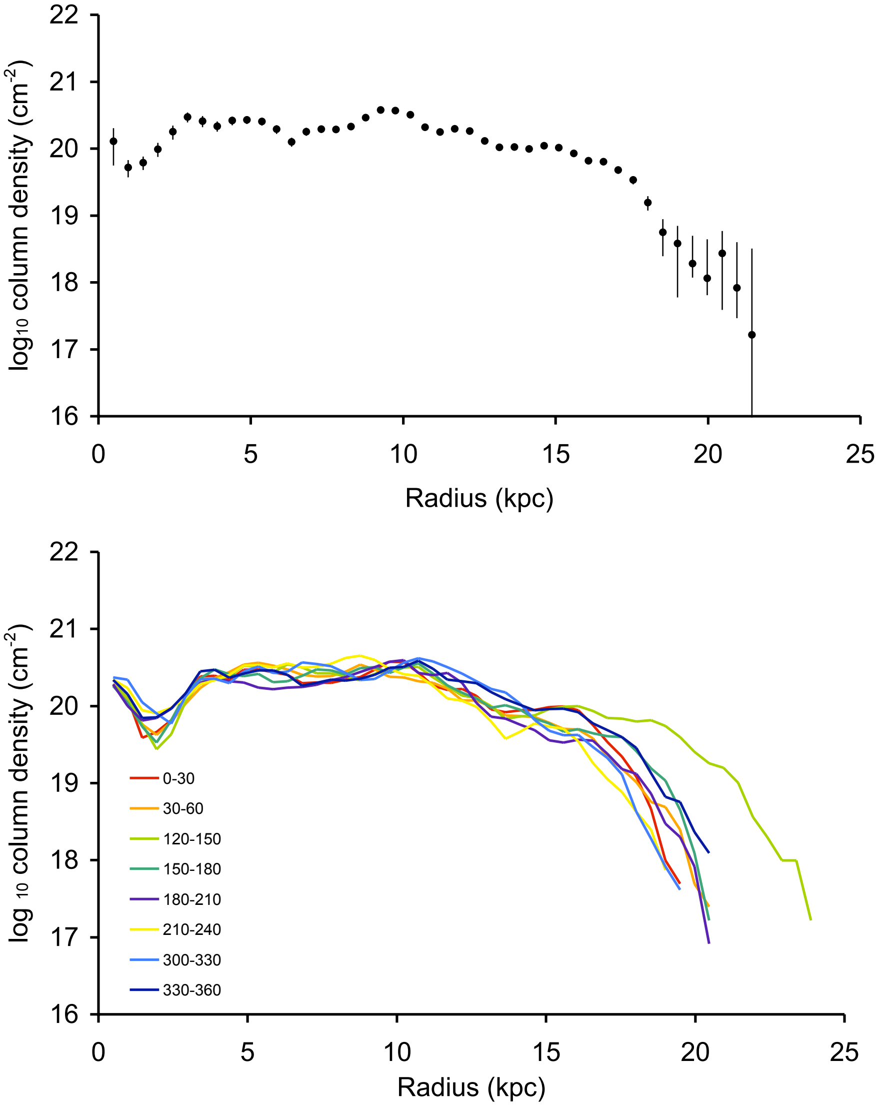

Figure 2.6: *Top panel*: Radial surface brightness profile of NGC 3351 obtained with ELLINT, in a sector with opening angle of 30° centered on the receding major axis; *Bottom panel*: Radial H I column density profiles derived within 30° sectors

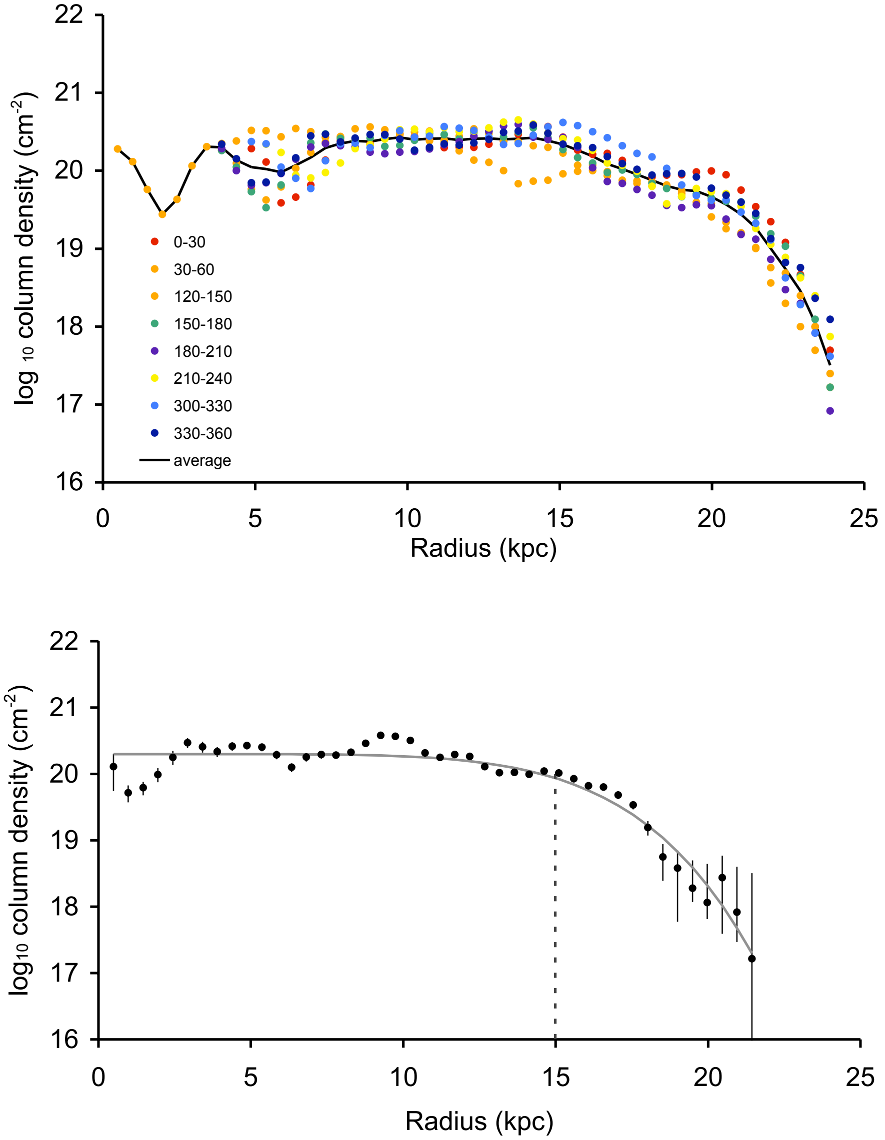

Figure 2.7: *Top panel*: this shows all profiles with their outer edge aligned with the 30–60° sector and the resulting averaged profile (solid line). Due to the alignment of the profiles, the radial units become physically meaningless, with the exception of the 30–60° sector. *Bottom panel*: Sérsic–like fit applied to the sector displayed in the top right panel (grey solid line). The dashed vertical represents the inflection radius r_i.

varies, the resolution becoming lower near the minor axis (see Table 2.1). For this reason, we will exclude from now on the 4 sectors bordering the minor axis, excluding effectively a 60 ° wedge centered on the minor axis. We see that there is very little variation from sector to sector within the inner 12 kpc. Beyond that radius, all profiles show a break followed by a steep drop. The location of the break varies, reflecting the fact that the H I distribution is lopsided.

We shifted the profiles in order to spatially align their outer edges. We took the $30° - 60°$ sector which extends out to 21.5 kpc, as the reference to which all other slices were aligned. This is shown in the top panel of Fig. 2.7. As can be seen from this graph, the edges look remarkably similar, lending support to the assumption that all regions of a galaxy are affected similarly. Note that the profiles need to be *shifted* and not normalized to some common scalelength. Stretching a profile would alter the slope of the edge, which is exactly what we need to avoid if we wish to study the detailed shape of the edge of NGC 3351.

As a final step we decided to average the 8 profiles into a single one (see Fig. 2.7, bottom panel). In doing so we avoid the problem of lopsidedness which would have plagued us if we would have performed a full 360 ° ELLINT average. Obviously, one should only consider the outer 5–10 kpc of this graph for further analysis, i.e., the averaging only makes sense for the outermost reaches of the H I disc (within, say 12 kpc one could average the profiles without shifting them; this would be equivalent to running an ELLINT, integrating over 360 °). The additional averaging reduces the noise by another factor of ~ 3, allowing us to reach a level of 6×10^{17} atoms cm^{-2} , even deeper than that achieved with the 100 hr archival VLA D–array data, but at 5× better resolution in the radial direction.

In all this we have assumed that the observed surface density profile is a true representation of the intrinsic H I distribution. It is not immediately obvious why this should be the case as a line of sight will traverse a disk of finite thickness, whose scaleheight may be appreciable in the outer regions, leading to all sorts of beam and line–of–sight smearing. We investigate this in great depth in the next chapter, Chapter 3. Suffice to say that projection effects tend to be negligible, except for galaxies where flaring of the outer disks is extreme, or that are seen nearly edge–on in which case the observed profile departs quite dramatically from the intrinsic surface density distribution. This holds true for simple 1–pixel wide profiles as well as for averages over 30° sectors, and is independent on azimuth in the galaxy.

2.5 Profile parameterisation

2.5.1 Sérsic profiles

Initially we attempted to fit a broken exponential to the radial profiles. This was unsatisfactory, though, as the fits depended on where we judged the break to lie and which points to use, especially for the fit to the edge. Also, the H I profile in the inner part is remarkably flat, resulting in an exponential with infinite scale length which becomes meaningless.

We therefore searched for a different parameterisation of the profiles and adopted a Sérsic $r^{1/n}$ relation (Sérsic 1968), a description which is largely applied to fit the luminosity profiles of early type galaxies. The Sérsic $r^{1/n}$ relation in its simplest form can be written as follows:

$$I(r) = I(0)\, e^{-cr^{1/n}} \tag{2.4}$$

where $I(0)$ is the central intensity, r the radius, c is a constant, and n is the Sérsic index. Graham (2001) and Trujillo *et al.* (2001) prefer a slightly modified representation where the radius is normalized by the effective radius, r_e, which encloses half of the light and then proceed to discuss the relation of Sérsic index, n, and effective radius for elliptical galaxies. For reference, an exponential profile has $n = 1$ and the well–known $r^{1/4}$ law for elliptical galaxies has $n = 4$.

As will be shown below, we are finding values for n more like ~ 0.2. This results in profiles which are flat from the origin until a characteristic radius at which point the value drops rapidly, and subsequently eases towards zero intensity. The Sérsic index n controls the steepness of the drop. Rather than using r_e we prefer a slightly different parameterisation where we normalize the radius by r_i instead. For values of $n < 1$, r_i is defined as the radius where the slope reaches maximum steepness before flattening off. This occurs where $\partial^2 I(r)/\partial r^2 = 0$ which is where $r_i^{1/n} = (1-n)/c$. Therefore r_i, being more related to the location of the edge, is more appropriate than r_e. We can then write the Sérsic law in terms of r_i as:

$$I(r) = I(0)\, e^{-(1-n)\left(\frac{r}{r_i}\right)^{1/n}} \tag{2.5}$$

We fit the above relation to curves of the logarithm of the surface density. So, for fitting purposes we adopted the relation :

$$logI(r) = logI(0) - 0.4342 \times (1-n)\left(\frac{r}{r_i}\right)^{\frac{1}{n}} \tag{2.6}$$

Fig. 2.7 (bottom panel) shows the fit to the major axis profile of NGC 3351 (see also Table 2.4). $\log I(0)$ controls the level of the flat part of the surface density profile, say within R_{25}. The location of r_i is indicated by a vertical dashed line. The slope in the outer part is set by the slope index n.

Fig. 2.8 shows in a bit more detail the dependence of the shape of the fitted curve on n. The top panel shows, for three representative values of n (but for fixed r_i), the shape of the curve plotted on a linear scale; n determines the steepness of the decline and r_i is located where the slope is steepest. The bottom panel shows the same results, but with the intensities plotted on a logarithmic scale.

At this point it is useful to reflect upon the significance of r_i. At this radius, the H I surface density will have dropped to $e^{-(1-n)}$ or for $n \approx 0.2$ we find that $I(r_i) \approx 0.45 I(0)$ or a few $\times 10^{20}$ atoms cm^{-2}. Although this is a significant drop, it is thought to be well above the level at which ionization due to an extragalactic radiation field has any effect. Although there might be some merit in determining a fit to r_i for each individual segment and to align the profiles by r_i, all this will do is align the segments so they coincide where the H I column density has dropped by about 50%, but this is not where we see that the edge of the detectable neutral atomic gas is found, which is at column density levels an order of magnitude lower. In other words, to study what goes on at the true edge, we need to shift the profiles such that the outskirts overlap. This is illustrated in Fig. 2.9 which shows in the top panel column density profiles through NGC 3351 of individual sectors, all aligned to one and the same r_i. In the bottom panel we show the same kind of graph for NGC 925. Here we clearly see the effect of the H I distribution being lopsided which has the effect of distributing the H I over a larger extent in projected radius. This unfortunately implies that there is no easy, objective way to average the 8 sectors,

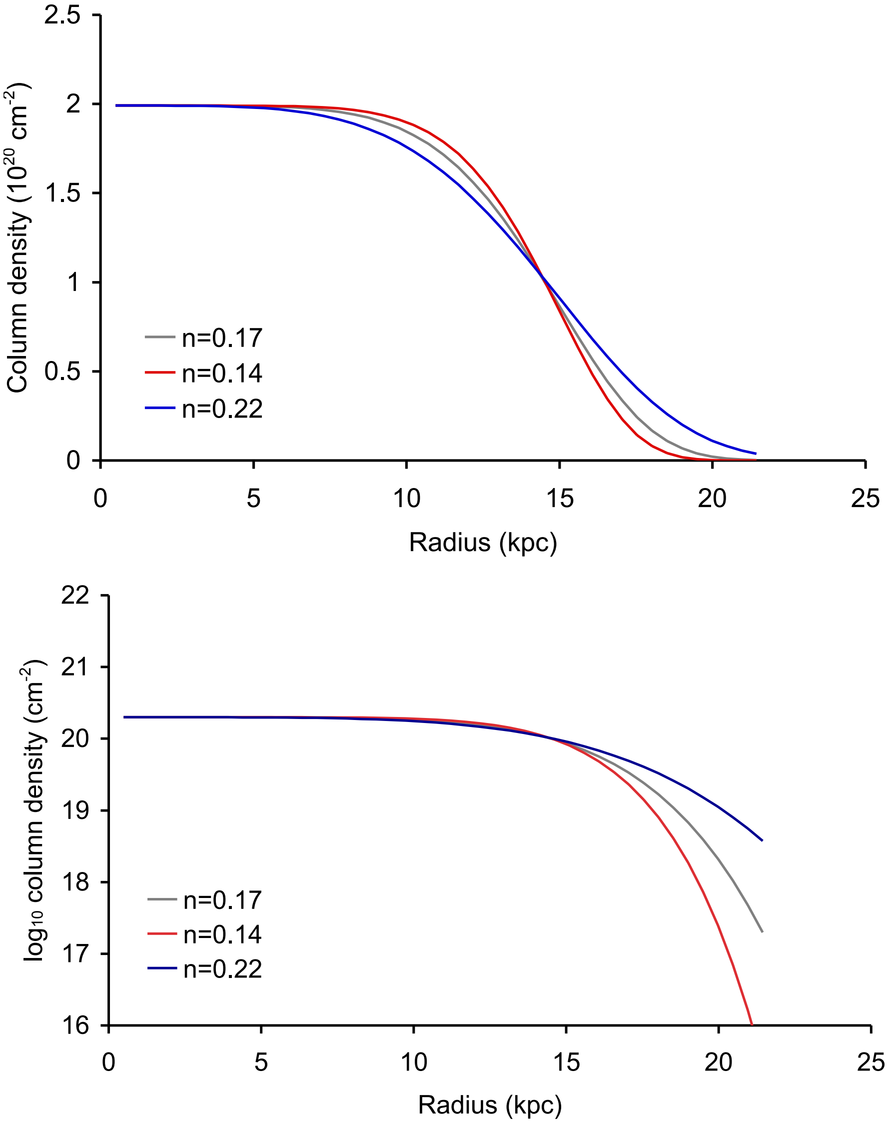

Figure 2.8: Exploring Sérsic-type fits, showing variations with n.*Top panel:* linear intensity scale; *Bottom panel:* logarithmic intensity scale.

either by normalizing the radial profiles by r_i or by aligning (shifting) the profiles so the individual r_i's align, and then apply the Sérsic–type fit. As explained in the previous section, to study the H I in the outskirts, the individual sectors would need to be aligned "by eye" so the edges line up.

Table 2.4: Sérsic $r^{1/n}$–style fit applied to a single 30° sector around the major axis.

object	$\log I(0)$ atoms cm^{-2}	r_i atoms cm^{-2}	n kpc	H I Mass 10^9 $\mathcal{M}_\odot$	χ^2_{red}
NGC 925	20.87 ± 0.19	15.36 ± 1.80	0.17 ± 0.05	4.19	1.14
NGC 3184	20.69 ± 0.20	16.62 ± 1.87	0.14 ± 0.05	3.20	0.99
NGC 3198	20.59 ± 0.15	35.23 ± 3.77	0.16 ± 0.05	11.50	1.48
NGC 3351	20.30 ± 0.21	14.99 ± 2.30	0.17 ± 0.07	1.07	2.06
NGC 3521	20.99 ± 0.16	22.85 ± 2.31	0.16 ± 0.04	12.20	1.16
NGC 3627	20.73 ± 0.28	7.72 ± 2.09	0.22 ± 0.12	0.80	1.52
NGC 5194	20.80 ± 0.20	6.77 ± 2.71	0.33 ± 0.15	0.86	1.24
NGC 7331	20.80 ± 0.20	23.93 ± 4.18	0.18 ± 0.09	8.70	1.69
NGC 7793	21.01 ± 0.20	6.23 ± 1.18	0.21 ± 0.09	0.98	1.05

2.5.2 Application to the THINGS subsample

The above methodology has been applied to all galaxies in our sample. Figures 2.10 and 2.11, show for each candidate the deprojected integrated H I map. As mentioned in Section 2.4, discs do not present a perfectly symmetrical H I distribution, as amply demonstrated by these maps.

As was done for NGC 3351, single sector profiles were produced with an opening angle of 30 ° centered on the receding major axis. The exception is NGC 5194 which, due to the tidal interaction with its companion, forced us to narrow the opening angle to 15 ° around the approaching major axis. Figures 2.12 to 2.15 show for each object a single sector averaged radial profile and Sérsic–type fit. Table 2.4 summarizes the results of this parameterisation in terms of fitted values for $I(0)$, r_i, and n. In addition to these we also present values of the H I mass as derived by (Walter *et al.* 2008).

Figs. 2.12 to 2.15 show the generally good fits, especially in the outer parts of

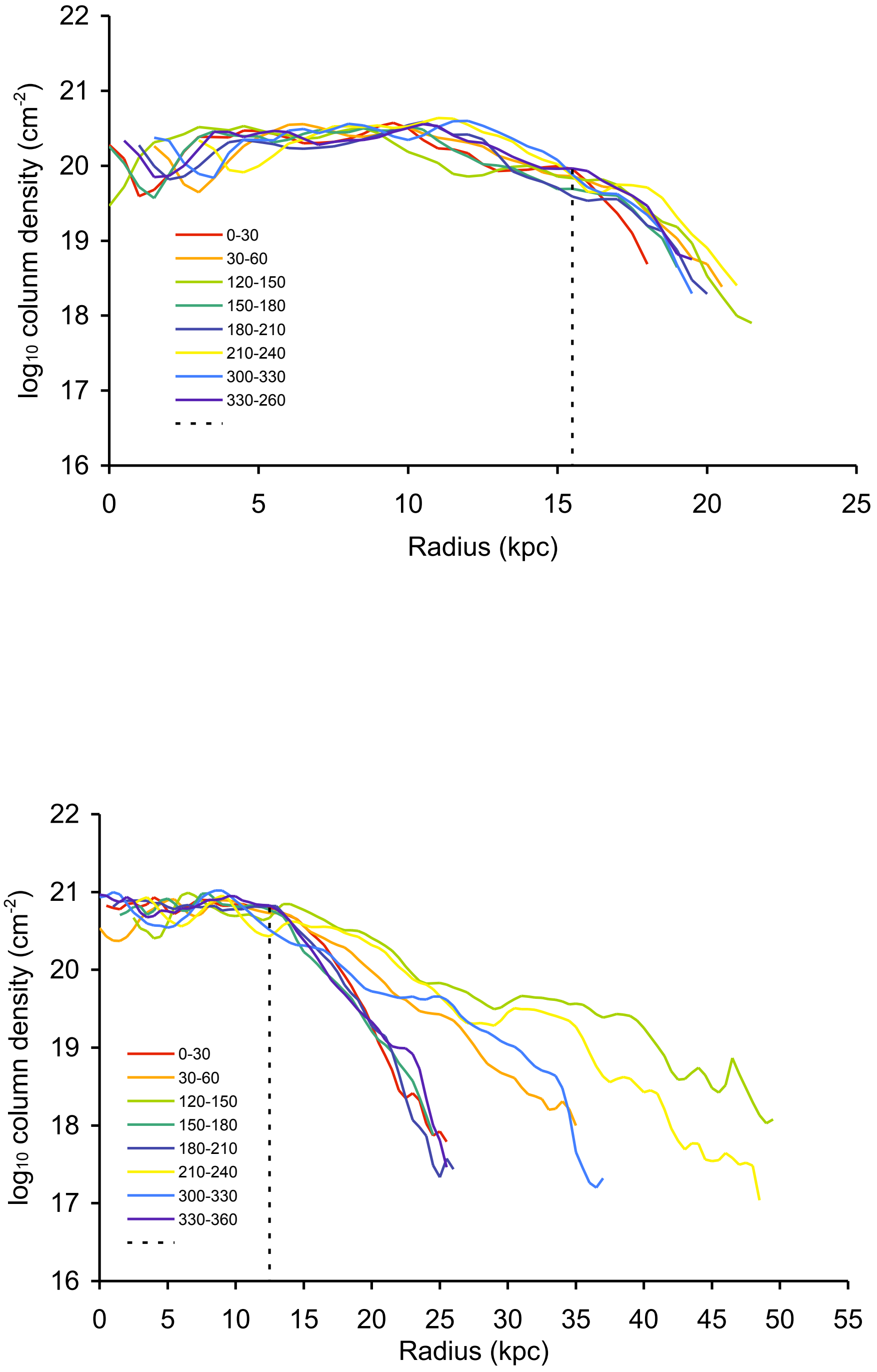

Figure 2.9: Aligning column density profiles obtained per 30° segment by r_i . *Top panel:* NGC 3351; *Bottom panel:* NGC 925

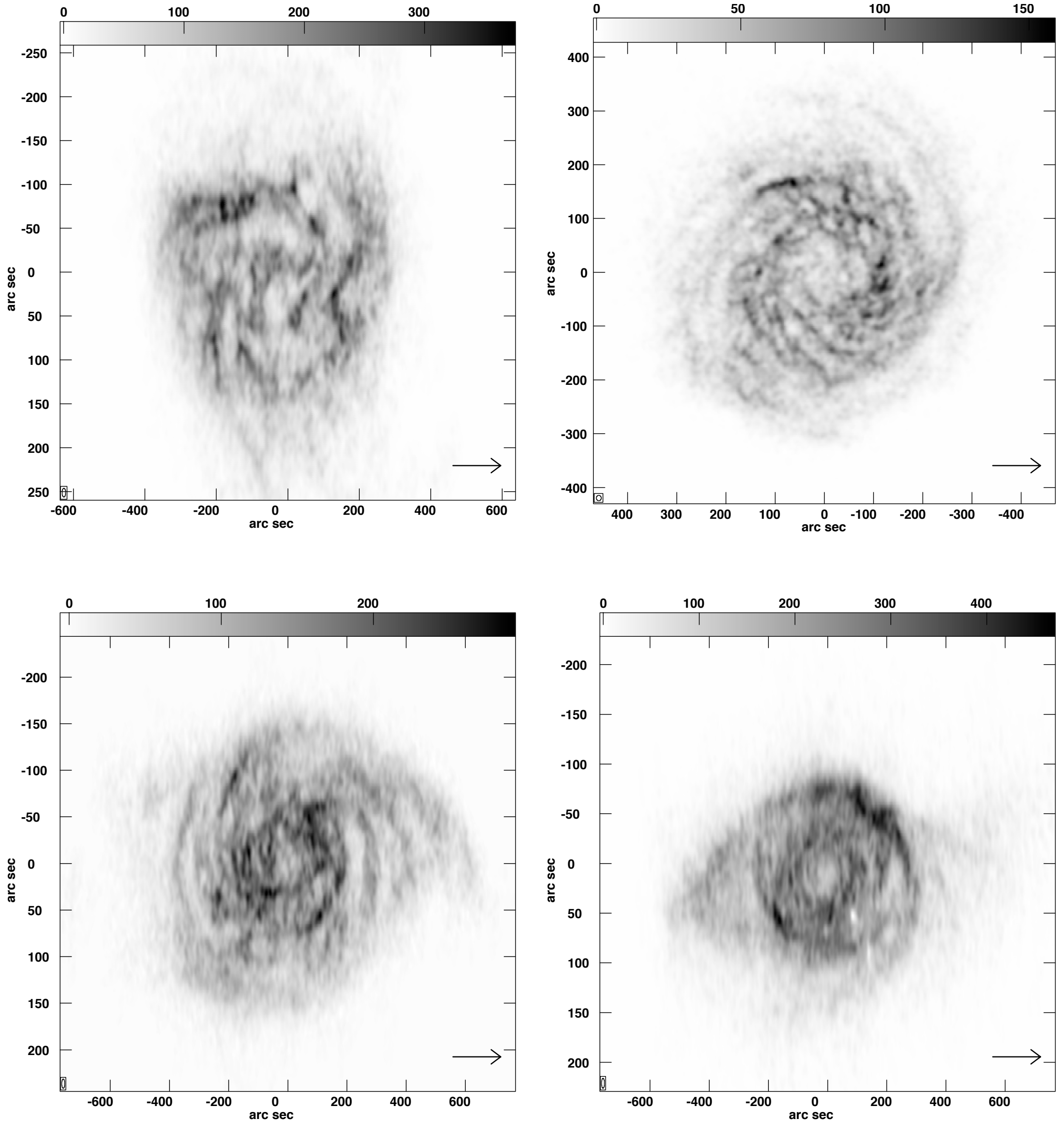

Figure 2.10: Deprojected integrated H I maps of: (from top to bottom, left to right) NGC 925, NGC 3184, NGC 3198 and NGC 3521. The arrow indicates the direction of the receding major axis of the galaxy. The respective deprojected synthesised beams are plotted in the bottom left corner of each map.

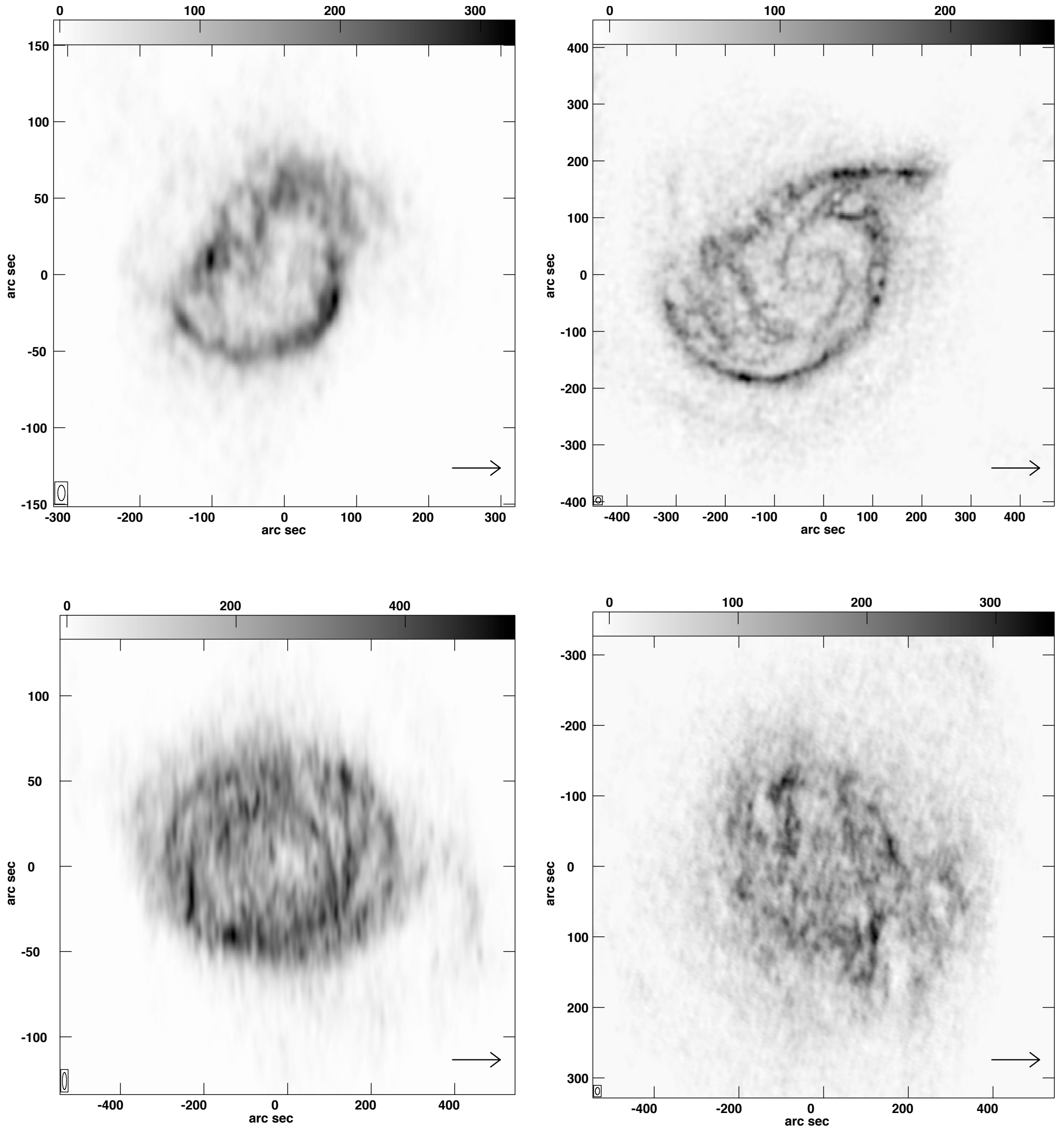

Figure 2.11: De-projected integrated H I map of: (from top to bottom, left to right) NGC 3627 , NGC 5194 , NGC 7331 and NGC 7793. The arrow indicates the direction of the receding major axis of the galaxy. The respective deprojected synthesised beams are plotted in the bottom left corner of each map.

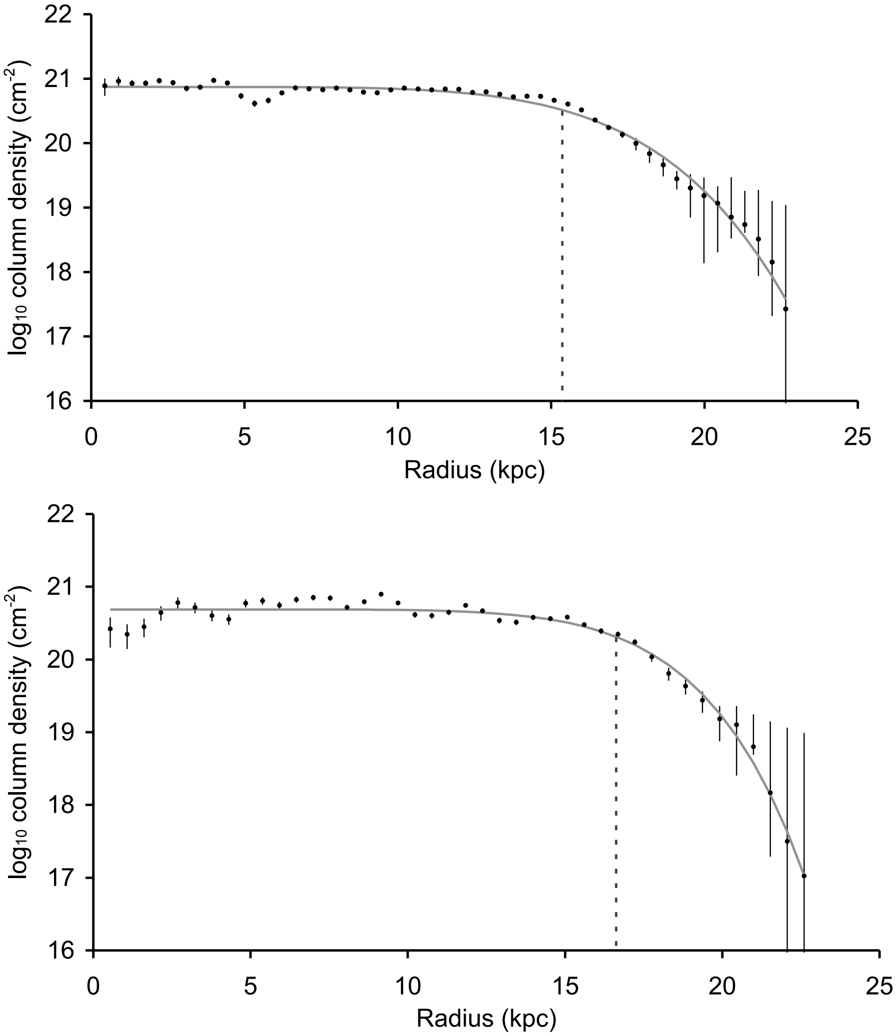

Figure 2.12: Sérsic fitting to the 30° sectors around the receding major axis and respective r_i radius represented by the vertical dashed line. From top to bottom: NGC 925 and NGC 3184.

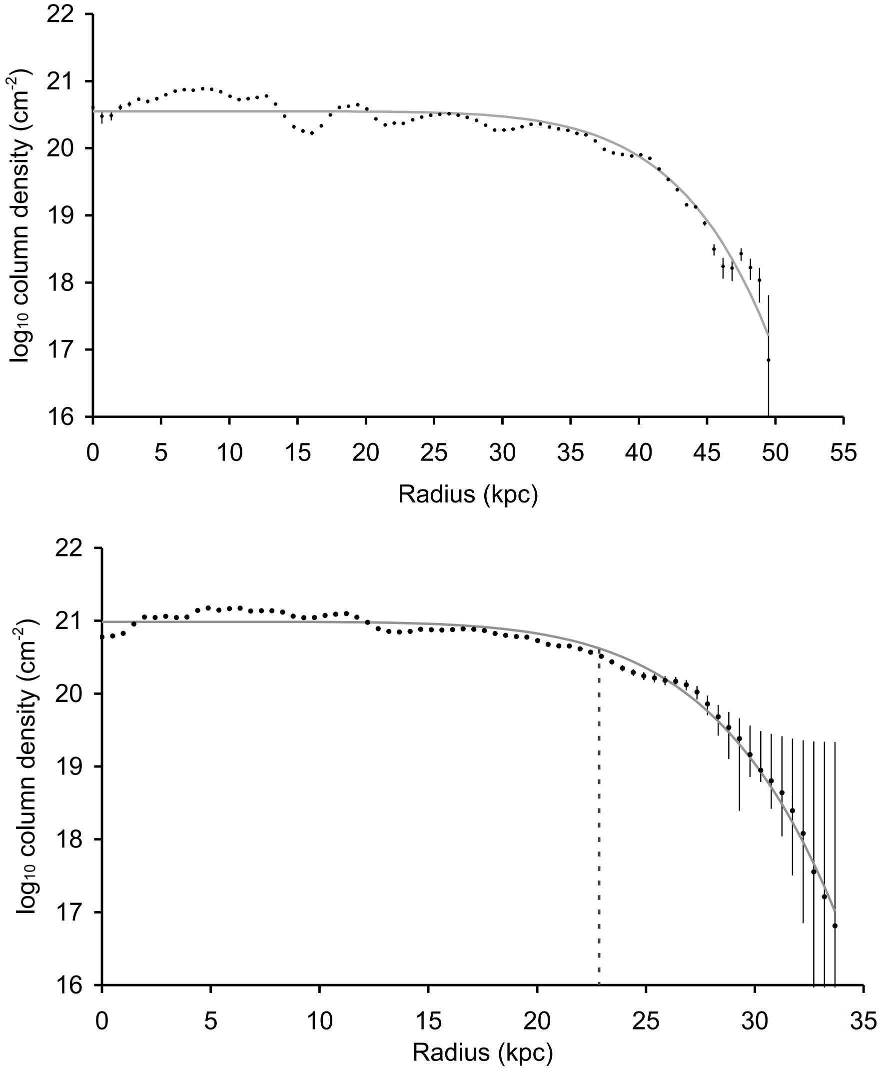

Figure 2.13: Sérsic fitting to the 30° sectors around the receding major axis and respective r_i radius. From top to bottom: NGC 3198 and NGC 3521.

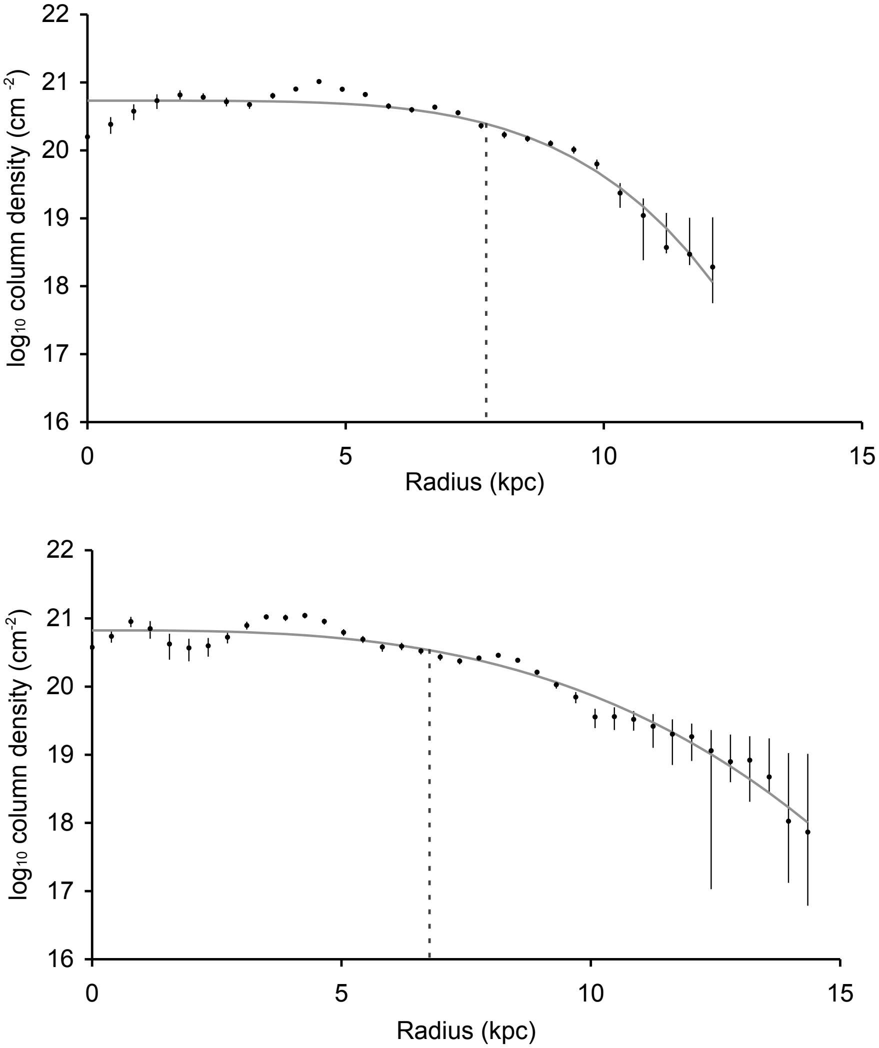

Figure 2.14: Sérsic fitting to the 30° sectors around the receding major axis and respective r_i radius represented by the vertical dash line. From top to bottom NGC 3627 and NGC 5194.

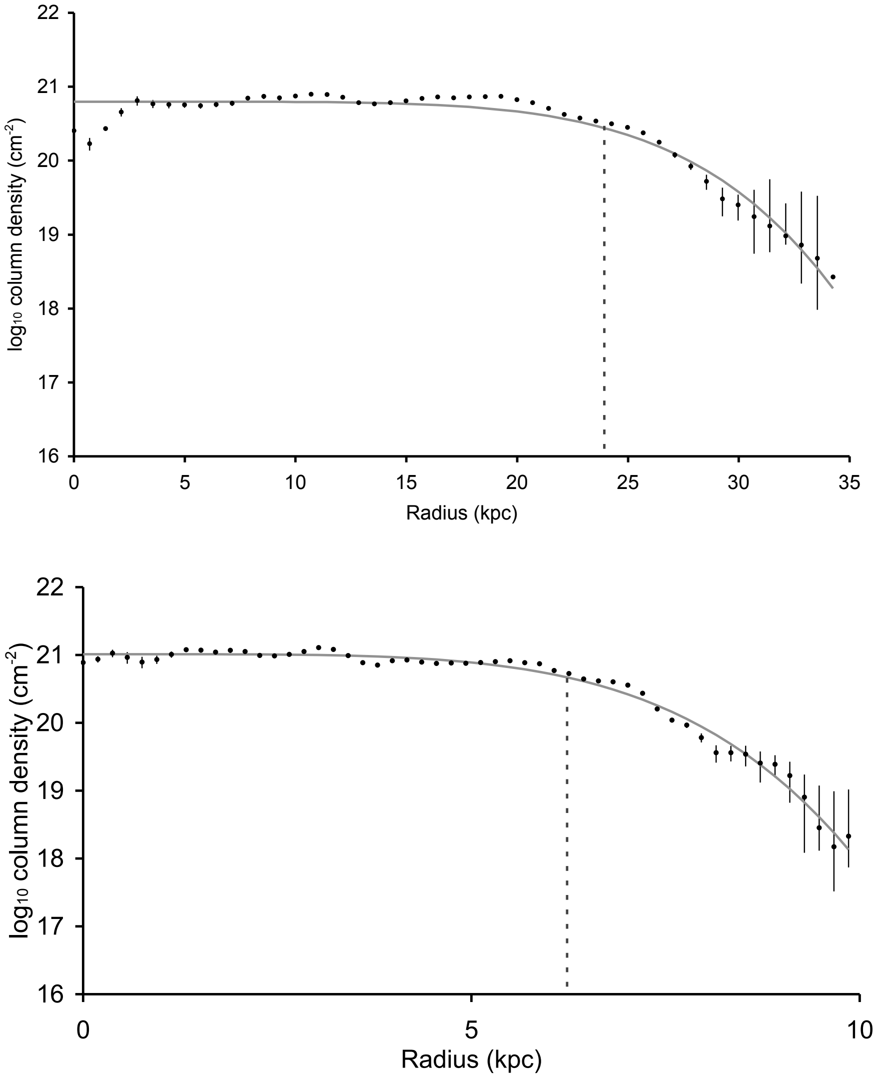

Figure 2.15: Sérsic fitting to the 30° sectors around the receding major axis and respective r_i radius. From top to bottom: NGC 7331 and NGC 7793.

the discs. It is worth mentioning the limitations of the fit in the inner parts of some discs (e.g., NGC 3351, NGC 3184, NGC 3627) which is caused by the fact that they show a deficiency of neutral hydrogen. In these regions molecular hydrogen generally dominates as can be seen in the baryonic mass profiles presented in Figures 2.16 to 2.19. Here we plot the radial mass density profiles of the stars and H_2 (both from Leroy *et al.* 2008) and our H I profiles. This figure shows that in all cases where we have information about the molecular gas, the H I dominates completely in the outer parts (see Leroy *et al.* 2008, for a more in depth treatment). As in this chapter we concentrate on the outer edges, we can safely ignore the contribution of molecular hydrogen, in the very inner parts of galaxies, as well as ignore the slight dip in H I column density in the centres of some galaxies which affects the goodness of fit for the inner pixels. More generally, the deviations of the observed profiles from the constant density part of the Sérsic profile is, of course, due to genuine density variations in the disc, such as spiral arms, which explains why they exceed the range set by the error bar on the profile. This skews the χ^2 values which should be interpreted with some care.

The $\log I(0)$ values lie within a narrow range of 20.3 to 21.0 cm^{-2} , with typical variations of 0.2 dex as presented in Table 2.4. These values agree with the transition from H I –to–H_2 as discussed by Bigiel *et al.* (2008) and Leroy *et al.* (2008, and references therein). The radius r_i varies from galaxy to galaxy as expected for objects spanning a range of sizes. The typical uncertainties associated with r_i are of order 2.5 kpc. As far as the slope index n is concerned, 8 out of 9 objects present a narrow range of values, from 0.14 to 0.22. This implies that within the uncertainties (≈ 0.06) the galaxies show a remarkably similar declining H I surface density in their outer parts. The exception here is NGC 5194 which presents a higher slope index value of 0.33 ± 0.15. This is the only object in our sample which is obviously interacting. The presence of the stream of neutral hydrogen (clearly seen in Figure 2.11 must be responsible for this less steep decline.

In addition to fits on a single sector around the receding major axis, we produced fits of 8 sectors for all galaxies in our subsample. We present the results in tabular and graphical form in the appendix (Tables A.1–A.3 and Figs. A.1–A.9).

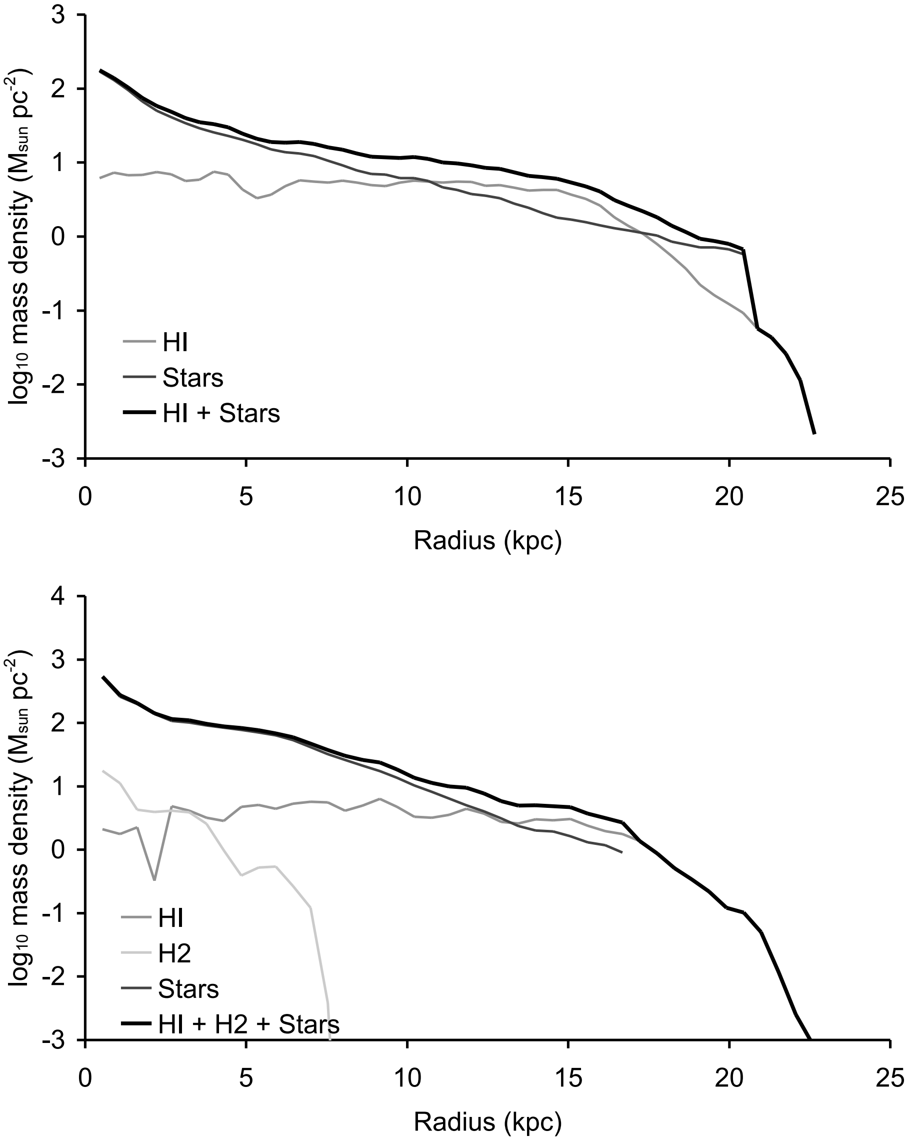

Figure 2.16: Radial mass density profiles of stars, H I and H_2 (when available): On top panel NGC 925 and on bottom panel NGC 3184.

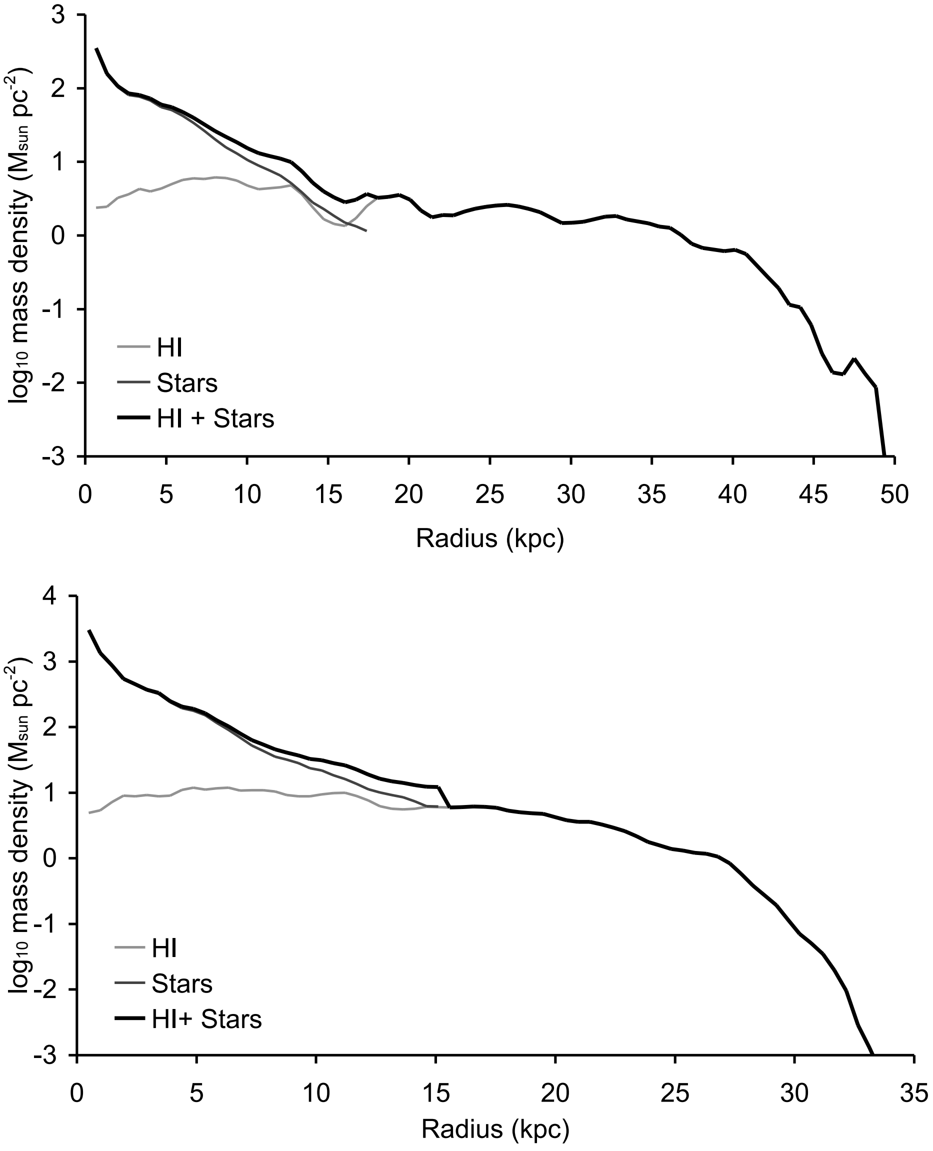

Figure 2.17: Radial mass density profiles of stars and H I : on top panel NGC 3198 and on bottom panel NGC 3521.

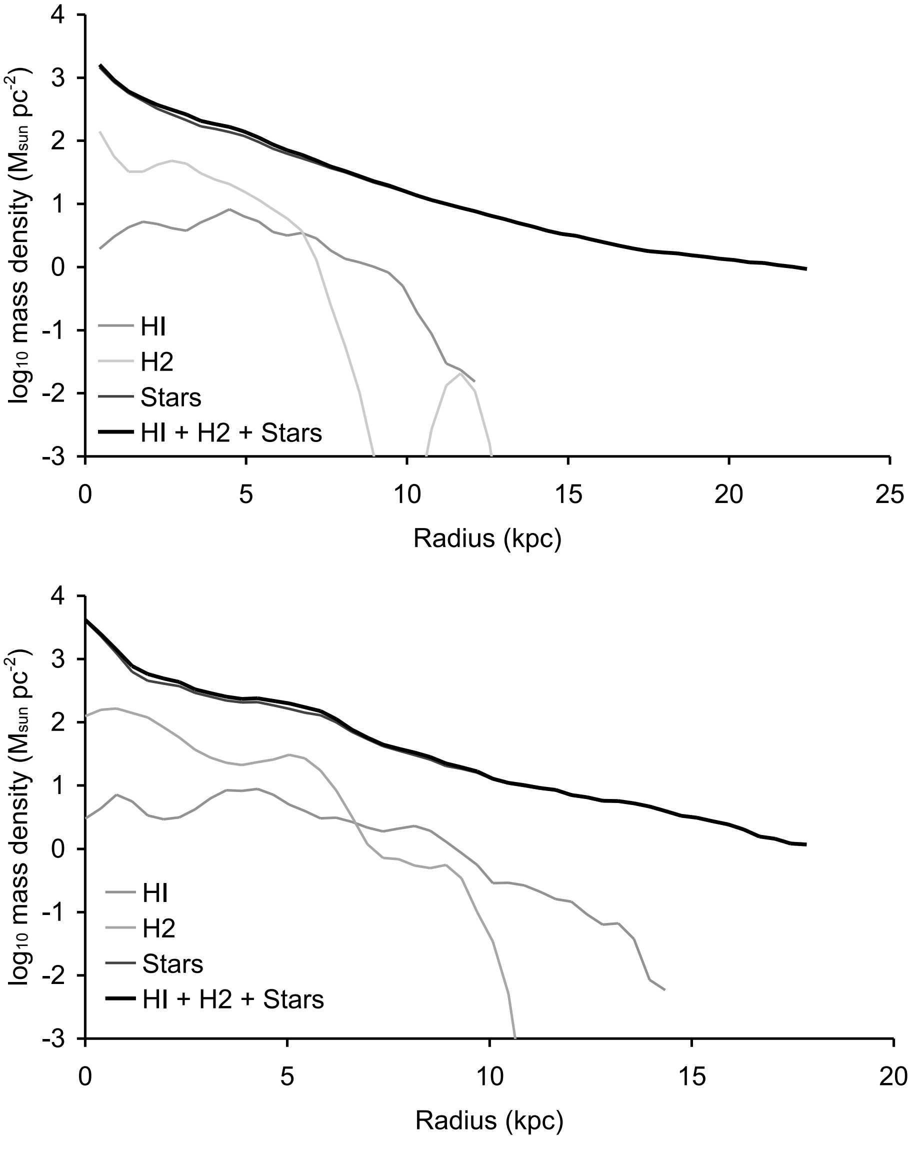

Figure 2.18: Radial mass density profiles of stars H I and H_2 (when available): on top panel NGC 3627 and on bottom panel NGC 5194.

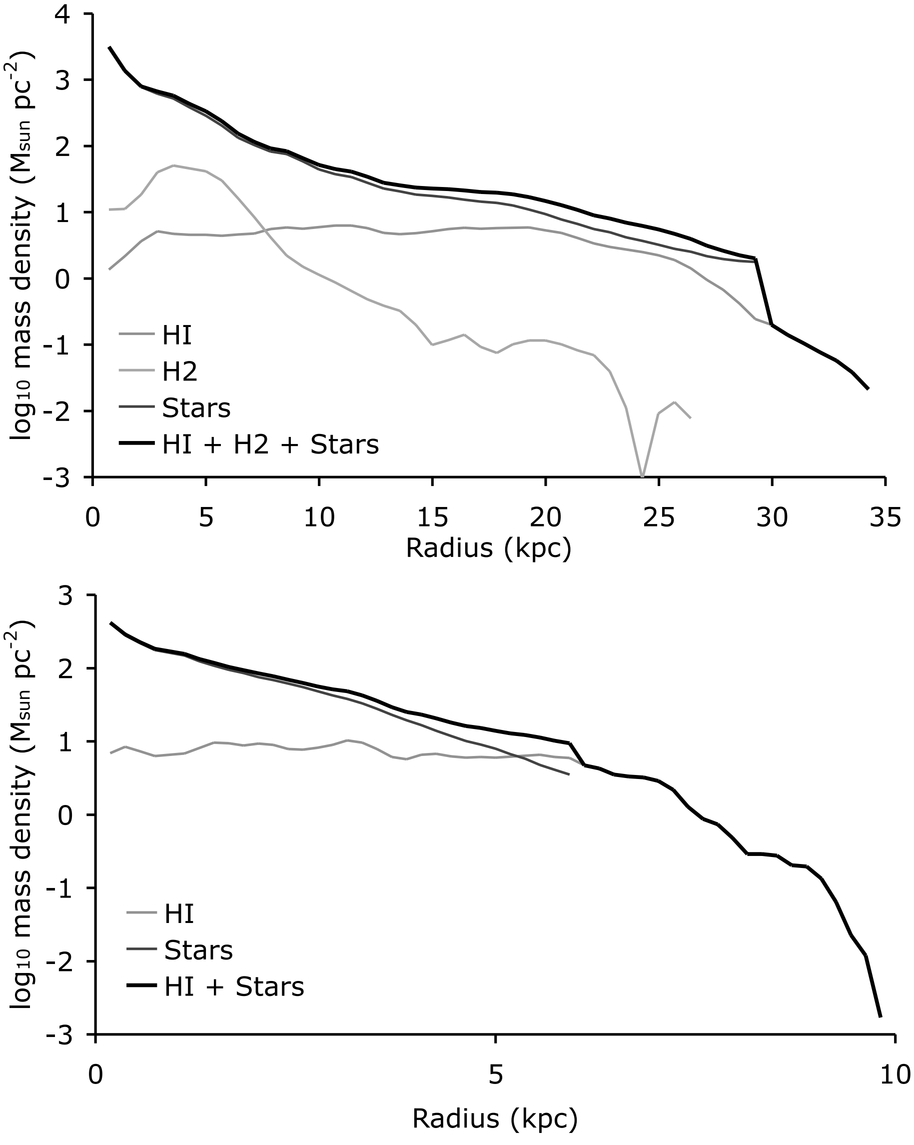

Figure 2.19: Radial mass density profiles of stars, H I and H_2 (when available): on top panel NGC 7331 and on bottom panel NGC 7793.

2.5.3 General trends

In this section we investigate if there is any correlation between galaxy properties such as mass, optical size, SFR and metallicity (values taken from Walter *et al.* 2008) with slope index, n, and characteristic radius r_i.

We looked for correlations of n with the above mentioned parameters but found none. Assuming a scenario where n controls the slope of the Sérsic–type fit, the steepness of the slope of the declining disc is not expected to be physically related with parameters such as the SFR, metallicity, or optical size. When correlating n with H I derived parameters such as inclinations and gas and dynamical mass, no significant trends emerged either.

We tested the statistical dependence between both pairs of variables by running a Spearman's rank correlation test. In addition to the linear correlation coefficient, hereafter ρ, this test also retrieves the statistical significance of the assumed correlation, expressed as the two-sided significance of its deviation from zero, which we shall designate by p. Small values of p indicate a significant correlation.

In the top panel of Fig. 2.20 we show a plot of $\log n$ versus $\log r_i$. This shows a weak trend in the sense that H I discs with larger characteristic radii have smaller values for n, i.e., a steeper slope. For these variables we found a correlation coefficient of $\rho = -0.62;\ p = 0.1$.

A more convincing trend is visible in the bottom panel of Fig. 2.20, where we plot the log H I mass as function of the log of the characteristic length, r_i. The data can be fitted with a power law : $M_{\mathrm{HI}} \propto r_i^{1.37}$. The correlation coefficient here is $\rho = 0.95$; $p = 2.6 \times 10^{-4}$. The implication is that galaxies with larger r_i are bigger and have a larger gas mass. The increase in M_{HI} with radius is lower than r_i^2 which is what would be expected if all galaxies would have the same average H I surface density.

A plot of $\log R_{25}$ as a function of the log of the characteristic radius, r_i, is presented in the top panel of Fig. 2.21. We express the size of the discs in angular scale to avoid introducing a spurious relation with distance. We find no relation between the optical size as measured via R_{25}, and the size of the H I disc as expressed by a correlation coefficient $\rho = -0.17$; $p = 0.97$. We also present in a log–log plot our characteristic scale length r_i against $r_{3.6}$, the scale length of the exponential disc as derived from

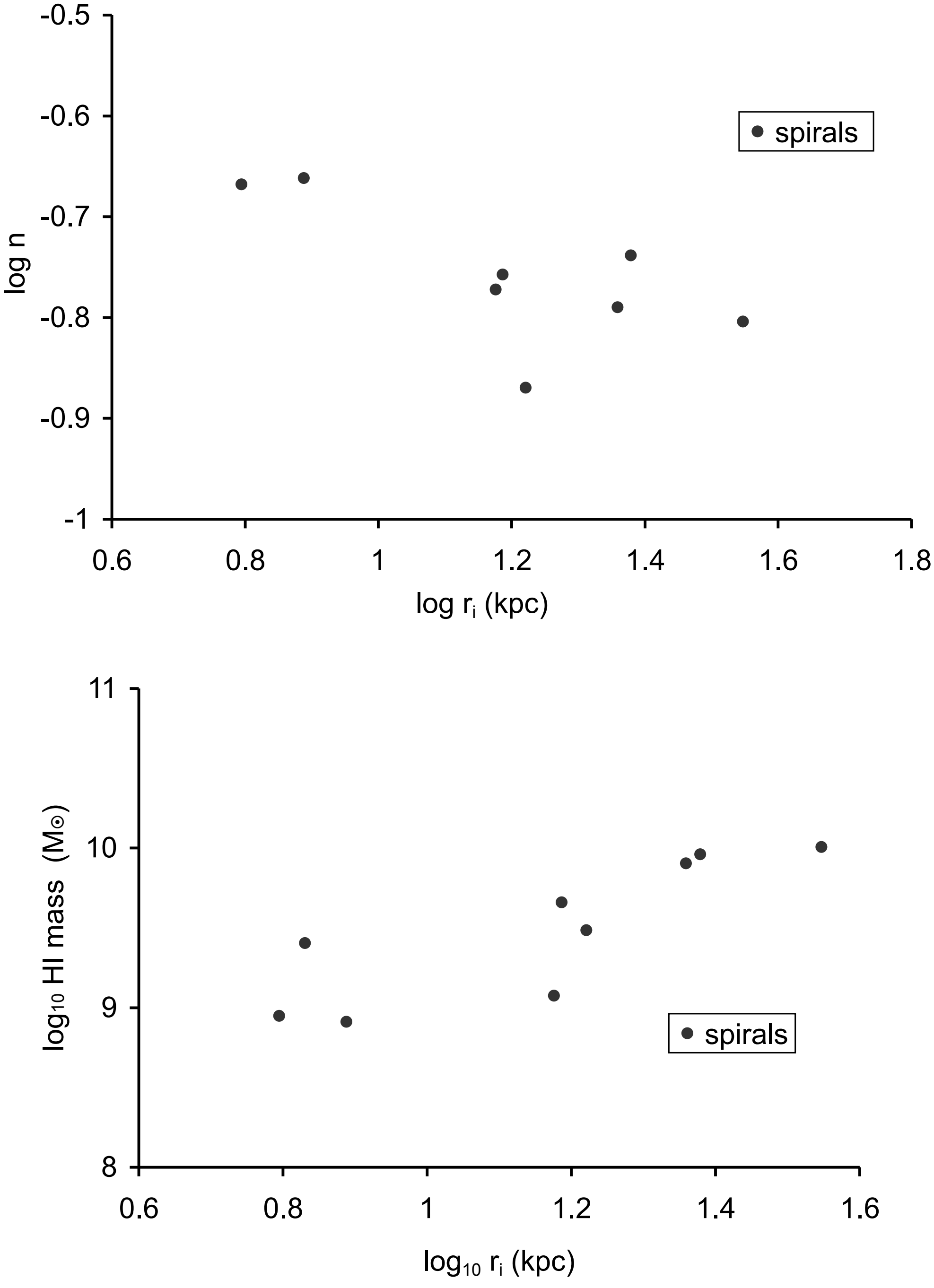

Figure 2.20: *Top panel:* Plot of $\log(n)$ as a function of $\log(r_i)$; *Bottom panel:* log H I mass versus $\log(r_i)$

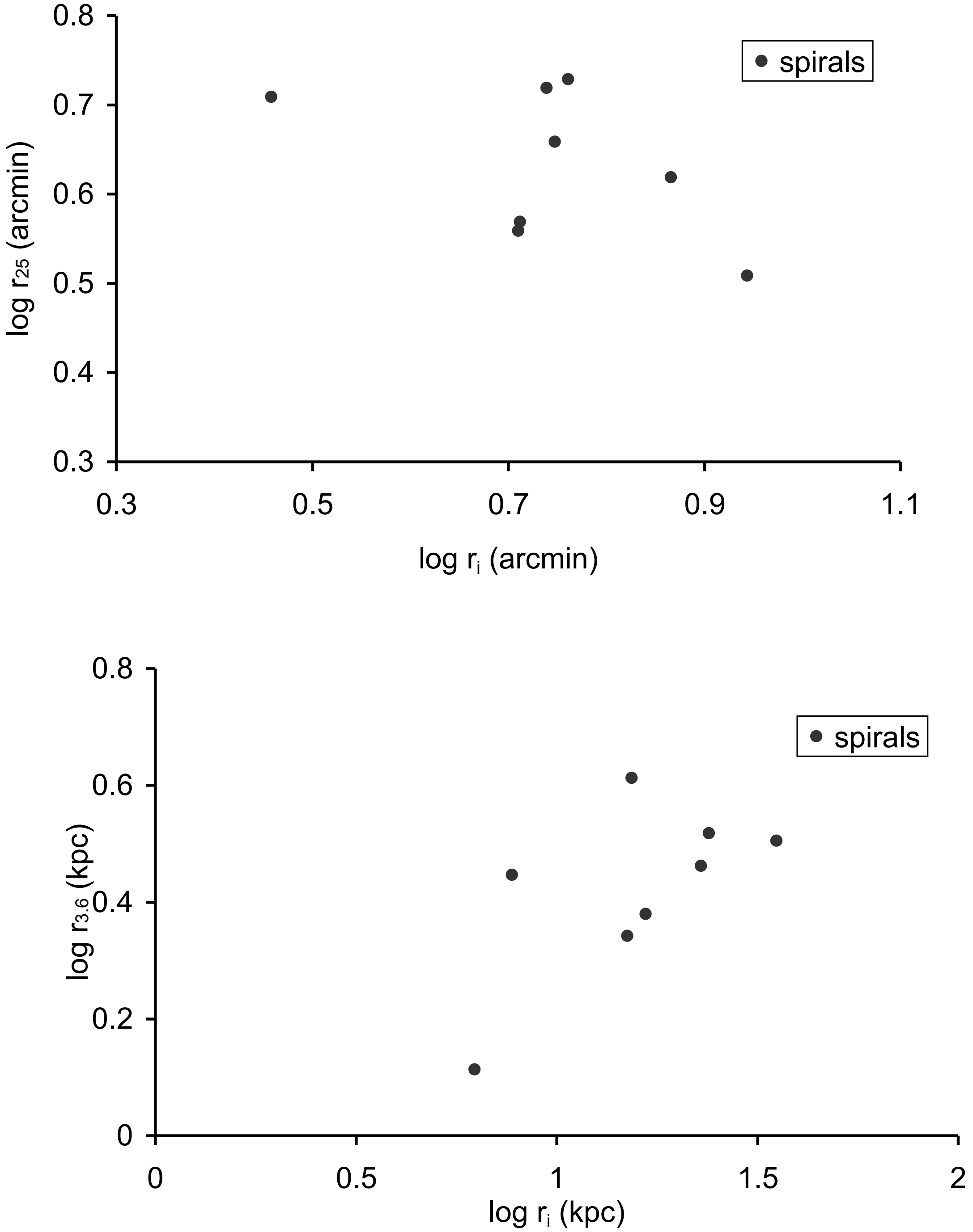

Figure 2.21: *Top panel:* Plot of $\log R_{25}$ as a function of $\log r_i$; *Bottom panel:* $\log r_3.6$ versus $\log r_i$.

Spitzer 3.6 μm IRAC observations taken from Leroy *et al.* (2008). We find a weak correlation in the sense that larger NIR scale lengths tend to imply larger values for r_i as well. In this case both variables show a Spearman's rank correlation coefficient $\rho = 0.64$; $p = 8.5 \times 10^{-5}$. We revisit these relations in Chapter 5 where we will provide a discussion of our results after having extended our work to the realm of dwarf irregular galaxies.

2.6 Analysis

2.6.1 The size of the atomic gas disc

Contrary to the optical wavelength regime where the extent of galaxies is routinely expressed in units of R_{25}, no such common yard stick has emerged to measure the extent of the neutral, atomic gas discs. If anything, the definitions which have been proposed had more to do with limitations of the instruments than an intrinsic property of the galaxies under study. For instance, Bosma (1981) introduced $R_{1.82}$, the radius at which the column density measures 1.82×10^{20} atoms cm^{-2} (which corresponds to an integrated brightness temperature of 100 K km s^{-1}). Broeils & Rhee (1997), define the H I diameter at a level of 1 $\mathcal{M}_\odot$ pc^{-2} or 1.25×10^{20} atoms cm^{-2}. As can be seen from Fig. 2.22, for some galaxies this limit falls only barely below the average H I column density and in all cases the H I extends well beyond these previously proposed limits.

As in the optical, there are two ways to go about defining the H I radius of a galaxy: one can either base this measurement on some characteristic scale length or one can set a surface brightness threshold. Using our Sérsic–type fit, we find a characteristic radius, r_i. As we have seen in Sect. 2.5.1, at this radius the surface brightness has dropped to about 45% of the average value found across most of the disc inside of r_i, or a few $\times 10^{20}$ atoms cm^{-2}, similar in magnitude to the definitions proposed to date. Fig. 2.22 shows that the steep decline really only sets in beyond $\sim 1.2 r_i$ where for a typical $n = 0.18$ the surface brightness has dropped to ~10% of the average level. If one were to push the detection threshold down by another order of magnitude, down to 1% of the average value, something which is well below what is currently possible, the radius would grow to $1.36 r_i$, a mere 13% increase. This presupposes that the H I column density will continue to follow the same Sérsic curve. In other words, $1.2r_i$ is a useful radius to characterize the size of a galaxy as measured in H I .

Not all observations will lend themselves to the kind of Sérsic–type fitting and a more straight forward method is obviously required. If we are allowed to extrapolate the finding from our THINGS subsample which says that the median surface brightness within r_i is 5×10^{20} atoms cm^{-2} and that a galaxy edge can be defined at $1.2r_i$, or equivalently where the average surface brightness has dropped to 10%, this then suggests a surface brightness level of 5×10^{19} atoms cm^{-2} (or $0.4\,\mathrm{M}_\odot\,\mathrm{pc}^{-2}$). Using a constant surface density threshold in the face of galaxies showing a range in average surface brightness from 2×10^{20} atoms cm^{-2} to 10×10^{20} atoms cm^{-2} would imply a range in radius normalised to units of r_i of $1.1r_i$ to $1.27r_i$. Choosing a set level of 5×10^{19} atoms cm^{-2} has the added advantage of it being well within reach of current instruments. This level also happens to coincide with the critical density, N_c, defined by Maloney (1993) and is the level below which a substantial fraction of the gas is expected to become ionized by the extragalactic radiation field.

2.6.2 Probing the edge

In the introduction we refer to the suggestion that the radial truncation of the neutral gas discs have their origin in an isotropic extragalactic radiation field. We explore this in qualitative terms in the remainder of this Chapter. A more quantitative approach will be the topic of future work.

Figs. (A.1–A.9) show that the surface density profiles of the individual sectors show a very similar behaviour. Whatever determines the run of column density as a function of radius seems to be independent of azimuth within the galaxy. There are some column density profiles which do not conform, such as NGC 5194 (M 51). On the side of the galaxy which faces the early–type companion NGC 5195 the H I extends much further out and the profile suggests that the H I that was originally there has been distributed over a larger range in radius. For a fixed total amount of gas per segment, the column density in the direction toward NGC 5195 has then gone down. Something similar must be happening in lopsided H I discs (see Fig.2.9, bottom panel).

The fitting results obtained in Section 2.5.1 are encouraging, showing that the parameter n which determines the slope of the decline of the H I surface density with

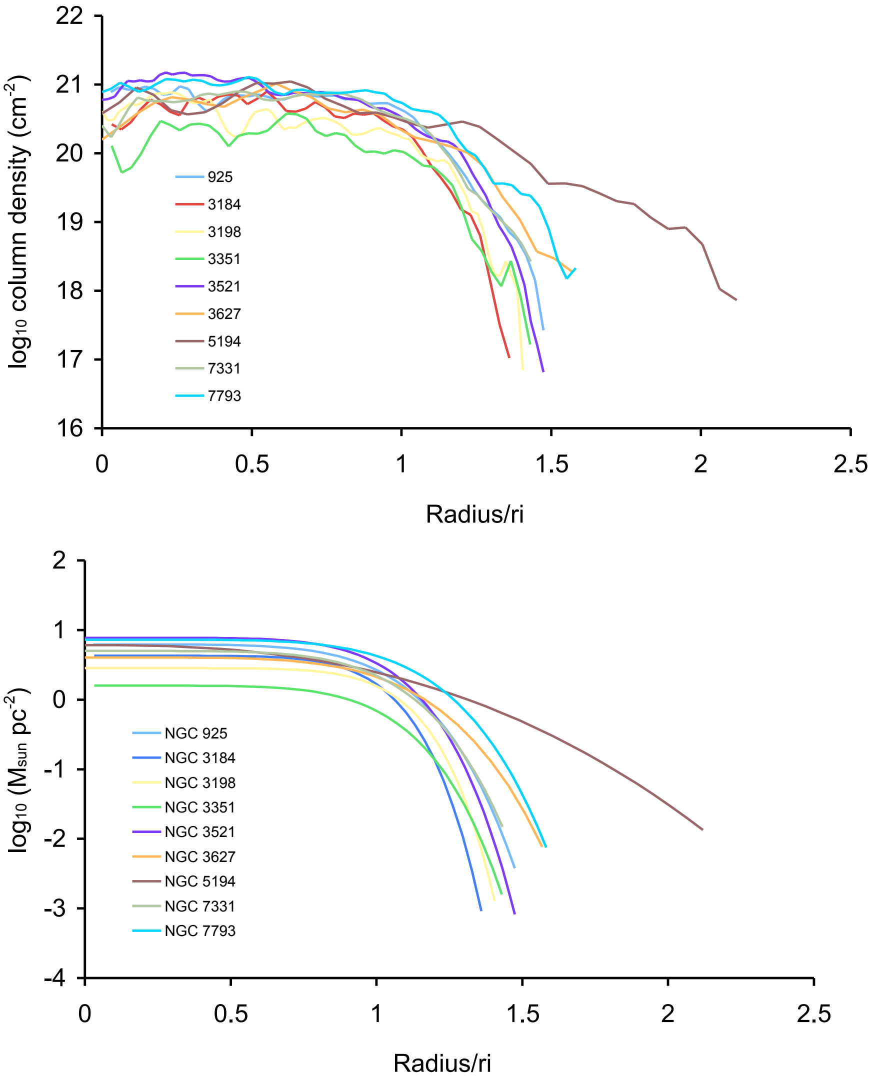

Figure 2.22: Radial profiles scaled to their respective characteristic radius, r_i. In bottom panel we chose to present the Sérsic fitted profiles rather then the ELLINT radial profiles.

radius, is similar throughout our sample of in principle fairly isolated galaxies (with the exception of NGC 5194). This is highlighted in Fig. 2.22 which shows the observed radial surface density profiles normalized by r_i as well as the resulting Sérsic–type fits, also normalized to r_i: the profiles all share a similar shape. This figure also illustrates, as already alluded to above, the fact that r_i is where the H I edge is located. As argued earlier, the edge is found nearer $r_i \approx 1.35$. Fig. 2.23 explains this using as example the column density profile of NGC 3351. This profile can be divided into three regions, a central region at almost constant H I column density, a transition around r_i where a general decline sets in, and finally a precipitous drop at around $1.3r_i$.

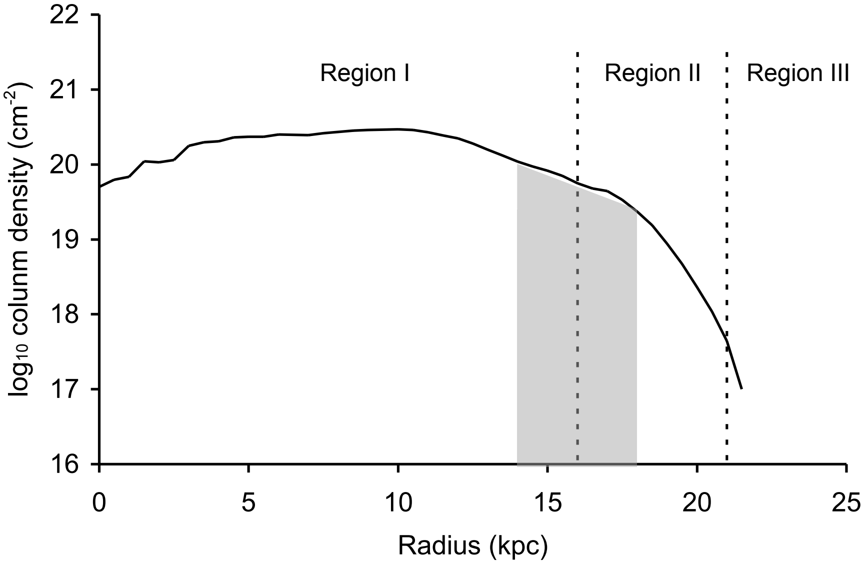

Figure 2.23: Sketch based on the observed column density profile of NGC 3351 indicating three regimes. The vertical line separating Region I from Region II is located at r_i. See text for details.

Therefore, if we wish to find out what is happening at the edge of the atomic gas disc, and compare the edges of the galaxies in our sample, we need to shift the profiles so their outermost regions (Region III in Fig. 2.23) overlap. This is done in Fig. 2.24, where in the top panel we show the individual profiles, each based on the average of 8 sectors, each 30 ° wide. Before averaging, the individual sectors where shifted to make their outer edges coincide. In the bottom panel we show the same curves but shifted so the outer edges of the averaged profiles of individual galaxies are made to overlap. This panel clearly shows the three regimes. It is important to note that the transition from Region I to II near r_i cannot be due solely to ionization by an extragalactic radiation field. The column densities of $\sim 10^{20}$ atoms cm^{-2} are way too high for the H I layer to be affected. In fact, such a column density, if ionized, would produce a healthy Hα emission measure (EM) and the required flux of an extragalactic radiation field would far exceed any reasonable value for the extragalactic flux.

Going back to Maloney's paper (Maloney 1993), he thought that to a good approximation the H I in the outer part of NGC 3198 follows an exponential decline with a scale length of $R_H = 10.9\,\mathrm{kpc}$. He, of course, needs this kind of decline for the column density to drop sufficiently so that in the outermost regions the remaining H I can be ionised. Problem is, though, that most H I profiles remain flat or have such large R_H scale lengths that the column density never drops down to N_c, his critical column density of around 5×10^{19} atoms cm^{-2}. Moreover, we would argue based on the results presented here that fitting an exponential to what we refer to as Region II is fraught with difficulty as the scale length depends sensitively on which part of the curve one applies a fit to (and if the outermost points are low because of ionization, one should exclude those from any fit).

What we find is that a Sérsic–type parameterisation represents well the run of surface density with radius all the way out to the last measured point. Although we can not rule out that an extragalactic UV field ionizes the outermost regions of a galaxy, our data do not show a break or knee at Maloney's critical column density. So although an extragalactic radiation field might contribute at the low column density end, it cannot be responsible for the transition from Region I to II. Instead, a different mechanism must be responsible for causing a wide variety of galaxies to have such similar radial profiles. Possibly this is related to how baryonic matter accumulates and eventually settles within Dark Matter haloes. If this conjecture is correct, the outer edges tell more about the haloes and their gas accretion history than an extragalactic radiation field. Although various groups are pushing their numerical galaxy formation simulations to resolutions which are detailed enough to predict the detailed structure

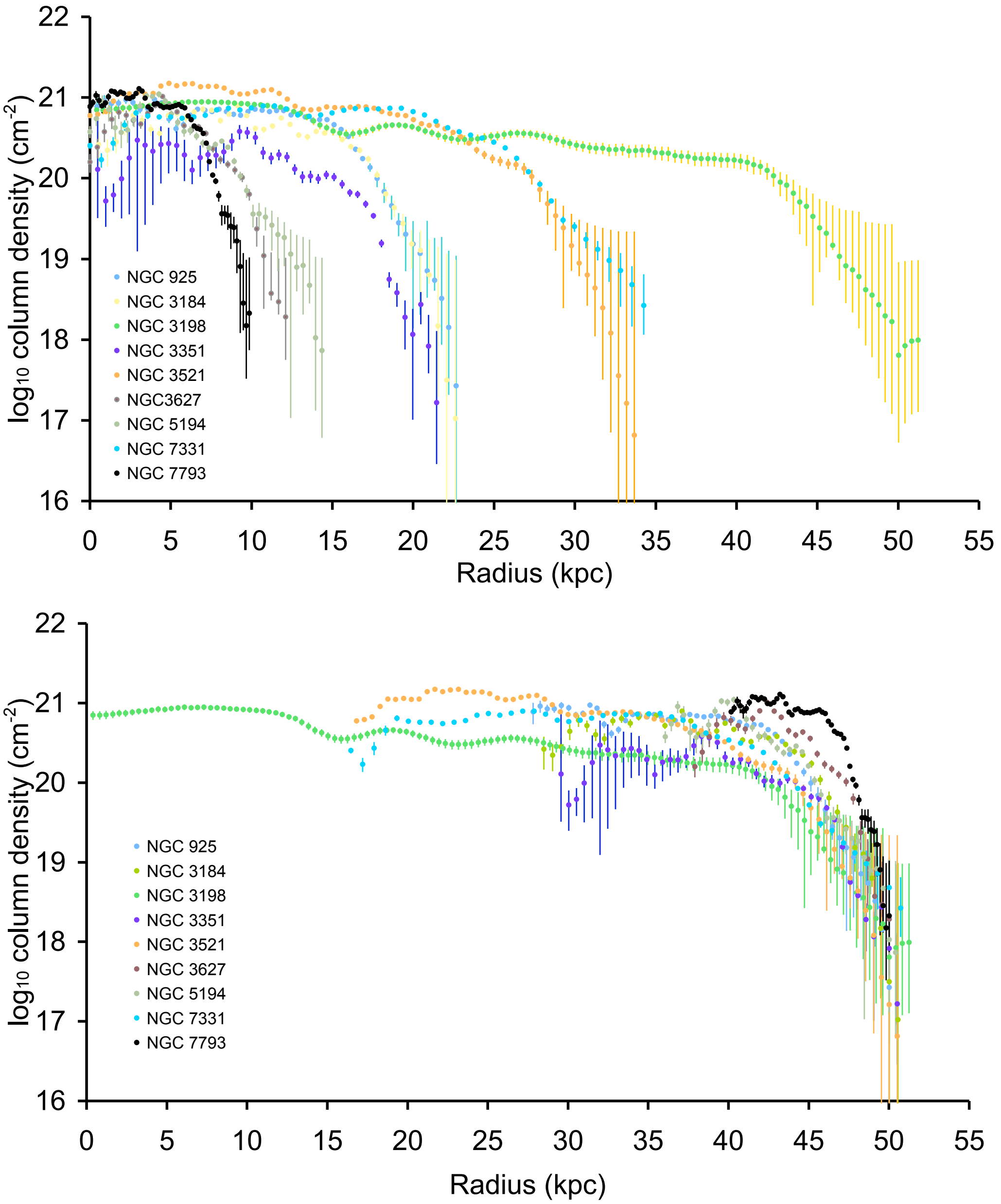

Figure 2.24: *Top panel*: Plots of the profiles of all galaxies in the subsample obtained after shifting and averaging the individual 8 sectors per galaxy (see text for details); *Bottom panel*: The same profiles, but shifted so their outer edges align, taking as reference the profile of NGC 3198.

of galaxies at $z = 0$ (Governato *et al.* 2007; Portinari & Sommer-Larsen 2007), results in the literature invariably have focussed on the resulting *stellar* distribution. A first comparison of simulations of the neutral gas (Sommer–Larsen, priv. comm.) shows surprisingly good, qualitative agreement with observations, lending support to our conclusion that the extent and shape of the outer H I discs are set by the way galaxies assembled.

2.7 Final remarks

In this Chapter we revisit the H I distribution in the outer parts of spiral galaxies, and the possible influence on the neutral gas disks by an isotropic extragalactic radiation field. Our analysis makes extensive use of the THINGS survey, its high spatial resolution and excellent sensitivity enabling such a study for the first time across a sizeable sample of disk galaxies, the only previous studies having been based on unpublished sensitive, but low spatial resolution data on NGC 3198. We present a novel strategy to reach the best possible column density sensitivity. Rather than a simple 360° azimuthal average which if a galaxy shows some lopsidedness will effectively average out any edge in the radial direction, we split the galaxy in 30° sectors, each of which can be fit independently and which, after applying shifts to align the outermost part of the profiles, can be averaged.

We took care to verify that no spurious edges were introduced as a result of the data reduction, for example via the blanking technique used by Walter *et al.* (2008) but that the edges are real features inherent to spiral galaxies. A three–parameter Sérsic–like fit to the H I surface density distribution as a function of radius provides a surprisingly good parameterisation. The parameters which we fit are: the central neutral hydrogen column density, $I(0)$, a characteristic radius r_i which is where the profile has its steepest decline, and a slope index n.

We find that the slope index n for 8 out of the 9 objects in our sample present a very narrow range of values, 0.14 to 0.22, which implies that the radial column density profiles decline in a similar manner, irrespective of Hubble type or galaxy size. Scaling the profiles by their corresponding r_i shows 8 out of 9 disks extending up to $\approx 1.35\ r_i$. In both cases the exception is the galaxy NGC 5194 (M 51) which is obviously interacting with NGC 5195 which explains why this galaxy does not fit the mould.

Based on our results we propose a new definition for a neutral hydrogen radius, R_{HI}, which we set at a level of 5×10^{19} atoms cm^{-2} . Short of doing a Sérsic–type fit to a galaxy and agreeing on, e.g., measuring the extent at $1.2r_i$, this level of 5×10^{19} atoms cm^{-2} will for most galaxies give an extent which is in the range $1.1 - 1.3r_i$.

Finally, we recognise three radial column density regions, an inner region with almost constant H I column density, a transition region around r_i where the H I rapidly decreases, followed by a precipitous drop near $1.3r_i$. As we argue, the initial decrease beyond r_i is difficult to reconcile with ionization as the column densities are still high and well above the critical column density introduced by Maloney (1993). We conjecture that the H I distribution might be set by other factors which are related to how Dark Matter haloes acquired their baryonic components in the first place. If ionisation plays a rôle, it must be restricted to the outermost reaches of galaxies, once the column density has dropped below few $\times 10^{19}$ atoms cm^{-2} .

Appendix A

Additional data of spirals

A.1 Sérsic profiles: individual 30° sectors of THINGS spirals

We present in Tables A.1–A.3 the results of the fitting process described in the main text for each 30° sector of all galaxies in our subsample, excluding the sectors immediately bordering the minor axis. Figs. A.1 to A.9 (top panel) show the 30° sectors of each individual galaxy, plotting the logarithm of the column density against radius. In the bottom panel we present the residuals defined as the difference between the logarithm of the measured column density and the logarithm of the fitted column density obtained via the Sérsic–like parameterisation.

Table A.1: Sérsic $r^{1/n}$–style fit applied to individual 30° sectors of NGC 925, NGC 3184, NGC 3198, and NGC 3351. The χ^2_{red} values quoted here are adapted from Table 2.4 and assumed to be representative throughout all the sectors of the objects.

object	sector °	$\log I(0)$ atoms cm^{-2}	r_i kpc	n	χ^2_{red}
NGC 925	0–30	20.92 ± 0.22	12.50 ± 2.86	0.30 ± 0.08	1.14
	30–60	20.80 ± 0.20	15.24 ± 4.58	0.37 ± 0.10	
	120–150	20.80 ± 0.23	10.40 ± 7.17	0.57 ± 0.17	
	150–180	20.88 ± 0.22	11.65 ± 2.94	0.30 ± 0.09	
	180–210	20.92 ± 0.22	11.90 ± 2.58	0.30 ± 0.07	
	210–240	20.81 ± 0.22	10.59 ± 4.78	0.52 ± 0.12	
	300–330	20.80 ± 0.20	14.20 ± 4.41	0.39 ± 0.10	
	330–360	20.91 ± 0.20	14.51 ± 3.15	0.27 ± 0.08	
NGC 3184	0–30	20.71 ± 0.20	15.63 ± 1.97	0.13 ± 0.06	0.99
	30–60	20.71 ± 0.21	14.69 ± 1.85	0.16 ± 0.05	
	120–150	20.78 ± 0.23	13.85 ± 3.58	0.25 ± 0.11	
	150–180	20.72 ± 0.22	14.52 ± 3.46	0.25 ± 0.10	
	180–210	20.63 ± 0.21	16.22 ± 2.52	0.17 ± 0.07	
	210–240	20.72 ± 0.22	15.15 ± 3.09	0.21 ± 0.09	
	210–240	20.72 ± 0.22	15.15 ± 3.09	0.21 ± 0.09	
	300–330	20.66 ± 0.22	14.85 ± 2.97	0.22 ± 0.09	
	330–360	20.66 ± 0.20	16.58 ± 2.10	0.16 ± 0.06	
NGC 3198	0–30	20.80 ± 0.20	21.92 ± 6.58	0.38 ± 0.10	1.48
	30–60	20.74 ± 0.18	28.68 ± 5.98	0.29 ± 0.08	
	120–150	20.79 ± 0.20	21.18 ± 5.23	0.34 ± 0.08	
	150–180	20.67 ± 0.20	23.11 ± 6.21	0.34 ± 0.10	
	180–210	20.64 ± 0.15	34.51 ± 3.52	0.13 ± 0.05	
	210–240	20.73 ± 0.18	26.73 ± 4.50	0.25 ± 0.07	
	300–330	20.76 ± 0.18	25.10 ± 3.80	0.25 ± 0.05	
	300–330	20.69 ± 0.18	26.71 ± 5.29	0.28 ± 0.08	
NGC 3351	0–30	20.25 ± 0.19	15.93 ± 1.73	0.11 ± 0.06	2.06
	30–60	20.28 ± 0.21	14.69 ± 2.29	0.16 ± 0.08	
	120–150	20.24 ± 0.19	17.63 ± 2.31	0.15 ± 0.07	
	150–180	20.25 ± 0.20	16.04 ± 1.96	0.12 ± 0.06	
	180–210	20.25 ± 0.21	14.83 ± 2.14	0.15 ± 0.07	
	210–240	20.37 ± 0.23	13.29 ± 2.76	0.19 ± 0.11	
	300–330	20.38 ± 0.21	14.49 ± 2.04	0.14 ± 0.07	
	300–360	20.32 ± 0.20	15.67 ± 2.45	0.15 ± 0.09	

Table A.2: Sérsic $r^{1/n}$–style fit applied to individual 30° sectors of NGC 3521, NGC 3627, NGC 5194, and NGC 7331. The χ^2_{red} values quoted here are adapted from Table 2.4 and assumed to be representative throughout all the sectors of the objects.

object	sector °	$\log I(0)$ atoms cm^{-2}	r_i kpc	n	χ^2_{red}
	0–30	20.90 ± 0.19	17.63 ± 3.90	0.33 ± 0.08	
	30–60	20.82 ± 0.18	18.76 ± 4.16	0.34 ± 0.08	
	120–150	20.97 ± 0.22	12.65 ± 4.06	0.43 ± 0.09	
NGC 3521	150–180	20.91 ± 0.22	12.59 ± 5.07	0.46 ± 0.12	1.16
	180–210	20.90 ± 0.21	14.17 ± 5.79	0.46 ± 0.12	
	210–240	21.01 ± 0.23	11.60 ± 4.49	0.44 ± 0.11	
	300–330	21.03 ± 0.24	9.16 ± 3.80	0.51 ± 0.10	
	330–360	20.88 ± 0.20	15.97 ± 3.54	0.31 ± 0.08	
	0–30	20.74 ± 0.31	5.94 ± 2.55	0.39 ± 0.13	
	30–60	20.62 ± 0.31	6.24 ± 3.10	0.42 ± 0.15	
	120–150	20.69 ± 0.34	5.06 ± 2.19	0.32 ± 0.16	
NGC 3627	150–180	20.77 ± 0.42	2.78 ± 2.79	0.56 ± 0.24	1.52
	180–210	20.70 ± 0.28	7.07 ± 1.83	0.26 ± 0.10	
	210–240	20.72 ± 0.31	5.79 ± 2.64	0.42 ± 0.14	
	300–330	20.90 ± 0.41	2.42 ± 2.35	0.59 ± 0.21	
	300–360	20.76 ± 0.37	2.43 ± 3.60	0.72 ± 0.30	
	0–30	20.78 ± 0.22	12.14 ± 3.55	0.30 ± 0.12	
	30–60	20.68 ± 0.18	15.04 ± 1.81	0.15 ± 0.06	
	120–150	20.78 ± 0.27	6.81 ± 3.05	0.42 ± 0.14	
NGC 5194	150–180	20.81 ± 0.26	7.38 ± 2.53	0.35 ± 0.12	1.24
	180–210	20.80 ± 0.24	9.66 ± 3.12	0.29 ± 0.14	
	210–240	20.96 ± 0.25	7.81 ± 2.65	0.41 ± 0.10	
	300–330	20.72 ± 0.22	11.68 ± 3.68	0.27 ± 0.15	
	330–360	20.76 ± 0.21	12.17 ± 2.80	0.19 ± 0.14	
	0–30	20.86 ± 0.21	19.56 ± 3.94	0.27 ± 0.07	
	30–60	20.83 ± 0.22	19.13 ± 4.62	0.29 ± 0.09	
	120–150	20.92 ± 0.27	12.34 ± 6.4	0.48 ± 0.14	
NGC 7331	150–180	20.84 ± 0.29	12.78 ± 10.30	0.50 ± 0.25	1.69
	180–210	20.79 ± 0.21	20.39 ± 5.05	0.34 ± 0.08	
	210–240	20.81 ± 0.22	19.46 ± 4.29	0.29 ± 0.08	
	300–330	20.76 ± 0.20	22.81 ± 4.53	0.26 ± 0.08	
	330–360	20.88 ± 0.23	16.32 ± 4.93	0.39 ± 0.09	

Table A.3: Sérsic $r^{1/n}$–style fit applied to individual 30° sectors of NGC 7793. The χ^2_{red} value quoted here is adapted from Table 2.4 and assumed to be representative throughout all the sectors of the objects.

object	sector °	$\log I(0)$ atoms cm^{-2}	r_i kpc	n	χ^2_{red}
NGC 7793	0–30	20.97 ± 0.22	5.34 ± 1.78	0.35 ± 0.12	1.05
	30–60	20.98 ± 0.22	5.45 ± 1.86	0.36 ± 0.12	
	120–150	20.95 ± 0.19	6.81 ± 1.39	0.25 ± 0.09	
	150–180	21.26 ± 0.29	3.51 ± 2.84	0.49 ± 0.26	
	180–210	20.93 ± 0.20	6.26 ± 1.34	0.26 ± 0.09	
	210–240	20.87 ± 0.20	6.42 ± 1.86	0.35 ± 0.10	
	300–330	21.03 ± 0.21	5.82 ± 1.50	0.28 ± 0.11	
	330–360	21.11 ± 0.24	3.46 ± 1.55	0.52 ± 0.11	

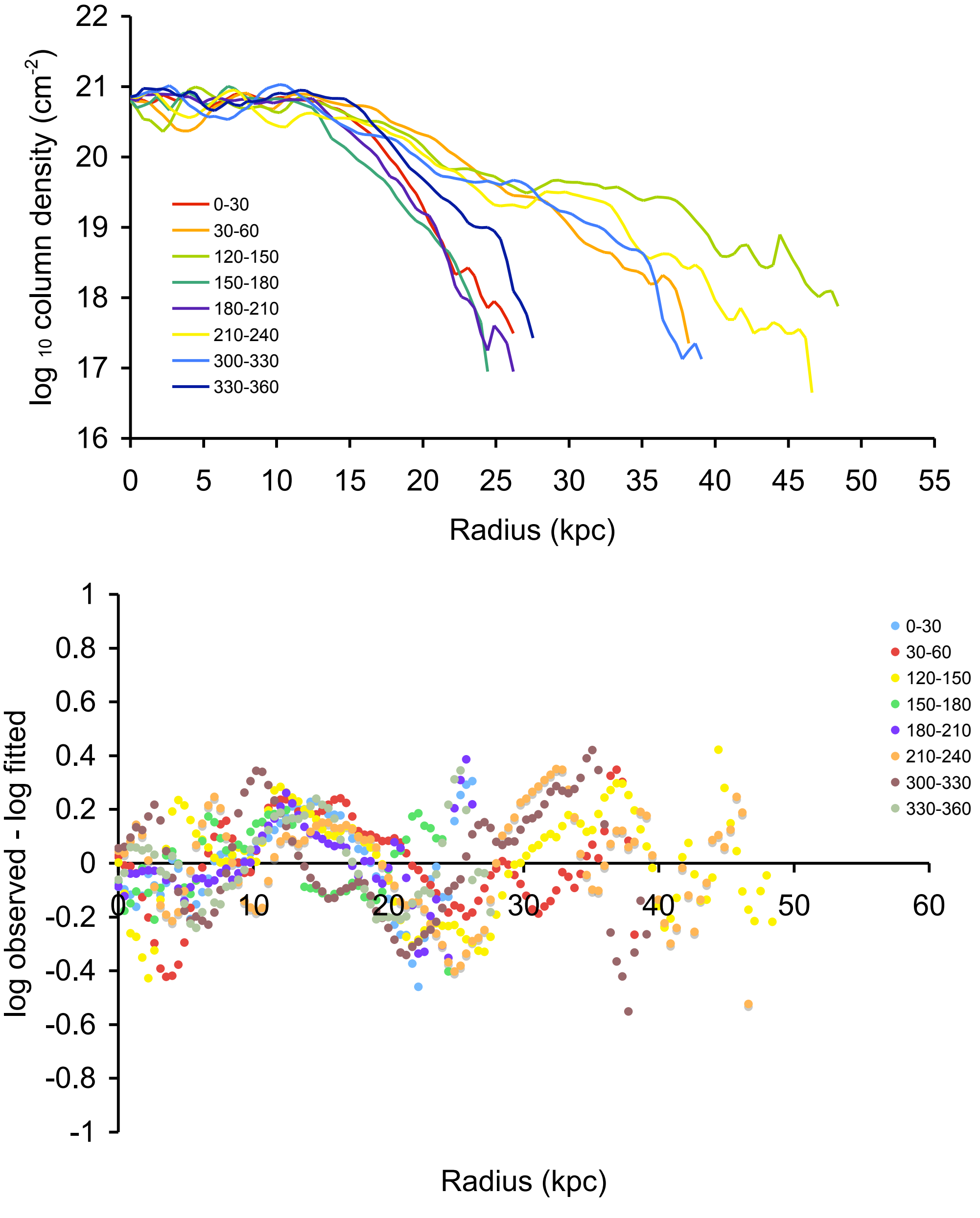

Figure A.1: *Top panel:* individual 30° sectors of NGC 925 ; *Bottom panel:* residuals after a Sérsic–like fit for each 30° sector.

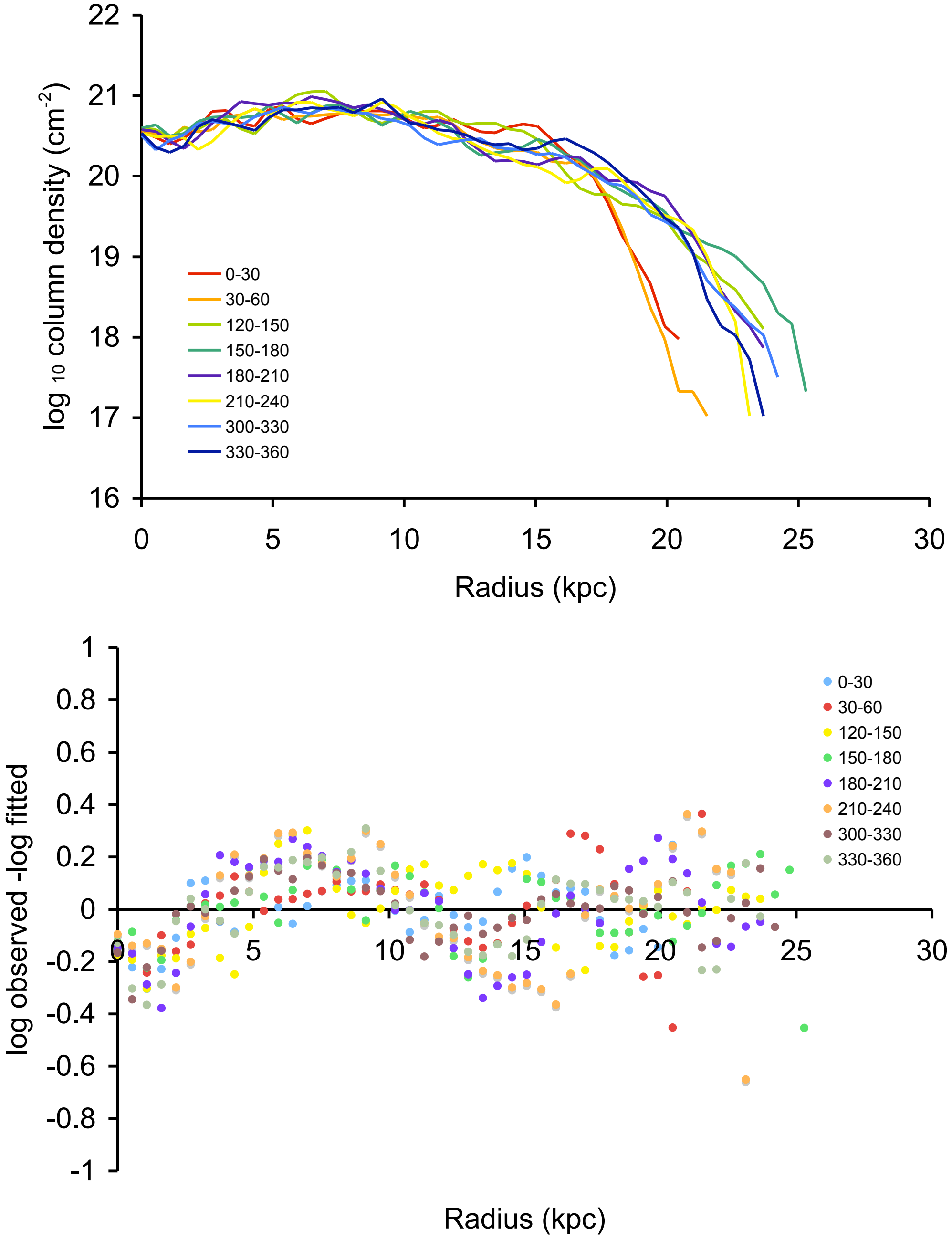

Figure A.2: *Top panel:* individual 30° sectors of NGC 3184 ; *Bottom panel:* residuals after a Sérsic–like fit for each 30° sector.

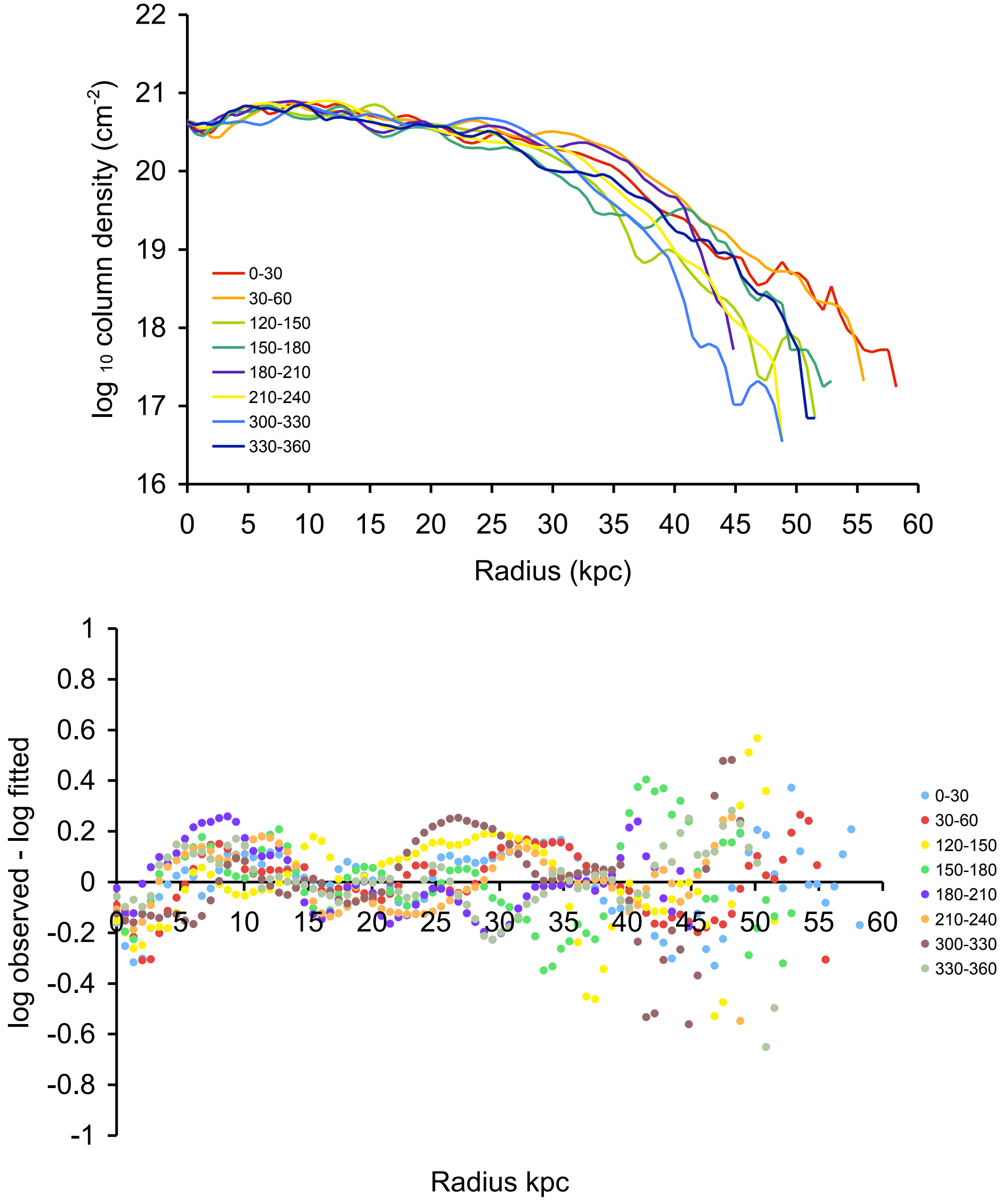

Figure A.3: *Top panel:* individual 30° sectors of NGC 3198 ; *Bottom panel:* residuals after a Sérsic–like fit for each 30° sector.

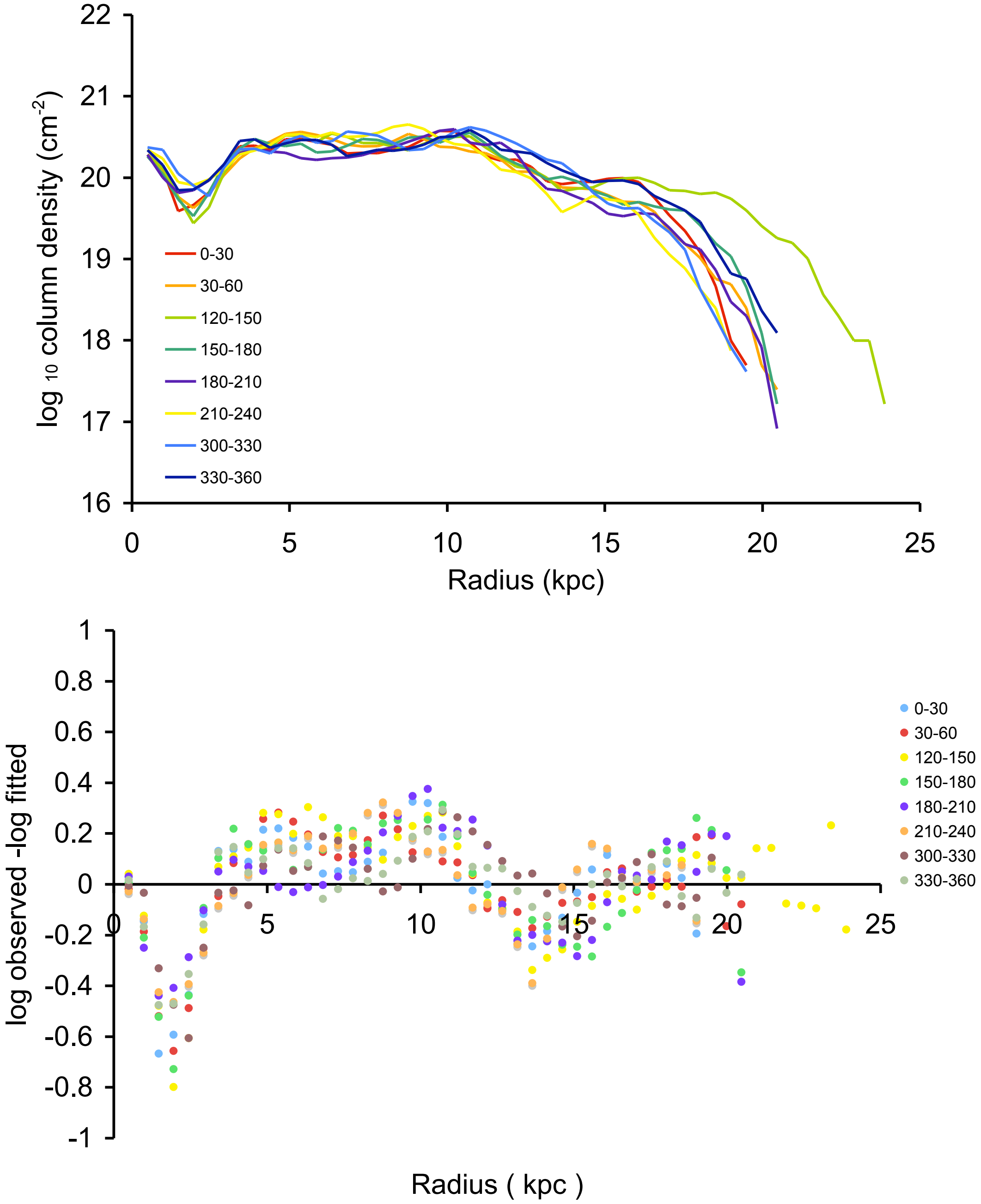

Figure A.4: *Top panel:* individual 30° sectors of NGC 3351 ; *Bottom panel:* residuals after a Sérsic–like fit for each 30° sector.

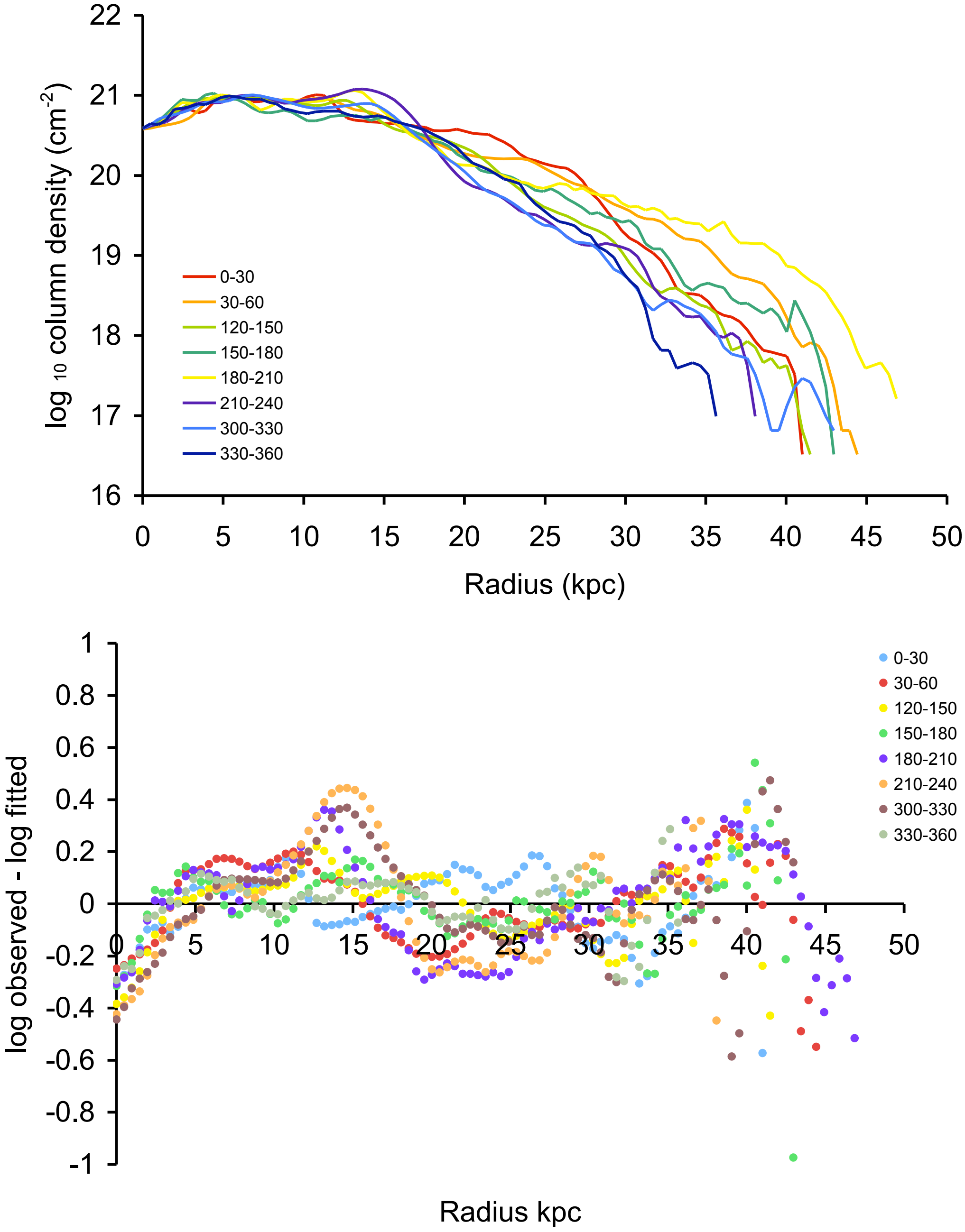

Figure A.5: *Top panel:* individual 30° sectors of NGC 3521 ; *Bottom panel:* residuals after a Sérsic–like fit for each 30° sector.

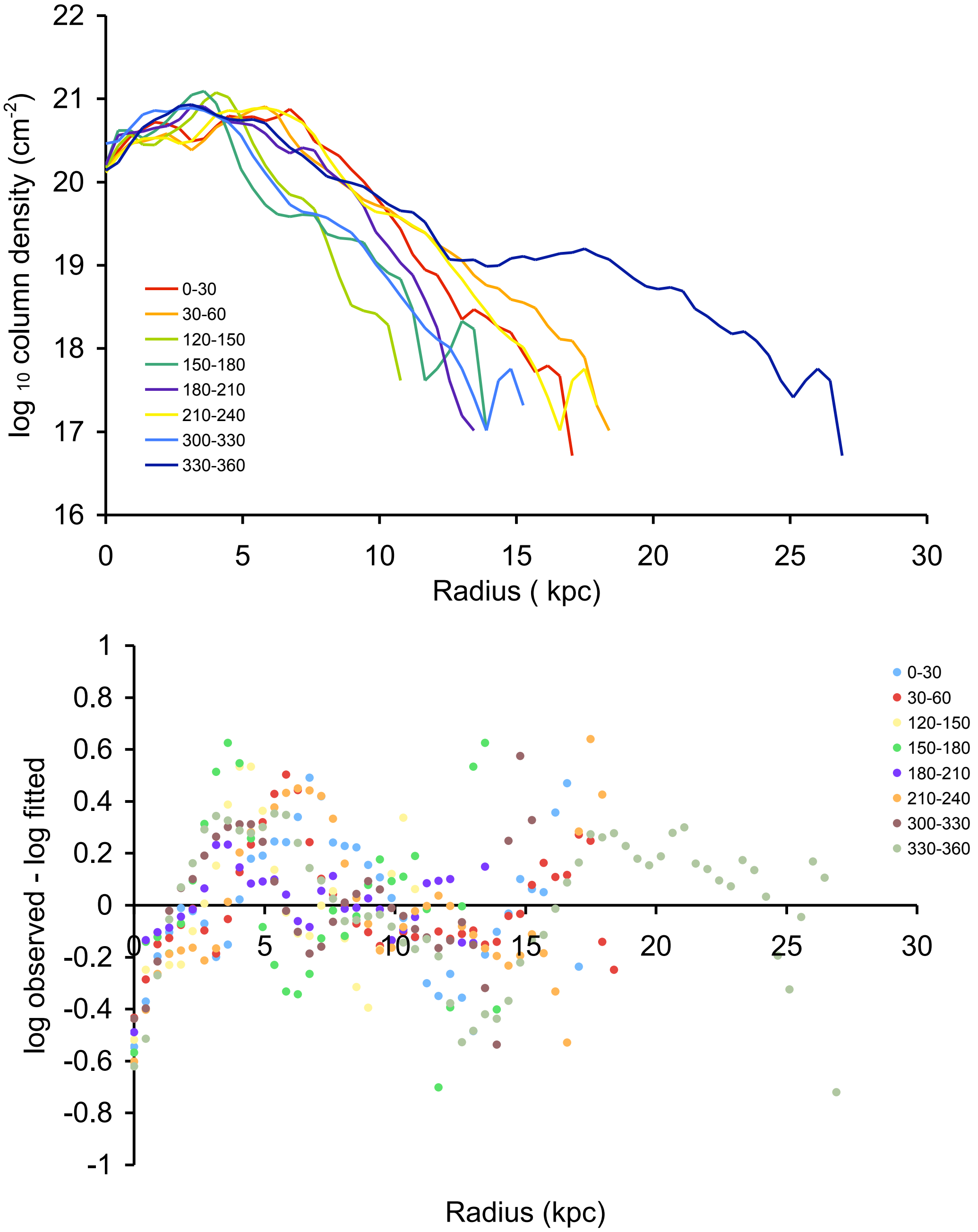

Figure A.6: *Top panel:* individual 30° sectors of NGC 3627 ; *Bottom panel:* residuals after a Sérsic–like fit for each 30° sector.

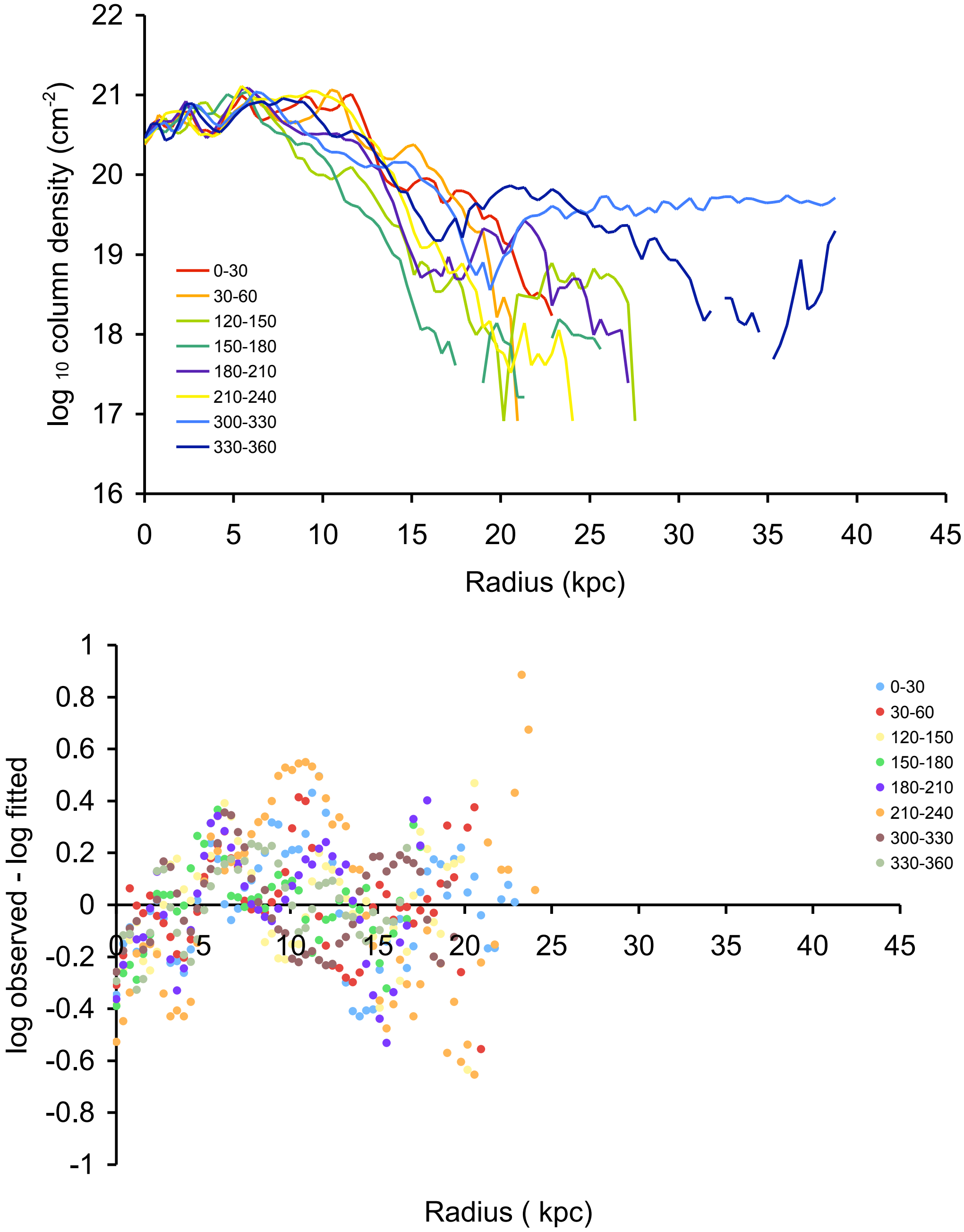

Figure A.7: *Top panel:* individual 30° sectors of NGC 5194 ; *Bottom panel:* residuals after a Sérsic–like fit for each 30° sector.

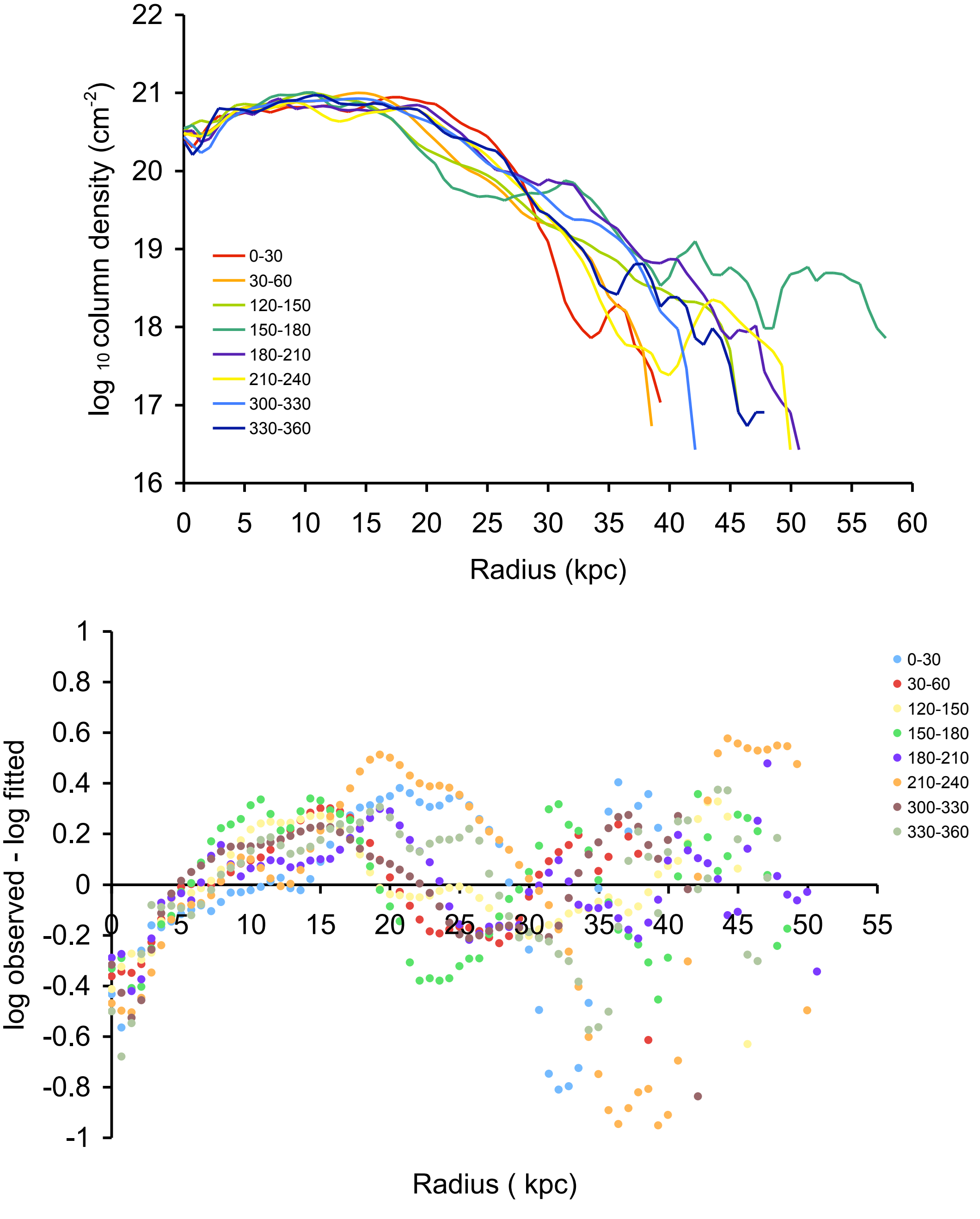

Figure A.8: *Top panel:* individual 30° sectors of NGC 7331 ; *Bottom panel:* residuals after a Sérsic–like fit for each 30° sector.

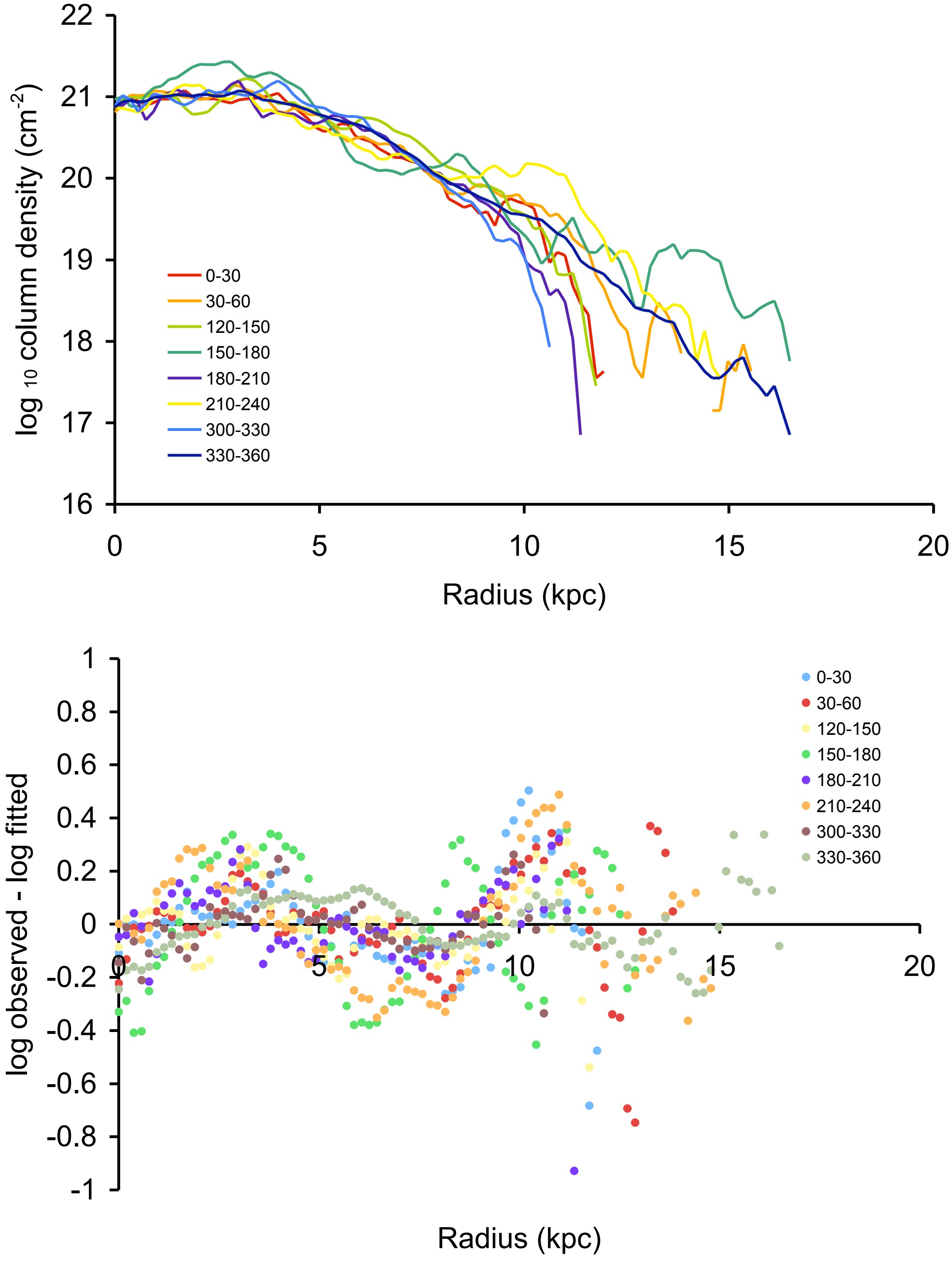

Figure A.9: *Top panel:* individual 30° sectors of NGC 7793 ; *Bottom panel:* residuals after a Sérsic–like fit for each 30° sector.

Chapter 3

Simulations of H I discs

3.1 Introduction

In Chapter 2, we tested the suitability of the THINGS sub–sample of spiral galaxies to probe the decline of neutral hydrogen at the outskirts of H I discs, especially verifying that the data reduction process was not a contributing source of the slopes found. This led to a demonstration which showed that edges are real attributes of H I disc of spiral galaxies.

We now turn our attention to a much more complex matter, as we question the nature of the observed edges and how closely these reproduce the intrinsic distribution of gas in these galaxies at large radii. In other words, we aim to understand how the morphology of the edges as obtained through our interferometric measurements relates to the true distribution of gas.

As mentioned in Chapter 1, we know that spiral galaxies are characterized by having a thin H I disc where the ratio between co–planar gas and perpendicular gas lies somewhere in the 1:30 range. To what extent could our radial profiles (ELLINT and 1–pixel wide as shown in Chapter 2) be affected by both the geometrical orientation on the sky of the H I disc and the vertical scaleheight distribution of the gas.

To shed light on this matter, we choose to work with GALMOD, a task implemented in GIPSY (van der Hulst *et al.* 1992) to create a "model" data cube of the distribution of neutral hydrogen in the disc of spiral galaxies. It is *not* our intention with this chapter to compete with high–resolution galaxy formation simulations such as those presented for instance by Governato *et al.* (2007). Our perspective is more to focus on understanding the current distribution of gas in galaxies, inferring how the intrinsic edge of a galaxy and the radial profiles obtained by us are related.

Our strategy is simple and it is based on a comparison between H I maps and radial profiles of both observations and models created by GALMOD. As we will explain in more detail in the next section, amongst other parameters, GALMOD allows as input, a radial gas distribution of a disc to generate models. By fully controlling the input of this parameter and comparing it with the output radial gas distribution of the generated model, we will be able to infer differences inherent to the variations of other parameters employed to run the models, such as inclination and scaleheight distributions of the disc.

We decided to build models of galaxies with an increased complexity, starting with a model of a constant H I distribution sharply truncated (model A) up to a close representation of two observed radial distributions of galaxies: NGC 3198 and NGC 3351. The latter two were already studied in depth in Chapter 2. These objects are representative examples of a highly inclined (NGC 3198) and more face–on (NGC 3351) disc.

3.2 GALMOD

As mentioned previously, GALMOD is a software tool used to create a “model” data cube of the distribution of neutral hydrogen in the disc of spiral galaxies.

The philosophy behind the programme is to assume a RA and DEC position of a real data cube (here characterized in Table. 3.1) and populate that region of the sky with concentric rings of H I clouds created via Monte–Carlo simulations. Each ring is then characterized by a rotation velocity, VROT, a velocity dispersion, VDISP, a surface brightness density, DENS, a vertical scaleheight perpendicular to the plane of the ring, Z0, an inclination, INCL and a position angle, PA. GALMOD also allows the user to define the number of H I clouds generated and their distribution across the data cube using the parameters CDENS and CMODE. The clouds are placed evenly in the region of any given ring with a random height derived from a specific geometry of the vertical density distribution.

To run the task, besides providing an “observed” data cube of the galaxy one needs a rotation curve and radial H I surface brightness distribution. Our strategy, when exploring the GALMOD n parameter space is to study *one* at a time, fixing all remaining parameters.

3.3 Pipeline and radial profiles

GALMOD assumes for the spatial resolution the pixel size of the observed data cube which in this case corresponds to 1.5″ (Table. 3.1). Therefore, the model data cube needs to be smoothed to match the 10″ resolution of the observed data cube using the task SMOOTH implemented in GIPSY. H I maps are created by summing all channels with task SUM. Both sets of resolutions (1.5″ and 10″) are used in the initial exploration of the parameter space, especially in the first two models (A and B). Later on in this Chapter we only make use of the 10″ sets, matching the resolution of the observations. We also make use of the two different kinds of radial profiles (an ELLINT 30° sector centred along the kinematically receding semi–major axis, and 1–pixel wide profiles), created in a similar manner as previously described in Chapter 2.

GALMOD produces model data cubes in Westerbork Units (hereafter WU) where 1 WU = 5 mJy beam^{-1}. To convert our integrated H I maps to the appropriate units (Jy beam^{-1} m s^{-1}), we apply a scaling factor of WU×ΔV, where ΔV is the channel width (in km s^{-1}), see Table. 3.1.

3.4 Galaxy models

3.4.1 Model A: H I disc with a constant surface brightness

The simplest galaxy we can construct is an H I disc with a constant surface brightness sharply truncated at its edge. We take as the observed data cube, the 10″ resolution NGC 3198 data cube obtained from the THINGS project. We choose for the input of the DENS parameter, DENS_A: a constant surface brightness at a column density of 1×10^{21} atoms cm^{-2} (see Fig. 3.1), which corresponds to some of the values of $\log I(0)$ found in Sect. 2.5.1. We made our model $\sim$ 37 kpc radius to match the size of NGC 3198. We choose for our rings a width of 10″ to match the resolution of our observations. As seen in Chapter 2, the surface brightness of the inner parts of radial profiles can be affected by the presence of molecular gas or stellar bar. For that reason we decided to avoid dealing with the very inner rings in our models.

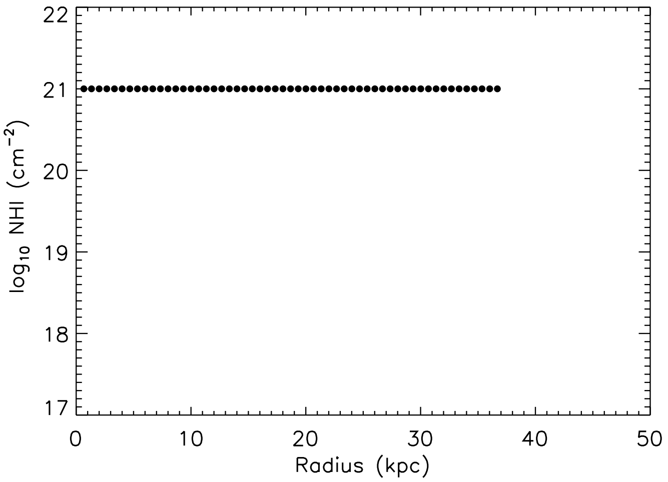

Figure 3.1: The column densities of model A series, DENS_A, in logarithmic scale as a function of radius. The constant column density across the H I disc is at a level of $1{\times}10^{21}$ atoms cm^{-2}.

After preliminary tests, it was found that the best layer geometry to match models with observations is a $sech^2\,(z/z_0)$ vertical distribution which agrees with previous models created by Fraternali & Binney (2006) of extraplanar gas in spiral galaxies. We assumed a constant scaleheight of the gas of $z_0 = 330\,$pc.

3.4.2 GALMOD default parameters

Starting with modA01, we first need to set the default parameters needed. We use a constant position angle of 215° and inclination of 72° throughout, as derived from the THINGS project Walter *et al.* (2008). The rotation curve is an approximation of the the values presented by (de Blok *et al.* 2008), where we forced the curve to an asymptotic rotation velocity of 150 km s^{-1} from 10 kpc onwards, as seen in Fig. 3.2, which we designate by VROT_A.

Table 3.1: Characterisation of the input data cube of NGC 3198

Parameter	Value
α (J2000)	$10^h\ 19^m\ 55.0^s$
δ (J2000)	$+45^\circ\,32'\,58.9''$
V_{hel} (km s^{-1})	780
Image size (pixels)	1024 × 1024
Pixel size ($''$)	1.5
Number of channels	72
Channel width (km s^{-1})	5.2

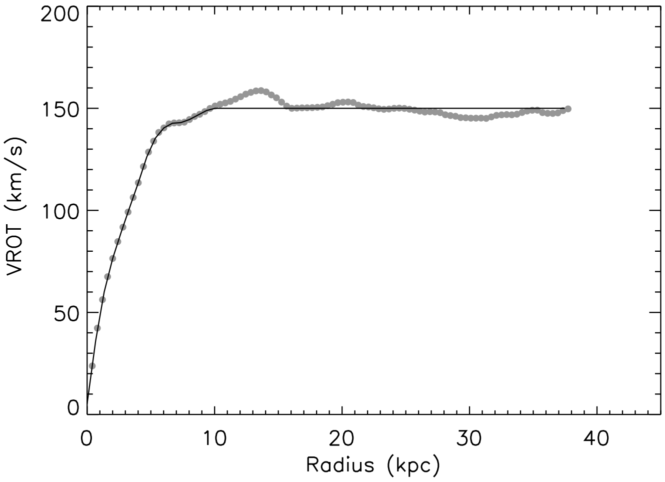

Figure 3.2: The rotation curve of NGC 3198 as derived by de Blok *et al.* (2008) here represented in light grey circles; The solid black line is the approximation, VROT_A, employed in the model data cubes.

In Fig. 3.3 (top left panel) we present an integrated H I map of our model. As stated, we ignored the inner points when calculating the model which is why the H I map shows no values there. It presents a smooth and symmetrical gas distribution with sharp boundaries. The position–velocity diagram (Fig. 3.3, top right panel) taken along the semi–major axis of our model reflects the input rotation curve steeply rising up to ~ 10 kpc and remaining flat onwards. We also show in Fig. 3.3 two individual velocity channels of our model data cube, showing the distribution of H I clouds in the different channels calculated by GALMOD.

In Fig. 3.4 we plot on a logarithmic scale the radial profiles (ELLINT plus 1–pixel wide) as a function of radius for two resolutions: the original $1.5''$ pixel size and the $10''$ resolution corresponding to the SMOOTHed data. These radial profiles are compared with DENS_A, the input for the DENS parameter of GALMOD. As expected the surface brightness pertaining to the radial profiles remains constant throughout the model. The 1–pixel wide density profile stops abruptly where the input density profile runs out of gas. There is therefore no noticeable line–of–sight blending taking place. When smoothing to $10''$, the profile drops according to the imposed beam width. Also, using a $30°$ wide segment centred on the semi-major axis to derive the surface density profile causes some minimal smoothing. However, in all these cases, the drop is precipitous and, with the exception of the last measured point, is a faithful representation of the input profile.

Fig. 3.4 also shows a slight offset between the input model surface density and the output density. This offset corresponds to a factor of ~ 1.13 and can be traced back to the fact that GALMOD calculates the model in units of W.U. per pixel. When converting to column density we assumed instead of a square $1.5'' \times 1.5''$, a gaussian beam with a FWHM of $1.5''$. This results in a slightly different conversion from W.U., or mJy, to units of kelvin brightness temperature. That difference is exactly 1.13. Rather than correcting the graphs we decided to leave them in their current form as this allows for easier comparison between input and output curves.

3.4.3 CMODE and CDENS: surface density of the H I clouds

In modA02 and modA03 we investigate the variation of the CDENS parameter, which according with to the task description influences the surface density of the generated

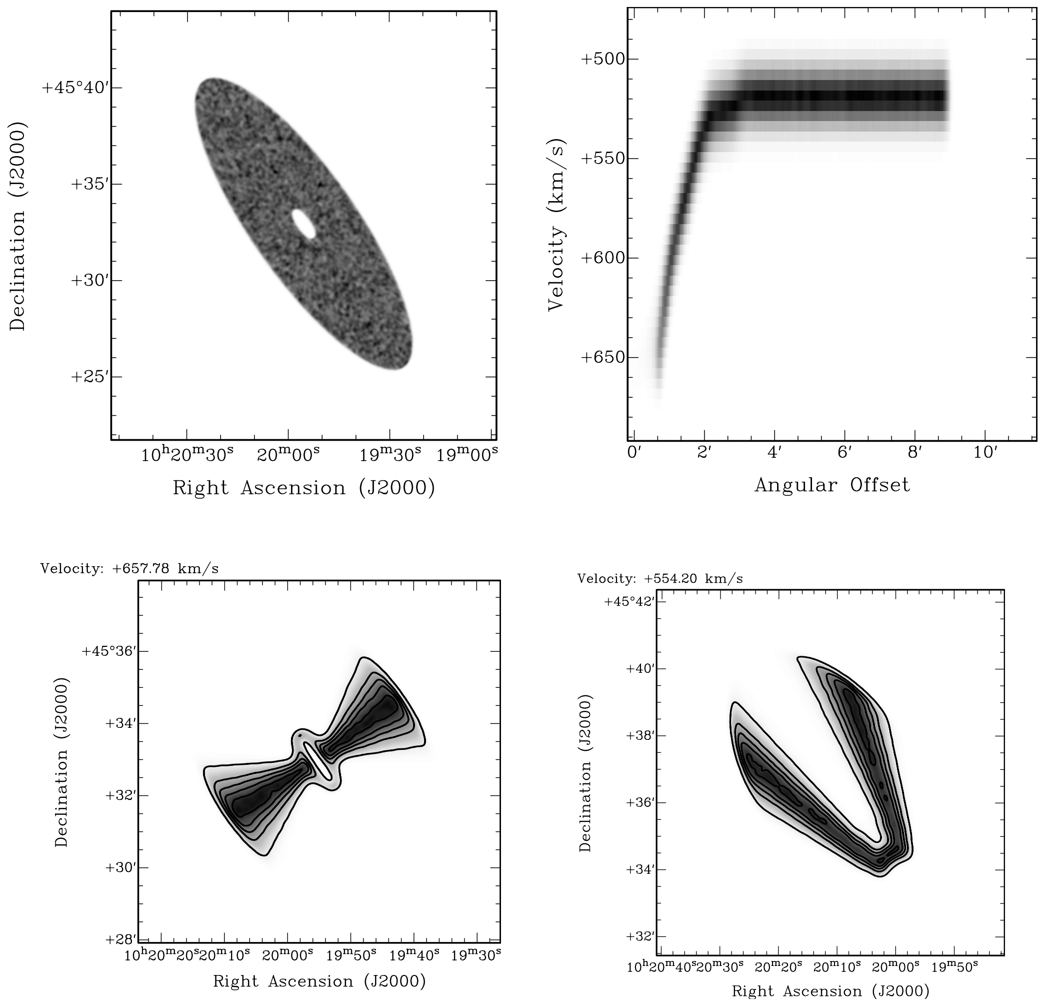

Figure 3.3: The integrated H I map of modA01 with a 10″ resolution (top left panel). In the the top right panel we present the position-velocity map along the kinematical semi–major axis at a PA of 215° , which is representative of the rotation curve of the model. In the bottom panels we present two individual velocity channels.

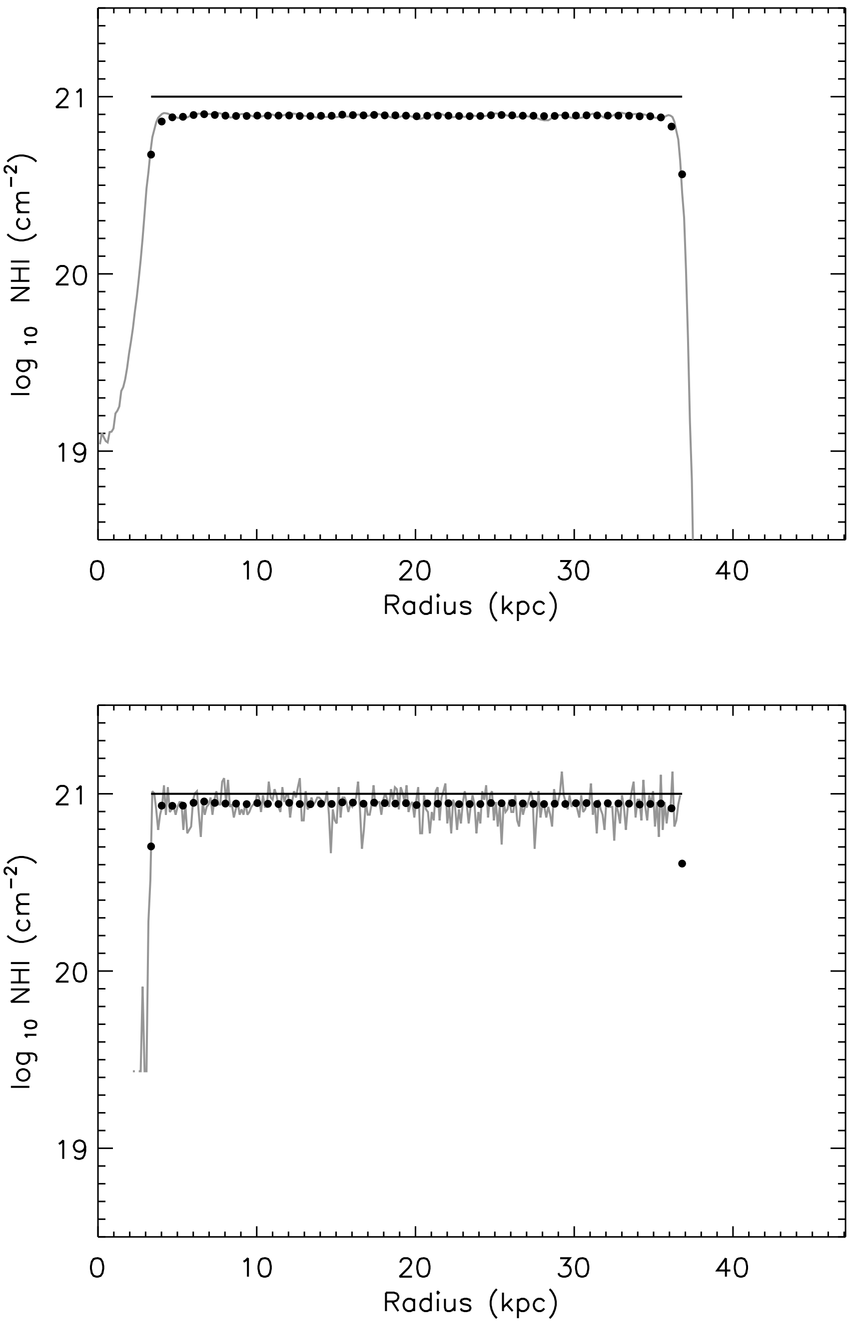

Figure 3.4: A comparison amongst the surface density of the model identified as modA01, that uses DENS_A for its input gas density distribution, which is here represented as a solid black line, the 1–pixel wide radial profile (solid grey line) and the radially averaged ELLINT profile (solid black dots). In the top panel we present data corresponding to a resolution of 10 arcsec (SMOOTHed data); in the bottom panel, data at 1.5 arcsec (original GALMOD resolution)

H I clouds per area of a pixel. Coupled to this is the CMODE parameter which determines the dependence if the signal of the individual clouds with the surface density of H I . The task description also recommends keeping CMODE to its default parameter of 1.0. In this case, individual clouds are given the same weight when contributing towards to total signal measured. CDENS is always expressed in units of 1×10^{20} atoms cm^{-2} and has a default value of 1.0. For this test all other parameters of the model were left as in modA01, as seen in Table 3.2. For ModA02 CDENS was set to 0.1, which implies that within the area of a pixel we would have, on average, a 0.1 cloud with NH I =1×10^{21} atoms cm^{-2} to give 1×10^{20} atoms cm^{-2} units of CDENS; for modA03, CDENS was set to 10 which results in having 10 H I clouds at NH I =1×10^{19} atoms cm^{-2} per area of pixel.

The resulting integrated H I maps can be seen in Fig. 3.5 and radial profiles obtained are shown in Fig. 3.6. modA02 is populated with fewer H I clouds in its *(RA,DEC)* distribution when compared with the saturated look of the disc of modA03 as shown in Fig. 3.5. This is a direct result of the difference in the number of clouds per pixel area in both maps. This difference is also noticeable when we compare both models for the same velocity channel as presented in bottom panels of Fig. 3.5. Concerning the radial profiles of modA02 and modA03 (Fig. 3.6), modA02 shows more scatter than modA03 as a result of it having fewer clouds per pixel area.

3.4.4 Inclination of the disc

We now focus our attention on the inclination parameter, INCL, and how this affects the measured column density along the line of sight. Given the thin disc geometry of spiral galaxies, it is customary to refer to face–on column density, i.e., corrected by a factor proportional to the cosine of inclination. In the following, we test the effect of different inclinations to the radial profiles.

We created 5 models, modA06, modA07, modA08, modA09 and modA10 with the following inclinations: 0° , 30° , 45° , 60° and 90° , respectively. In this trial, all other GALMOD parameters were left with their default values as listed in Table 3.2.

In Fig.3.7 we present the integrated H I maps of the models at different inclinations created at a resolution of $1.5''$. Looking at modA06 to modA10 we see how the disc tilts towards the line of sight, starting as a face–on circular disc (modA06; top left

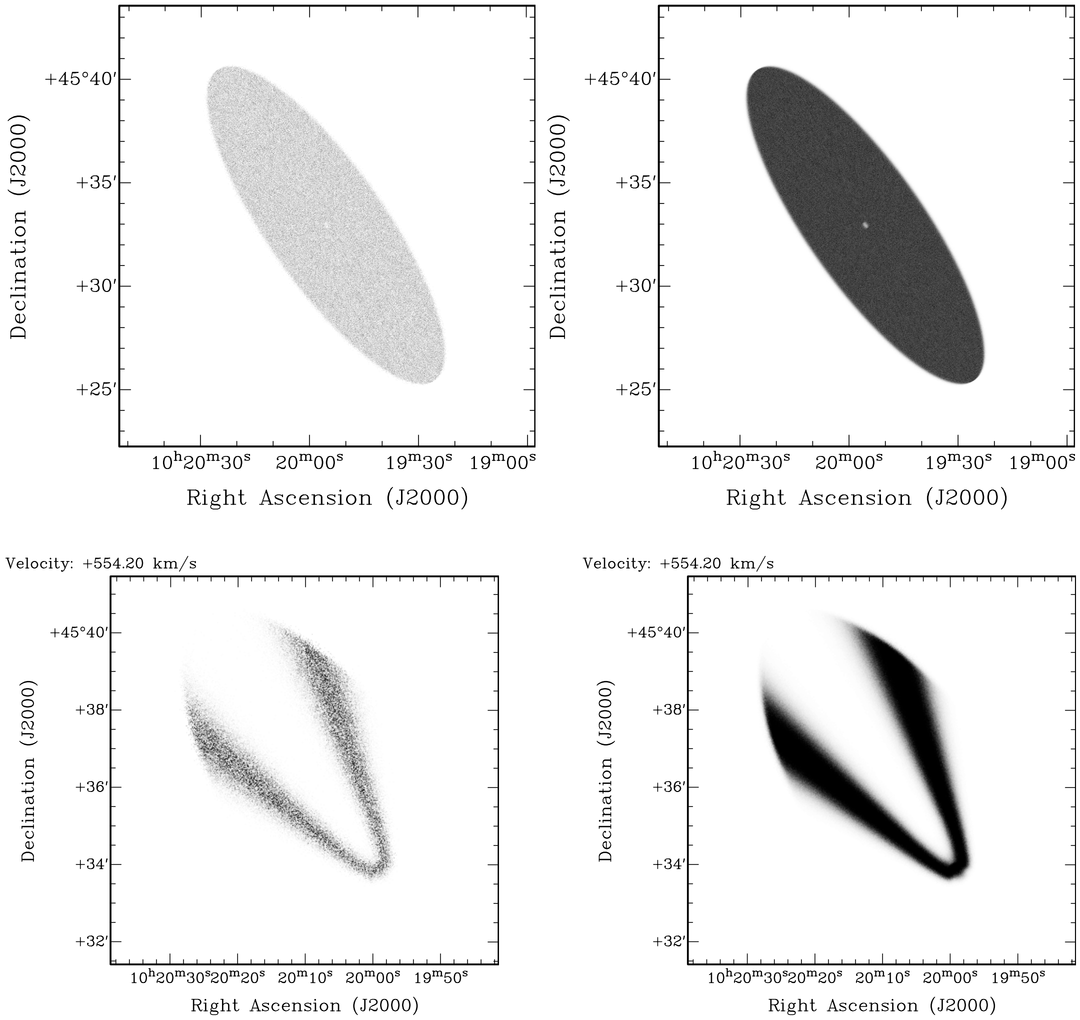

Figure 3.5: Integrated H I maps of modA02 (top left panel) and modA03 (top right panel) where we change the number of H I clouds by varying the CDENS parameter. In the bottom panels, we present the same velocity channel for both models, modA02 on the left and modA03 on the right. All maps refer to the 1.5″ dataset.

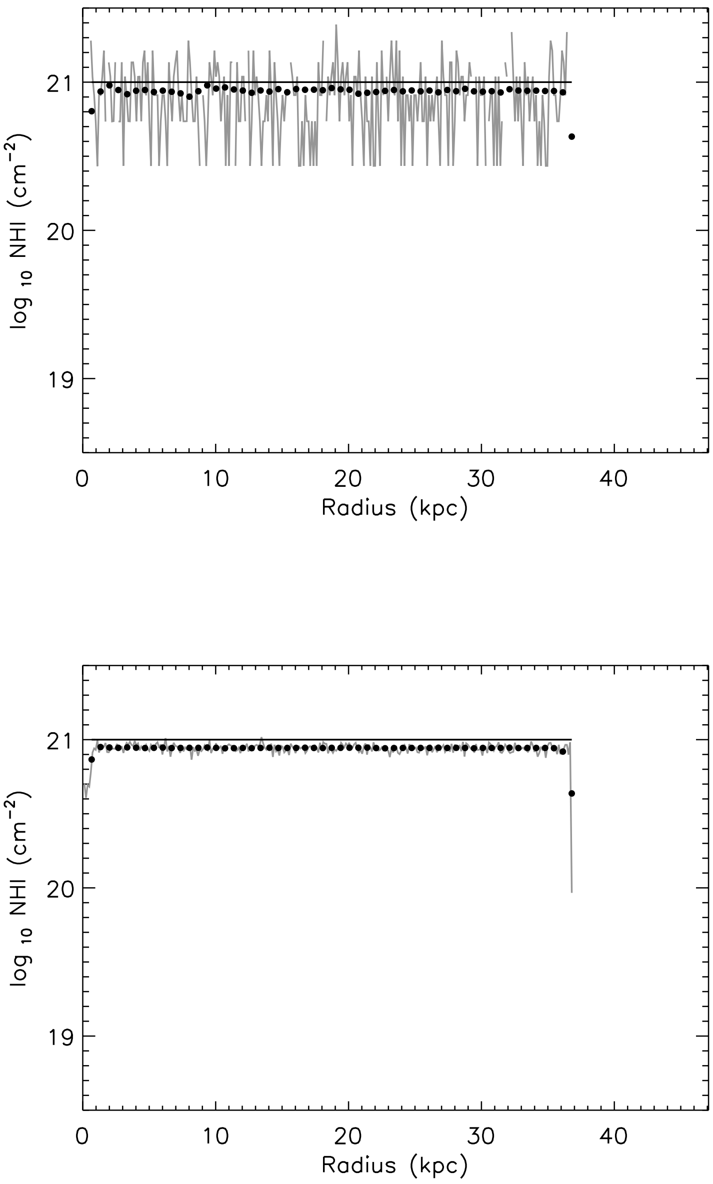

Figure 3.6: Variation of the number of H I clouds for modA02 (top panel) and modA03 (bottom panel). We plot the DENS_A distribution (solid black line), the 1–pixel wide radial profile (solid grey line) and the radially averaged ELLINT profile (solid black dots).

panel) with an inclination of 0° and ending in an edge–on disc (modA10; bottom panel) with an inclination of 90° .

In Fig. 3.8, we plot the same velocity channel at $\sim$ 673 km s^{-1} for all 5 models with different inclinations. It is worthwhile to notice that when an object is face–on as in modA06, the entire area of the disc appears in this velocity channel map.

We finally present in Fig. 3.9 the impact different inclinations have on the 1–pixel wide and ELLINT radial profiles. As seen, no major differences emerge from models modA06 to modA09: the scatter in the 1–pixel wide profile is quite similar amongst the 4 models. The ELLINT profiles all show an abrupt H I edge with only modA10 showing the observed profile deviating from the input surface density, as shown in Fig. 3.9. Column densities of the 1–pixel wide profile begin higher than the DENS_A distribution input, at $\sim 1.6 \times 10^{21}$ cm^{-2}, smoothly declining down to $\sim 3 \times 10^{20}$ cm^{-2} at 37 kpc. The ELLINT radial profile follows the 1–pixel wide profile behaviour out to $\sim$ 12 kpc, declining steeper onwards.

Overall, we find that, except for highly inclined discs, column densities as derived in our 1–pixel wide and ELLINT radial profiles are in good agreement with the input column densities of DENS_A in GALMOD. For completeness, we mention that ELLINT does not allow us to use an inclination of 90° as it cannot divide by cos(90°) in order to derive a radial surface brightness corrected to face–on. The ELLINT results for the edge–on models were therefore calculated assuming an inclination of 89° .

3.5 Model B: H I disc with an exponential declining edge

The next case we are going to study is an improvement of model A, where we divide the model into two different regions. We add to the inner region with a constant column density value, a second region where we have an exponential decline to represent the outskirts of the H I disc. With this, we create model B, choosing column densities values as shown in Fig. 3.10, where we plot on a logarithmic scale NH I as a function of radius. Model B column densities, DENS_B, is defined by a maximum radius, R_{max} $\sim$ 37 kpc. As in model A, the inner region is characterized by a constant column density of log (NH I) = 21 atoms cm^{-2} out to a radius of 30 kpc which encloses

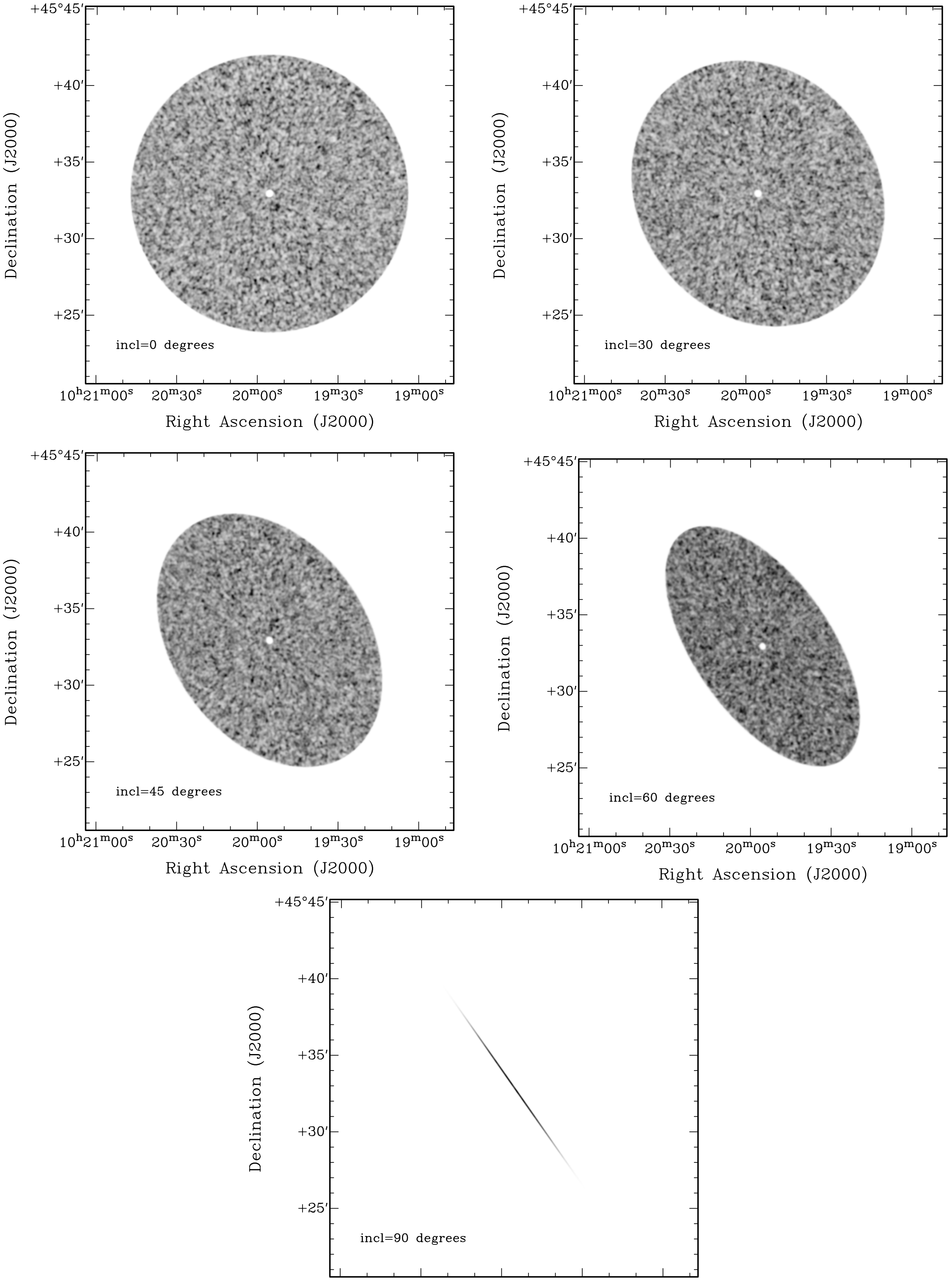

Figure 3.7: Integrated H I maps of modA06 (top left panel), modA07 (top right panel), modA08 (middle left panel), modA09 (middle right panel) and modA10 (bottom panel), created with different inclinations. The inclination is listed in each map. All maps refer to the 1.5″ resolution dataset.

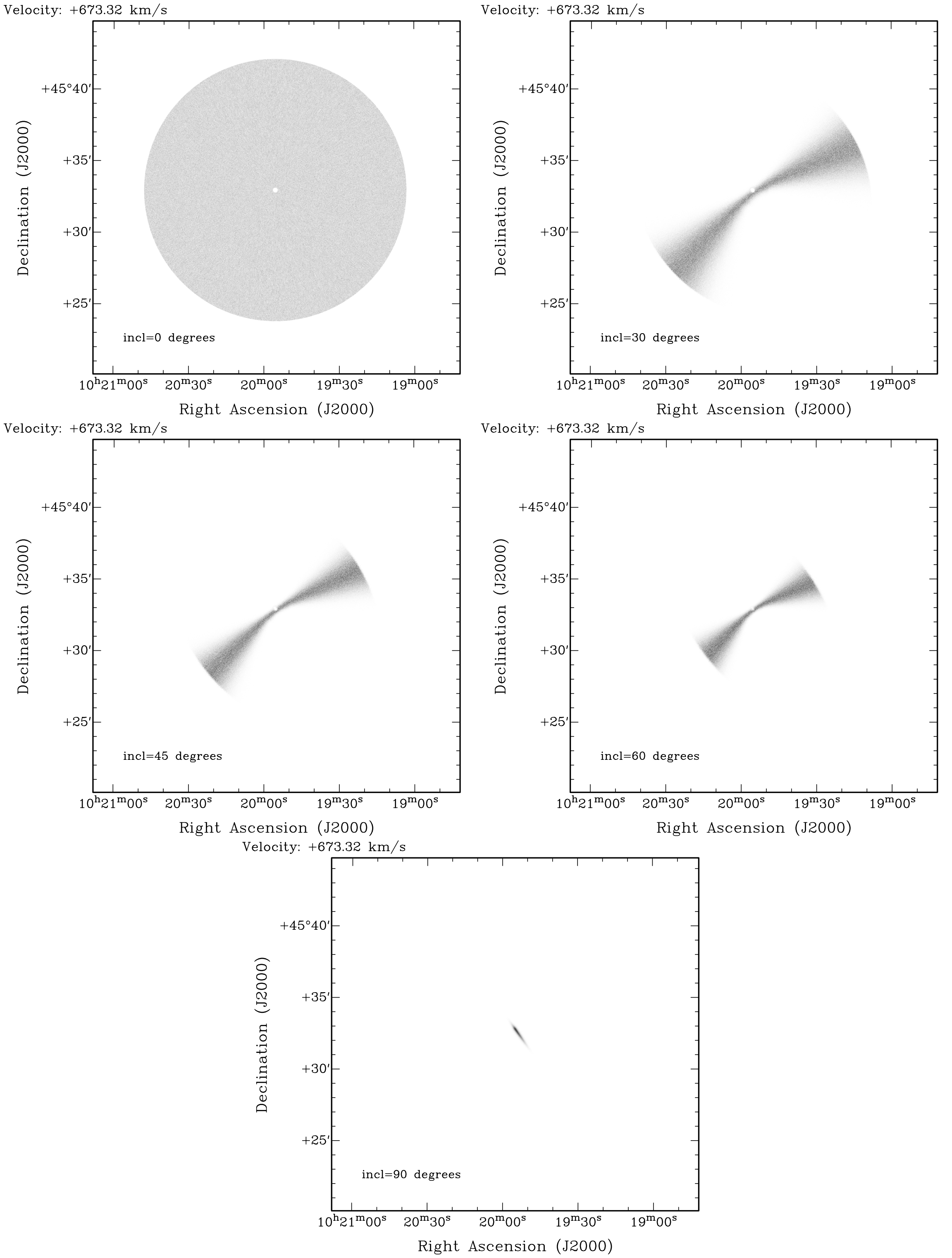

Figure 3.8: Individual velocity channel at $\sim$ 673 km s^{-1} for modA06 (top left panel), modA07 (top right panel), modA08 (middle left panel), modA09 (middle right panel) and modA10 (bottom panel); all models were generated with different inclinations listed in each map. All maps refer to the 1.5″ resolution dataset.

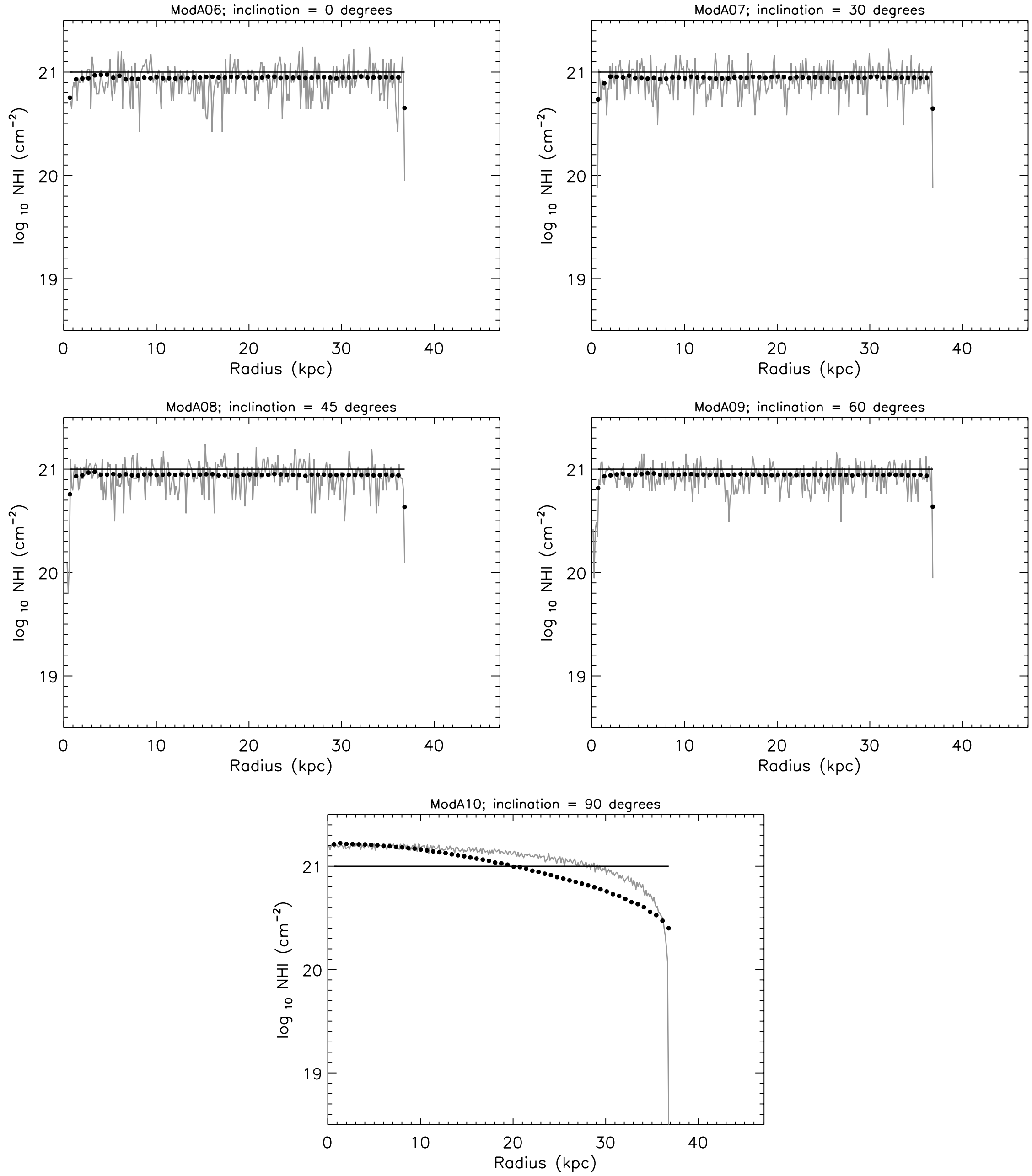

Figure 3.9: Column densities as a function of the radius for modA06 to modA10. The plots are shown on a log–linear scale. The solid black line represents DENS_A distribution used as an input in GALMOD. The 1–pixel wide profile can be seen in the grey solid line, whereas the ELLINT profile is represented by the solid black dots. In all plots we present the inclination of the disc.

80 % of the size of the disc. This is followed by a second outer region with a size corresponding to the last 20% where we make the neutral gas decline exponentially down to log (NH I) = 18 atoms cm^{-2}.

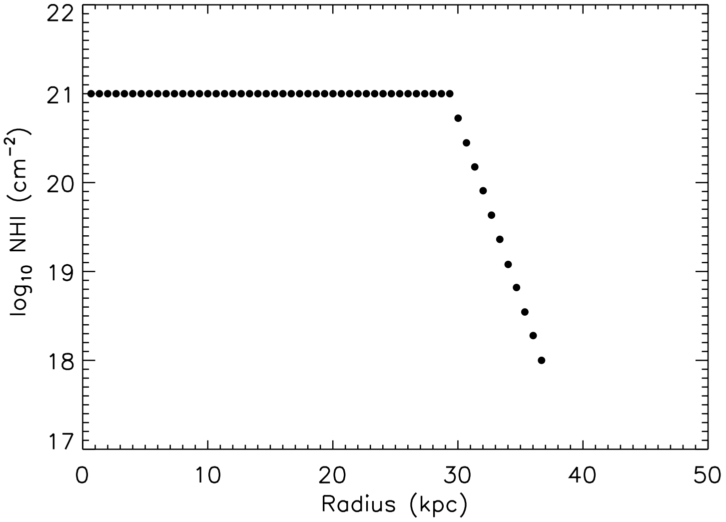

Figure 3.10: The column densities of model B, DENS_B, in logarithmic scale as a function of radius. The constant column densities across the H I disc are at a level of 1×10^{21} atoms cm^{-1} out to 30 kpc, followed by an exponential decline down to a column density of 1×10^{18} atoms cm^{-1} at 37 kpc.

As seen in Chapter 2, spiral galaxies show signatures of declining surface brightness values at their outskirts. Although the disc here created presents a simplified H I decline, our goal is to analyse how well GALMOD reproduces the two regimes and more importantly how this translates in terms of radial profiles. Finally we chose the scale of inner and outer region in model B at a proportion of 80% and 20%, following closely similar proportions found in NGC 3198 and NGC 3351 as studied in Chapter 2. As in model A, we made our model use the same sky area, pixel size, ring width and channel velocity width (5.2 km s^{-1}) as NGC 3198. We also use the approximation of the NGC 3198 rotation curve as presented in Fig. 3.2. The general properties of Model B are summarized in Table 3.2.

In the following, we run a number of models for Model B. We vary parameters

CDENS and CMODE parameters, and introduce an exponential scaleheight, for the gas distribution as well as study different inclinations of the disc.

3.5.1 Model B: GALMOD default parameters

The first trial we ran, modB_01, was based on GALMOD default parameter values as summarized in Table 3.2. We used an inclination of 72° , PA of 215° and constant scaleheight of 0.33 kpc. CMODE and CDENS were left at their default values of 1.0. We used a $sech^2\,(z/z_0)$ for the vertical layer geometry.

In Fig. 3.11, we present an integrated H I map at 1.5″ resolution. The map presents a uniform distribution of the H I clouds surrounded by a fuzzy outer edge. This is better seen when we zoom in on the North-East region of the disc (Fig. 3.11; right panel).

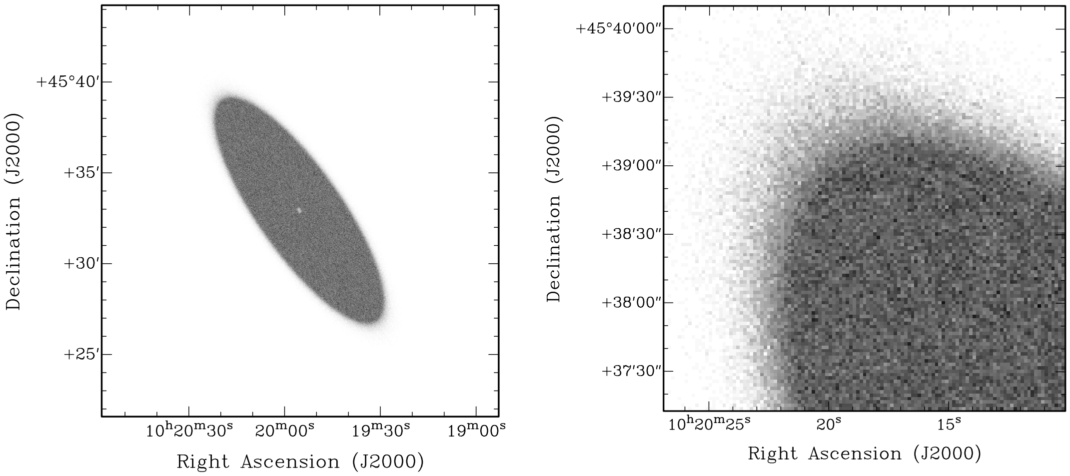

Figure 3.11: Integrated H I map of modB_01. In the left panel we present the entire disc and on the right, we zoom–in on the Northeast region of the disc. Both maps were created with 1.5″ resolution.

The 1–pixel wide and ELLINT profiles are shown in Fig. 3.12, where we plot on a logarithmic scale the column density values as a function of radius. As can be seen, both profiles successfully reproduce the inner region and the break–point of the DENS_B density distribution (here represented by the solid black line). However, the 1–pixel wide radial profile (grey solid line) does not probe entirely the outer region of the model stopping at a level of $\sim$ log (NH I) = 19.5 atoms cm^{-2} at $\sim$ 32 kpc. The

ELLINT radial profile (solid black dots) probes the input density parameter down to the lower column density level of log (NH I) = 18 atoms cm^{-2}. To make our analysis more quantitative, we present column density scatter plots of ELLINT result against the model input, and the 1–pixel wide profile against the model on a log–log scale. This is shown in the bottom panels of Fig. 3.12, where we apply a linear regression between both pairs of variables. In each graph we indicate the slope of the fit to the points: a, for the comparison with the ELLINT results, and b, for the 1–pixel wide profile. The log–log plots are a convenient way to judge if the result of the simulations corresponds on a 1–to–1 basis with the model input, i.e. a slope a and b being close to 1.00. The graphs use a log–log scale so as to cover the 4 orders of magnitude column density range.

From this trial we draw the conclusion that there is excellent agreement between input densities and output radial profiles. This is confirmed by both slope $a = 0.99$ and slope $b = 1.13$.

3.5.2 Model B: optimization of the number of H I clouds

As shown in Fig. 3.12, the CMODE and CDENS default parameters values do not allow the entire probing of the disc of model B by the 1–pixel wide profile. To try to correct for this in the following trial we optimize the CMODE, CDENS parameters. To do so we built 5 models: modB_02, modB_03, modB_04, modB_05 and modB_06: in the first 4 models, modB_02 to modB_05, we vary the CDENS parameter as follows: 0.1, 5, 8 and 10, and therefore increasing the number of individual clouds generated leaving the CMODE parameter fixed to 1. In modB_06, we used CDENS = 10 and CMODE = 0. When CMODE=0, CDENS is interpreted as the number of clouds per area of pixel in the ring and the signal contribution of a single cloud is proportional to the surface density of the ring. All the other parameters were left as in the previous case as summarized in Table 3.2.

Since no major differences emerge from the integrated H I maps, we do not present them here, focussing our attention to the results of the radial profiles shown in Fig. 3.13. From modB_02 to modB_05 we increase the value of CDENS which translates into a better probe of the outer region of model B by the 1–pixel wide profiles (solid grey lines). If in model modB_02 we do not reach values of log (NH I) below

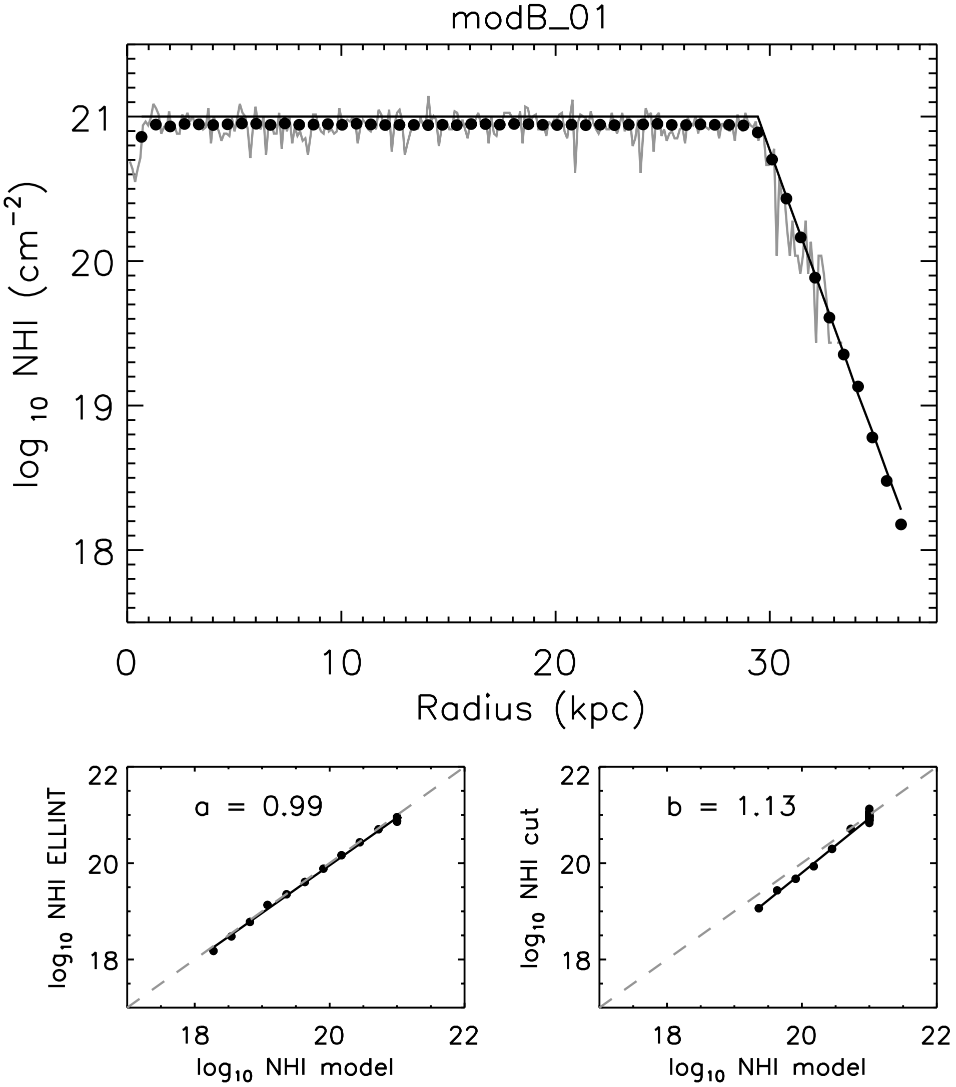

Figure 3.12: The H I column density values as a function of radius of modB_01. The plot is on a log-linear scale. The solid black line represents the input of the DENS parameter. The 1–pixel wide profile can be seen as the grey solid line, whereas the ELLINT profile is represented by the solid black dots. The smaller bottom panels represent log–log scatter plots between radial profiles and DENS parameter: on the left , the ELLINT–model and on the right the 1–pixel wide–model scatter plot. Scatter is represented by the solid black dots. The fit is shown by the solid black line. In addition we present for guidance purposes the dash grey line with a slope of 1.00

10^{21} atoms cm^{-2}, in modB_05 we fully probe the entire disc down to levels of log (NH I) ∼ 18 atoms cm^{-2}. Moreover we find that the slopes of modB_06 ($a = 0.99$ and $b = 1.02$) indicate negligible differences between radial profiles and DENS_B, reenforcing our choice of CMODE and CDENS parameters for model B. Another trend worth mentioning is the decrease of the scatter of the 1–pixel wide radial profiles when increasing the CDENS parameter. It is with modB_06 that we obtain the best result, and find a good compromise between probing the outer region and scatter in the profile, electing to use this set of parameters, CDENS=10 and CMODE=0 as the optimum values for this particular disc. It is worth mentioning that the ELLINT profiles are oblivious to the fine–tuning of the CDENS and CMODE parameters seen in the 1–pixel wide profiles. This is due to the efficiency of azimuthally averaging along the 30° arc–wide segment which encloses many peripheral discrete clouds as shown in Fig. 3.11. This is confirmed if taking into account the minimal variation of the slope a between models.

3.5.3 Model B: effects of scaleheight

All the models created so far kept a constant scaleheight as a simplification. However, as mentioned earlier in the introduction of this thesis the scaleheight increases with radius (see some recent papers on the 3–D H I distribution by Banerjee *et al.* 2010; Banerjee & Jog 2008; Kalberla & Dedes 2008; Narayan *et al.* 2005). The next step is to allow the scaleheight to vary and study the effects on the radial profiles. In this trial, we test three different radial scaleheight distributions as seen in Fig. 3.14 for three models: modB_07, modB_08 and modB_09. All models start at a typical height at the centre of the disc, h_C of 100 pc . In the first model, modB_07, the scaleheight distribution, SHA, at the outskirts of the disc, or maximum scaleheight, h_R, grows to 1 kpc at R_{max}. This is represented in Fig. 3.14 by solid black dots. For modB_08, h_R grows to 2 kpc at R_{max} (dark grey dots; SHB) and the for third, modB_09, h_R grows to 4 kpc at R_{max} (light grey dots; SHC). This also means that we are dealing with ratios between radius of the disc R_{max} and maximum scaleheight h_R of 1:36, 1:18 and 1:9 respectively. For all three models we decide to use the optimized set of CDENS / CMODE values as derived in the previous section. For complete details on the parameter values we refer the reader to Table 3.2.

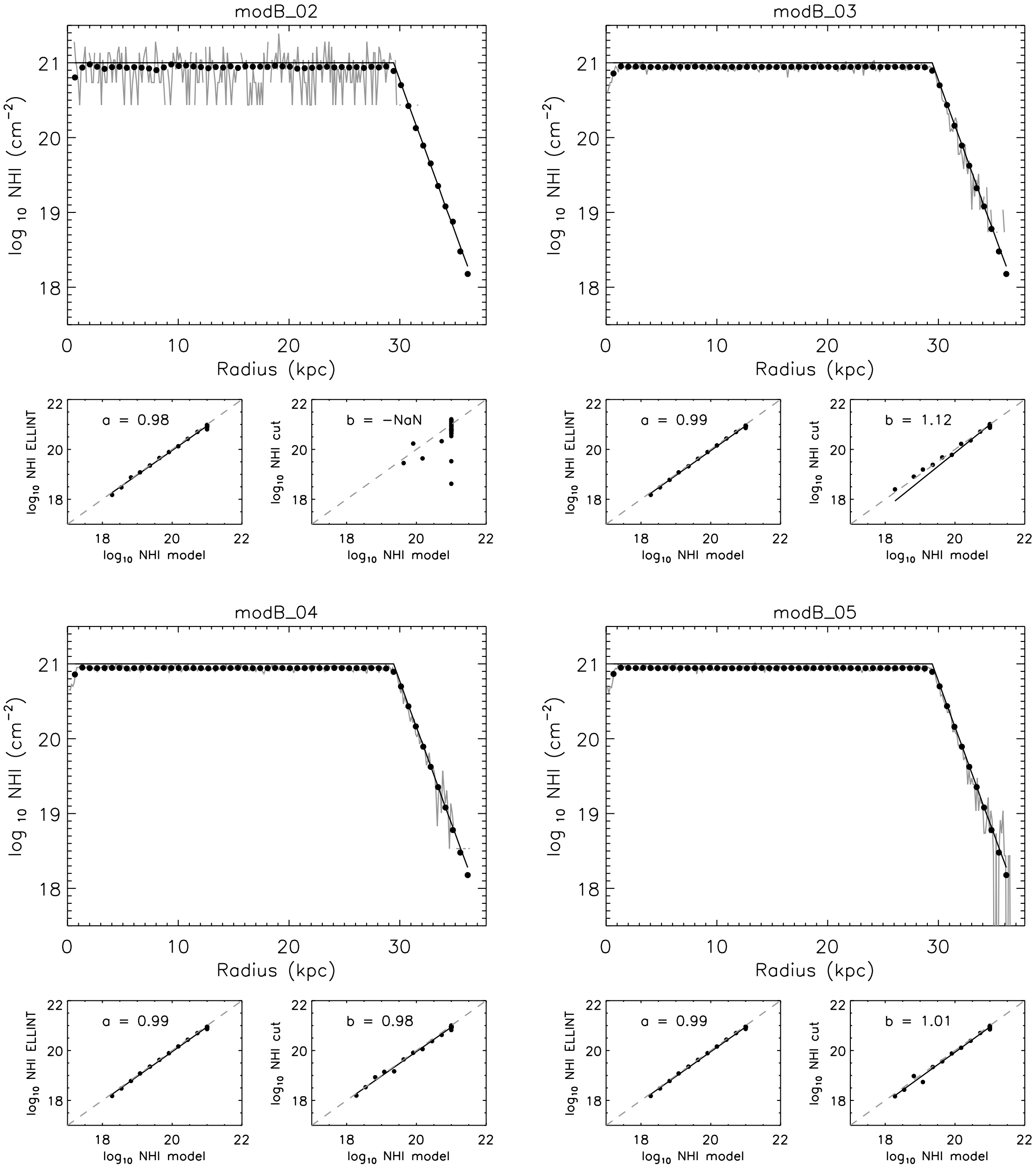

Figure 3.13: Radial profiles of modB_02 to modB_06, where we vary the parameters CDENS and CMODE. The solid black line represents the DENS_B distribution. The ELLINT profiles are represented by the solid black dots whereas the 1 wide-pixel profiles are shown in light grey. All models shown have CMODE=1 except for the final panel, modB_06, where we chose CMODE=0. Please note that the lack of H I clouds on the outer region of model modB_02 is responsible for the divergence of the linear regression between the 1-pixel profile and the model input, hence coefficient *b* is represented by -NaN.

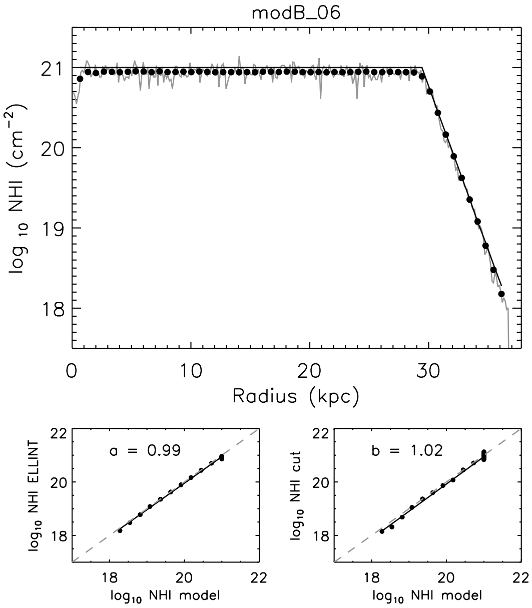

Figure 3.13: Radial profiles of modB_02 to modB_06. (Continued)

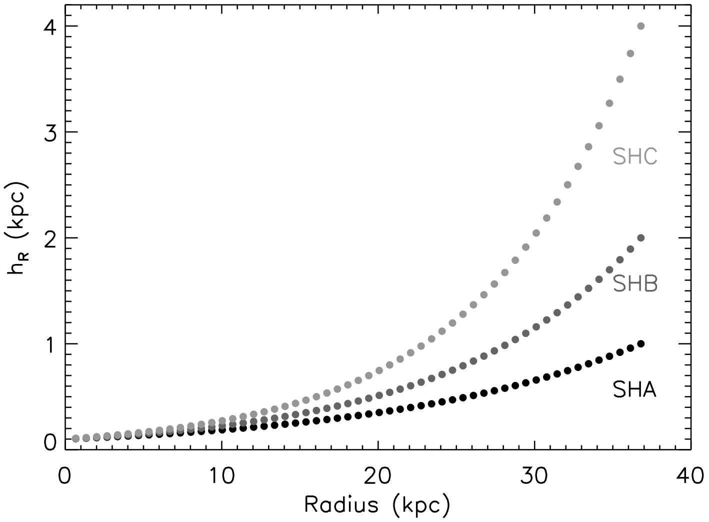

Figure 3.14: The three vertical scaleheight distributions of the gas in kpc as a function of radius. For all, the behaviour was assumed exponential, varying from 100 pc from the centre towards 1 kpc (black solid dots; SHA), 2 kpc (dark grey solid dots; SHB) and 4 kpc (light grey solid dots; SHC) at the outskirts of the galaxy.

Fig. 3.15 shows the different morphology of modB_07 (left) and modB_09 (right). Although the shape and size of both discs are similar, modB_09 appears more diffuse at the outer edge.

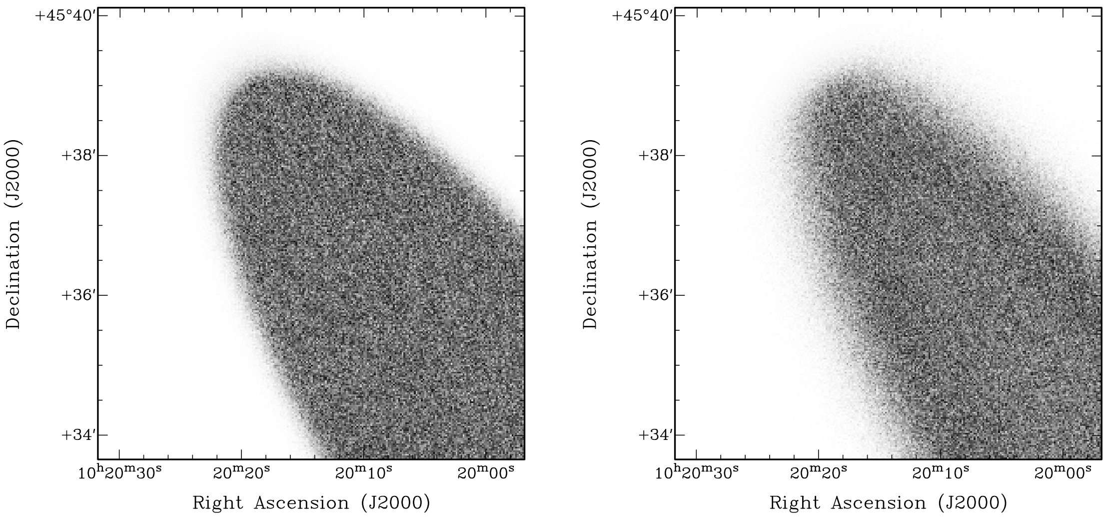

Figure 3.15: Zoom of the northeast region of the H I disc of modB_07 (on the left) and modB_09 (on the right). Both maps were created with 1.5″ resolution.

The radial profiles of modB_07, modB_08 and modB_09 are shown in Fig. 3.16. Overall, radial profiles through modB_07 and modB_08 reproduce well both regions of the disc, whereas modb09 provides a less satisfactory agreement between input density and output profiles. The first thing worth mentioning is that no differences emerge between the model with a constant scaleheight (see modB_06 in Fig. 3.13) and modB_07 (Fig. 3.16; top panel), where the scaleheight has an exponential behaviour.

The average radial profile of modB_08 (Fig.3.13, middle) smooths the turnover between the two regions and this effect is emphasized in modB_09 (bottom panel). Also in these two models we see a difference between the outer slope of the 1–pixel wide and ELLINT radial profiles, the former dropping more steeply than the latter. This is corroborated when analysing the scatter slopes of the three models: modB_07 shows the least scatter (slope $a = 0.96$ and slope $b = 1.04$), with the largest difference between radial profile and DENS_B slope $a = 0.84$, obtained for the ELLINT radial profile of modB_09 (created with SHC, where $h_R = 4$ kpc). We conclude from the above that flaring up to scale heights of 2 kpc has no noticeable effect on the derived surface density curves. Even flaring of 4 kpc at the disc edge has only a modest effect on the ELLINT profile whereas the 1–pixel wide profile still manages to retrieve the intrinsic gas surface density distribution.

3.5.4 Model B: discs at different inclinations

We finish the study of model B with an analysis of the radial profiles for different inclined discs. Similar to the study of model A in Sect. 3.4.4 we ran six models, modB_10 to modB_15 at 0° , 30° , 45° , 60° , 75° and 90° inclinations. We added an inclination of 75° (modB_14) to introduce an intermediate step between 60° and 90° to help with the analysis of the transition between a highly inclined disc and an edge–on disc. We ran all the models with a radial vertical scaleheight distribution, SHA (exponential growth up to 1 kpc at R_{max}). The remaining parameters of the models can be seen in Table.3.2.

We chose not to present the integrated H I maps or an individual velocity map of the models as their morphology is quite similar to those of model A as shown in Fig. 3.7 and Fig. 3.8. In Fig. 3.17, we present the radial profiles obtained for the different models at different inclinations. As shown, all radial profiles follow the density of model B for different inclinations with the exception of modB_15 (bottom right panel).

3.6 Models of spiral galaxies

Based on our experience with GALMOD in the previous sections, we decided to try to create more realistic looking models. We decided to model NGC 3198 and NGC 3351 not only to complement the studies of these two objects from Chapter 2, but also because these two objects are good examples of an inclined (NGC 3198) and nearly face–on (NGC 3351) disc.

3.6.1 Modeling NGC 3198: the case of an inclined H I disc

To model the disc of NGC 3198 via the tilted rings approach, we need information about the radial distribution of the neutral gas component as well as kinematical

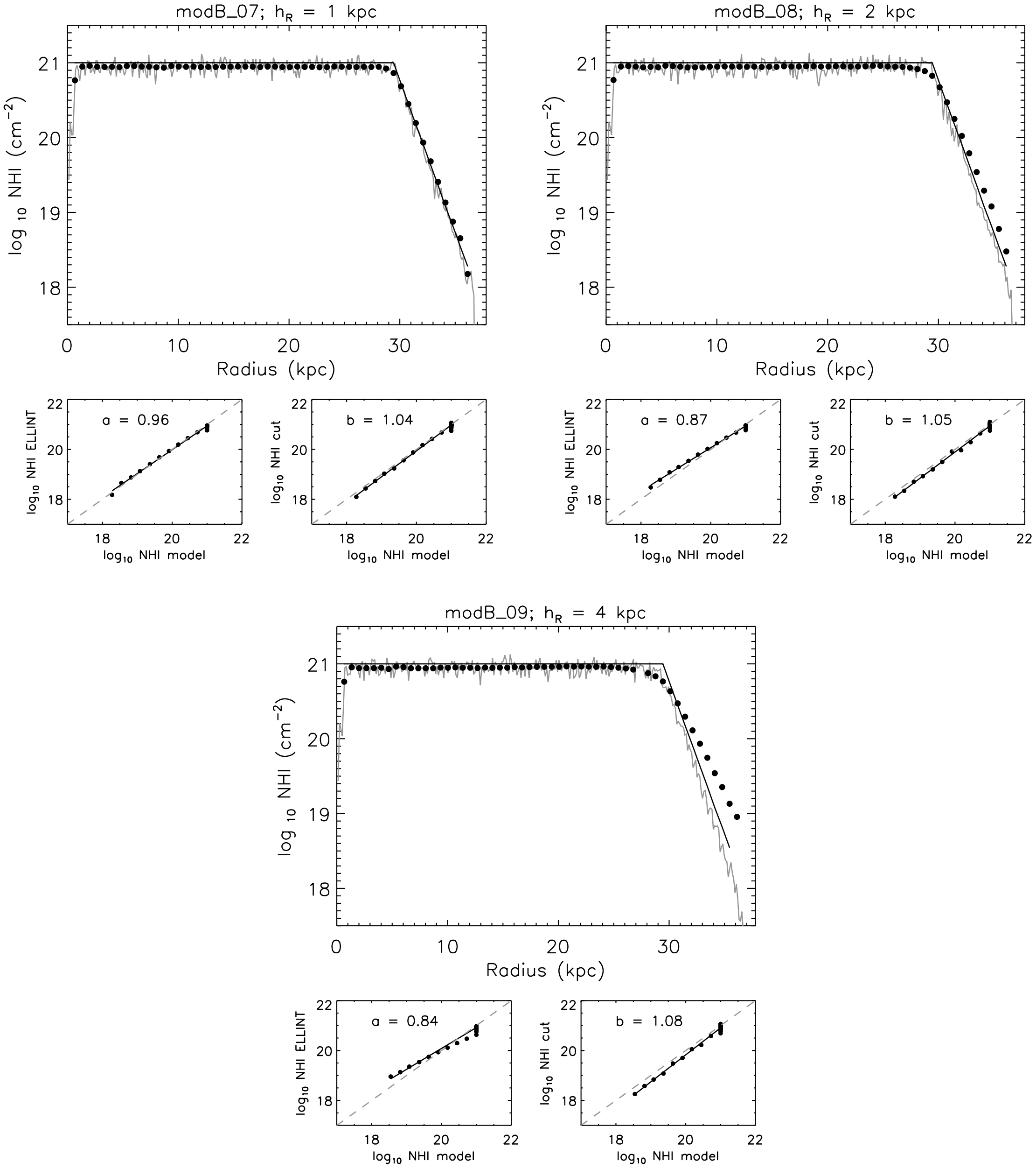

Figure 3.16: Radial profiles obtained for models modB_07 (top panel), modB_08 (middle panel) and modB_09 (bottom panel). In all three models the scaleheight grows exponentially with the maximum scaleheight reached shown in the title of each individual panel. The DENS input parameter is here represented by the solid black line. The 1–pixel wide and the ELLINT radial profiles are shown as a solid grey line and solid black dots respectively.

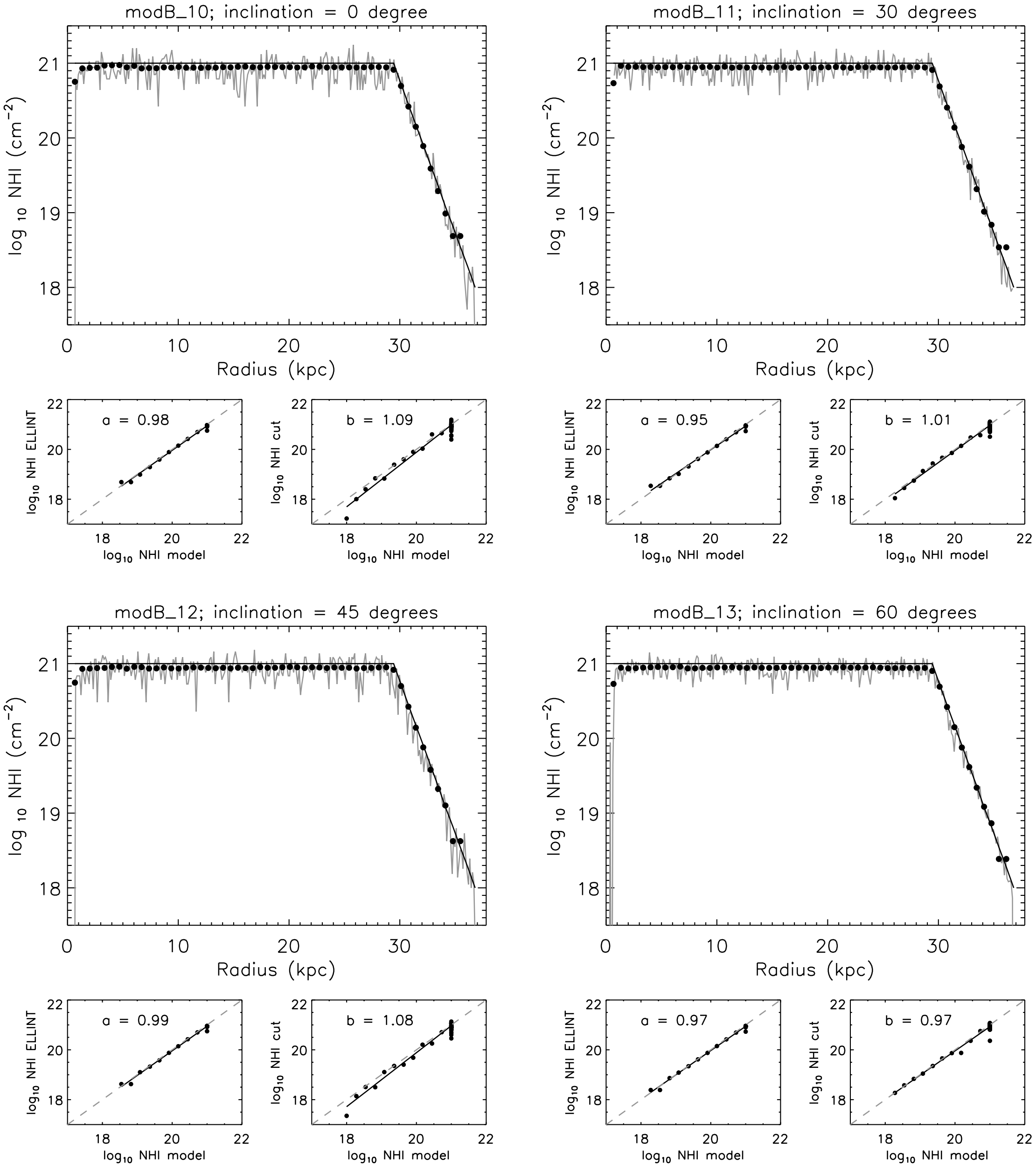

Figure 3.17: Radial profiles of models modB_10 to modB_15 for different disc inclinations (shown at the top of each individual panel). The DENS_B density distribution is represented by the solid black line. The 1–pixel wide and the ELLINT radial profiles are shown as solid grey line and solid black dots, respectively.

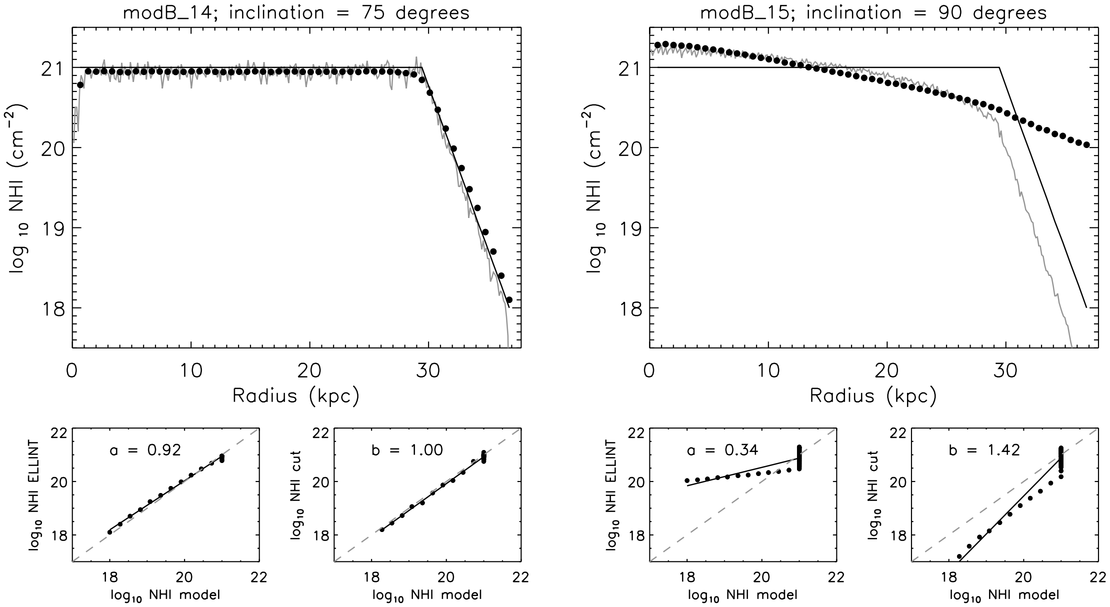

Figure 3.17: Radial profiles of models modB_10 to modB_15 for different disc inclinations. (Continued). Please note that the poorly fitted slopes a and b of model modB_15 result from crowding of points at high column densities, biasing the fits.

Table 3.2: GALMOD parameters for models A and B

OUTSET	VROT km s^{-1}	DENS cm^{-2}	Z0 $''$	INCL °	PA °	CMODE	CDENS
modA01	VROT_A	DENS_A	5	72	215	1	1
modA02	VROT_A	DENS_A	5	72	215	1	0.1
modA03	VROT_A	DENS_A	5	72	215	1	10
modA06	VROT_A	DENS_A	5	0	215	1	1
modA07	VROT_A	DENS_A	5	30	215	1	1
modA08	VROT_A	DENS_A	5	45	215	1	1
modA09	VROT_A	DENS_A	5	60	215	1	1
modA10	VROT_A	DENS_A	5	90	215	1	1
modB_01	VROT_A	DENS_B	5	72	215	1	1
modB_02	VROT_A	DENS_B	5	72	215	1	0.1
modB_03	VROT_A	DENS_B	5	72	215	1	5
modB_04	VROT_A	DENS_B	5	72	215	1	8
modB_05	VROT_A	DENS_B	5	72	215	1	10
modB_06	VROT_A	DENS_B	5	72	215	0	10
modB_07	VROT_A	DENS_B	SHA	72	215	0	10
modB_08	VROT_A	DENS_B	SHB	72	215	0	10
modB_09	VROT_A	DENS_B	SHC	72	215	0	10
modB_10	VROT_A	DENS_B	SHA	0	215	0	10
modB_11	VROT_A	DENS_B	SHA	30	215	0	10
modB_12	VROT_A	DENS_B	SHA	45	215	0	10
modB_13	VROT_A	DENS_B	SHA	60	215	0	10
modB_14	VROT_A	DENS_B	SHA	75	215	0	10
modB_15	VROT_A	DENS_B	SHA	90	215	0	10

Additional GALMOD parameters: POS: -3,0; VSYS: 660 km s^{-1} ; RADII: 10:550:10 except for modA01 (50:550:10); VDISP: 10 km s^{-1} ; LTYPE: 2; NV=72.

parameters of the gas on each ring, such as rotation velocity, position angle and inclination.

In this section we employ the radial distribution of the gas as mentioned in Chapter 2, derived from the THINGS 10″ resolution integrated H I map shown in Fig. 3.18 and used this as input for DENS, the parameter describing the radial density designated DENS_{3198}. It is based on an ELLINT 30° sector centred on the major axis and averaged in 10″ radial bins. Its radial distribution resembles model B in the manner of having two distinct regions: an inner region with column densities at a level of log (NHI)~ 20.5 atoms cm^{-2} out to a radius ~ 40 kpc and a exponentially declining outerpart. As in model B, the inner region encloses 80% of R_{max}, where R_{max} (~ 48 kpc) is the radius of the disc as measured by the last ring obtained by the ELLINT radial profile. The column densities along the inner part of the galaxy are no longer constant but show variations due to density variations in the disc. The HI in the outer region of the disc decreases steeply down to column density levels of log (NHI) ~ 18 atoms cm^{-2} , which corresponds to the last $0.2\,R_{\mathrm{max}}$ of the disc.

We now also employ the true rotation curve of the galaxy as derived by de Blok *et al.* (2008) as seen in Fig. 3.19 (top panel). The author derives the rotation curve out to a radius of 37 kpc, allowing the PA and the inclination on each ring to vary as a free parameter (see Fig. 3.19, middle and bottom panels, respectively). Overall, there is not a large dispersion in the values of the rotation curve around the asymptotic velocity of $\sim$ 150 km s^{-1} from 7 kpc onwards. The PA values vary from 200° at the centre of the disc to 215° at 37 kpc. We replicate the last values of the rotational velocity, PA and inclination of the rings beyond 37 kpc and designate these parameters by VROT_{3198}, PA_{3198} and INCL_{3198}, respectively.

NGC 3198: optimizing the number of clouds at a constant scaleheight

In this first trial we will create a single model of the H I disc of NGC 3198, mod3198_01, where we address two questions. First, we will try to infer optimized values for parameters CMODE and CDENS. It still remains unclear if two different combinations of these parameters could originate similar models and hence similar radial profiles. We turn to what we have learned from model B in Sect. 3.5.2 where we fine–tuned these values. As seen, when CMODE =1, the increase of CDENS translated in a

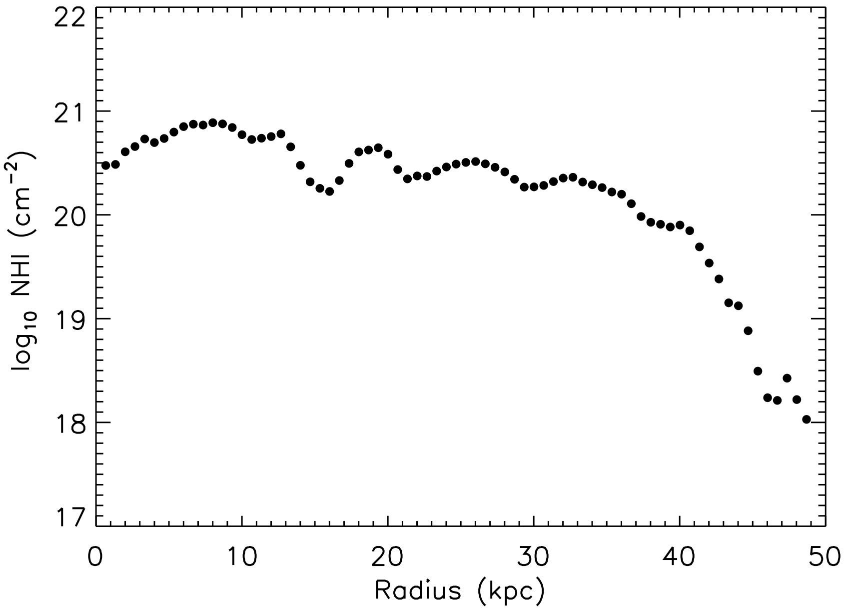

Figure 3.18: ELLINT radial profile of NGC 3198 as derived in Chapter 2 which will be applied as the DENS parameter input, DENS_{3198}

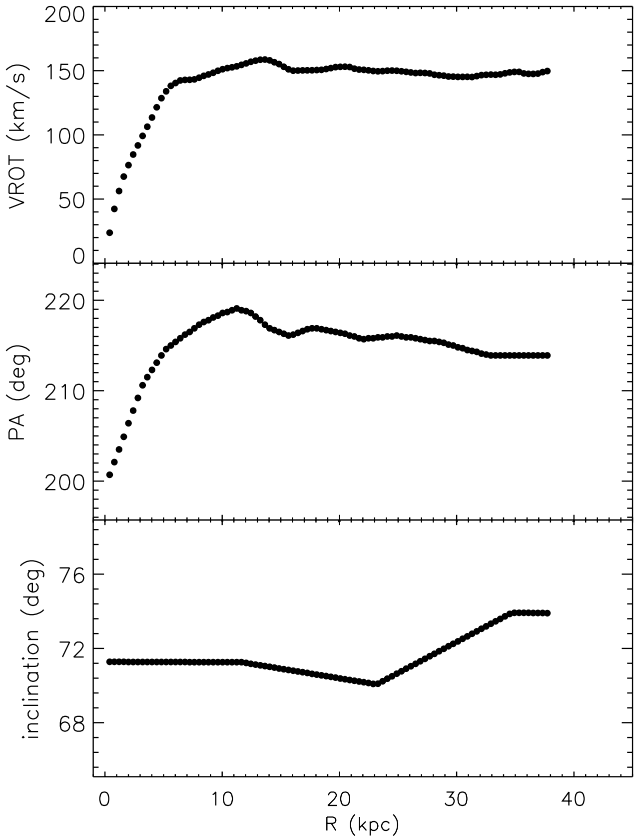

Figure 3.19: The rotation curve (top panel; VROT_{3198}), the PA (middle panel; PA_{3198}) and the inclination (bottom panel; INCL_{3198}) of NGC3198 as a function of radius as derived by de Blok *et al.* (2008).

profile with less scatter, with a better coverage of low column densities in the outer regions of the disc out to levels of log (NH I) $\sim$ 18 atoms cm^{-2}. We decide to use CMODE=1 and CDENS=5 in mod3198_01. The second question we address is the influence of a radial vertical scaleheight distribution. In this trial we decided to keep the scaleheight at constant value of 1 kpc throughout the rings. This value is justified in detail in the next section and corresponds to a ratio of 1:35 between the the diameter of the disc (R$_{max}$) and the scaleheight at R$_{max}$ designated by h_{3198}. All remaining parameters used in mod3198_01 can be consulted in Table 3.3.

In Fig. 3.20, we present integrated H I maps of both observations of NGC 3198 (top left panel) and model H I disc (mod3198_01; top right panel). We also present an overlay in false colours of model and observations (bottom left panel) and the galaxy with contours of the model superimposed. The morphology of the H I disc modelled in this first run is characterized by at least 5 concentric bright rings as shown in Fig.3.20 (top right panel). The first inner ring is brightest with column densities of the order of $\sim 5 \times 10^{20}$ atoms cm^{-2}, and as we move towards larger galactic radii, the rings grow fainter. Beyond the last ring there is a faint envelope surrounding the galaxy where column densities are at a level of $\sim 10^{18}$ atoms cm^{-2}. This is fully supported when analyzing the overlay of the contours of the model on the observations of the galaxy as presented in the bottom right panel. Also, when moving towards the outskirts of the disc we see that the modelled ring covers a larger area than the observed galaxy. This is due to the presence of a modest warp in the disc which has been properly discussed in Sect. 2.2. The gas kinematics study performed by (de Blok *et al.* 2008), deliberately excludes the region of the warp, which means that from 37 kpc onwards, the rotation velocity of the gas, PA and inclination values are replicated and might not represent of the true and complex kinematics of the warp.

In Fig. 3.21, we also present two individual channel maps of NGC 3198 overlaid with contours of mod3198_01. In both, the regions covered by the the model follows closely those of the observations with the exception of the north and northeastern gas filaments in the velocity channel map at $\sim$ 554 km s^{-1} (left panel), where the model is unable to reproduce the gas thought to be part of the warp.

The radial profiles of mod3198_01 are shown in Fig. 3.22. Both 1–pixel wide and ELLINT profiles follow closely the input density DENS$_{3198}$ with scatter slopes of

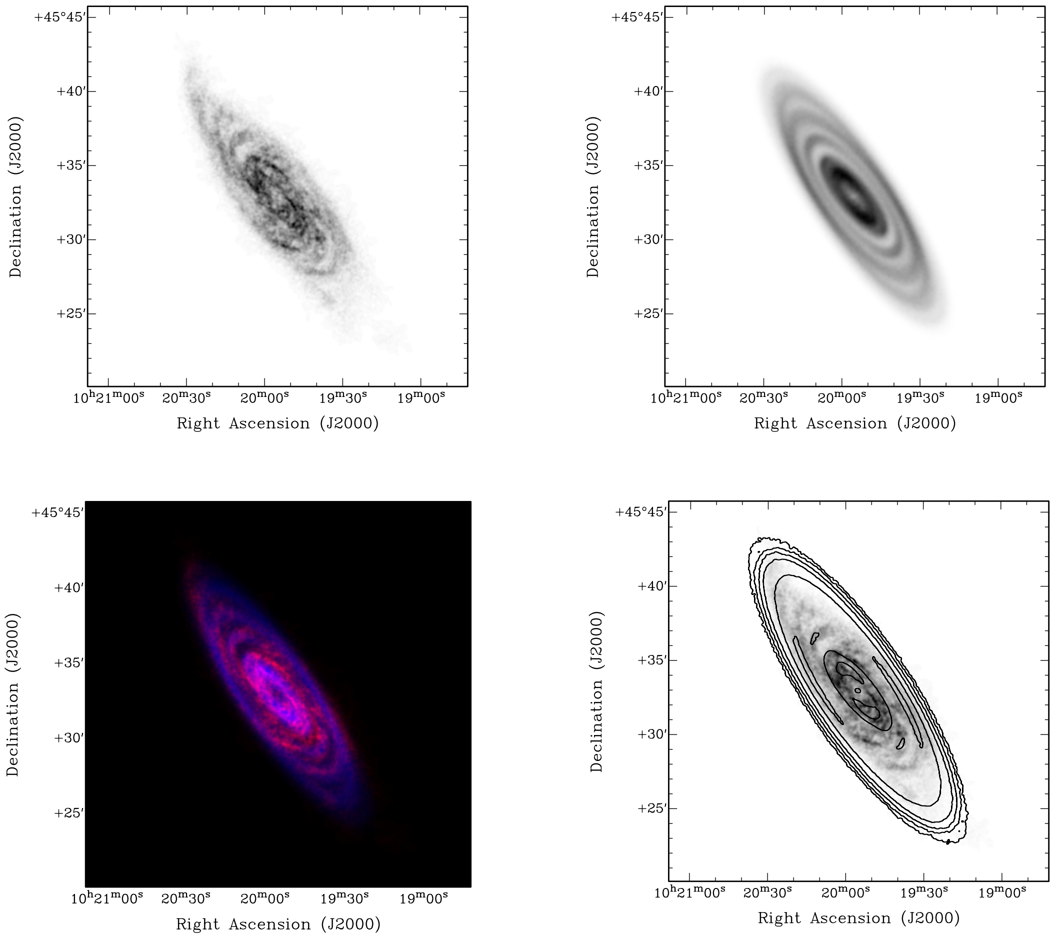

Figure 3.20: *Top left:* THINGS integrated H I map of NGC 3198 at a resolution of $10''$. *Top right:* Simulated integrated H I map based on mod3198_01. *Bottom left:* False colour image of the model (in blue) and the object (in red). *Bottom right:* Observed integrated H I map with model contours at a level of : 1, 3, 10, 30, 100, 300, and 500×10^{18} atoms cm^{-2}.

$a = 0.90$ and $b = 1.00$.

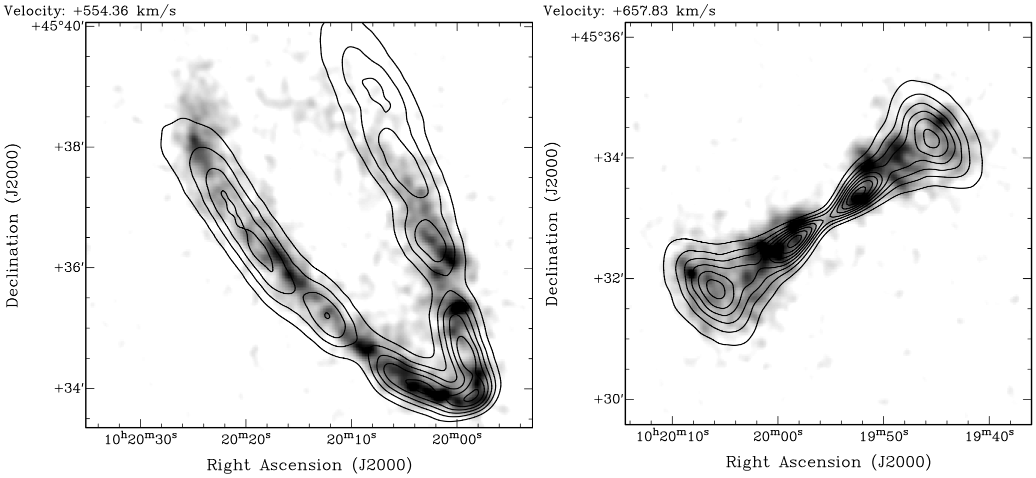

Figure 3.21: Individual velocity channel at 554.36 km s^{-1} (left panel) and 657.83 km s^{-1} (right panel) obtained from velocity contours of mod3198_01 superimposed on the matching regions of the observed data cube.

NGC 3198: influence of an exponential vertical scaleheight

Numerical studies of the H I vertical scaleheight distribution of local galaxies such as our Galaxy have been made by Narayan *et al.* (2005) followed by Banerjee & Jog (2008) for M 31. Commonly, these models take into account both the rotation curve as well as the H I scaleheight distribution to try to constrain the shape and density of dark matter haloes. Because disc and halo dominate different regions of the galaxy within a few radial scale lengths, the authors derive a radial dependence of the scaleheight in an isothermal disc mainly as function of velocity dispersion of the gas and stars. The influence of the dark matter halo is expected to dominate only the outer parts of disc. For NGC 3198 (Banerjee *et al.* 2010, priv. comm.) they predict a vertical scaleheight distribution of $\sim$ 1 kpc at R_{max} based on the baryonic component of such disc neglecting the influence of the halo. This justifies the Z0 value employed in mod3198_01 which is also used as a benchmark to test three different scaleheight distributions as shown Fig. 3.23. The parameters describing the

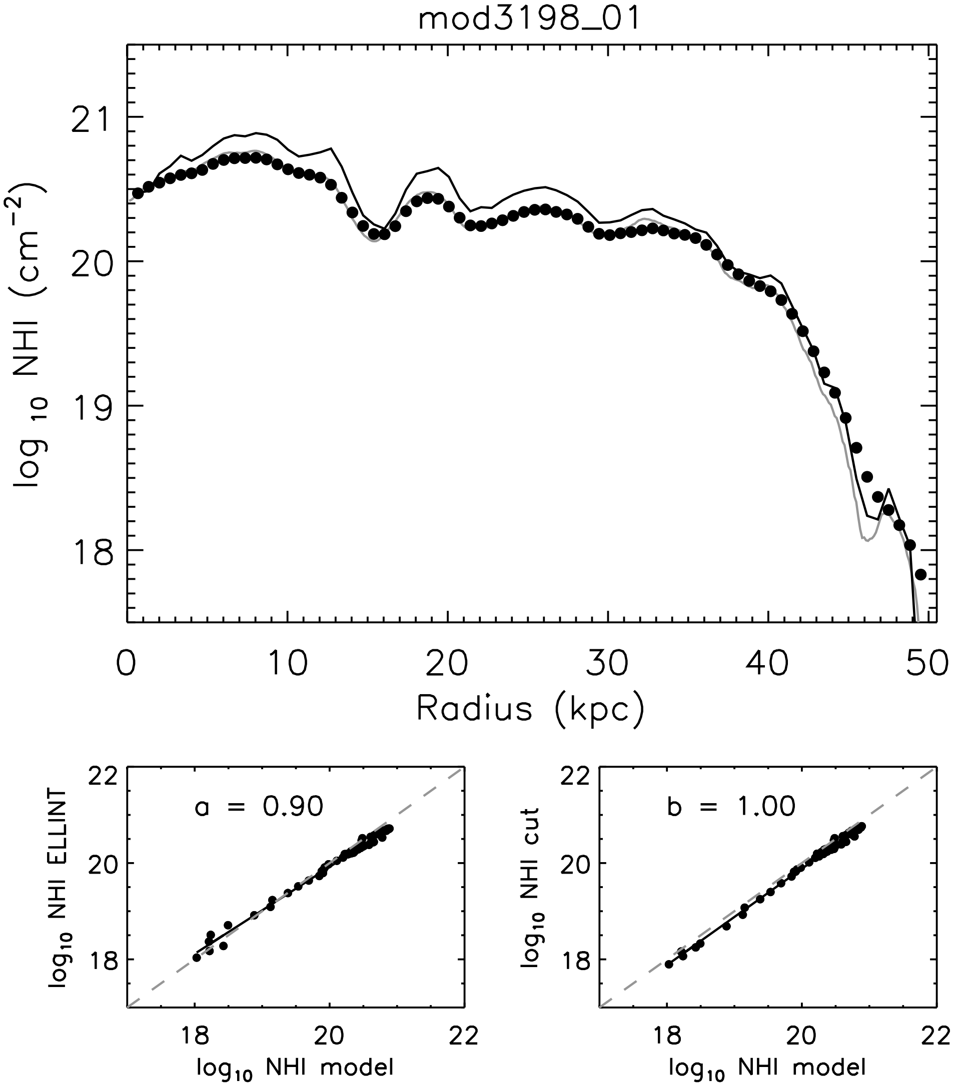

Figure 3.22: The radial profiles and log–log scatter slopes for mod3198_01. The gas density parameter, DENS_{3198}, is shown as a solid black line. The 1–pixel wide and the ELLINT radial profiles are presented as solid grey line and solid black dots respectively.

scaleheight distribution are as follows: SH1 starts out at a scale height of $h = 0.1\,\mathrm{kpc}$, exponentially increasing to 1 kpc at R_{max} (black solid dots); SH2 doubles the SH1 values, starting at $h = 0.2\,\mathrm{kpc}$ and growing to 2 kpc at the edge of the disc (dark grey dots); SH3 starts at $h = 0.05\,\mathrm{kpc}$ and also reaches 1 kpc, like SHA (light grey dots). These scaleheight distributions translate in to ratios between scaleheight at the galaxy edge and radius of the HI disc of 1:50, 1:25 and 1:50, respectively.

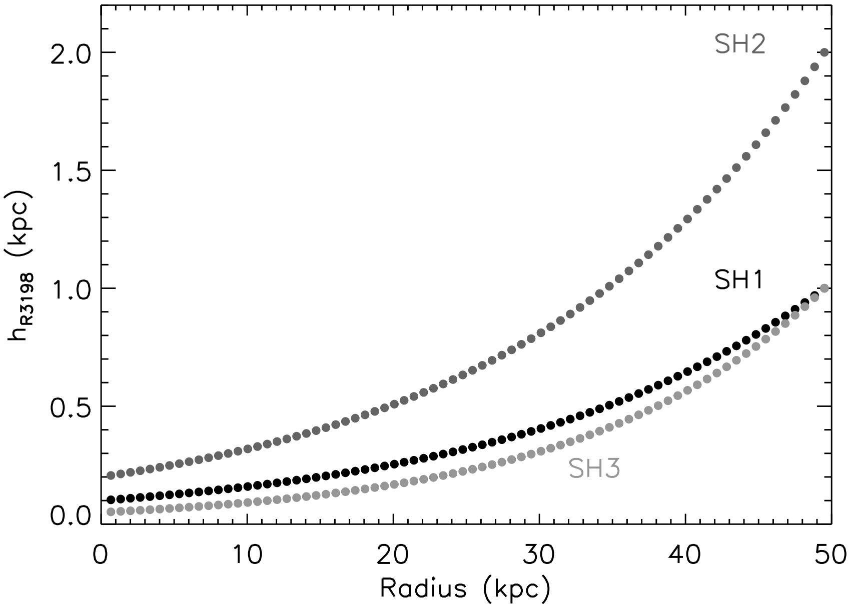

Figure 3.23: The three vertical scaleheight distributions of the gas as a function of radius. For all, the behaviour was assumed exponential varying from 0.1 kpc from the centre towards 1 kpc (black solid dots), 2 kpc (dark grey solid dots) and 1 kpc (light grey solid dots) at the outskirts of the galaxy.

The three vertical scaleheight distributions mentioned above: SH1, SH2 and SH3 were used to create mod3198_02, mod3198_03 and mod3198_04 respectively, keeping all the remaining input parameters the same as summarized in Table 3.3. In Fig. 3.24 we show the three sets of radial profiles created for this trial. The inner 80% of the disc is virtually the same in all three models and is not affected by the introduction of an exponential scaleheight.

As expected already from running models A and B, creating a simulated galaxy

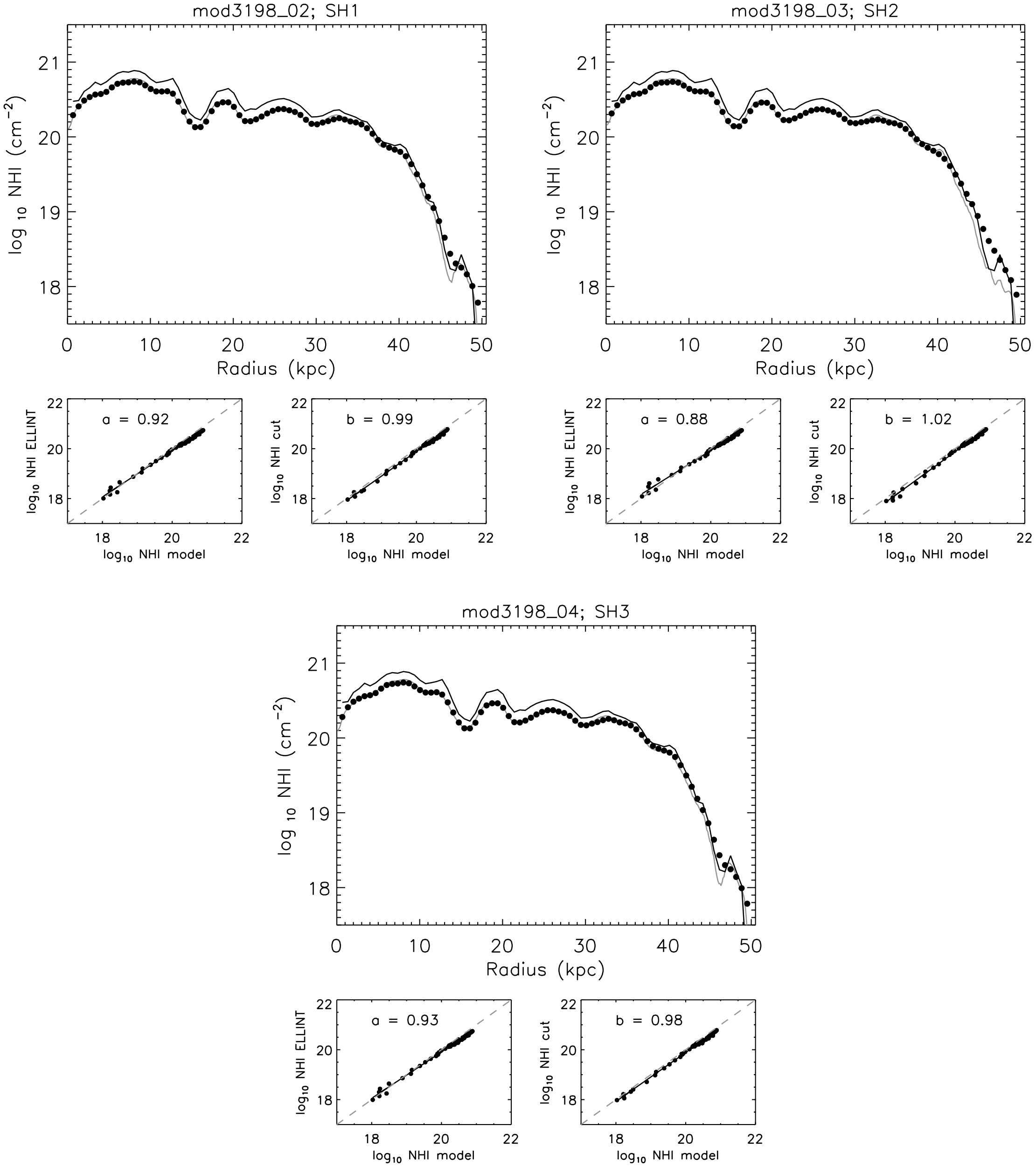

Figure 3.24: Radial profiles of mod3198_02 (top panel), mod3198_03 (middle panel) and mod3198_04 (bottom panel) with the respective scaleheight distributions SH1, SH2 and SH3. Solid black represents the DENS input parameter of GALMOD. The light grey solid line is the 1–pixel wide profile, whereas the black solid dots pertain to the ELLINT profile. All profiles were created at $10''$ spatial resolution.

that more closely resembles an observed object, such as NGC 3198, does not lead to a change in our main conclusion which is that the method developed and employed in Chapter 2 to extract from observations the H I surface density profile, results in a profile that is not or only marginally affected by projection or line–of–sight averaging effects. Strong flaring combined with a substantial inclination does draw the derived profile away from the intrinsic one (mod3198_03). The good news is, however, that such an effect can be diagnosed by comparing the 1–pixel wide profile with the ELLINT one, the former following more closely the intrinsic distribution.

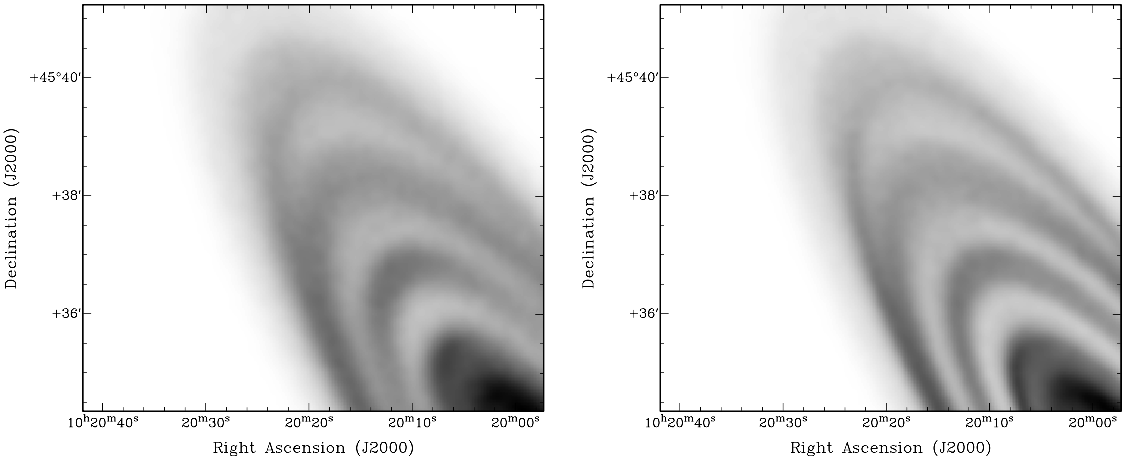

Figure 3.25: Zoom of the northeast region of the H I disc of mod3198_01 (left) and mod3198_02 (right).

3.6.2 Modeling NGC 3351: a face–on H I disc

We now turn our attention to the face–on disc of NGC 3351, following closely what has been previously widely described for NGC 3198.

We use as input for the DENS parameter, the column density profile as derived in Sect. 2.4, which we reproduce in Fig. 3.26 and define by DENS_{3351}. It was obtained at $10''$ spatial resolution. We can loosely divide NGC 3351 into two distinct regions, the inner disc which extends to 16 kpc is characterized by an averaged column density of 2×10^{20} atoms cm^{-2}. In the outer disc column densities drop to a level of $\sim 10^{18}$ atoms cm^{-2}. R_{max} is the radius of the H I disc of NGC 3351 measured at a level of 10^{18} atoms cm^{-2} which corresponds to ~ 21 kpc.

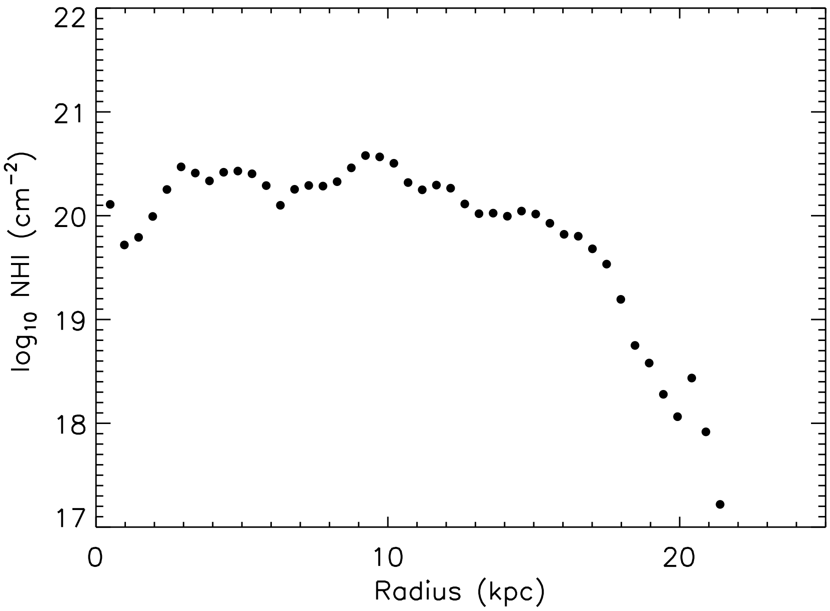

Figure 3.26: NGC 3351 ELLINT radial profile at 10″ spatial resolution used as an input for the DENS parameter of GALMOD which we designate by DENS_{3351}.

As far as the rotation curve of the object is concerned, although NGC 3351 is part of the THINGS project it has not been included in the sub–sample of high resolution rotation curves derived by de Blok *et al.* (2008) because of its relatively face–on orientation. It has been target of many kinematical studies (Peterson *et al.* 1976; Devereux *et al.* 1992) most of them related to the kinematics of stars and HII regions in the disc. For the purpose of this Chapter it is sufficient to approximate the rotation curve as follows. Under the usual assumptions of gas in circular orbits in a thin, inclined disk, we extracted the position velocity diagram along the kinematical major axis.

Therefore:

$$V_{\rm obs} = V_{sys} + V_{\rm rot} \sin({\rm incl}) \tag{3.1}$$

where V_{obs} is the observed rotational velocity taken from the position–velocity diagram, V_{rot} is the circular velocity of the gas in the plane of the galaxy, and V_{sys} is the systemic velocity. We used an inclination of 41° and systemic velocity of 780 km s^{-1} (Walter *et al.* 2008).

The result is shown in Fig. 3.27, in which we draw as a solid black line the rotation curve we assumed for calculating our models for NGC 3351. The velocities we have obtained are comparable to those presented by Devereux *et al.* (1992) within errors of 10 km s^{-1} to 20 km s^{-1} . We derived an averaged velocity for the flat part of the rotation curve of $\sim$ 190 km s^{-1} which is also in good agreement with the 210 km s^{-1} maximum amplitude of the circular velocity derived by Tamburro *et al.* (2008).

NGC 3351: model at a constant scaleheight

To the best of our knowledge, the vertical scaleheight distribution of the H I disc of NGC 3351 has not been previously studied, so we decided on an average scaleheight value Z0 = 1 kpc as a starting point for our constant scaleheight model, mod3351_01. As far as CMODE and CDENS are concerned we use 1.0 and 5.0, respectively. A complete description of the values employed in this trial can be found in Table 3.3.

In Fig. 3.28 we present a comparison between the integrated H I map of NGC 3351 and mod3351_01. We also show in false colours an overlay of observations with the

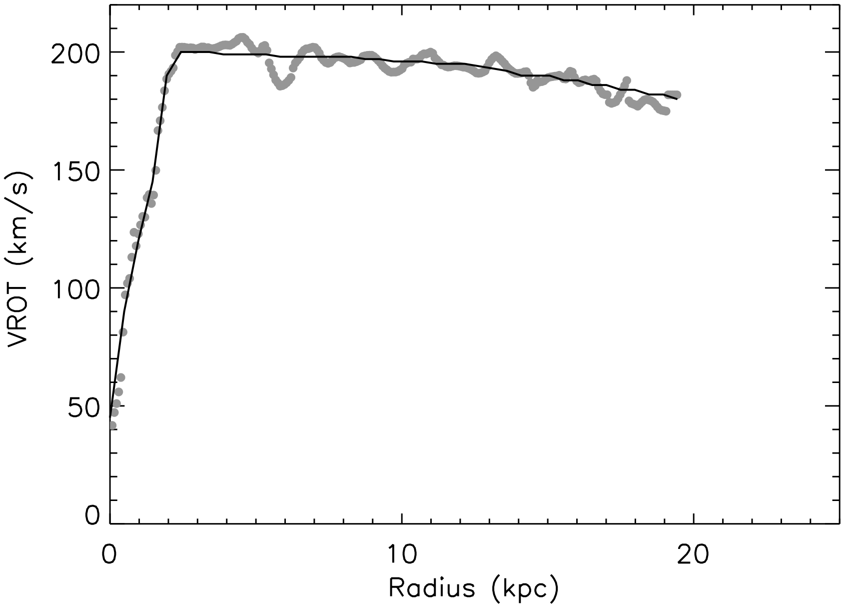

Figure 3.27: The solid grey dots represent the circular velocities in the rotating disc of NGC 3351. The solid black line is an approximation to the rotation curve of the galaxy VROT_{3351} used to generate the models of this galaxy.

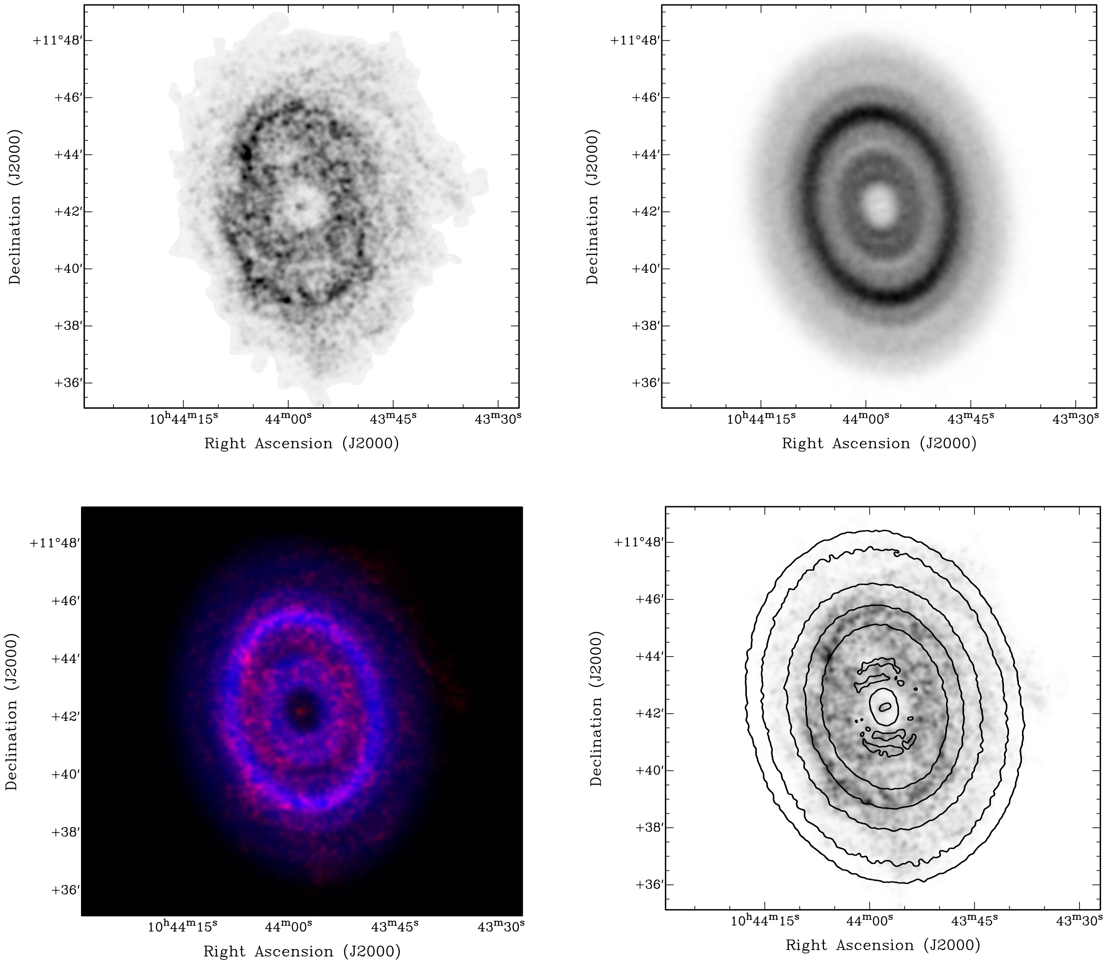

Figure 3.28: (top left) We present the THINGS integrated H I map of NGC 3351 at a resolution of 10″; (top right) the mod3351_01 model of the galaxy; (bottom left) we show a false colour image of the the model (in blue) and the object (in red); (bottom right) observed integrated H I map with model contours at a level of: 1, 3, 10, 100, 300 and 500 $\times 10^{18}$ atoms cm^{-2}.

model (left bottom panel) and model contours overlaid on the observed integrated H I map.

Mod3351_01 as presented in Fig. 3.28 shows an ensemble of concentric rings, the brighter one closely following the diffuse arm–like features of the spiral structure of NGC 3351 (see top left panel of Fig. 3.28). Fig. 3.29, shows two individual velocity channels of NGC 3351 with superimposed as contours the corresponding velocity channel map of mod3351_01. We find good agreement across most of the disc with only the outermost regions showing some mismatch between the location of the H I and the model, most likely due to the H I being lopsided (see Chapter 2).

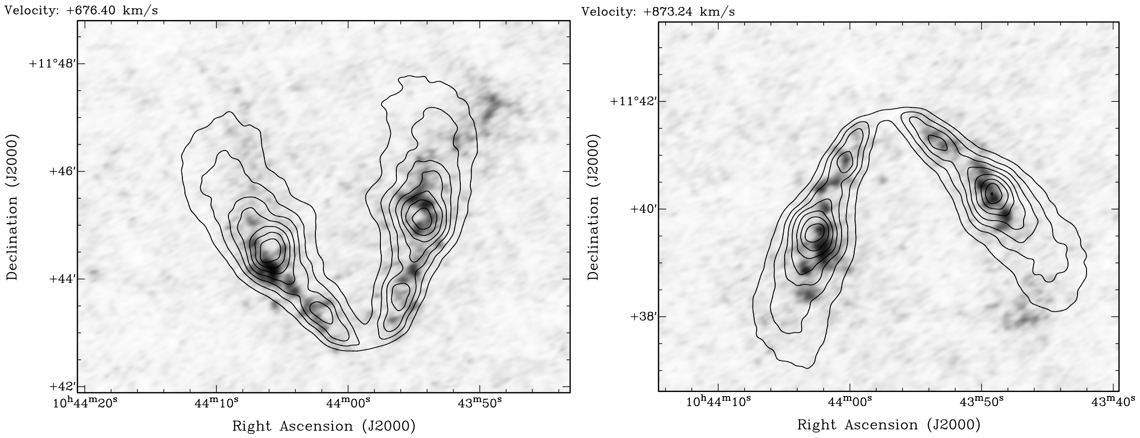

Figure 3.29: Two individual velocity channels, 676.40 km s^{-1} (left panel) and 873.24 km s^{-1} (right panel). The velocity contours of the model are superimposed on the corresponding velocity channels of the observed data cube.

In Fig. 3.30, we present the radial profiles of mod3351_01. The ELLINT (black dots) and 1–pixel wide profiles (grey line) are closely aligned and both follow the input DENS_3351 density distribution (black line), including in the outer part of the H I disc. This is corroborated by the scatter slopes for this model ($a = 0.95$, $b = 0.98$).

NGC 3351: models with exponentially increasing scaleheights

The introduction of an exponentially increasing scaleheight distribution in the NGC 3351 models was studied by creating 4 scaleheight distributions as seen in Fig. 3.31. Scale

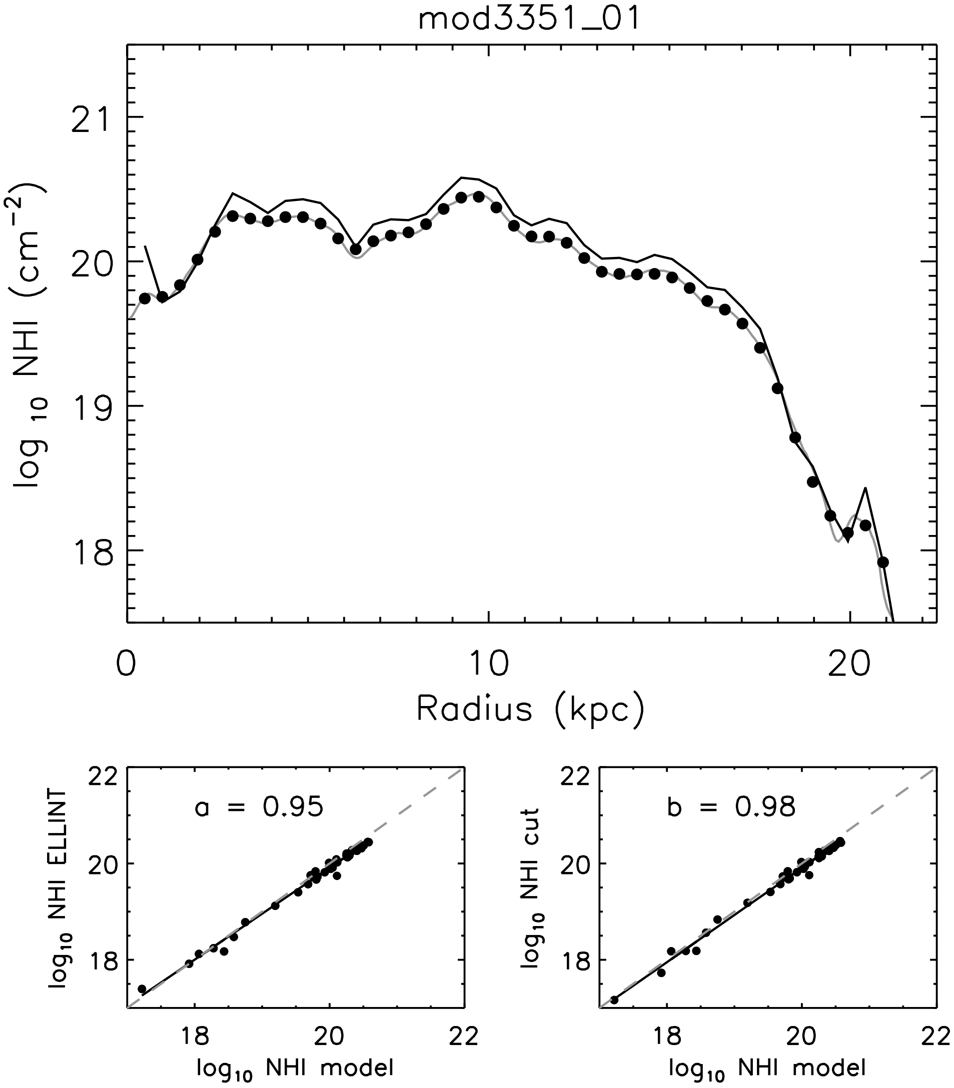

Figure 3.30: Radial profiles and log–log scatter slopes obtained with mod3351_01. The input DENS parameter is represented by a solid black line. The 1–pixel wide and the ELLINT radial profiles are shown as solid grey line and solid black dots respectively.

height distribution SH4 starts at $h_C = 0.1$ kpc, exponentially increasing up to 1 kpc at R_{max}. Scale height distribution 5 (SH5), distribution 6 (SH6) and distribution 7 (SH7) double, triple and quadruple the run of scaleheight used for SH4. These scaleheight distributions imply a ratio between the scaleheight at the edge of the disc and radius of H I distribution of 1:21 (SH4), 1:11 (SH5), 1:7 (SH6) and ∼ 1:6 (SH7). For each specific scaleheight distribution SH4, SH5, SH6 and SH7 we created the following models: mod3351_02, mod3351_03, mod3351_04 and mod3351_05 with their parameters summarized in Table. 3.3.

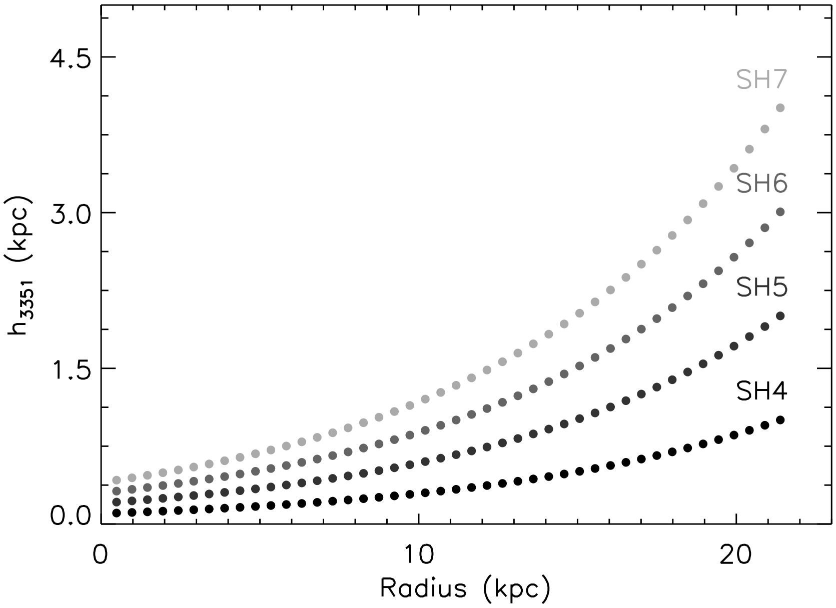

Figure 3.31: The four vertical scaleheight distributions of the gas in kpc as a function of radius. The behaviour was assumed exponential varying from 0.1 kpc from the centre towards 1 kpc (black solid dots), 2 kpc (dark grey solid dots), 3 kpc (intermediate grey solid dots) and 4 kpc (light grey solid dots), at the outskirts of the galaxy.

The resulting radial profiles of these models are presented in Fig. 3.32. As shown, none of the different scaleheight distributions shows any difference in their radial profiles. This is corroborated by the values of the scatter slopes obtained for these models. Neither do major changes in the outer slope of the disc emerge by increasing the scaleheight distribution of the gas for NGC 3351, nor are there significant variations between the constant and exponentially growing scaleheight distributions.

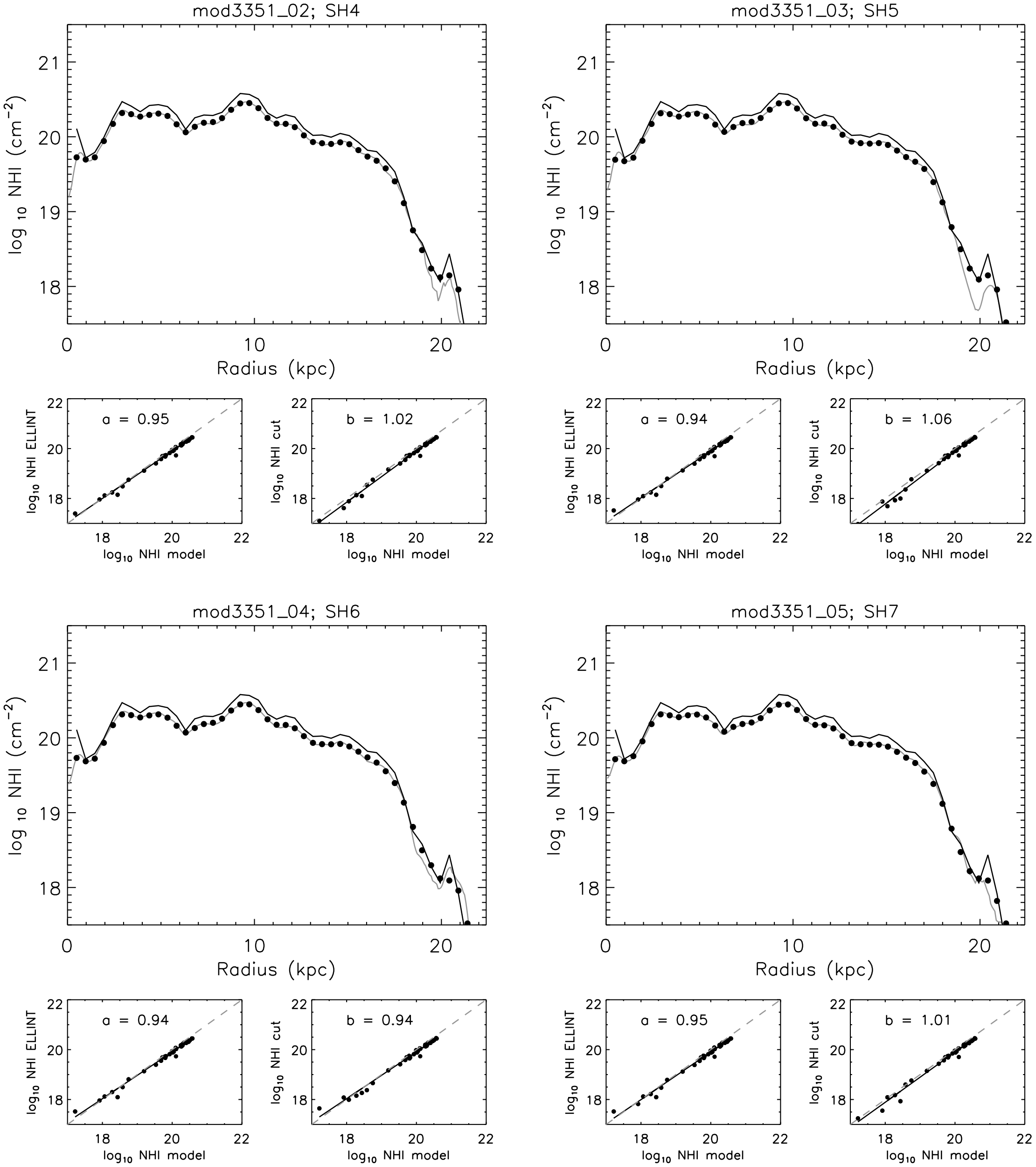

Figure 3.32: The radial profiles of mod3351_02 (top left panel), mod3351_03 (top right panel), mod3351_04 (bottom left panel) and mod3351_05 (bottom right panel).

Table 3.3: GALMOD parameters for NGC 3198 and NGC 3351

OUTSET	VROT km s^{-1}	DENS cm^{-2}	Z0 ″	INCL °	PA °	CMODE	CDENS
mod3198_01	$VROT_{3198}$	$DENS_{3198}$	15	$INCL_{3198}$	PA_{3198}	1	5
mod3198_02	$VROT_{3198}$	$DENS_{3198}$	SH1	$INCL_{3198}$	PA_{3198}	1	5
mod3198_03	$VROT_{3198}$	$DENS_{3198}$	SH2	$INCL_{3198}$	PA_{3198}	1	5
mod3198_04	$VROT_{3198}$	$DENS_{3198}$	SH3	$INCL_{3198}$	PA_{3198}	1	5
mod3351_01	$VROT_{3351}$	$DENS_{3351}$	21	192	41	1	5
mod3351_02	$VROT_{3351}$	$DENS_{3351}$	SH4	192	41	1	5
mod3351_03	$VROT_{3351}$	$DENS_{3351}$	SH5	192	41	1	5
mod3351_04	$VROT_{3351}$	$DENS_{3351}$	SH6	192	41	1	5
mod3351_05	$VROT_{3351}$	$DENS_{3351}$	SH7	192	41	1	5

Additional GALMOD parameters for mod3198: POS: -3,0; VSYS: 660 km s^{-1} ; RADII: 10:740:10; VDISP: 10 km s^{-1} ; LTYPE: 2; NV=72.
Additional GALMOD parameters for mod3351: POS: 1,0; VSYS: 780 km s^{-1} ; RADII: 10:440:10; VDISP: 10 km s^{-1} ; LTYPE: 2; NV=70.

3.7 Radial profiles in different sectors of the models

As a final test we revisit the exercise performed in Sect. 2.4 on NGC 3351, where this galaxy was divided into twelve 30° sectors. We focus on what differences might occur as a function of azimuth within the plane of the disc of the chosen sector. In the following we focus on how similar are the radial profiles in any random direction disregarding the origin of the drop. To investigate this we divided modB_07 and mod3198_02 into eight 30° sectors and calculated a radial profile for each, excluding as before the 60° wedge centred around the minor–axis of the disc as discussed in Sect. 2.4. The radial profiles for both models are presented in Figs. 3.33 and 3.34. We see that, for modB_07 there is very little variation from sector to sector within the inner 80 % of the disc. Beyond that, profiles decline with slightly different slopes, but the differences are marginal. As far as the sectors of mod3198_02 are concerned, no significant variations are found either.

3.8 Simulations of H I discs: conclusions

The four sets of models lend confidence to the assumption that was made in Chapter 2 that the observed H I surface density profile represents the intrinsic density distribution, and their subsequent interpretation. We summarise our conclusions as follows:

- In model A (Sect. 3.4.2), a constant surface density distribution sharply truncated at the edge, smoothing to a 10″ resolution or using ELLINT introduces beam smearing at the sharp edge. The amount of beam smearing is slight, though, and only minimally affects the observed surface density profile.
- Extensive tests using model B which introduces a disc with two regions, an inner disc with a flat density distribution followed by an exponentially declining outer disc, also show that the derived density distribution faithfully represents the input density profile.

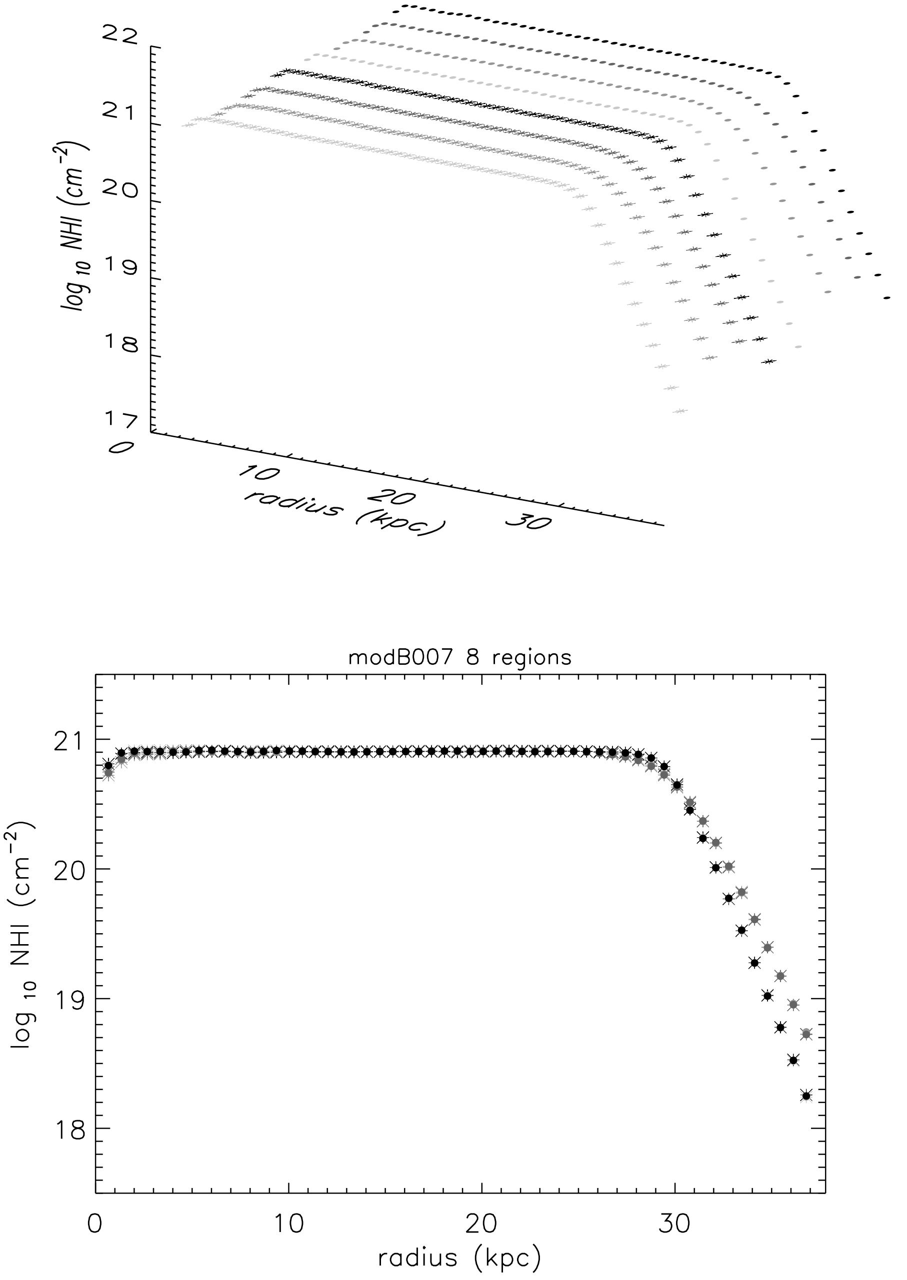

Figure 3.33: The individual ELLINT radial profiles obtained with modB007. In the top panel we present from front to back the following sectors: 0° to 30°, 30° to 60°, 120° to 150°, 150° to 180°, 180° to 210°, 210° to 240°, 300° to 330° and 330° to 360° measured anti–clockwise from the receding semi–major axis. All profiles were derived in 10″ bins. In the bottom panel we present an overlay of all the profiles.

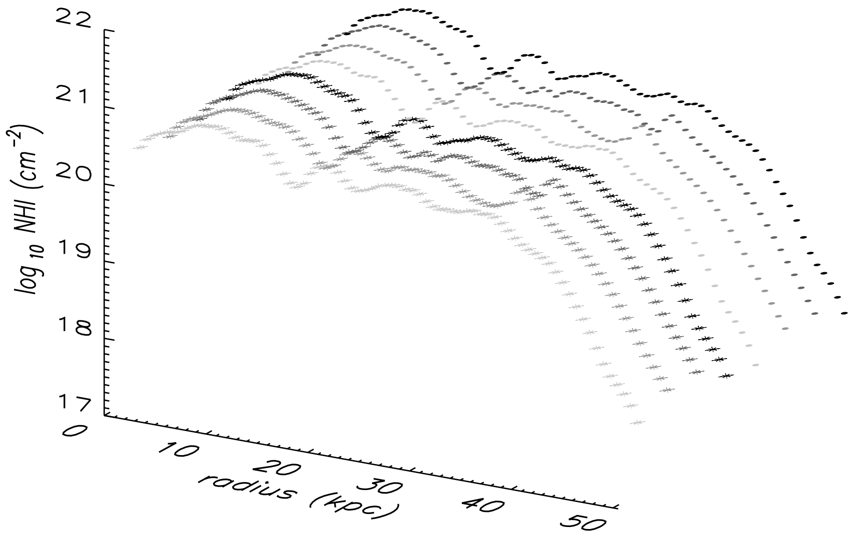

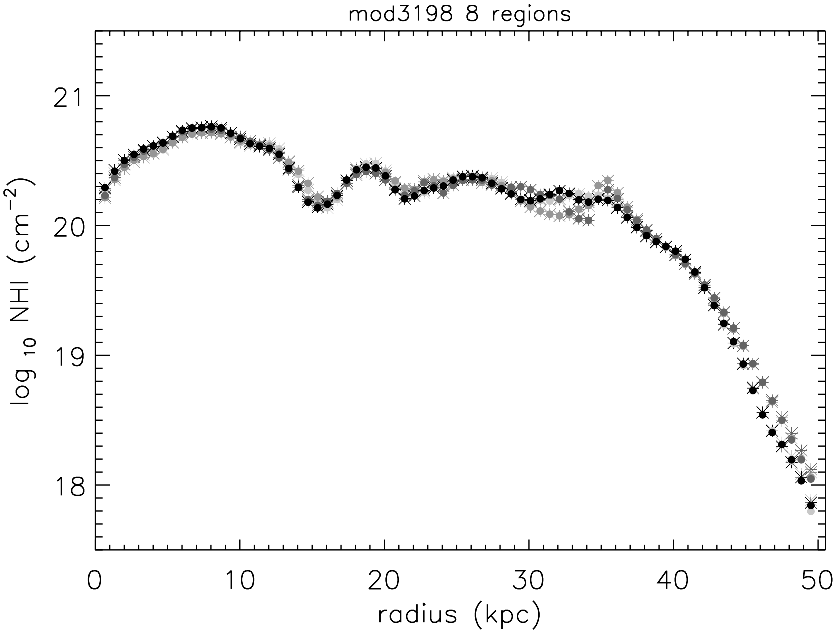

Figure 3.34: As in Fig. 3.33 we present the individual ELLINT radial profiles obtained with mod3198_02. In the top panel we present from front to back the following sectors: 0° to 30°, 30° to 60°, 120° to 150°, 150° to 180°, 180° to 210°, 210° to 240°, 300° to 330° and 330° to 360° measured anti–clockwise from the receding semi–major axis. All profiles were derived in 10″ bins. In the bottom panel we overlay all the profiles.

- We find that only discs observed at high inclination ($> 75°$), i.e. nearly edge–on galaxies, the radial profiles significantly deviate from the input density profile.
- There is no significant difference between the radial profiles obtained for a disc with a constant scaleheight distribution of 1kpc, and those which flare. We tested discs with an exponential increase in scaleheight as a function of radius and conclude that flaring has to be dramatic (e.g. model SHC) and the disc in a near to edge–on orientation. But even then the 1–pixel wide profile closely follows the input profile.
- In addition to creating simple density distributions, we mimicked the galaxies NGC 3198 and NGC 3351, the former being highly inclined and the latter a more face–on object. We again found that gas surface density profiles extracted using the same methodology in Chapter 2, where we analysed the observations, retrieve the input model density distributions.
- Within a disc, the choice of the segment to average in the ELLINT radial profile has no noticeable effect either, individual profiles showing little variation between them (as in Chapter 2, sectors near the semi–minor axis were excluded as projection effects and line–of–sight blending can become substantial).

We thus conclude that, with the exception of nearly edge–on galaxies, the observed surface density profiles are a faithful rendering of the intrinsic density distributions and that any line–of–sight blending or beam smearing can largely be ignored.

Chapter 4

NGC 765 - A disturbed H I giant

This chapter is based on a paper accepted for publication by the Monthly Notices of the Royal Astronomical Society

In this Chapter we present NGC 765, a galaxy which resembles the giant LSB Malin 1 but is closer by a factor of 4–5 and hence provides us with an opportunity to study such an extraordinary system in more detail. Moreover the large H I disc of NGC 765 is compared with the spiral galaxies presented in Chapter 2. We present NRAO Very Large Array (VLA) D–array archival data of this galaxy. We provide an overview of archival and literature multi–wavelength properties of NGC 765. We also briefly discuss the data reduction for the H I, radio continuum, optical, and X-ray data. We present our results, where we focus on the morphology and kinematics of the gaseous disc and provide a brief discussion in the light of galaxy formation and evolution.

4.1 NGC 765 archive properties

NGC 765 (also known as UGC 1455) is classified as a late-type SAB(rb)bc galaxy (de Vaucouleurs *et al.* 1991), and presents the signature of a central bar. According to the NASA/IPAC Extragalactic Database (NED) it has a heliocentric recession velocity of 5118 km s^{-1} . Throughout this chapter we assume a distance of 72 Mpc based on H_0=72 km s^{-1} Mpc^{-1}, which makes $1'' = 350\,$pc. The galaxy has an extrapolated disc central surface brightness of $\mu(0) = 22.27$ in the B–band (de Jong 1996), or only

Table 4.1: General information on NGC 765 and companion galaxies.

	NGC 765	NGC 765a	UGC 1453	Reference
Type	SAB(rc)bc	...	Irr	1
RA (J2000)	01h 58m 48s	01h 59m 55.9s [3]	01h 58m 45.8s	1
DEC (J2000)	$24^\circ\,53'\,32.9''$	$24^\circ\,58'\,29.9''$ [3]	$24^\circ\,38'\,34.6''$	1
Distance	72 Mpc	72 Mpc [3]	72 Mpc	1
V_{hel}	5118 km s^{-1}	4900 km s^{-1} [3]	4897 km s^{-1}	1
R_{25}	$62.6''$	...	$\sim 1.4'$	1
m_B	13.6	...	...	1
L_B	$3 \times 10^{10} \mathcal{L}_\odot$	...	...	2
Inclination	21°	...	30° [4]	3
Position Angle	251°	...	...	3
H I flux	38.3 Jy km s^{-1}	0.53 Jy km s^{-1}	1.54 Jy km s^{-1}	3
H I mass	$4.7 \times 10^{10}\ \mathcal{M}_\odot$	$6.5 \times 10^{8}\ \mathcal{M}_\odot$	$1.9 \times 10^{9}\ \mathcal{M}_\odot$	3

Reference: 1 - Taken from NED; 2 - Derived using $M_{\odot,B} = 5.48$ and a distance of 72 Mpc; 3 - This study; 4 - Taken from LEDA.

about 0.5 mag fainter than the Freeman (1970) value and therefore brighter than the $\mu(0) \geq 23$ limit usually adopted to define an LSB (Impey & Bothun 1997). The galaxy was included in a sample of (LSB) galaxies by Schombert (1998). The detection of nuclear emission of [N II], [S I] and [O I] lines suggests the presence of a low-luminosity AGN (hereafter LLAGN), which according to Schombert (1998) are more likely to be found in H I–rich, large galaxies. This galaxy and its closest companion, UGC 1453, are thought to be part of a group of 14 galaxies [GH83]024 (Garcia 1993). In Table 4.1 we summarise some basic information on NGC 765 and its companion galaxies, stating in advance that NGC 765a is an uncatalogued companion discovered in this study. Both NGC 765a and UGC 1453 are discussed in more depth in Section 4.3.

Table 4.2: Observational setup for the NGC 765 VLA data.

Parameter	Value	
Object	NGC 765	
Instrument	VLA	
Configuration	D–array	
Project ID	AS0625	
Primary calibrator	3C48	
Secondary calibrator	3C48	
Central velocity	5189 km s^{-1}	
FWHM of primary beam	32′	
Total bandwidth	3.125 MHz	
Number of channels	64	
Channel spacing	0.049 MHz	(11 km s^{-1})
FWHM of synthesised beam	43.5″ × 42.3″	(∼ 15 kpc)
rms noise	0.2 mJy beam^{-1}	(0.065 K)

4.2 Observations and Data Reduction

4.2.1 H I data reduction

The VLA D–array observations of NGC 765 are in the public domain under project ID AS0625. The galaxy was observed in a set of 3 runs, on 1998 January 17, 18 and 19, over periods of 5 hours each on source. Both polarisations were recorded. All data reduction was performed using the 31DEC06 version of Classic AIPS. Table 4.2 summarises the observational setup.

3C48 was observed interspersed with the target source, in scans lasting 3 minutes. This calibrator was used both as primary calibrator (flux and bandpass) with an estimated flux of 16.50 Jy at 1395.29 MHz as well as to determine the complex gain (i.e., as secondary calibrator). Antenna 12 was flagged in both polarisations in the first and last runs since visibility amplitudes deviated by approximately 30 percent relative to the average. Flagging and bandpass calibration were performed with standard tasks.

We deleted the first and last eight velocity channels due to sensitivity loss at the edges of the 3125 kHz wide band centred at a frequency of 1396.5 MHz. The *uv*–data of individual runs were merged into a single data set using the task DBCON.

The data cube was generated using IMAGR. We employed a ROBUST=0 weight in order to obtain the best compromise between resolution and sensitivity. The cube was cleaned to a flux threshold of 2σ. We separated real emission from noise following the conditional blanking method employed by Walter *et al.* (2008). We convolved the cube to 70 arcsec resolution, storing in a masking cube regions of emission that were above 2σ over three consecutive velocity channels. Using the latter cube we then masked our original 43.5×42.3 arcsec cube. The *zero* and *first* order moment maps (total surface brightness and velocity field), were created with the task XMOM. Because of the modest angular resolution the channel maps could be cleaned down to the noise and therefore there was no need for residual flux scaling (Walter *et al.* 2008).

NGC 765 was detected from 5015 km s^{-1} to 5239 km s^{-1} in velocity. Its integrated H I spectrum is shown in Figure 4.1. The corresponding channel maps are presented in Sect. B.1. In Fig. 4.2 we present an H I column density map of NGC 765 and its two nearby companions: UGC 1453 to the South of NGC 765, and to the North–East the uncatalogued small companion NGC 765a.

We constructed a radio–continuum map using the first five channels of the 48 available, which were thought to be free of line emission. These five channels were employed to perform the continuum subtraction of the above mentioned data cube. The *uv* data of the channels were averaged in frequency using the task AVSPC, mapped and CLEANed with IMAGR in a similar manner as described above. The 1σ noise level corresponds to 0.15 mJy. In Fig. B.3, we present the continuum emission contours at 1395.39 MHz.

We detect a source with a flux density of 2.16 mJy ($L_{1.4\,\mathrm{GHz}} = 1.3 \times 10^{21}$ W Hz^{-1}, for an assumed distance of 72 Mpc), coincident with the optical nucleus of NGC 765. The NRAO VLA Sky Survey (NVSS; Condon *et al.* 1998) at 1.4 GHz found no radio continuum emission associated with this galaxy (Stokes I at a 3 σ rms of 1.5 mJy). The Faint Images of the Radio Sky at Twenty–Centimeters (FIRST) VLA–survey (Becker *et al.* 1995) does not cover this area. No continuum emission was detected for NGC 765a and UGC 1453. We found another 7 radio–continuum sources in the field of NGC 765. For further details we refer the reader to the material in Sect. B.2.

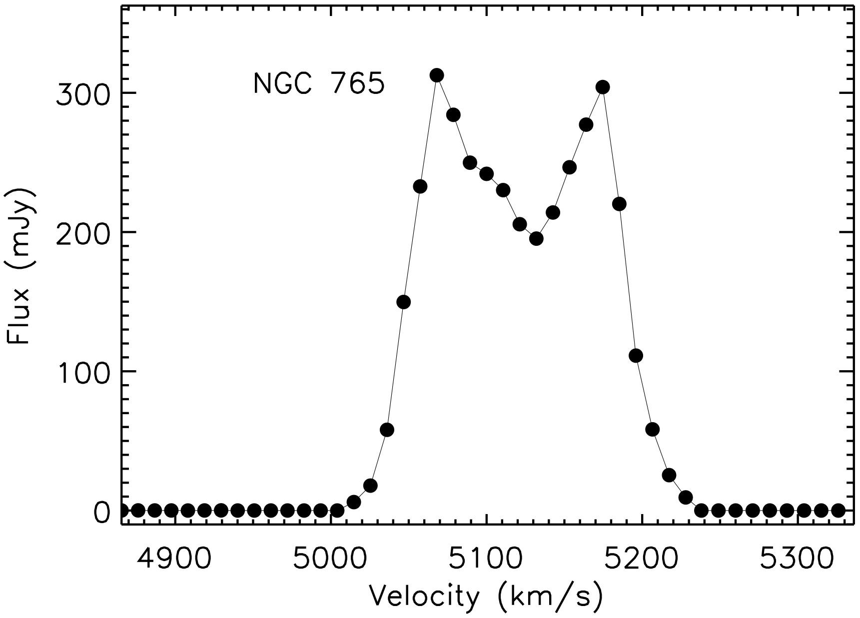

Figure 4.1: Integrated H I spectrum of NGC 765. Note that the integrated flux in each channel map is based on the blanked image cube, hence the flux being at exactly zero for those channels deemed without emission.

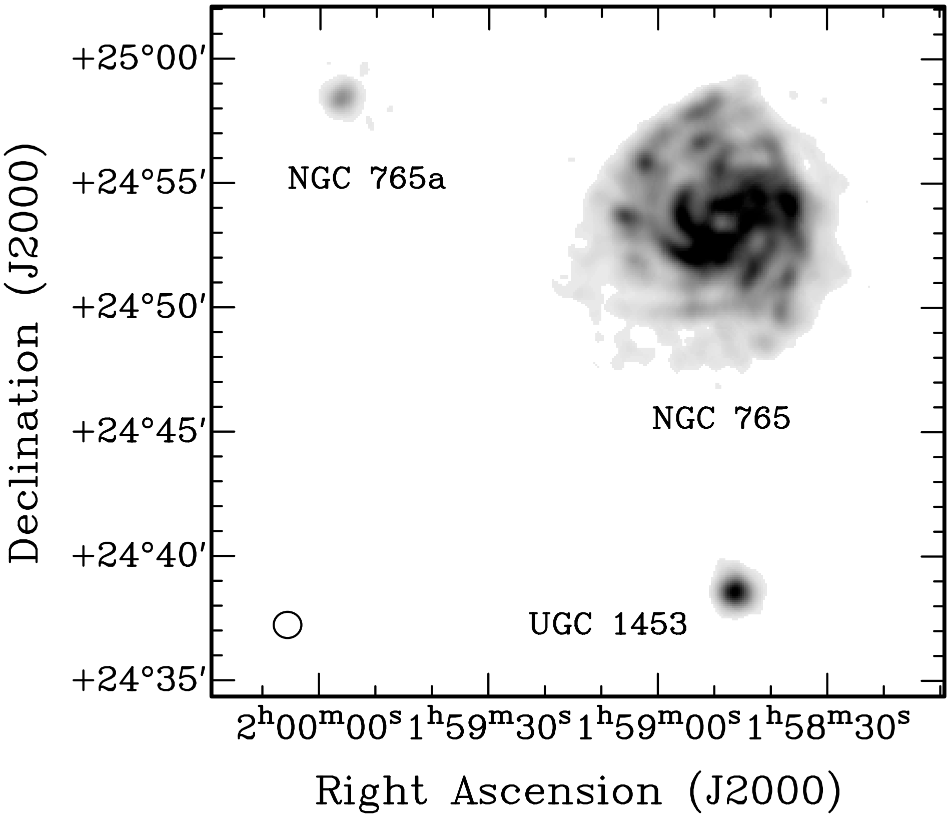

Figure 4.2: Total intensity greyscale H I map of NGC 765. The greyscale ranges from 0 to 225 K km s^{-1}. The resolution is 43 × 42 arcsec and is indicated by the circle in the bottom left corner of the image. NGC 765a and UGC 1453 can be seen to the Northeast and South of the image respectively.

4.2.2 Optical data reduction

Optical observations of NGC 765 were acquired with the Isaac Newton Telescope (INT) on 2009 January 22, with the Wide Field Camera (hereafter WFC). The galaxy was observed in three exposures of 600 seconds in the Sloan R filter at a central wavelength of 6240 Å. Data reduction followed the standard Cambridge Astronomical Survey Unit (CASU) pipeline. In Fig. 4.3 we present the optical INT image of NGC 765. The PSF is ~ 1.3 arcsec or 0.45 kpc. The galaxy presents an inner bright core and what seems to be a bar oriented NNE–SSW. It is not clear if there is an associated stellar ring. Stellar arms, tightly wound around the core, indicate disc rotation in an anti–clockwise direction. Faint traces of at least two arms can be seen as far out as 45 kpc from the nucleus. Both arms seem to bifurcate in the outskirts. According to de Jong & van der Kruit (1994) the optical diameter measured at 25 $\mathrm{mag\,arcsec^{-2}}$ in the B–band is 62.6 arcsec (22 kpc).

We produced an optical surface brightness profile based on elliptical isophote fitting using the projection on the sky as determined by our rotation curve fit (Sect. 4.3.2). Obvious foreground stars were removed and replaced by 2–D interpolation using pixel values of an annulus surrounding the affected area. A 2–D second order spline was fit to remove the background. Although the background fit produced a remarkably good result, we could see some slight systematic offset due to the bright foreground star towards the south–east corner of the field, potentially affecting the area due South of the galaxy. We therefore restricted the radial profile, using only the northern half of NGC 765, employing $3''$ radial bins.

The resulting profile is shown in Fig. 4.4. The INT data were acquired under non ideal conditions and hence were not calibrated. In light of this, we bootstrapped our radial profile to the one published by de Jong & van der Kruit (1994). Where our profiles overlap, agreement is excellent. Our data go deeper by almost 2 magnitudes in R, down to 26.5 $\mathrm{mag\,arcsec^{-2}}$, allowing us to follow the faint stellar disc out to about 50 kpc in radius. We derive a scale length for the stellar disc between 5 and 25 kpc of 7.8 kpc in good agreement with de Jong & van der Kruit (1994) who found values of 8.4 kpc and 5.7 kpc in B and K_S, respectively. The extrapolated central surface brightness at R–band is 20.9 $\mathrm{mag\,arcsec^{-2}}$ which, assuming a $B-R=1.40$ (taken from de Jong & van der Kruit 1994) then agrees with their B–band value of

$\mu_B(0) = 22.27$. Between 30 kpc and 38 kpc the profile shows a secondary maximum, beyond which, it declines again at the same rate. This feature can be traced to a faint, broad stellar arm, i.e., this is not an artefact or due to a problem with background subtraction.

4.2.3 X–ray data reduction

Das *et al.* (2009) present 0.5 arcsec resolution *Chandra* X–ray observations of a small sample of Malin 1–type galaxies, including NGC 765. As they only refer to emission coming from its centre, we decided to retrieve the observations from the archive (project ID 7764) and independently reduce and analyse them. The data were obtained with the ACIS–S instrument (AXAF CCD Imaging Spectrometer) on 2007 July 11, for a total exposure time of 3.79 ks. Data reduction of the observations was performed using standard procedures included in the *Chandra* Analysis of Observations package (CIAO version 4.0). We ran *wavdetect* with a 3σ detection threshold in order to detect point sources in the NGC 765 H I field. Six sources were detected above 3σ and are shown in Sect. B.3, Fig. B.4. We confirm emission coincident with the galaxy nucleus at an X–ray luminosity in the 0.2–10 keV energy band of $L_X 1.7 \times 10^{40}$ erg s^{-1}, in agreement with Das *et al.* (2009).

4.3 Results

4.3.1 NGC 765 H I content and morphology

We detect an H I integrated flux of 38.3 Jy km s^{-1} which, assuming as usual optically thin emission, corresponds to a total H I mass of 4.67×10^{10} $\mathcal{M}_\odot$. This is consistent with the Westerbork Synthesis Radio Telescope (hereafter WSRT) wide-field survey (Braun *et al.* 2003), where it was derived to have a total H I flux of 39.7 ± 0.66 Jy km s^{-1} (effective beam size of 50.3×46.8 arcmin) and a total H I mass of 4.6×10^{10} $M_\odot$. Arecibo observations (Schulman *et al.* 1994), with a beam of 3.3 ± 0.1 arcmin, gave an integrated H I flux of 11.1 Jy km s^{-1} which implies an H I mass of 1.4×10^{10} $M_\odot$, but these observations were based on a single pointing at the centre and therefore missed a substantial part of the H I belonging to NGC 765. The total H I mass derived for

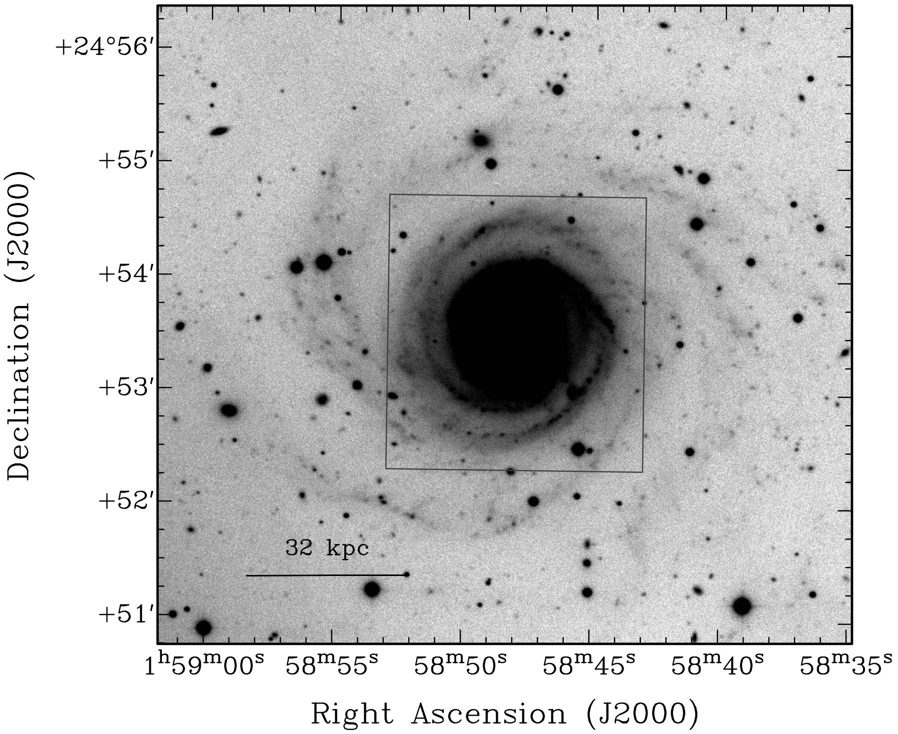

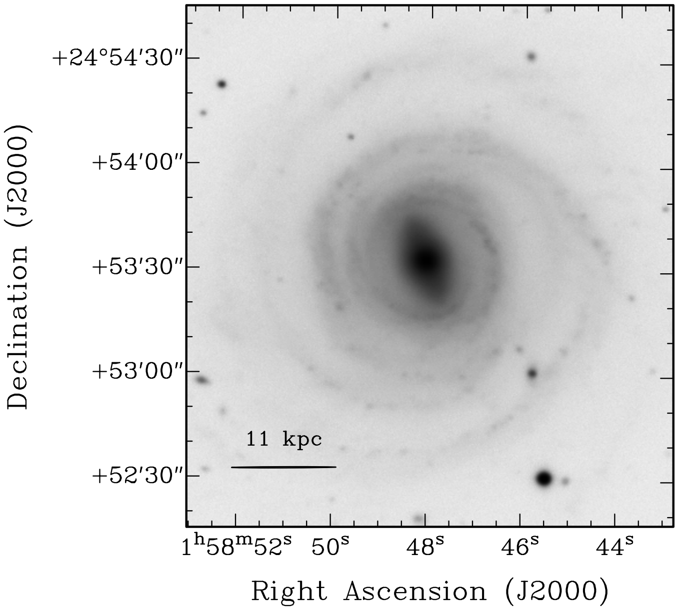

Figure 4.3: Optical image of NGC 765 acquired with Wide Field Camera on the INT. On the top, we saturate the central core to bring out the low–luminosity spiral arms. On the bottom, we zoom in on the central region indicated by the box in the top panel, to expose the central bright core and bar.

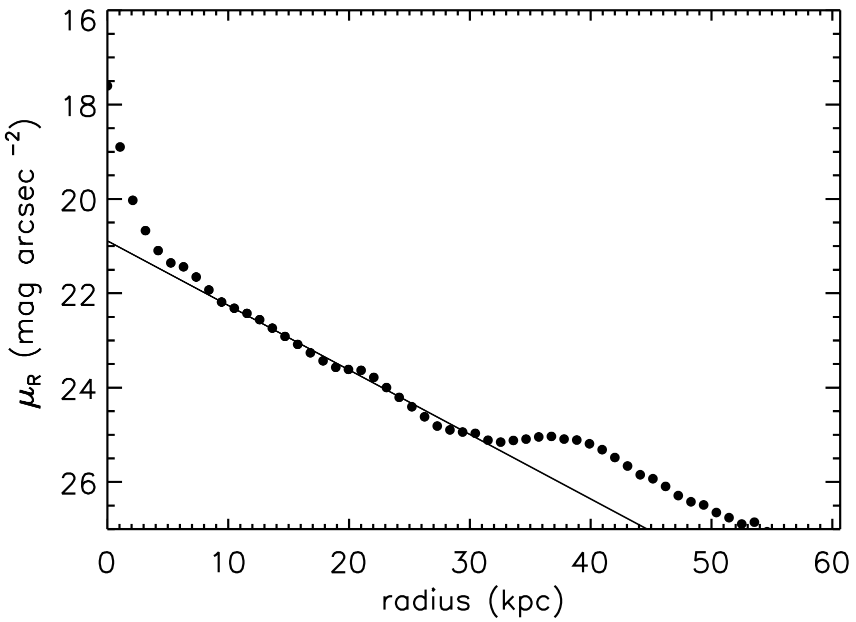

Figure 4.4: Optical surface brightness profile of NGC 765 derived from elliptical isophote fitting on the INT WFC R–band image. Only the northern half of the galaxy was used. We also shown the fit to extrapolate the central surface brightness.

NGC 765 exceeds by one order of magnitude the median H I mass in the LSB survey by O'Neil *et al.* (2004). It also exceeds by a factor of 3 the mean value obtained by Roberts & Haynes (1994) for Sab–Sbc HSB spiral galaxies within the RC3-UGC sample. The H I mass to luminosity ratio for NGC 765 is $M_{HI}/L_B \sim 1.6$, i.e., of the same order as the median $M_{HI}/L_B = 2.8$ found for LSBs by O'Neil *et al.* (2004), and 5–10 times larger than the median for HSB galaxies (Roberts & Haynes 1994).

NGC 765 has an extended H I distribution with a diameter of 240 kpc. In Fig. 4.5 (left) we present H I contours overlaid on the optical image, highlighting the disproportionately large H I disc compared to the optical. The H I structure shows an unresolved central depression with a size $\sim 50 \times 30$ arcsec, better seen in the right–hand panel of Fig. 4.5 where we present the H I distribution, overplotted with velocity contours. The inner gas distribution follows the spiral arms. We can identify at least three of them: two to the East and one to the Southwest. The average H I column density out to 50 kpc, i.e., where the H I spiral arms dominate, is 5×10^{20} atoms cm^{-2}. To the East the column density drops beyond that radius to reach a plateau at 2×10^{20} atoms cm^{-2}, populated with H I clumps (see below).

The outer disc of NGC 765 is asymmetrical or lopsided. This can be appreciated in Fig. 4.6, where we present average surface brightness profiles along the major axis: one along the receding side of the galaxy (hereafter West profile) and the other along the approaching side of the galaxy (hereafter East profile). These were created using the ellipse integration task ELLINT available in GIPSY. The profiles are derived from 30° wide sectors centred around the major axis and binned every 40 arcsec. This process has the advantage of compensating for the loss of signal–to–noise when moving to larger galactic radii by averaging over larger areas, allowing us to recover information all the way out to the periphery of the diffuse disc. In Fig. 4.6, we plot column densities (in atoms cm^{-2}) on a logarithmic scale as a function of linear radius (in kpc). Each side of the galaxy presents a different signature. Both profiles start out at the same level of 5×10^{20} atoms cm^{-2} and show a sudden drop near 50 kpc (2.5 arcmin). The eastern profile settles to a plateau of 2×10^{20} atoms cm^{-2} followed by a rapid decline near 100 kpc out to the last measured point at 120 kpc. The western profile declines smoothly from 70 kpc, extending also out to 120 kpc. Both halves together result in a total H I extent of 240 kpc, measured at a column density of 2×10^{19} atoms cm $^{-2}$.

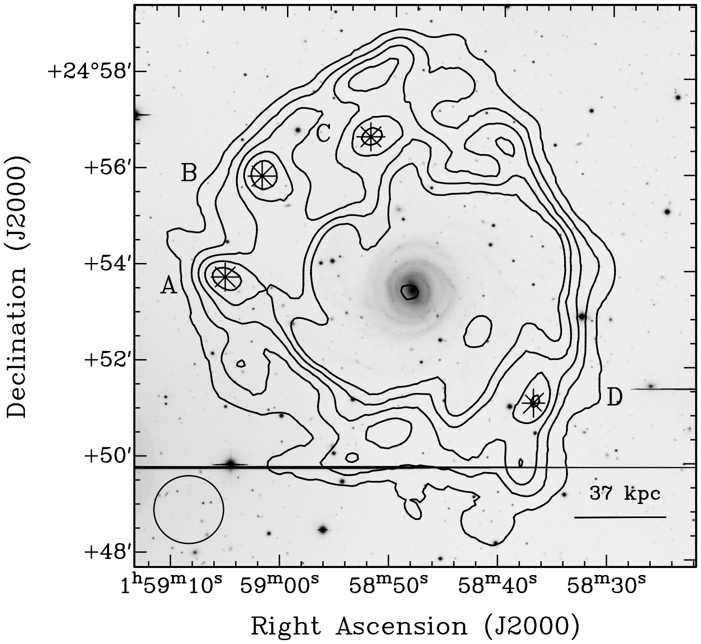

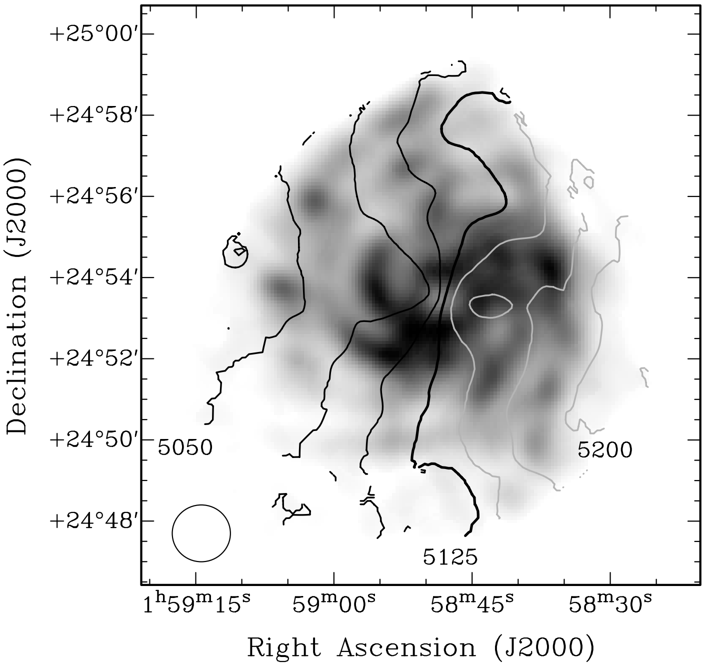

Figure 4.5: Top: H I contours overlaid on the INT optical image. The contours are at a level of 0.5, 1, 1.5, 2 and 2.5 $\times 10^{20}$ atoms cm^{-1}. Four compact H I regions are marked with asterisks and labeled A to D (see Sect. 4.3.1). The horizontal stripe at a declination of approximately 24°50′ is due to bleeding of a bright foreground star along a CCD column (the original orientation of the CCD was rotated by 90°). Bottom: Velocity field of NGC 765 overlaid on an H I surface brightness map. Contours are heliocentric velocities ranging from 5050 km s^{-1} to 5200 km s^{-1}, in steps of 25 km s^{-1}. The systemic velocity of 5125 km s^{-1} is shown as a thick black contour and a few contours are labeled with their velocity in km s^{-1}. The West side of the galaxy is receding (light grey contours). In both maps we represent the H I beam size in the bottom left corner.

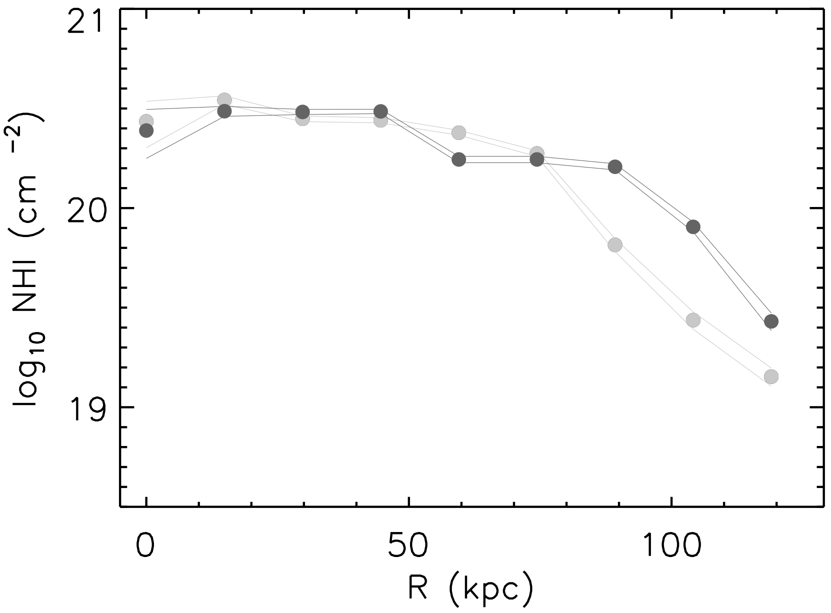

Figure 4.6: Radially averaged surface brightness profiles of NGC 765 along the semi–major axis: the western profile (light grey dots) and the eastern profile (black dots). In both profiles the lines bracket the uncertainty in the profile.

Table 4.3: Basic properties of H I compact regions

Name	α J(2000)	δ J(2000)	Flux Jy km s^{-1}	Mass 10^8 $\mathcal{M}_\odot$
A	$01^h\,59^m\,04.6^s$	$24^\circ\ 53'\ 39''$	2.1	10.2
B	$01^h\,59^m\,01.5^s$	$24^\circ\ 55'\ 49''$	2.2	10.5
C	$01^h\,58^m\,51.6^s$	$24^\circ\ 56'\ 43''$	2.3	9.2
D	$01^h\,58^m\,38.1^s$	$24^\circ\ 50'\ 05''$	1.4	6.3

Notes: Column 1: Source name; Column 2 & 3: Right ascension and declination; Column 4: Integrated flux; Column 5: H I mass.

The low surface density outer disc of NGC 765 is populated by several unresolved or marginally resolved compact H I regions, notably in the North–East. They are prominent in the integrated H I map (Fig. 4.5) as well as in the channel maps (Fig. B.1). Spectra taken at their location are indistinguishable from neighbouring areas at the spatial and velocity resolution of the present data, except for their higher surface brightness. Integrated properties of several of these clumps are given in Table 4.3 (H I masses, were derived using task ISPEC, which retrieves the flux of a region along individual velocity channels). The compact H I regions are labeled in Fig. 4.5.

Given that they are at best marginally resolved, their physical sizes must be less than 10 kpc; their masses are of order 10^8 $\mathcal{M}_\odot$. Together they represent $\sim$ 10 per cent of the total H I mass of NGC 765. Their properties are comparable to those of the companion galaxies detected in our field: NGC 765a and UGC 1453 (see Sect. 4.3.3) and fall within the mass interval for H I–rich companions found by Pisano & Wilcots (2003). The H I masses of the compact H I regions are, however an order of magnitude higher than the range quoted by Wilcots (2001) for H I clumps in discs. In addition, regions A and C present optical counterparts (Fig. 4.7). In both of these, the stellar counterparts and the H I gas are aligned but interestingly do not follow the spiral arms. Neither of the remaining compact H I regions coincides with an optical, radio–continuum or X–ray counterpart.

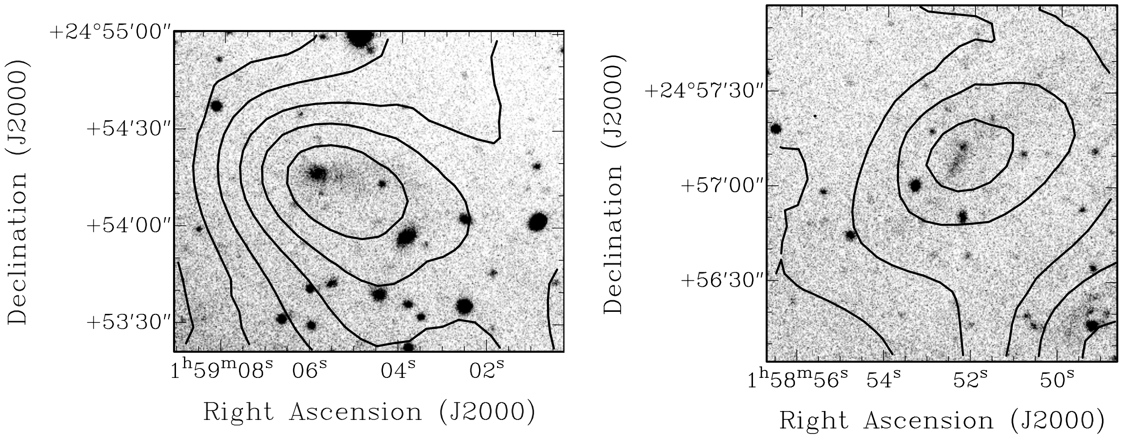

Figure 4.7: Close–up of compact H I regions A (top) and C (bottom) overlaid on the INT optical image.

4.3.2 Velocity field and kinematics

The velocity field presented in Fig. 4.5 (right) shows steeply rising rotation in the inner part (up to ~ 40 arcsec in radius) that is basically unresolved by our beam and a flat rotation curve onwards. Between $2.5 \leq r \leq 3.0$ arcmin there seems to be a kink in the isovelocity contours, best seen on the North side. The position–velocity (PV)–diagrams shown in Fig. 4.8 are taken along the major (PA= 256°) and minor axis (PA= 166°) of the galaxy (see below). We see that both Western and Eastern sides are fairly symmetric within the inner 3 arcmin, with velocities rising quite steeply to a flat level of rotation after just 40 arcsec, and a jump in velocity at ~ 3 arcmin. The ellipse visible in the minor axis diagram (Fig. 4.8, right) is a consequence of the presence of a bar, causing streaming motions in the central part, and our ~ 43 arcsec beam: emission from both the receding and approaching sides enters the beam simultaneously.

We used the task ROTCUR in GIPSY (Begeman 1987) to model the velocity field of NGC 765. ROTCUR treats the observed velocity field as a series of tilted rings. As already mentioned by Begeman (1987), this task becomes increasingly unreliable for low inclination (face–on) galaxies. Given the low inclination of NGC 765 our results should therefore be treated with some caution. Having said that, NGC 765 provides a unique opportunity to probe its dynamical mass and hence the contribution from

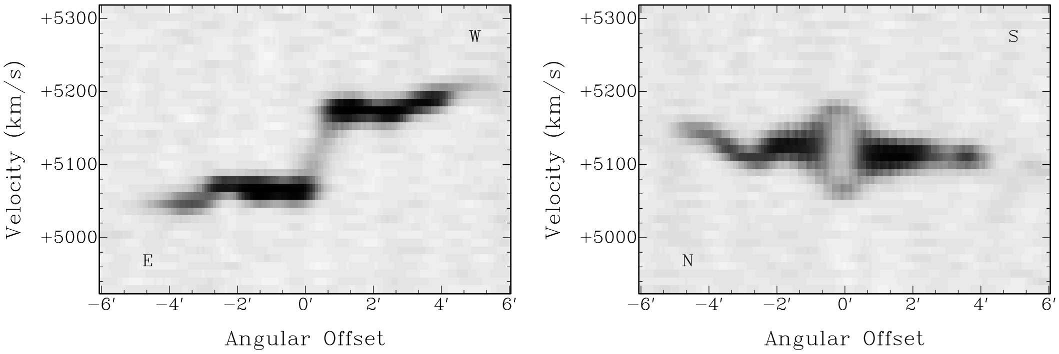

Figure 4.8: Position-velocity map along the kinematical major axis of NGC 765 at a PA of 256° (left panel), showing the rotation of the galaxy. In the right–hand panel we show the position–velocity diagram taken along the minor axis (PA of 166°).

the Dark Matter halo out to an unprecedented distance.

It should also be noted that beam smearing will affect the derived rotation curve, mostly in the inner part. This is nicely illustrated in the case of Malin 1 by Sancisi & Fraternali (2010) who reanalysed the VLA data obtained by Pickering *et al.* (1997), taking beam smearing fully into account. In the case of NGC 765, with 12 independent beams across the galaxy, beam smearing will affect the derived rotation in the innermost region only and has no impact on our conclusions.

We used concentric rings with a width of 40 arcsec, matching the resolution of the integrated H I map. We fitted for each ring the systemic velocity, rotation velocity, position angle, inclination and central position. Starting values of the systemic velocity and centre position were taken from the optical properties presented in Table 4.1. The position angle of 270° was chosen after visual inspection of the data cube and velocity field. The inclination of NGC 765 in NED is listed as 0° . The position velocity diagram along the major axis shows a clear velocity gradient with a peak–to–peak range of about 150 km s^{-1}, arguing against NGC 765 being nearly face–on. Neither the optical map nor the integrated H I map can be used to derive a reliable inclination based on the minor to major axis ratio. The central region of the optical image is dominated by the bar while the outer disc is of too low surface brightness; the H I map is clearly lopsided. We therefore decided to use as initial value 45° . After two iterations a systemic velocity of $V_{sys} = 5125$ km s^{-1} was obtained, consistent with the value retrieved from NED of 5118 km s^{-1} .

We then proceeded to constrain the remaining free parameters. The major axis PV–diagram shows a jump to slightly higher velocities around 2.5 arcmin radius, near where the H I column density drops to a plateau of 2×10^{20} atoms cm^{-2}, and the galaxy takes on a decidedly lopsided look. Galaxy rotation curves are observed to be flat out to the last measured point and we therefore concluded that the outer H I disc must be slightly warped. Hence we fixed the rotation curve to a flat 160 km s^{-1} beyond $\sim$ 100 arcsec, allowing for a smooth variation in position angle and inclination. We show in Fig. 4.9 (middle and bottom panels) the ROTCUR results for fits to each side of the galaxy separately. The inclination varies from a constant 21° in the inner, high H I surface brightness part to around 30° in the outskirts.

The dynamical mass of NGC 765 was derived using the thin disc approximation (van Moorsel 1982):

$$\mathrm{M_{dyn}} = 0.76\frac{\mathrm{R_{HI}V^2}}{\mathrm{G}} \tag{4.1}$$

where $\mathrm{R_{HI}}$ is the radius of the last measured point of the rotation curve and V is the rotation velocity respectively. For NGC 765, at a radius of 320 arcsec or 112 kpc and a velocity of 160 km s^{-1} , we derive a dynamical mass of 5.1×10^{11} $\mathcal{M}_\odot$.

4.3.3 Companions

Fig. 4.2 includes two companions of NGC 765 detected in H I: NGC 765a and UGC 1453. Both objects are seen across nine consecutive velocity channels towards the low-velocity edge of our bandwidth (4860 – 4950 km s^{-1}). In Fig. 4.10 (left) we see NGC 765a as H I contours overlaid on a DSS optical image. The positional accuracy of the DSS images are typically $1''$. A faint optical counterpart coincident with the H I peak can be seen. In the case of UGC 1453, H I contours are overlaid on the INT optical image (Fig. 4.10, right). It is possible to see faint flocculent, arm–like structure, typical of an irregular galaxy.

NGC 765a is a newly detected H I source. It is marginally resolved. A gauss fit on the integrated H I map gives a deconvolved size of 13.8×8.5 kpc for the assumed distance of 72 Mpc, at a position angle of 134° . We used AIPS task ISPEC to derive a flux of 0.53 Jy km s^{-1}, which translates to an H I mass of 6.5×10^8 $\mathcal{M}_\odot$. The projected angular distance to NGC 765 is 16.2 arcmin or 338 kpc and the radial velocity difference is 225 km s^{-1} .

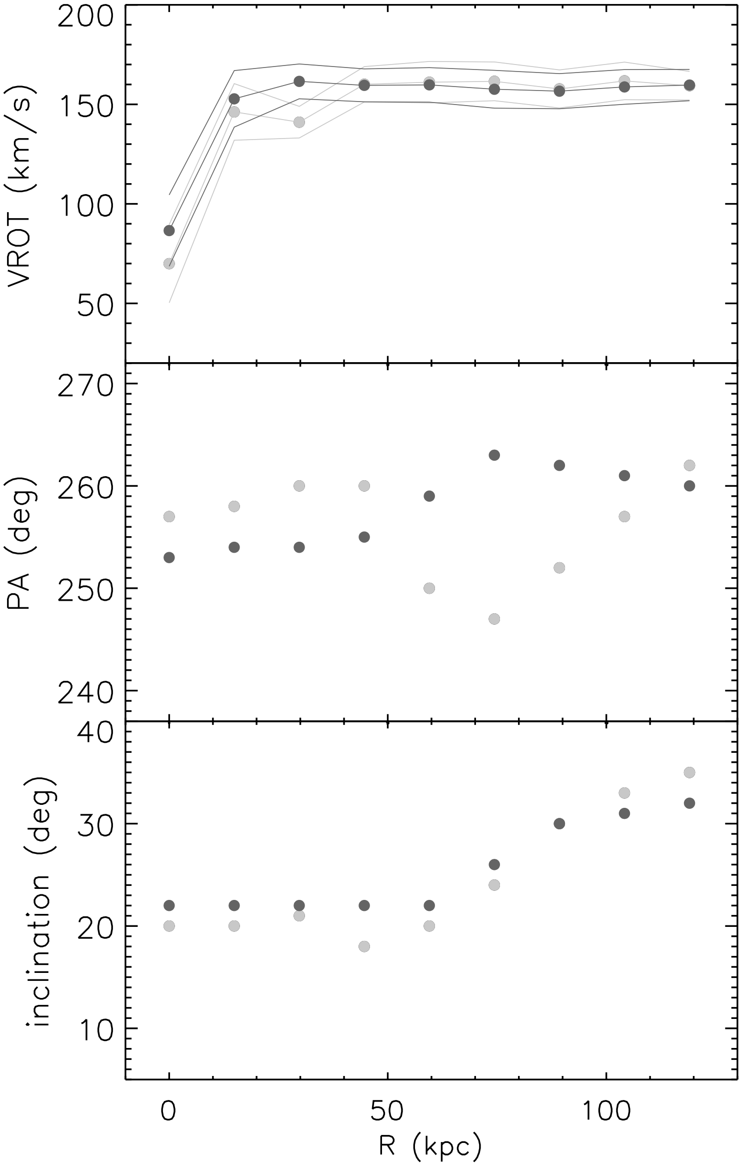

Figure 4.9: Rotation curves for individual halves of NGC 765 (top panel) with respective values of position angle (middle panel) and inclination (bottom panel) as a function of radial distance in kpc. The black dots represent the kinematically approaching (East) side of the galaxy whereas the light grey dots correspond to the receding (West) side. In the top panel, thin light and dark lines represent the uncertainties.

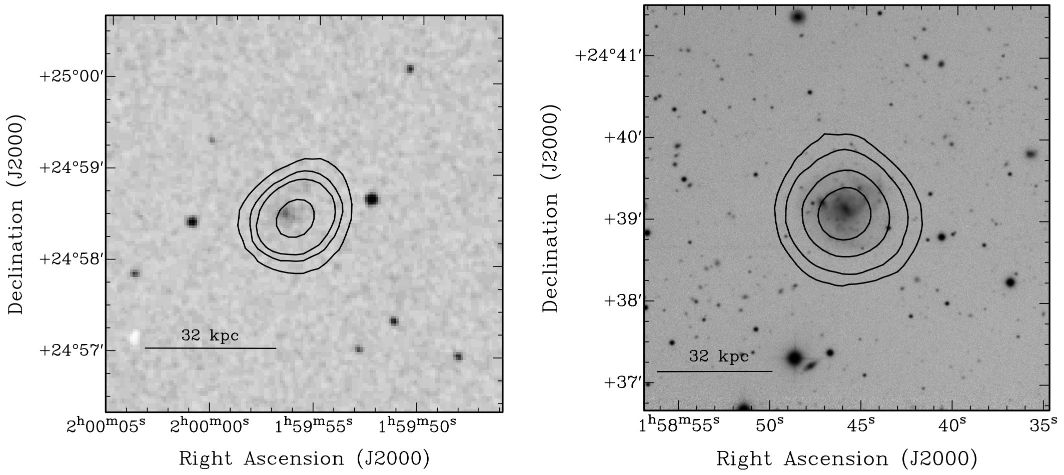

Figure 4.10: The left–hand panel presents H I contours of NGC 765a overlaid on a DSS optical image. The contours are 0.5, 0.8, 1 and 1.5 $\times 10^{20}$ atoms cm^{-2}. The right–hand panel shows H I contours of UGC 1453 overlaid on an INT optical image. The contours are at column densities of 0.5, 1, 2 and 3 $\times 10^{20}$ atoms cm^{-2}.

Whereas NGC 765a is uncatalogued, UGC 1453 is a known 17 mag irregular galaxy at a measured velocity of 4897 km s^{-1} (NED). It has as an optical size of 1.5 × 1.3 arcmin. Like NGC 765a, it is marginally resolved with our beam and we derive an intrinsic diameter for the bulk of the H I of 17 kpc. We derive an integrated flux of 1.54 Jy km s^{-1} and an H I mass of 1.9 $\times 10^{9}$ $\mathcal{M}_{\odot}$. The mass falls within values typical for Sm or Im galaxies (Roberts & Haynes 1994). Because the detection falls at the low-velocity edge of the band, we might be missing some of the integrated flux, given the 2.66 Jy km s^{-1} value reported by Giovanelli *et al.* (1986) and Schneider *et al.* (1990) based on Arecibo neutral hydrogen observations. Springob *et al.* (2005) list 2.57 Jy km s^{-1}. This means that we might also be underestimating its H I extent. We derive a projected angular distance from NGC 765 of 14.8 arcmin or 310 kpc and a radial velocity difference of 221 km s^{-1}.

4.3.4 Nuclear activity

NGC 765 shows signatures of a bar, a structure that is capable of transporting gas from the inner regions of a galaxy to its nucleus. The presence of nuclear emission lines of [N II], [S I] and [O I] and the detection of a compact low–luminosity radio–

continuum source (Sect. 4.2.1), strongly suggests the presence of an LLAGN. This is further strengthened by the detection of the central X–ray source (Sect. 4.2.3; Sect. B.3; Das *et al.* 2009). The X–ray luminosity ($L_X \approx 1.7 \times 10^{40}$ erg s^{-1}) and radio–continuum luminosity ($L_{1.4\,GHz} = 1.3 \times 10^{21}$ W Hz^{-1}) are typical of low-luminosity AGN (Ho *et al.* 2001; Desroches & Ho 2009).

The detection of AGN activity (in radio and X–rays) is quite common, with Desroches & Ho (2009) quoting 20–25% for late-type (Hubble types Scd–Sm) galaxies. Filho *et al.* (2006) found the same fraction for a sample of bright local galaxies taken from the Palomar survey of bright galaxies (Ho *et al.* 1997). As mentioned by Das *et al.* (2009), very little is known about nuclear activity of LSBs, although those LSBs that have well–developed bulges, like NGC 765, seem to follow the same evolutionary path as bulge–dominated HSBs.

4.4 Discussion

4.4.1 The extent and morphology of the H I disc

The inner region (2–4 arcmin or 40–80 kpc diameter) of NGC 765 appears to have the normal morphology of a spiral galaxy, as shown in Fig. 4.5. It has a central bar as do 70% of disc galaxies (e.g. Erwin 2005). The neutral gas distribution, as seen in in Figs. 4.2 and 4.5, and as described in Sect. 4.3.1, reveals an H I–poor central region, which is common in cases of a bar. The H I spiral arms trace well their optical counterparts.

Based on its central surface brightness it is classified as an LSB, its $\mu_B(0)$ of 22.27 mag arcsec^{-2} falling below the range of 21.65 ± 0.3 mag arcsec^{-2} of HSB galaxies (Freeman 1970). This is further confirmed by its large 7.8 kpc scale length for the exponential disc (e.g., Sprayberry *et al.* 1995). NGC 765 is unique, though, for the linear size of its H I disc. The fact that we can trace the neutral hydrogen out to 240 kpc in diameter, makes this the largest H I disc ever measured in a local spiral galaxy, on a par with the more distant Malin 1. The total H I content of 4.7×10^{10} $M_\odot$ equally puts it in the category of giant LSBs (O'Neil *et al.* 2004), as does the resulting $M_{HI}/L_B \sim 1.6$.

There is a clear difference though when we compare NGC 765 with some of the

Table 4.4: R_{HI} to h ratios of some galaxies from the literature and NGC 765

Object	R_{HI} (kpc)	h (kpc)	R_{HI}/h
Malin 1	100	82.0	1.2
F568–6 (Malin 2)	90	18.3	4.9
UGC 6614	50	13.6	3.7
NGC 7589	39	12.6	3.1
NGC 765	120	7.8	15

Note: optical scale lengths were determined on *R*–band images except for Malin 1, where the *V*–band was used.

other well known Malin 1 cousins in the sense that the radius of its H I disc compared to optical scale length is considerably larger. This is illustrated in Table 4.4 where we compare NGC 765 with the H I radius–to–optical scale length of the four giant LSBs observed by Pickering *et al.* (1997).

NGC 765 can be divided into two regimes, inner and outer disc, with the transition at ~ 50 kpc. At that radius the optical disc has become too faint to be traced any further, we find a jump in velocity in the major axis position–velocity diagram which we interpret as being due to a modest warping of the disc beyond 50 kpc, and at this same radius we find that the H I column density drops from a constant level of $5 \times 10^{20}\,\mathrm{cm}^{-2}$ to a plateau of $2 \times 10^{20}\,\mathrm{cm}^{-2}$.

The outer H I disc is asymmetrical, is at a lower column density, and is populated by compact H I regions. These regions typically measure < 10 kpc and have H I masses of $10^{8-9}\,\mathcal{M}_{\odot}$ (of the same order as those of dIrr galaxies). Discrete H I clumps lacking an optical counterpart have been found around galaxies, typically within 50 kpc and $60\,\mathrm{km\,s}^{-1}$ (Wilcots 2001), and represent perhaps the fossil evidence of the process of galaxy formation.

Hierarchical galaxy formation predicts the assembly of galaxies via a merger of smaller units. Indeed, there is observational evidence for major or minor mergers, in the form of interacting galaxies, accretion of dwarfs, H I clumps, or in the case of cold accretion, filaments or streams of material, as highlighted by Sancisi *et al.* (2008) and van der Hulst & Sancisi (2005). The stellar counterparts present within the compact H I regions A and C as shown in Fig. 4.7 lend evidence that they could be fossil remnants of past mergers in a process similar to the Sagittarius (Sgr) dwarf galaxy discovered by Ibata *et al.* (1994), a tidal stream that is observed near the Milky Way (Martínez-Delgado *et al.* 2001, and references therein). Simulations performed by Ibata & Razoumov (1998) show that the Sagittarius dwarf with a mass of $\sim 10^9 \mathcal{M}_\odot$, would survive several encounters with the Milky Way and produce distortions in the H I disc of the Galaxy. In addition, simulations by Peñarrubia *et al.* (2006) also point to the fact that an extended outer disc ($\sim$ 200 kpc) of an M 31 size galaxy could be created via the merger of a dwarf companion with a mass of $\sim 10^9 - 10^{10} \mathcal{M}_\odot$.

Based on this, it is fair to speculate that over its lifetime, NGC 765 has accreted H I through a series of merger events with dwarf galaxies with H I masses of the order $10^{8-9}\ \mathcal{M}_\odot$, enlarging the size of the disc and acting as a reservoir of H I fuel for future star formation (Pisano & Wilcots 2003; Sancisi *et al.* 2008).

In support of this, NGC 765 belongs to a galaxy group, [GH83]024 (Garcia 1993) and the field contains two companions within $\sim$340 kpc, which have H I masses and sizes similar to the compact H I regions present in the outer disc of NGC 765. The accretion scenario would also fit in with the kinematical and morphological lopsidedness of the H I disc. In their study of the spiral galaxy NGC 6946, Boomsma *et al.* (2008) interpreted lopsidedness, signatures of sharp edges of the H I disc and wiggles in the velocity field as possible indicators of accretion. All these signs are present in NGC 765. Besides, if gas is indeed being accreted, it does not necessarily start out in an orbit co–planar with the inner disc, which could explain why gas in the outer parts resides in a plane with a different orientation. Having said that, the fact that NGC 765 belongs to a group increases the probability of it having suffered tidal interactions which are able to to produce lopsidedness or excite an oscillation in the z–direction.

Sancisi *et al.* (2008) report that 25% of galaxies with observational evidence of tidal interaction have clumps of gas with masses of order $10^{8-9}\mathcal{M}_\odot$, which corresponds to the H I masses of the compact H I regions of the outer disc of NGC 765. Pisano & Wilcots (2003) show evidence that these companions are statistically in circular orbits, their masses are low, and therefore will not strongly affect the host's morphology.

This is also corroborated by Bournaud *et al.* (2005), who investigate via N–body simulations that mergers with mass ratios in the range from 20:1 to 7:1 will trigger significant lopsidedness in their hosts on time scales of at least a few Gyrs. In our case, we estimate that NGC 765a and UGC 1453 could have been gravitationally bound to NGC 765 over the past $\sim$ 9 Gyr. If accreted, these would represent between 1 to 4 per cent of its H I mass.

There are two problems, though, with this scenario. One is that the amount of H I in NGC 765 is considerable and that a large number of minor mergers would be required. The other problem is that the period of rotation in the outer disc is of order 4–4.5 Gyr which makes for a very long relaxation time. So perhaps we are dealing with nature rather than nurture, the structure of NGC 765 being defined more by the initial conditions of its formation (Dalcanton *et al.* 1997; Hoffman *et al.* 1992) and less by its merger history.

4.4.2 Surface brightness profiles and SFR

What remains intriguing about NGC 765 is the enormous disparity between the optical and H I discs. With such large amounts of H I both in the outskirts and spiral arms, R_{25} ends well before we run out of gas. We question why this gas is not forming stars at large galactocentric distances.

GALEX observations (see Fig. 4.11) do not reveal any trace of a young stellar population due to recent star formation in the outer disc, implying that the conditions for star formation are not right. Schaye (2004) quotes a minimum gas column density necessary for a transition from warm atomic to cold molecular of around 3 to 10 $\mathcal{M}_\odot$ pc^{-2}, equivalent to 4 – 12 $\times 10^{20}$ atoms cm^{-2}, assuming a model of a self–gravitating disc containing dust and metals that is exposed to UV radiation. Similarly Leroy *et al.* (2008) and Bigiel *et al.* (2008) discuss the transition of H I–to–H_2 on sub–kpc scales making use of the THINGS high spatial and velocity resolution data. They point to an H I surface brightness limit of 9 $\mathcal{M}_\odot$ pc^{-2} or $\sim 10^{21}$ atoms cm^{-2} found in all THINGS galaxies, above which threshold molecular gas dominates.

We indeed find that column density peaks do not exceed $\sim 3 \times 10^{20}$ atoms cm^{-2} across the NGC 765 H I disc, suggesting that little, if any, gas will have made the transition from neutral atomic to the molecular phase, a condition encountered more

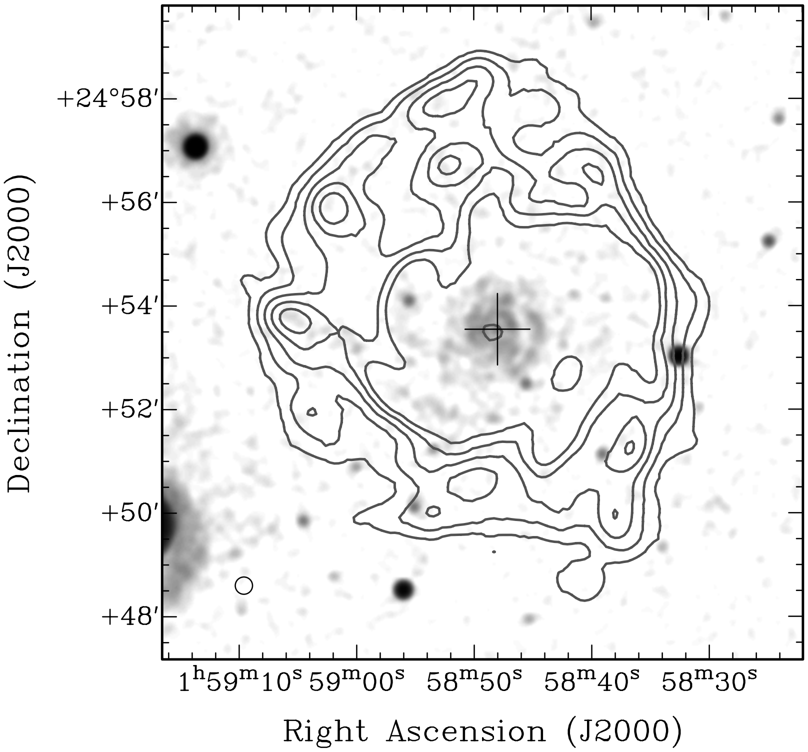

Figure 4.11: *GALEX* map smoothed to a 10 arcsec resolution. In grey contours we represent the H I extent at a column density of 0.5, 1, 1.5, 2 and 2.5 $\times 10^{20}$ atoms cm^{-2}. The optical centre of the galaxy is represented by a cross.

generally in spiral galaxies beyond R$_{25}$. NGC 765 is simply a more extreme case in the sense that the outer H I disc is much larger than in typical field spirals. This does imply that NGC 765 has an enormous reservoir of close to critical gas and that any perturbation such as a merger event could cause a major starburst.

4.4.3 Sérsic parameterisation of NGC 765

In Fig. 4.12, we parameterise the radial profiles using a Sérsic–like r$^{1/\mathrm{n}}$ power law. We use the method employed in Chapter 2. We summarise the results of the fit in Table 4.5. Both halves were successfully described by the power law fit and both present similar behaviour especially in the way that they decline, with a slope of n = 0.34. Having said that, both fits are poorly constrained for r$_\mathrm{i}$ and n due to our

Table 4.5: Results from the parameterisation of NGC 765 using a Sérsic $r^{1/n}$ power law.

Major axis	log(NH I) atoms cm^{-2}	r$_i$ kpc	n	χ^2_{red}
West	20.51 ± 0.57	68.84 ± 82.73	0.34 ± 0.57	2.82
East	20.48 ± 0.52	78.00 ± 71.59	0.34 ± 0.38	1.25

modest resolution, limiting the number of independent data points where the H I drop sets in. In addition the outer disc of this giant is simply too distorted by the presence of H I compact regions. Any conclusions drawn on signatures of edges in this giant disc might not be comparable to the isolated non–interacting spiral galaxies studied in Chapter 2.

4.5 Summary

In this chapter we present multi–wavelength observations of NGC 765. We highlight the more important results of this study:

- NGC 765 presents a large H I disc, 240 kpc in diameter for an assumed distance of 72 Mpc. This is one of the largest H I discs reported for a late type galaxy.
- Assuming an optical scale length of 7.8 kpc, NGC 765 presents an H I–to–optical ratio of 15. This is considerably larger than what has been found in other giant LSBs such as Malin 1.
- The H I disc morphology clearly presents two different regimes: an inner H I disk (< 50 kpc) tracing the spiral structure with the presence of at least three arms, and an outer, lower surface brightness plateau. This latter region is populated by several H I gas clumps of compact morphology.
- The galaxy has two nearby companions: NGC 765a, a previously uncatalogued companion, towards the Northeast. Towards the South we have UGC 1453,

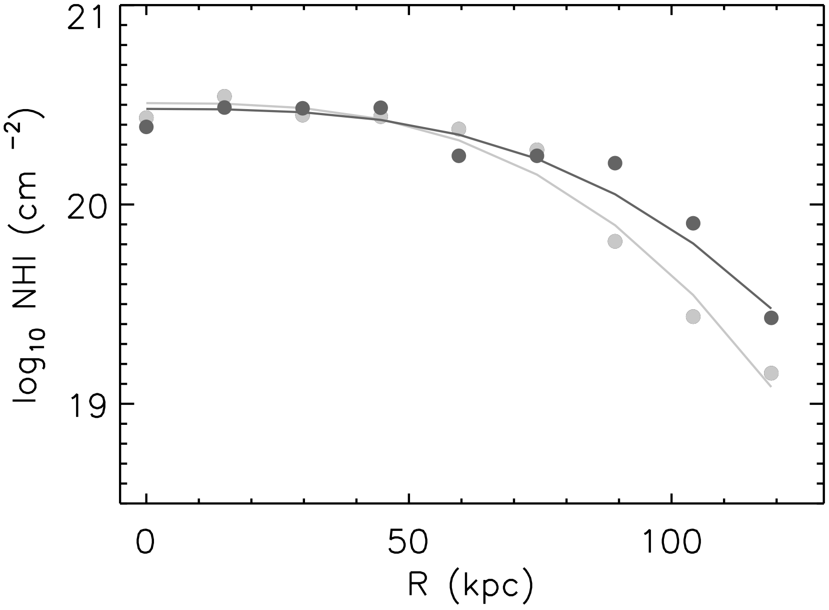

Figure 4.12: Sérsic power–law fit (represented by solid lines) versus the radially averaged surface brightness profiles (filled circles): the West profile (light grey) and the East profile (dark grey).

an irregular galaxy. We report the detection of a faint optical counterpart for NGC 765a.

- The outer disc of NGC 765 is slightly warped. It is populated with compact H I regions with sizes of ∼ 10 kpc and H I masses of $\sim 10^8\mathcal{M}_\odot$. These are possibly remnants of past mergers events.

- We detect 1.4 GHz radio–continuum emission from the NGC 765 optical core. This emission is weak, with a flux density of 2.16 mJy and a luminosity of $L_{1.4\,\mathrm{GHz}} = 1.3 \times 10^{21}$ W Hz^{-1}. No radio continuum emission is found related to the stellar or H I disc.

- *Chandra* X–ray data reveal emission coincident with the galaxy nucleus. We derive a luminosity of $L_X(0.2\text{–}10\ \mathrm{keV}) \approx 1.7 \times 10^{40}$ erg s^{-1}. The radio and X–ray emission is compatible with the nucleus being powered by a weak AGN, as also suggested by its optical nuclear emission lines.

- Star formation activity in NGC 765 is low, with no star formation detected in the outer disk, suggesting the gas is well below the threshold for star formation.

Higher resolution H I observations will be needed to more fully understand the origin, structure, and expected evolution of this truly extraordinary H I disc.

Appendix B

Additional data of NGC 765

B.1 NGC 765 channel maps

In Fig. B.1 we present the H I channel maps of NGC 765 as a set of grey–scale maps. They were generated using IMAGR choosing a ROBUST=0 weight in order to obtain the best compromise between resolution and sensitivity. The cube was cleaned to a flux threshold of 2σ.

B.2 Radio–continuum sources

There are several radio–continuum sources in the field of NGC 765, in addition to the source coinciding with the optical nucleus. Except for continuum source number 2, they fall outside of the outline defined by the H I, as can be seen in Fig. B.3. We present in Table B.1 the properties of the radio–continuum sources in the field of NGC 765. Of the eight sources detected above 4.5σ, sources 1 and 2 are found to fall within the H I disc. Source 2 coincides to within $17''$, or 5 kpc, with H I compact region B (see Sect. 4.3.1). Sources 4, 6, 7 and 8 were all detected by the NVSS as well. Source 3 has two 2MASS objects identified as possible counterpart. Source 4 was identified by 2MASS as a galaxy. The remaining sources have no NVSS detection or NED identification.

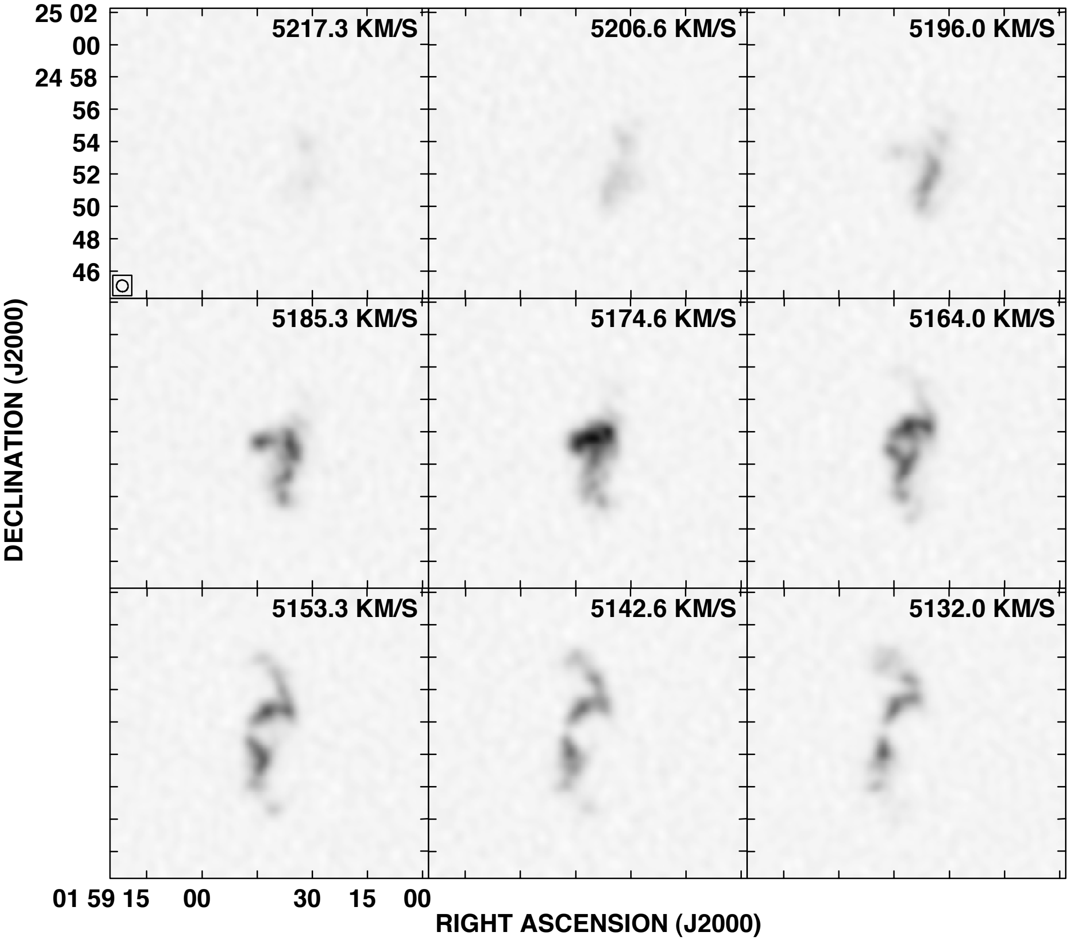

Figure B.1: Individual velocity channels of NGC 765. The beam is shown in the left bottom corner of the top left panel. Heliocentric velocities are indicated in each panel.

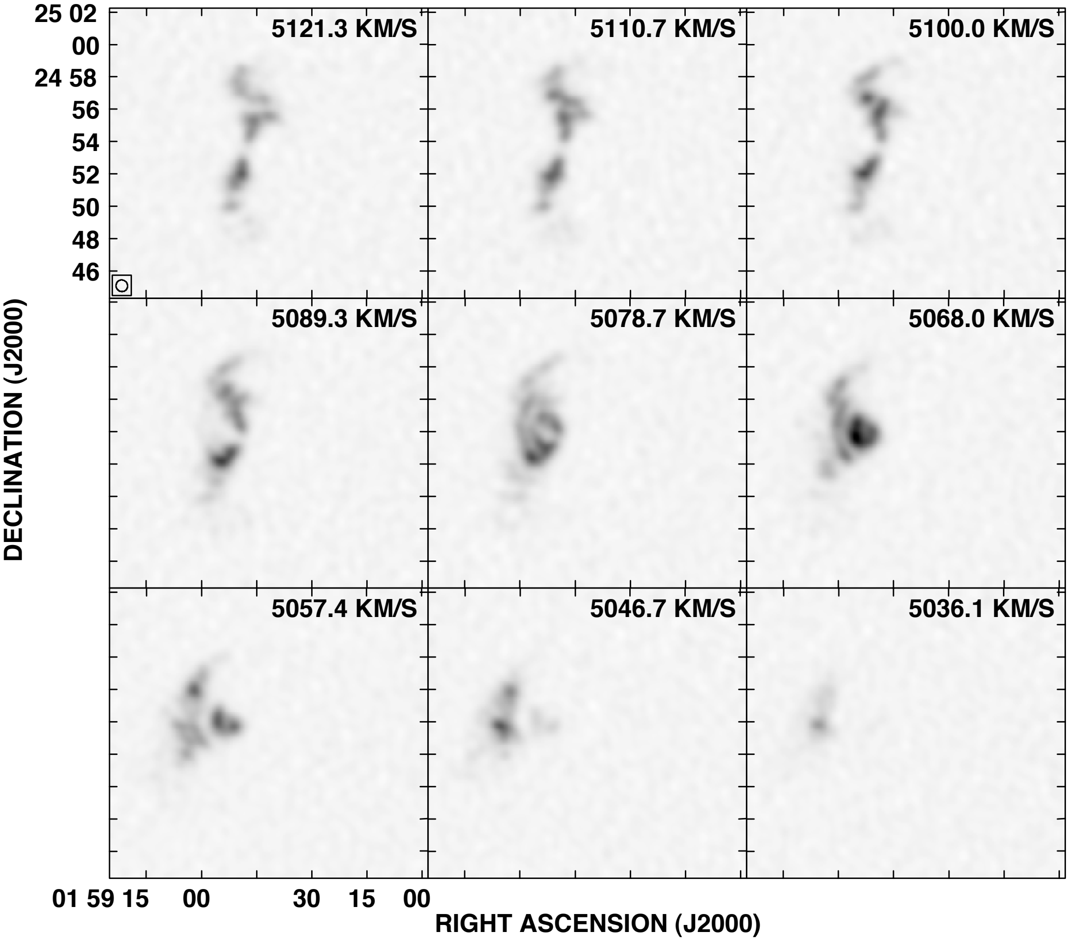

Figure B.2: Individual velocity channels of NGC 765 (Continued).

Table B.1: List of radio continuum sources detected in the vicinity of NGC 765.

Source	α (J2000)	δ (J2000)	Deconvolved size $'' \times ''$	$\mathrm{F_P}$ mJy	$\mathrm{F_I}$ mJy	PA °	S/N	Type	Identification
1	$01^h\,58^m\,48.5^s$	$24^\circ\ 53'\ 39''$	61×34	0.83	2.16	58	14	G	NGC 765
2	$01^h\,59^m\,01.9^s$	$24^\circ\ 56'\ 06''$	23×14	0.78	0.84	46	6	...	...
3	$01^h\,58^m\,31.7^s$	$24^\circ\ 59'\ 39''$	17×9	43.3	47.1	157	314	G, RadioS	2MASX J01583181+2459391 2MASX J01582855+2459367 NVSS J015831+245938
4	$01^h\,58^m\,24.1^s$	$24^\circ\ 59'\ 59''$	6×0	1.38	1.18	111	8	G	2MASX J01582399+2459598
5	$01^h\,58^m\,27.7^s$	$24^\circ\ 52'\ 53''$	51×29	21.0	37.0	21	247	RadioS	NVSS J015827+245252
6	$01^h\,58^m\,22.7^s$	$24^\circ\ 50'\ 22''$	52×43	18.8	40.3	37	269	RadioS	NVSS J015822+245022
7	$01^h\,58^m\,50.5^s$	$24^\circ\ 47'\ 46''$	17×13	1.44	1.37	36	9	...	...
8	$01^h\,59^m\,14.1^s$	$24^\circ\ 52'\ 44''$	12×7	4.03	3.97	137	27	RadioS	NVSS J015914+245248

Notes: Column 1: Source number; Column 2 & 3: Right ascension and declination; Column 4: Deconvolved source size; Column 5: Peak flux; Column 6: Integrated flux; Column 7: Position angle; Column 8: Signal–to–noise ratio; Column 9: object type — G denotes galaxy and RadioS radio source; Column 10: Identification.

B.3 X–ray sources

The data reduction of the Chandra archival observations of NGC 765 revealed a total of six sources in the general field, one coinciding with the nucleus. Because the photon statistics are low (see Table 4), we did not attempt to extract spectra, but instead opted to use the PIMMs tool (v3.9i) to convert source counts into fluxes. We assumed the appropriate Cycle 8 calibration curves for the ACIS-S detector, an input energy of 0.2-10 keV, a simple power law model with a weighted galactic absorption towards NGC 765 of 8.03×10^{20} cm^{-2} (Kalberla *et al.* 2005), fixed photon index of 2.0 (appropriate for LLAGN and for X-ray binaries) and a redshift of z=0.017 (NED). The results are presented in Table B.2.

X–ray source X3 (Table B.2 and Fig. B.4) is relatively compact, coincides with the optical nucleus of NGC 765 and with the nuclear radio–continuum source (Table B.1). It has an X–ray luminosity in the 0.2–10 keV energy band of $L_X \approx 1.7 \times 10^{40}$ erg s^{-1}. This low X–ray luminosity is typical of low–luminosity AGN (Ho *et al.* 2001).

Due to the low X–ray counts and lack of temporal information, the nature of the remaining X–ray sources in the field can not be established with certainty. Sources X4 and X5 (Fig. B.4) coincide spatially with stellar counterparts but are unidentified in both the NED and 2MASS catalogues. These could be background quasars but because of a lack of redshift information, we estimated their X–ray luminosities assuming they are at the distance of NGC 765, although there is no *a priori* evidence that they belong to this system. The low–luminosity and the off–nuclear position of sources X1, X2 and X6 suggest these are low luminosity X–ray binaries. Their luminosities have been estimated again assuming they are at the redshift of NGC 765.

In order to detect any hypothetical extended, diffuse X–ray emission, we subtracted the point sources from the image and interpolated the gaps with appropriate values for the background, using the statistics of the surrounding pixels. We then smoothed the image to a 5 arcsec beam. Contrary to (Das *et al.* 2009) who find a diffuse gas component associated with the galaxy centre and confined to the bulge at a luminosity of 5.5×10^{39} erg s^{-1}, we find no significant diffuse X–ray emission anywhere within the H I disc.

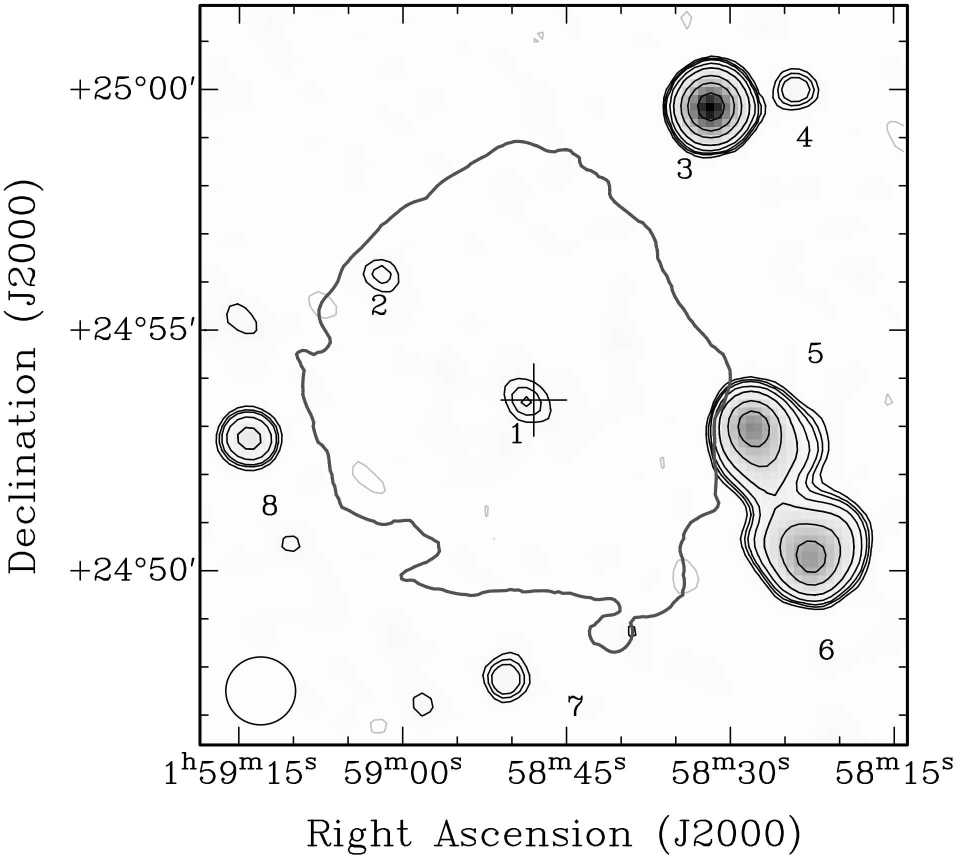

Figure B.3: The radio continuum emission of the NGC 765 field at 1.4 GHz. The contours are at (-2, 2, 3, 4.5, 6, 10, 20, 50, 100 and 200) times the rms of 0.15 mJy beam^{-1}. The negative contour is plotted as light grey. The extent of the H I disc of NGC 765 at a level of 5 $\times 10^{19}$ atoms cm^{-2} is plotted with a single dark grey contour. The optical centre of the galaxy is represented by the cross. Source 1 coincides with the optical centre of NGC 765.

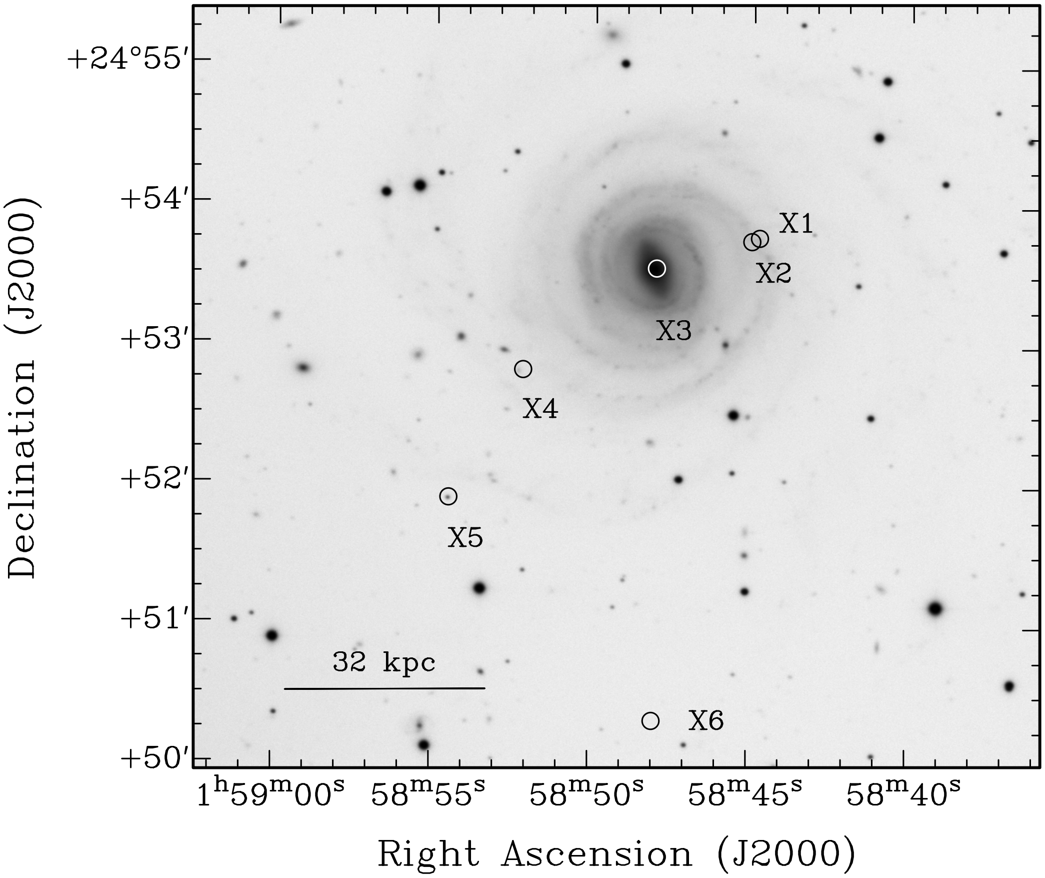

Figure B.4: The location of the detected Chandra X–ray sources overlaid on the optical INT map of NGC 765. The central source X3 coincides with the optical centre and the central radio–continuum source of NGC 765.

Table B.2: Chandra X–ray detections in the NGC 765 field.

source	α J(2000)	δ J(2000)	N_S	N_{bg}	S/N	Unabsorbed flux 10^{-14} erg s^{-1} cm^{-2}	Luminosity 10^{40} erg s^{-1}
X1	$1^h\,58^m\,44.7^s$	$24^\circ\ 53'\ 46.1''$	6.4	1.5	4.5	1.6	1.0
						0.9	0.6
						0.6	0.4
X2	$1^h\,58^m\,44.9^s$	$24^\circ\ 53'\ 44.6''$	15.2	2.6	5.8	3.7	2.3
						2.2	1.3
						1.5	0.9
X3	$1^h\,58^m\,48.0^s$	$24^\circ\ 53'\ 33.0''$	11.8	3.4	3.5	2.8	1.7
						1.7	1.0
						1.2	0.7
X4	$1^h\,58^m\,52.3^s$	$24^\circ\ 52'\ 48.5''$	7.5	2.1	3.6	1.8	1.1
						1.1	0.7
						0.8	0.5
X5	$1^h\,58^m\,54.5^s$	$24^\circ\ 51'\ 53.9''$	11.5	3.7	3.1	2.8	1.7
						1.6	1.0
						1.1	0.7
X6	$1^h\,58^m\,48.1^s$	$24^\circ\ 50'\ 19.4''$	13.5	4.8	3.0	3.3	2.0
						1.9	1.2
						1.3	0.8

Notes: Column 1: Source name; Column 2 & 3: Right ascension and declination; Column 4: Source counts; Column 5: Background counts; Column 6: Signal–to–noise ratio; Column 7: Unabsorbed X–ray flux in the energy bands: 0.2 – 10 keV (total; top row), 0.2 – 2 keV (soft; middle row) and 2 – 10 keV (hard; bottom row); Column 8: X–ray luminosity in the same energy bands, assuming a distance of 72 Mpc.

Chapter 5

Simulations and edges of dwarf galaxies

5.1 Introduction

As already mentioned in Chapter 1, in hierarchical models of galaxy formation, small objects form first, and merge to form large galaxies. Therefore dwarf galaxies assume the rôle of building blocks of larger structures. The gas in the dwarfs does not settle into a thin, dynamically well–ordered disc, and we know from simulations (e.g. Mashchenko *et al.* 2008) that, given their shallow potential wells, dwarfs are strongly affected by the large amount of energy released from supernovae and stellar winds which in some cases are enough to remove the entire gaseous component (Ferrara & Tolstoy 2000; Silich *et al.* 2006).

In fact, the neutral gas distribution in a dwarf galaxy will be resembling an oblate spheroidal structure with much more of a thick disc–like morphology if compared at the same linear scale with the thin discs of late–type galaxies (Brinks *et al.* 2002).

We are well aware that observed edges in radial profiles in an oblate disc of a dwarf might not be an accurate reflection of the intrinsic distribution of the neutral gas. To tackle this, we took NGC 2366, one of the dwarf galaxies of the THINGS survey and produced a collection of simple models with GALMOD for its dwarf disc.

5.2 Model of a dwarf galaxy: NGC 2366

NGC 2366 was chosen as a template for a collection of simple GALMOD models where we focus our attention on the radial scaleheight distribution Z0 and the inclination of the disc, INCL. The former can be directly linked with the thick disc morphology of dwarfs, the latter will directly affect the derived column densities along a line–of–sight piercing through such a thick layer. Since a rotation curve of this object was obtained by Oh *et al.* (2008) (see Fig. 5.1) and a study of the radial scaleheight distribution is available (Banerjee *et al.* 2010, priv. comm.), which closely follows the models of Narayan *et al.* (2005) and Banerjee & Jog (2008), and here presented in Fig. 5.2 and labelled SHD, all the necessary kinematical data required by GALMOD is available. Note that in both figures we simply replicate the last values of VROT, and Z0 in order to model the full extent of this galaxy.

As far as the radial surface brightness distribution of NGC 2366 is concerned, we decided to explore three different scenarios as shown in Fig. 5.3. DENS_{2366} was obtained in similar fashion to the average radial profiles presented in Sect. 2.4 with ELLINT. It was derived along a 30° wide–arc region along the kinematically receding semi–major axis of the object and binned in $10''$ intervals.

Contrary to the spiral discs studied in Chapter 2 and modelled in Chapter 3, which are characterised by a flat inner disc followed by a declining outer disc, NGC 2366 presents an inner region that starts declining from column densities higher than 10^{21} atoms cm^{-2} at a radius of ~ 2 kpc down to a few times 10^{19} atoms cm^{-2} out to 8.5 kpc . At this region column densities drop steeper reaching 1.6×10^{18} atoms cm^{-2} at $\mathrm{R}_{\mathrm{max}}$, the assumed radius of the dwarf disc at 10 kpc. model 1, is a scale–down version of model B from Chapter 3. It is characterized by a flat inner surface brightness of 1×10^{21} atoms cm^{-2} which dominates 80% of the disc. The last 20 % presents a exponential decline down to a column density of 1×10^{18} atoms cm^{-2}. model 2 is based on a double exponential fit to DENS_{2366} where both exponentials intersect at a radius of 8.5 kpc.

In contrast to Chapter 3, where we fine–tuned the vales of CDENS and CMODE, we opted to keep these values at their default values arguing this to be a very preliminary exercise to model dwarf discs. The other approximation we made was to use a constant position angle of 39.8° (and in some of the models a constant inclination of 63.8°)

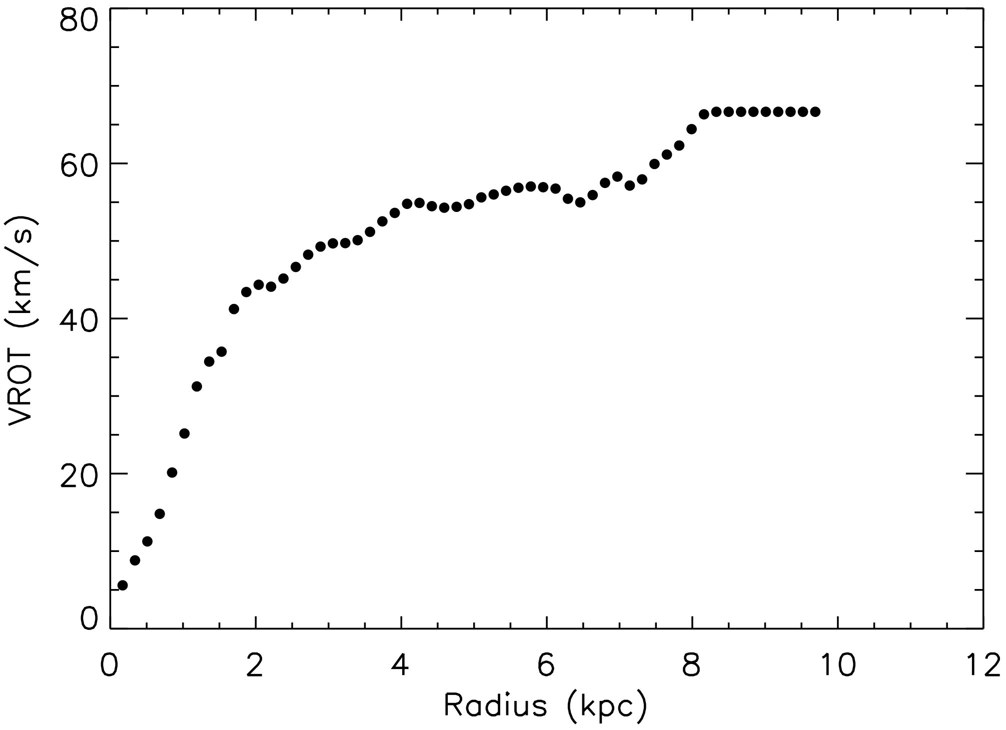

Figure 5.1: The rotation curve of NGC 2366 adapted from Oh *et al.* (2008).

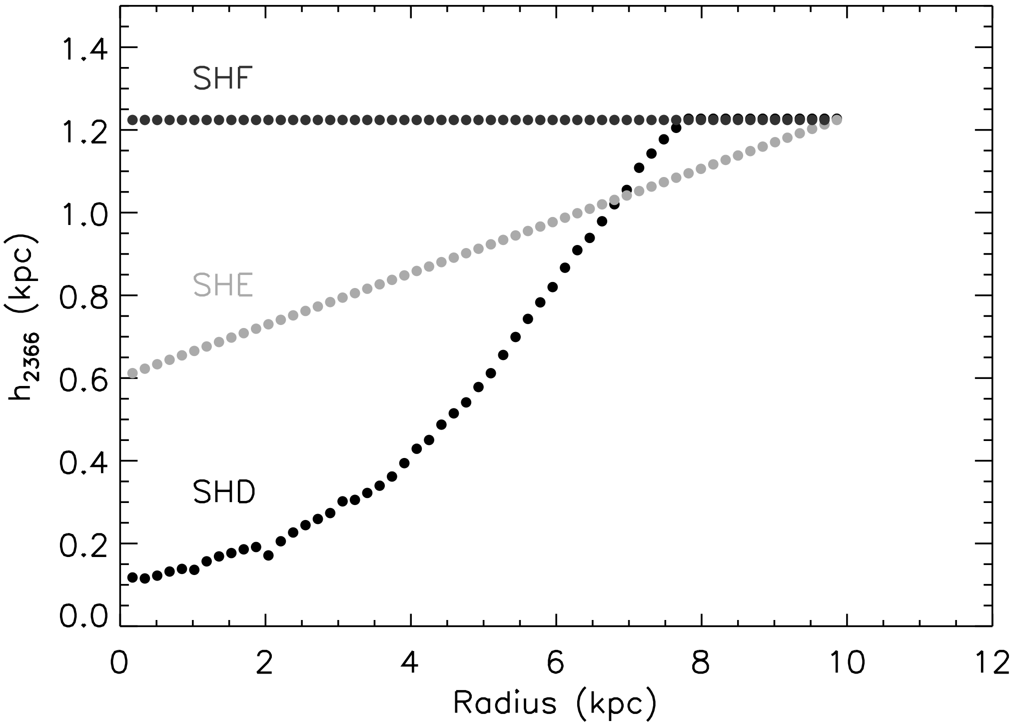

Figure 5.2: The three radial scaleheight distributions of NGC 2366 explored in this preliminary set of simulations. SHD was derived by Banerjee *et al.* (2010) (solid black dots). We also created SHE (solid light grey dots) which grows linearly from 0.6 kpc up to ∼ 1.2 kpc at $R_{\max}$. SHF (solid dark grey dots) maintains a constant scaleheight distribution throughout the disc at a level of ∼ 1.2 kpc.

throughout the disc. Both values were obtained from Walter *et al.* (2008). We summarise the GALMOD parameters of the models we explored in Table 5.1.

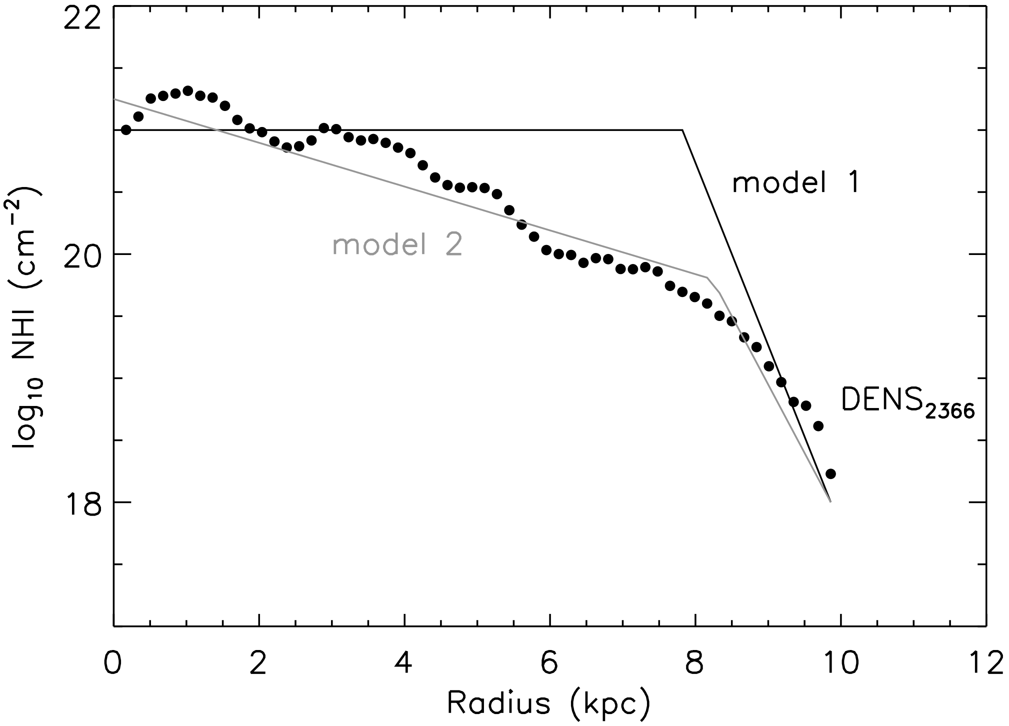

Figure 5.3: Three different radial surface brightness distributions for NGC 2366. DENS_{2366} is based on the ELLINT radial profile and here represented by the solid black dots. model 1 is an approximation to DENS_{2366} where we divide the disc into a flat inner part and an exponentially declining outer disc (solid black line). The solid light grey line pertains to model 2, where we fitted a double exponential to DENS_{2366} with a “knee” at 8.5 kpc.

In a first trial we created models N2366_01, N2366_02, and N2366_03 with an associated surface brightness density distribution of model 1, model 2 and DENS_{2366} respectively as shown in Fig 5.3. We employed the rotation curve above and scale-height distribution SHD (see Fig. 5.1 and Fig. 5.2).

In Fig. 5.4, we present integrated H I maps of N2366_01 to N2366_03 as well as an integrated H I map of NGC 2366 (top left panel). This dwarf object presents an asymmetric gas distribution characterized by the presence of two H I peaks in the inner core and a warped outer envelope. N2366_01, top right panel, presents a high H I saturation almost throughout its disc in accordance with the model 1 radial distribution. N2366_02 is shown in the bottom left panel and is a fairly good representation of NGC 2366 with a brighter inner core followed by a fainter H I outer disc. The N2366_03 integrated H I map (bottom right panel) is characterized by at least three concentric rings that have their origin in the ELLINT–derived radial profile, DENS_{2366}.

Following the same method as in Chapter 3, we present the radial profiles and log–log column densities scatter plots for ELLINT as a function of the model and the 1–pixel wide profile as a function of model. We perform a simple linear regression between both pairs of variables and present the slopes for both fits: *slope a* corresponds to the ELLINT–model log–log scatter plot whereas *slope b* to the 1–pixel wide one. For those cases where the retrieved surface brightness distribution is similar to the model input profile, the slopes should be close to 1.0.

The radial profiles obtained for the N2366_01 to N2366_03 models can be found in Fig. 5.5 to Fig. 5.7. Both ELLINT and 1–pixel wide radial profiles of model N2366_01 satisfactorily reproduce the break point separating the inner flat region from the outer declining region of the disc. It is also noticeable that for the ELLINT profile the steepness of the slope is shallower than the model 1 density profile. For the 1–pixel wide profile we are presented with the opposite case. This is confirmed by the slopes of the log–log scatter plots where the *slope a* is 0.84 and the 1–pixel wide–model is $b = 1.26$ (see Fig. 5.5). The same kind of analysis can be drawn for models N2366_02 (Fig. 5.6) and N2366_03 (Fig 5.7). In both cases the radial profiles follow more closely the input DENS parameter, to a point where in N2366_03 the ELLINT–model scatter plot suggests a strong correlation between model and observations ($a = 1.00$). This can be understood since N2366_03 does not present any abrupt variation of density in comparison to the break points present in N2366_01 and N2366_02.

As explained in Chapter 3, the slight offset we see in Fig. 5.5 between the input model surface density and the output density can be traced back to the fact that GALMOD calculates the model in units of W.U. per pixel. When converting to column density we assumed instead of a square 1.5″ ×1.5″ pixel, a gaussian beam with a FWHM of 1.5″. This results in a slightly different conversion from W.U., or mJy, to units of kelvin brightness temperature. That difference is exactly 1.13. As mentioned, rather than correcting the graphs we decided to leave them in their current form as this allows for easier comparison between input and output curves.

5.3 NGC 2366: models with different scaleheight distributions at different inclinations

As mentioned earlier, the ensemble of models here created will not exhaustively explore the parameter space of GALMOD and should be seen as a first approach to the modeling of H I discs of dwarfs. We decided to explore three different types of scaleheight distribution shown in Fig. 5.2, for a large range of disc inclinations, varying from face–on (INCL=0°) out to edge–on (INCL=90°) models. We perform this exercise using the model 1 density distribution arguing that this is one of the simplest density distribution one can generate. The three runs of models we created can be summarised as follows:

- eight models, N2366_04 to N2366_11, were created for disc inclinations: 0° , 15° , 30° , 45° , 55° , 65° , 75° , 90° ; for these we used a radial scaleheight distribution SHD obtained by Banerjee *et al.* (2010).
- eight models, N2366_11 to N2366_19, were generated with disc inclinations: 0° , 15° , 30° , 45° , 55° , 65° , 75° , 90° ; We make use of the radial scaleheight distribution SHE. This grows linearly from ∼0.6 kpc out to 1.2 kpc at R_{max}.
- eight models, N2366_20 to N2366_27, were produced for disc inclinations: 0° , 15° , 30° , 45° , 55° , 65° , 75° , 90° ; For these, we employed a constant radial scaleheight distribution, SHF = 1.2 kpc (or 72″).

For more details on individual parameters we refer the reader to Table 5.1. Radial profiles were obtained as previously explained, however we will restrict ourselves to only showing the most relevant three: N2366_20 (INCL = 0°), N2366_23 (INCL = 45°) and N2366_26 (INCL= 75 °) which we consider to be representative of the influence

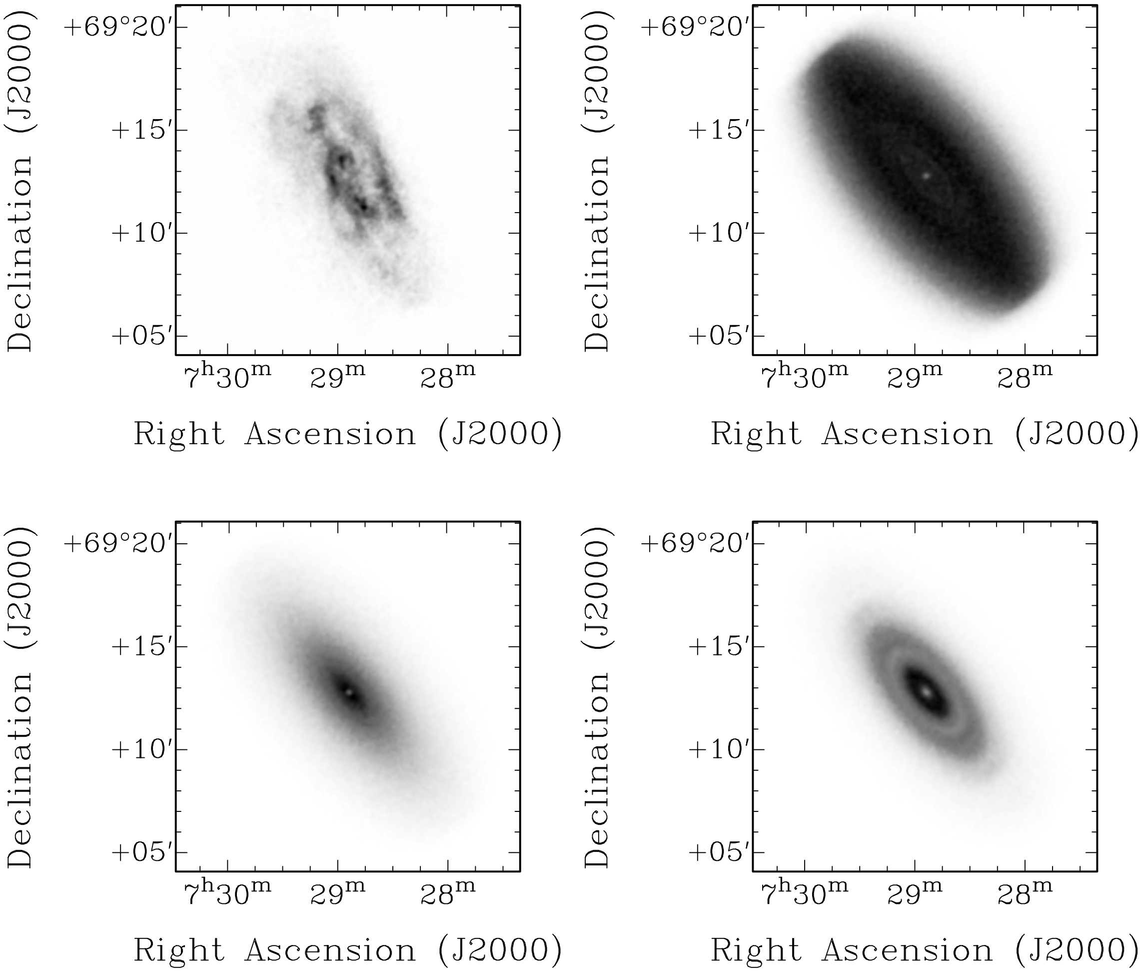

Figure 5.4: Integrated H I maps of NGC 2366 (top left panel), 2366_01 (top right panel), 2366_02 (bottom right panel) and 2366_03 (bottom right panel). All maps have the same spatial resolution of 10″.

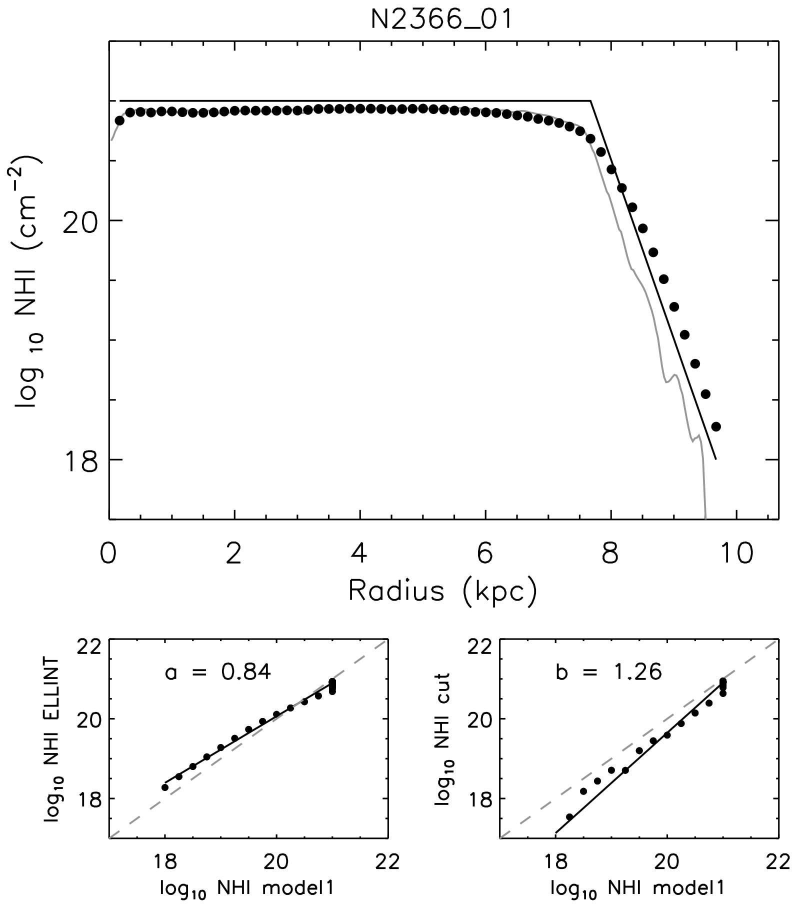

Figure 5.5: The radial profiles of 2366_01. In the top panel we present the DENS input parameter (solid black line). The radial ELLINT profile is represented by the black dots and 1–pixel wide profile by a solid grey line. The smaller bottom panels represent log–log scatter plots between radial profiles and DENS parameter: on the left, the ELLINT–model and on the right the 1–pixel wide–model scatter plot (solid black dots). A linear fit is shown by the solid black line. In addition we present for guidance purposes a dashed grey line with a slope of 1.00

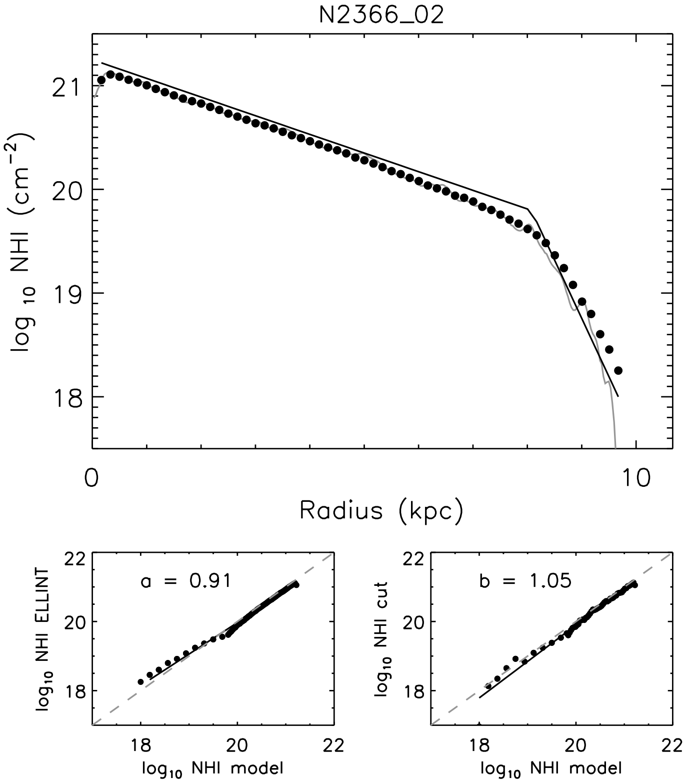

Figure 5.6: The radial profiles of 2366_02 and respective log–log scatter plots between radial profiles and DENS input. Please refer to the caption of Fig. 5.5 for further details.

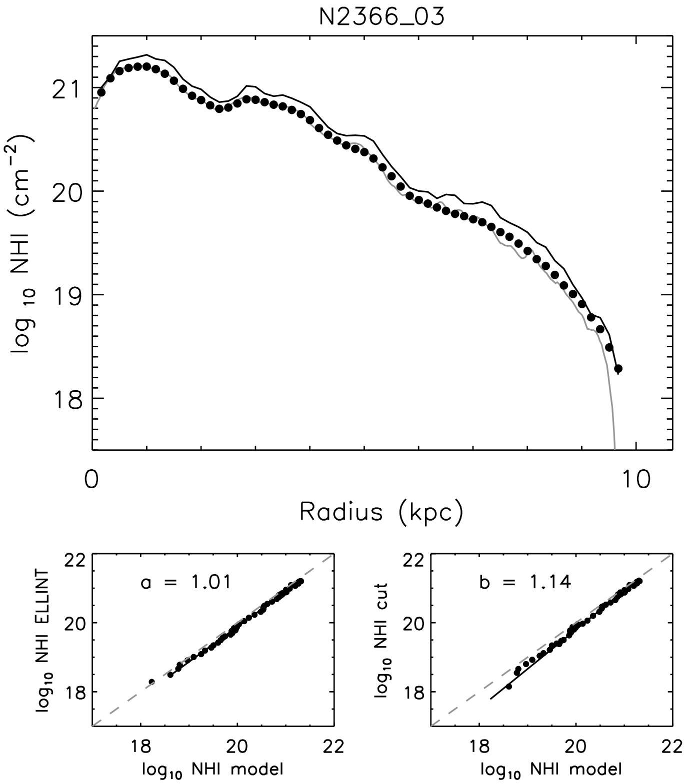

Figure 5.7: The radial profiles of 2366_03 and respective log–log scatter plots between radial profiles and DENS input. Please refer to the caption of Fig. 5.5 for further details.

of the orientation of the disc on the radial profile column densities. We do present in Table 5.2 a summary of the log–log scatter plots slopes obtained.

From the analysis of the resulting slopes, we can infer a division between radial profiles with inclinations INCL $< 60°$ and INCL $> 60°$. In the first group we find radial profiles that are good descriptions of the input radial column density. Concerning the ELLINT radial profiles, slopes are always higher than 0.93. For the 1–pixel wide profiles, apart from a few exceptions (N2366_05 and N2366_16) the typical deviations from the desired 1–to–1 relation is approximately 0.10 dex. We found the group of models with inclinations higher than 60° to exhibit larger deviations between input and output of radial density distributions. As shown, the ELLINT profiles at high inclinations present deviations of the order of 0.20 dex for a disc inclination of 65° , and increasing for an inclination of 75° . The relation breaks down altogether for edge–on discs (INCL=90°). This is illustrated in Fig. 5.8 to Fig. 5.10. The first two present radial profiles of a face–on disc and intermediately inclined disc, where we can verify the good agreement between radial profiles and input density. This breaks down for the highly inclined disc.

5.4 Radial profiles and Sérsic parameterisation in dwarfs

Encouraged by the results found for the ensemble of models created for NGC 2366 and given the signatures of a declining column densities present in the dwarfs sub–sample, we applied to them the same Sérsic parameterisation employed in Sect. 2.5.1 for spiral galaxies. We make use of the existing set of THINGS H I data cubes and integrated maps convolved to a common 10″ circular beam. In total there are 11 galaxies broadly classified as dwarf irregulars. The radial profiles were produced with the GIPSY routine ELLINT using a 30° sector centred on the major axis and averaged along 30° wide arcs in 10″ radial bins, matching the spatial resolution of our maps. We report the results of the fits in Table 5.3.

Figs. 5.11 to 5.16 show the set of ELLINT profiles of our targets with respective error bars, as well as an integrated H I map of the object mapped at 10″ resolution. We chose to plot column densities on a logarithmic scale as a function of linear

Table 5.1: GALMOD parameters for NGC 2366

Model	DENS	Z0	INCL	Model	DENS	Z0	INCL
	cm^{-2}	″	°	cm^{-2}	″	°	
				2366_12			0
				2366_13			15
2366_01	model 1			2366_14			30
2366_02	model 2	SHD	63.8	2366_15	model 1	SHE	45
2366_03	$DENS_{2366}$			2366_16			55
				2366_17			65
				2366_18			75
				2366_19			90
2366_04			0	2366_20			0
2366_05			15	2366_21			15
2366_06			30	2366_22			30
2366_07	model 1	SHD	45	2366_23	model 1	SHF	45
2366_10			55	2366_24			55
2366_11			65	2366_25			65
2366_08			75	2366_26			75
2366_09			90	2366_27			90

Additional GALMOD parameters for NGC 2366: POS: 5 -4; VSYS: 100 km s^{-1} ; VROT=$VROT_{2366}$ in km s^{-1} ; RADII: 10:580:10; VDISP: 10 km s^{-1} ; LTYPE: 2; CDENS=1; CMODE=1; PA=39.8° ; NV=66.

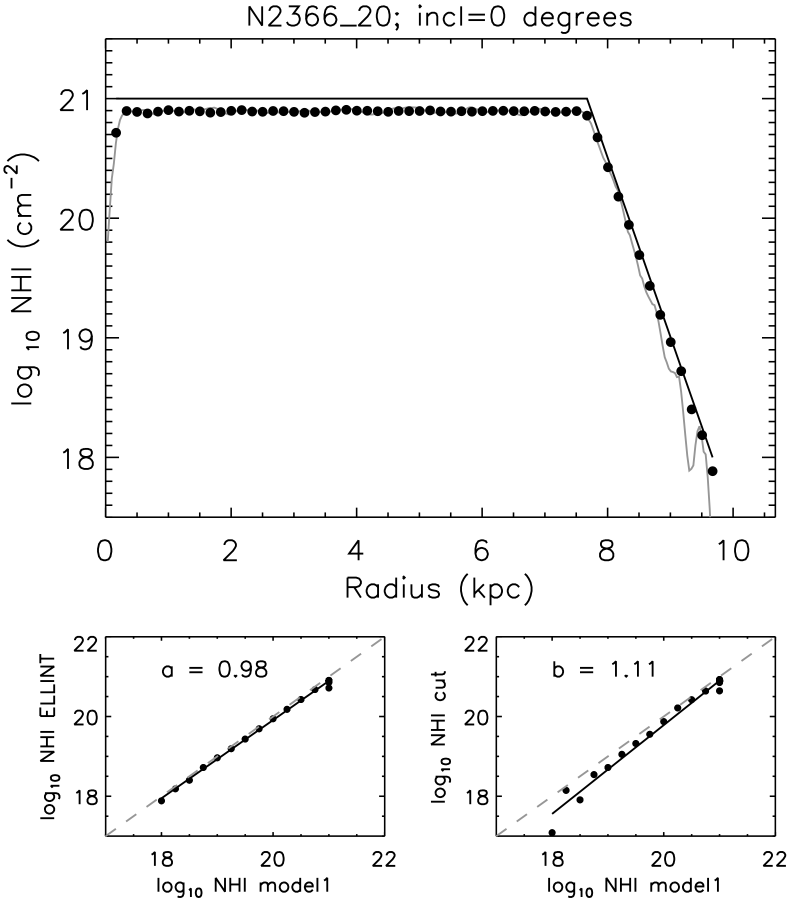

Figure 5.8: The radial profiles of model 2366_20 (INCL=0°). In the top panel we present the DENS input parameter (solid black line). The radial ELLINT profile is represented by the black dots and 1–pixel wide profile by a solid grey line. The smaller bottom panels represent log–log scatter plots between radial profiles and DENS parameter: on the left, the ELLINT–model and on the right the 1–pixel wide–model scatter plot (solid black dots). A linear fit through the dots is shown by the solid black line. In addition we present for guidance purposes the dashed grey line with a slope of 1.00

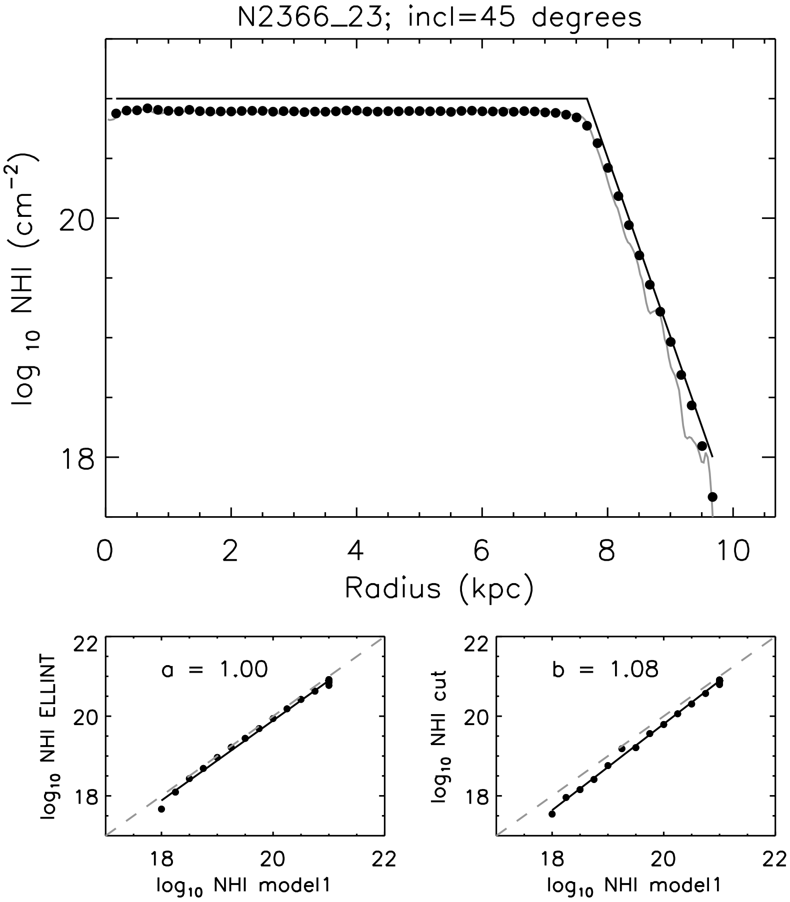

Figure 5.9: Radial profiles for N2366_23 (INCL=45°). Please refer to the caption of Fig. 5.8 for further details.

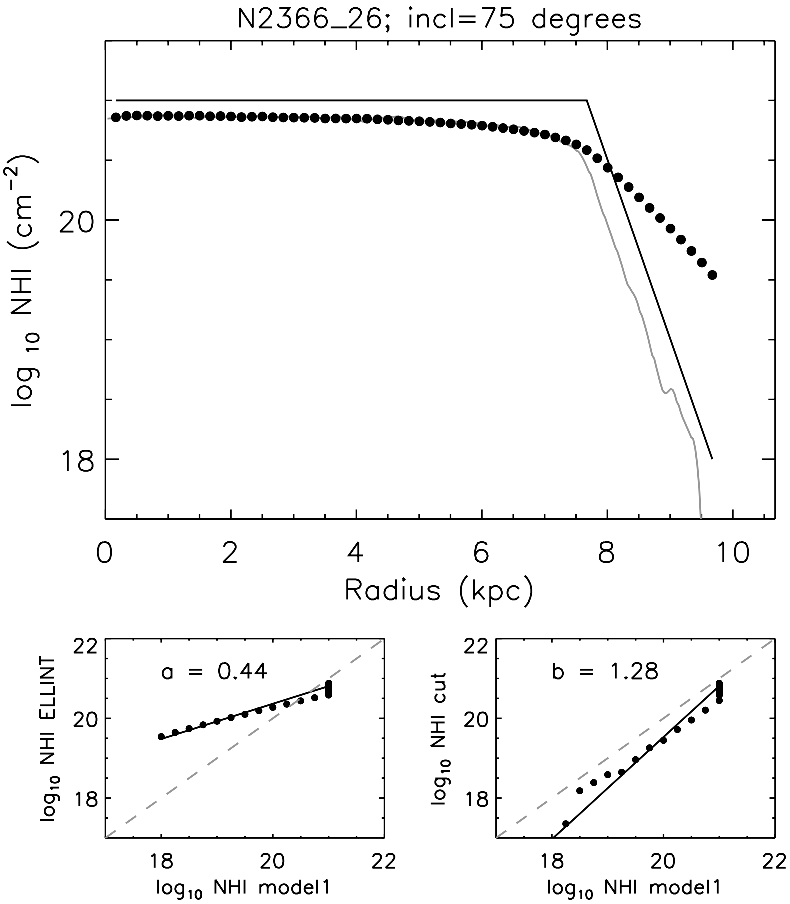

Figure 5.10: Radial profiles for N2366_26 (INCL=75°). Please refer to the caption of Fig. 5.8 for further details.

Table 5.2: The log–log scatter plots slopes form the collection of dwarf disc models

Model	slope a	slope b	INCL	Z0
N2366_04	0.98	1.11	0°	SHD
N2366_12	0.98	1.11		SHE
N2366_20	0.98	1.11		SHF
N2366_05	0.98	1.35	15°	SHD
N2366_13	0.98	0.95		SHE
N2366_21	0.98	1.06		SHF
N2366_06	0.98	1.05	30°	SHD
N2366_14	0.99	1.13		SHE
N2366_22	1.01	1.14		SHF
N2366_07	0.99	1.06	45°	SHD
N2366_15	0.99	1.18		SHE
N2366_23	1.0	1.08		SHF
N2366_10	0.94	1.19	55°	SHD
N2366_16	0.96	1.41		SHE
N2366_24	0.93	1.09		SHF
N2366_11	0.80	1.17	65°	SHD
N2366_17	0.81	1.13		SHE
N2366_25	0.79	1.16		SHF
N2366_08	0.49	1.35	75°	SHD
N2366_18	0.48	1.21		SHE
N2366_26	0.44	1.28		SHF
N2366_09	...	1.34	90°	SHD
N2366_19	...	1.29		SHE
N2366_27	...	1.31		SHF

radius. Overall, column densities vary within the typical values found in discs of spiral galaxies, from a few times 10^{21} atoms cm^{-2} down to a few times 10^{18} atoms cm^{-2} in most objects. They all show an H I decline towards the periphery of the disc. Ho II (Fig. 5.12) and NGC 1569 (Fig.5.14) are the two objects with the most irregular radial distribution, contrasting the smoother profiles such those of DDO 53, Ho I, M 81 DwA and M 81 DwB.

Table 5.3: Sérsic $r^{1/n}$ fit applied to dwarf radial profiles

object	$\log I(0)$ atoms cm^{-2}	r_i kpc	n	χ^2_{red}
DDO 154	20.79 ± 0.15	3.17 ± 1.39	0.53 ± 0.12	1.52
DDO 53	21.30 ± 0.58	0.11 ± 0.80	0.88 ± 0.64	3.22
Ho I	**21.04 ± 0.38**	**1.41 ± 1.97**	**0.53 ± 0.43**	**2.06**
Ho II	**21.25 ± 0.11**	**3.40 ± 0.60**	**0.36 ± 0.07**	**0.73**
IC 1574	**21.02 ± 0.10**	**7.30 ± 1.04**	**0.29 ± 0.06**	**2.36**
M 81 DwA	**20.70 ± 0.36**	**1.23 ± 0.75**	**0.33 ± 0.24**	**1.30**
M 81 DwB	21.32 ± 0.26	0.14 ± 0.36	0.81 ± 0.35	1.30
NGC 1569	21.35 ± 0.16	0.00 ± 0.08	1.00 ± 0.08	0.64
NGC 2366	21.24 ± 0.15	2.51 ± 1.20	0.53 ± 0.14	0.83
NGC 2976	20.91 ± 0.17	1.99 ± 0.63	0.35 ± 0.12	0.89
NGC 4214	**20.80 ± 0.18**	**3.50 ± 0.77**	**0.28 ± 0.09**	**0.74**

Overall, we obtained a good fit to all the dwarf profiles, even in cases where obvious morphological features were present. We highlight the fact that this sample presents a much richer variety of edge shapes ranging from nearly pure exponential profiles, characterized by $n \approx 1.0$ slopes and $r_i \approx 0.0$ (e.g., NGC 1569) to steeper profiles obtained for IC 2574 and NGC 4214, which resemble those found for spirals in Sect. 2.5.1. Many of the dwarfs, though present inclinations higher than 60° and based on what we have learned from analysing the models in Sect.5.3 we selected a sub–sample of five out of the eleven dwarfs of the THINGS sample: Ho I, Ho II IC 1574, M 81 DwA and NGC 4214 in order to compare their edges with those of spirals. The results for the sub–sample are in bold–face type in Table 5.3.

We plot in Fig. 5.17 the histograms for both log $I(0)$ and n parameters for dwarfs,

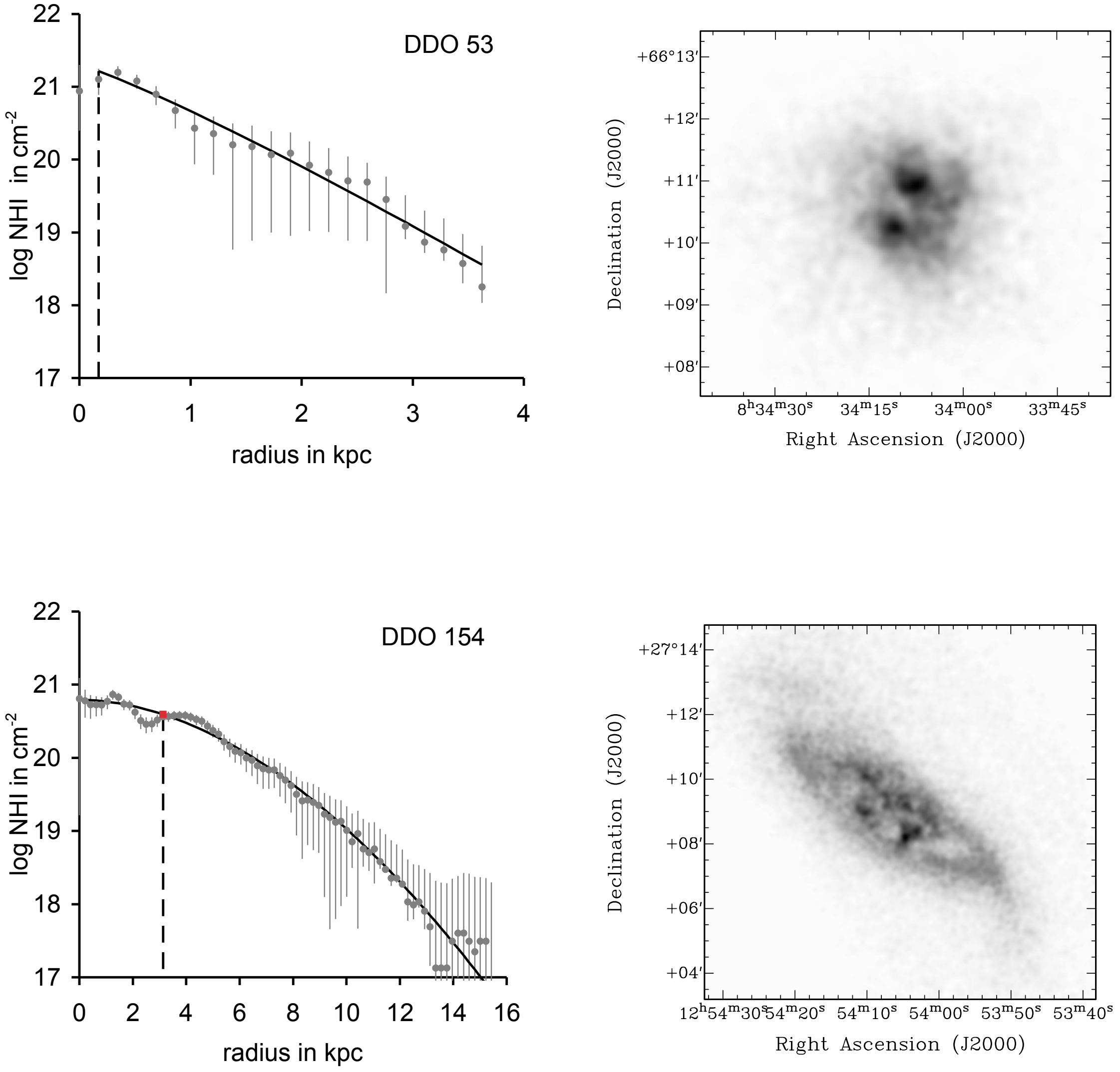

Figure 5.11: *Left panels:* The ELLINT radial profiles of DDO 53 and DDO 154, represented by grey solid dots with respective error bars. We also present the Sérsic fitted profile (solid black line) and location of r_i (dashed black vertical line). *Right panels:* the integrated H I map of DDO 53 (top) and DDO 154 (bottom) at a spatial resolution of 10″.

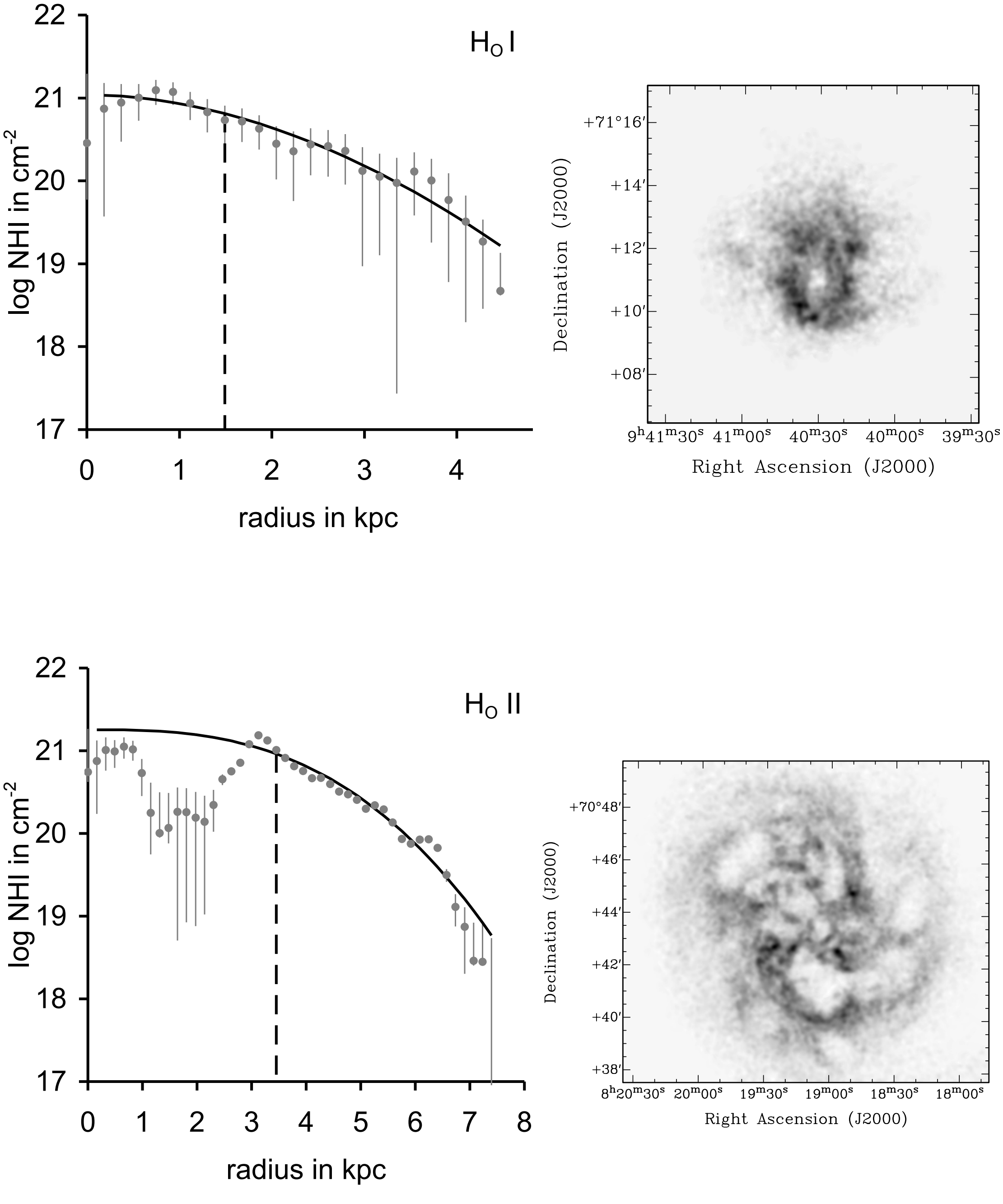

Figure 5.12: Same as Fig. 5.11 for dwarf galaxies Ho I and Ho II.

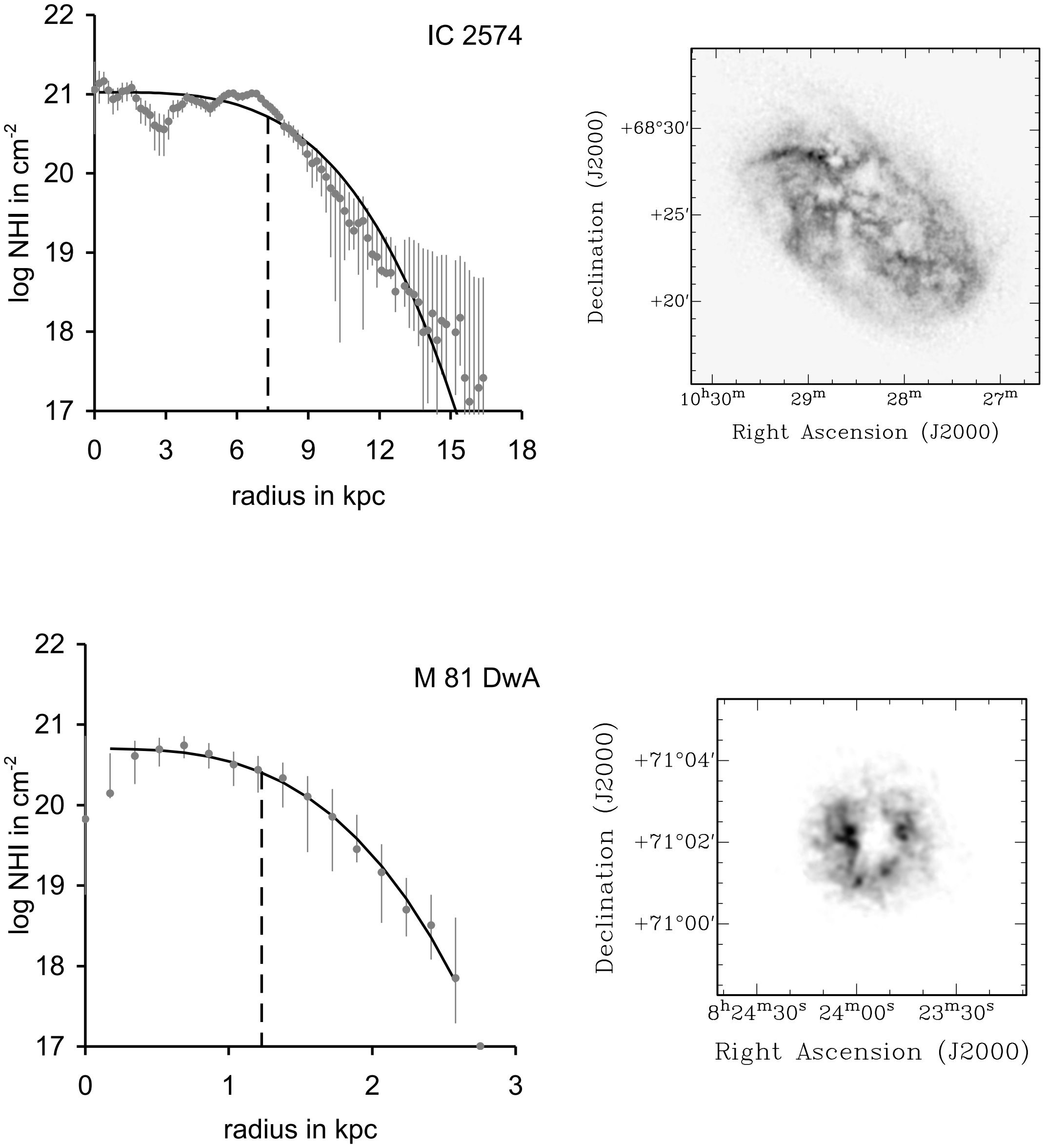

Figure 5.13: Same as Fig. 5.11 for dwarf galaxies IC 2574 and M 81 DwA.

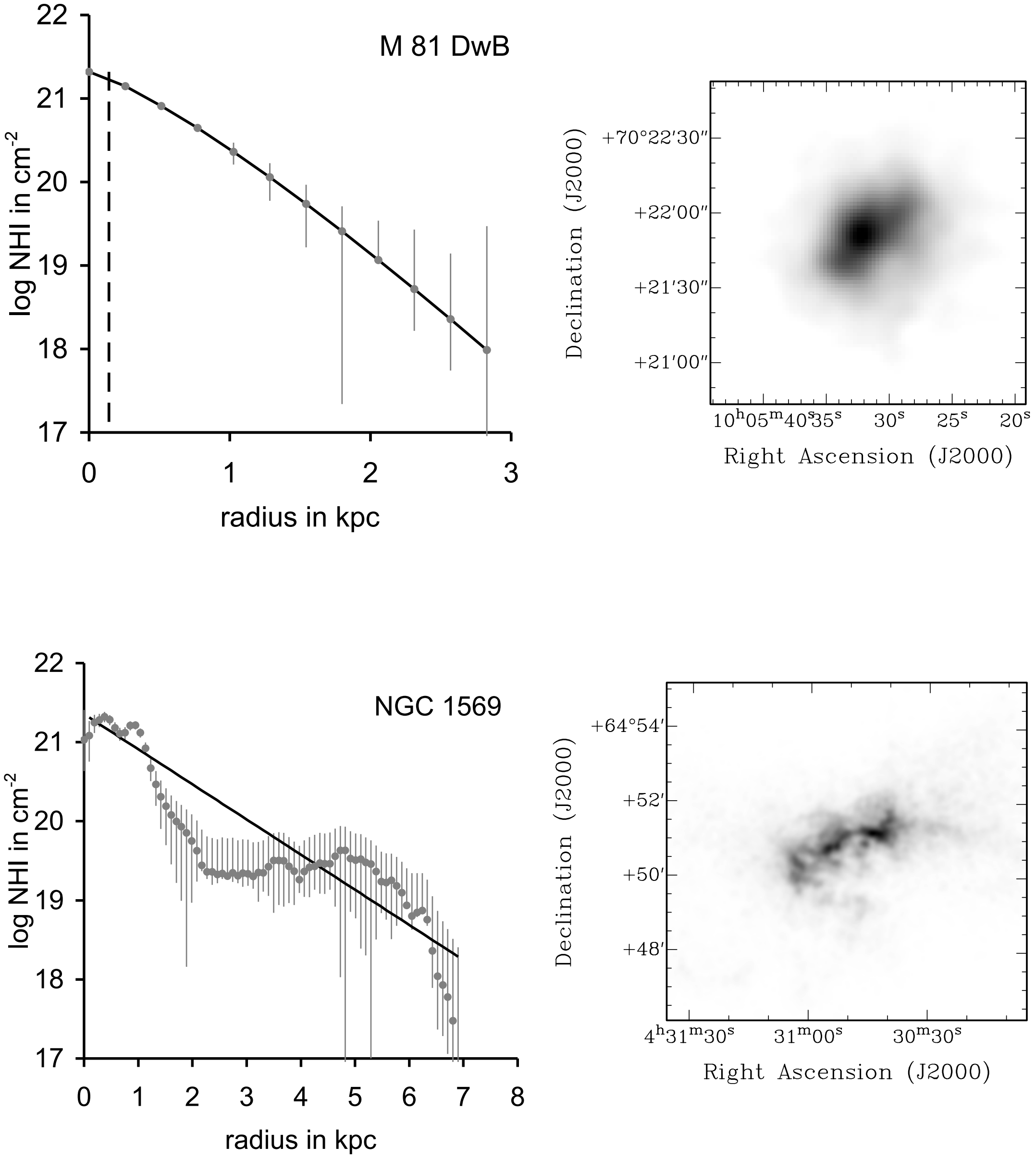

Figure 5.14: Same as Fig. 5.11 for dwarf galaxies M 81 DwB and NGC 1569.

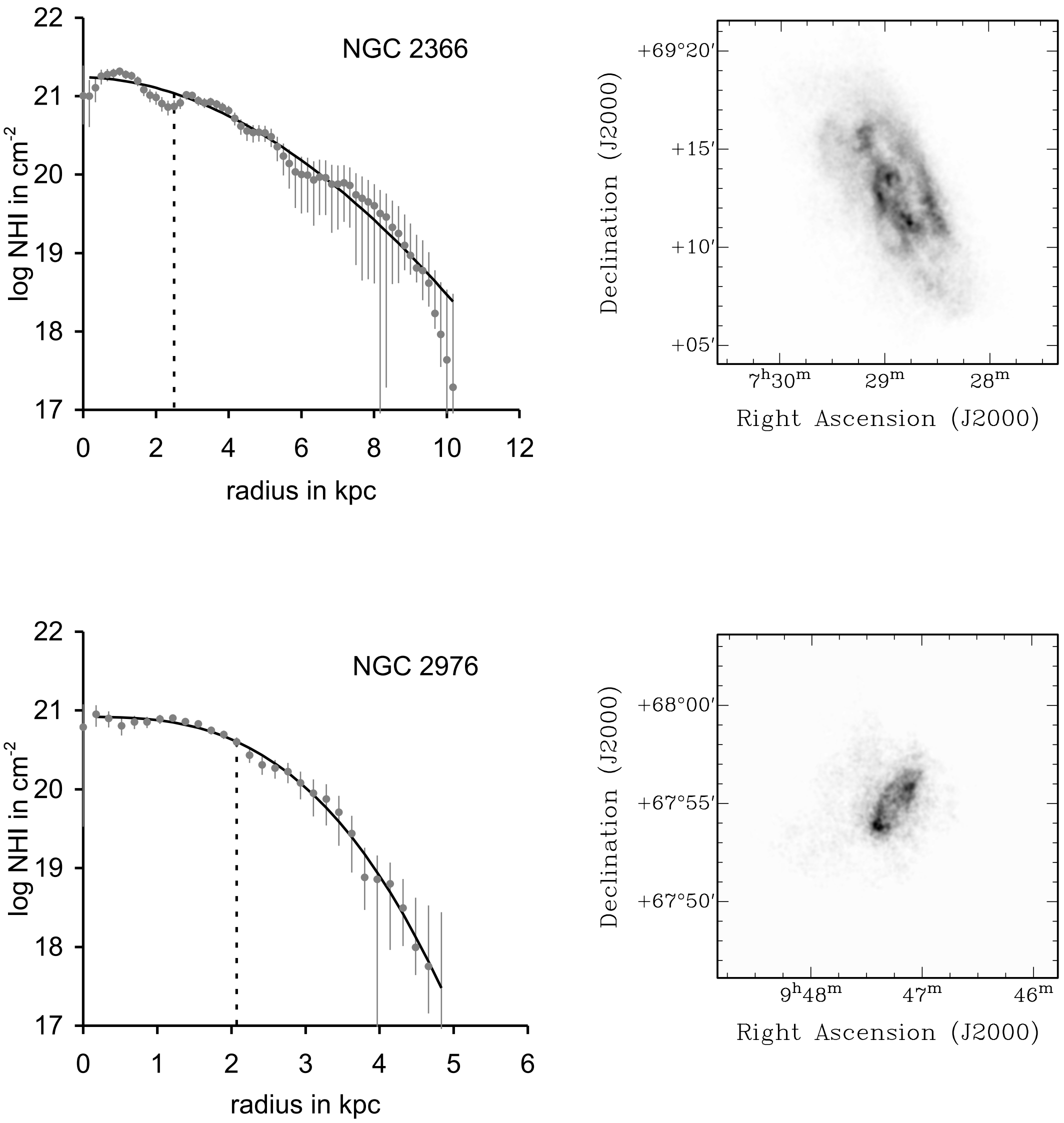

Figure 5.15: Same as Fig. 5.11 for dwarf galaxies NGC 2366 and NGC 2976.

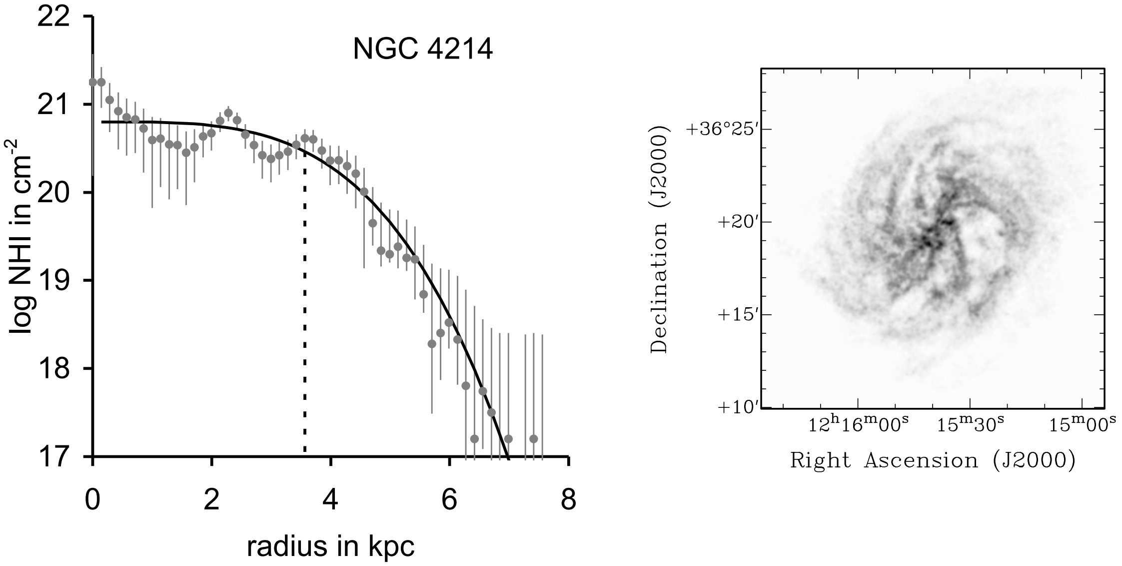

Figure 5.16: Same as Fig. 5.11 for dwarf galaxy NGC 4214.

adding to these the respective information obtained in Chapter 2 for spiral galaxies. The histograms highlight the fact that spirals and dwarfs populate different ranges of parameters and to a certain degree are complementary rather the overlapping. In relation to the slope index n, we clearly see spirals peaking around $n = 0.2$, whereas 3 out of 5 dwarfs peak at $n = 0.3$. With respect to the surface density $\log I(0)$, spirals clearly peak at $\log I(0) = 20.8$ atoms cm^{-2} while dwarfs are evenly distributed around a wider range of column densities.

5.5 Discussion and Conclusions

In a similar approach as in Chapter 2, we tested trends between fundamental characteristic of dwarf irregulars with the parameters of our Sérsic parameterisation of their H I surface density distribution. H I masses, r_{25} optical sizes, inclination, position angles and Star Formation Rate (SFR) were obtained from Walter *et al.* (2008), and Spitzer 3.6μm scale lengths, $r_{3.6}$, from Leroy *et al.* (2008). Plots of inclination and position angle against index slope n, and of SFR against r_i show no trends and are not reproduced here.

In the plots shown in Fig. 5.18 and Fig. 5.19, we revisit the 4 trends studied in Chapter 2 for spiral galaxies, and we do this by complemented the results for the dwarf sub–sample with the results obtained earlier for spirals. We plot in Fig. 5.18 (top panel) the relation between n as a function of r_i in a log–log plot for both dwarfs and spirals. A power law relation emerges between both parameters in the sense that $\log n \propto -0.33 \pm 0.05 \log r_i$. In this case both variables show a Spearman's rank correlation coefficient $\rho = -0.87; p = 9.5 \times 10^{-5}$. In other words, galaxies with larger inflection radii will follow a steeper decline when compared to smaller galaxies. Although speculative, in the limit of the smallest dwarfs the slope would then be expected to be compatible with an exponential decline, something we see in the smallest dwarfs in our sample: DDO 53 and M 81 DwB . Simulations of galaxy formation for galaxies across a range of initial masses (see Chapter 2 for details) show a similar trend, suggesting that this might be related to the depth and concentration of the potential well set by the Dark Matter halo.

In the bottom panel of Fig. 5.18 we show the relation between log M_{HI} and log r_i. This again seems to follow a power law with $\log M_{\mathrm{HI}} \propto 1.86 \log r_i$ or in other

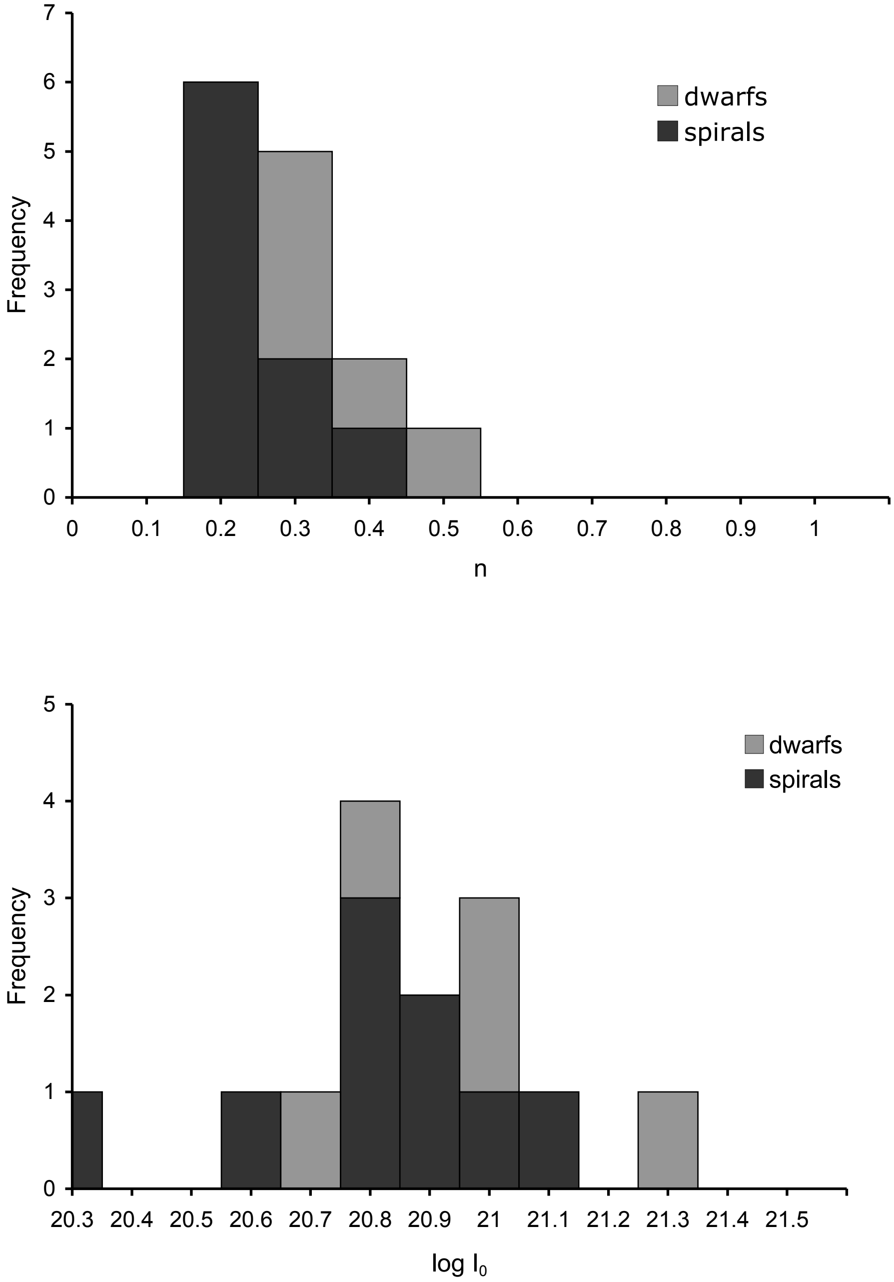

Figure 5.17: Histograms of Sérsic fitting parameters n (top panel) and log$I(0)$ for both dwarf (light grey) and spiral (dark grey) galaxies.

words, $M_{\rm HI} \propto r_i^{1.86}$. Here the correlation coeficient ρ is 0.96 with $p = 1.6 \times 10^{-7}$. It is interesting to note that if $M_{\rm HI} \propto r_i^2$, all galaxies would possess the same average H I surface density. We know from Leroy *et al.* (2008) that above a column density threshold of about $\sim 10^{21}$ atoms cm^{-2} there is a phase transition from neutral atomic to molecular gas. The relation of $M_{\rm HI}$ with r_i we find therefore indicates that if galaxies harbour a larger amount of H I (and it has not been converted to molecular gas), the gas will be spread over a larger area, i.e., a larger value for r_i.

Little can be inferred from the plot of logR_{25} as a function of the characteristic radius, r_i presented in Fig. 5.19 (top panel) as reflected by a Spearman's rank correlation coefficient $\rho = 0.5$; $p = 8.2 \times 10^{-2}$. Naively one might have expected that as r_i reflects the size of the H I disc, this would be related to the size of the optical galaxy, as claimed by (e.g. Broeils & Rhee 1997) in which the authors derive a diameter ratio between the H I and optical diameter of 1.7 ± 0.5 over a sample of 108 galaxies. We note, though, the physical ambiguity in determining R_{25} based on a magnitude threshold rather than a more meaningful stellar radial profile scale length. We therefore plot in Fig. 5.19 (bottom panel) our characteristic scale length r_i against $r_{3.6}$, the scale length of the exponential disc as derived from *Spitzer* 3.6 μm IRAC observations taken from Leroy *et al.* (2008), again in a log–log plot. In that case a power law can be fitted, approximated by $\log r_{3.6} \propto 0.58 \log r_i$. The Spearman's rank correlation coefficient between both variables is $\rho = 0.89$ with $p = 1.1 \times 10^{-4}$. Since $r_{3.6}$ can be associated to a stellar surface density (see Leroy *et al.* 2008, for further details), this might open the way to a more meaningful comparison of the relative contribution as a function of radius of the different baryonic components of a galaxy disc.

In summary, we explored the structure of the outer disk of galaxies at the small scale end, i.e., the discs of dwarf irregulars. We recognised that dwarf irregulars have thicker H I discs, both in relative as well as in absolute size as compared to larger, spiral galaxies. This implies that any line of sight probes a range of densities and z–scaleheights as it crosses the disc of a dwarf.

- In a preliminary exploration of the parameter space, and using fairly realistic parameters for the model density and scaleheight distribution of the gas, we find that for inclinations less than 60° the observed density profile closely follows the intrinsic profiles.

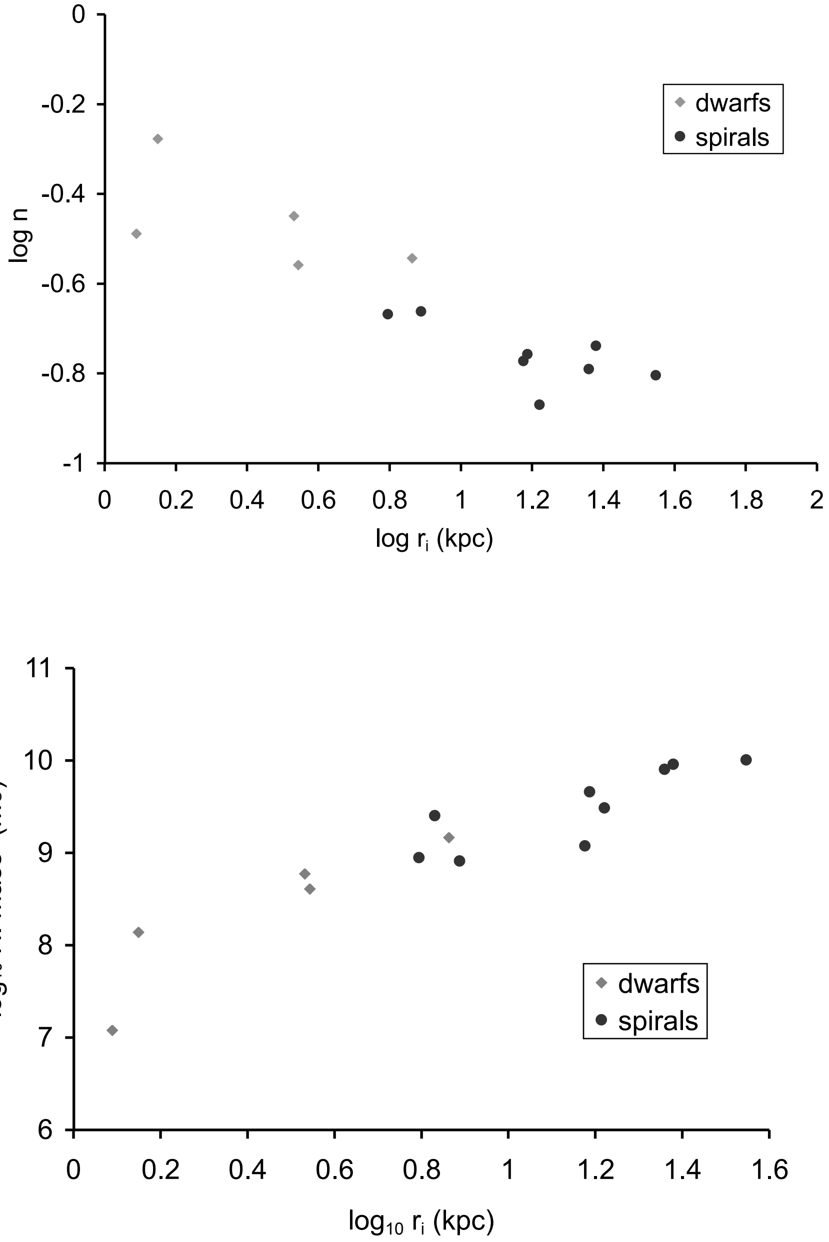

Figure 5.18: Top: log–log plot of n as a function of r_i. Bottom: log H I mass as a function of log r_i . The data pertaining to dwarf galaxies is shown in light grey diamonds whereas spiral galaxies are represented by black dots.

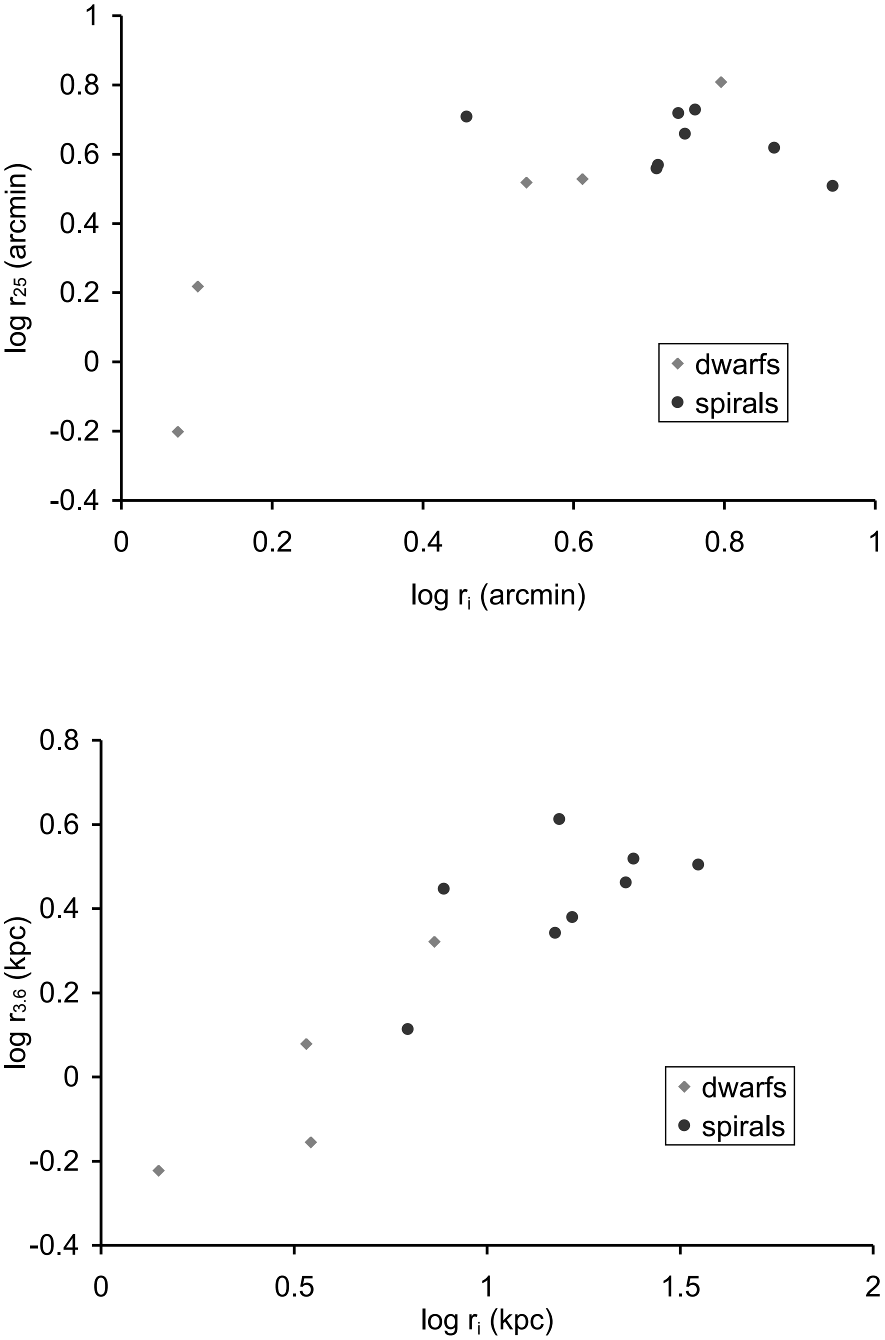

Figure 5.19: In top panel we plot of log R_{25} as a function of log r_i both in angular scales. The data pertaining to dwarf galaxies is shown in light grey diamonds whereas spiral galaxies are represented by black dots.

- For dwarfs with inclinations less than 60° there is only weak dependence on the exact dependence of scaleheight with radius, or the total extent in the z–direction.

- The discs of dwarfs show edges, like in spiral discs, but their decline is less steep, on average, and there seems to be a trend in the sense of less massive galaxies having a less steep slope.

- A higher H I content translates into a more extended disc. This relation is slightly less steep than one which would imply H I discs to have a constant surface density.

- There is no correlation of the inflection radius, r_i, with R_{25} but there is between $r_{3.6}$ and r_i, larger stellar scalelengths being linked to more extended H I disks.

Chapter 6

Conclusions

6.1 Final remarks

The project presented here has a strong observational emphasis and is based on interferometric observations of the 21–cm emission line of neutral hydrogen of a sample of galaxies of the local Universe. These observations show galaxies to be individual units, with sharply defined boundaries. Overall we focussed on what constitutes and delimits an H I disc, especially probing the distribution of neutral gas in the outer parts of spiral galaxies, and the possible influence on the neutral gas discs by an isotropic extragalactic radiation field, which was commonly assumed in the literature as a possible agent of ionisation (e.g. Sunyaev 1969; Maloney 1993). In the course of this thesis we have shown that discs most likely run out of material, as a direct consequence of galaxy formation, before any universal ionisation process sets in, at column densities below 10^{19} atoms cm^{-2}.

Our analysis made extensive use of the THINGS survey, its high spatial resolution and excellent sensitivity enabling such a study for the first time across a sizeable sample of disc galaxies. In the following we highlight the key points addressed in this thesis.

We started this project by revisiting the only previous studies based on unpublished sensitive, but low spatial resolution data on the spiral galaxy NGC 3198 (Maloney 1993). The author makes his analysis of the edge of NGC 3198, which occurs over a single beam, and therefore is unresolved. Hence the idea that at higher resolution, the edge of a galaxy could be properly probed by the THINGS survey, which has the potential to address the shortcomings of earlier observations. We also present a novel strategy to reach the best possible column density sensitivity. Rather than a simple 360° azimuthal average which, if a galaxy shows some lopsidedness will effectively average out any edge in the radial direction, we split the galaxy in 30° sectors, each of which can be fit independently and which, after applying shifts to align the outermost part of the profiles, can be averaged.

These radial profiles do exhibit strong signatures of edges in discs of spiral galaxies. However we pushed ourselves to understand if instrumental and/or observational biases could pollute our attempts to measure the true surface density distribution.

In Chapter 2, we took care to verify that no spurious edges were introduced as a result of the data reduction, since the data cubes undergo considerable processing before collapsing along the velocity axis, for example via the blanking technique used by Walter *et al.* (2008), but a comparison between radial profiles of non–blanked and blanked maps shows no evidence that blanking introduces any artefacts or truncations to the extent of the H I disc. The lack of short spacings in our interferometric data should not influence the recovery of emission up to scales as large as $7'$ as probed by the VLA. Edges occur in sub–kpc and sub–arc–minute scales and should not be affected by this effect. All this lends evidence that the edges are real features inherent to spiral galaxies.

Having convinced ourselves that the data processing does not induce any artificial edge, in Chapter 3 we addressed a different question of how closely the observed edges in the extracted radial profiles from the collapsed maps reproduce the intrinsic distribution of gas. To test this we created a collection of H I disc models using four different radial density distributions using the task GALMOD implemented in GIPSY. Model A was created with a constant density throughout its disc and a sharp truncation at its edge. Model B is characterised by an inner disc of constant gas surface density and an outer disc where the surface density decreases exponentially. We also modelled NGC 3198 and NGC 3351 as representative examples of an inclined and edge–on discs. For these two we used the radial density distribution as obtained with the task ELLINT. The 1–pixel wide ELLINT radial profiles obtained from the models were carefully compared with the input of the density distribution.

In model A we found that smoothing to a $10''$ resolution or using ELLINT with a

30° opening angle introduces some smearing at the sharp edge. The amount of beam smearing is slight and does not noticeably affect the derived surface density profile. Model B was used for more extensive testing, both in terms of investigating the effect of inclination as well as scaleheight of the gas.

In galaxies with a constant scaleheight but at different inclinations, those at high inclination ($> 75°$), i.e., nearly edge–on, produce radial profiles that significantly deviate from the input gas surface density profile. There are no significant differences between the radial profiles obtained for a disc with a constant scaleheight distribution of 1 kpc, and those which flare. We tested discs with an exponential increase in scaleheight as a function of radius and conclude that flaring has to be dramatic (e.g. model SHC in Chapter 3) and the disc in a near to edge–on orientation. But even then the 1–pixel wide profile closely follows the input profile.

In addition to creating simplified density distributions, we tested if more realistic looking models would behave like the simple ones. We used for this the galaxies NGC 3198 and NGC 3351, the former being highly inclined and the latter a more face–on object. We again found that gas surface density profiles extracted using the same methodology as in Chapter 2, where we analysed the observations, closely match the input model density distributions.

In Chapter 2, we averaged 8 segments, each 30° wide, in order to increase the signal to noise at the galaxy edge. We therefore checked if there was any dependence on azimuth of the segments but found little variation between them (as in Chapter 2, sectors near the semi–minor axis were excluded as projection effects and line–of–sight blending can become substantial).

This led us to the conclusion that, with the exception of nearly edge–on galaxies, the observed surface density profiles are a faithful rendering of the intrinsic density distributions and that any line–of–sight blending or beam smearing can largely be ignored.

Another fundamental aspect of this work was the characterisation of the radial profiles which exhibit a rapid decline of neutral hydrogen at the peripheries of discs. A preliminary attempt to fit a broken exponential revealed to be unsatisfactory. Using a three–parameter Sérsic–like fit to the H I surface density distribution as a function of radius provided a surprisingly good parameterisation. The parameters which we fitted were: the central neutral hydrogen column density, $I(0)$, a characteristic radius

r_i which is where the profile has its steepest decline, and a slope index n.

We found that the slope index n for 8 out of the 9 objects in our sample presented a very narrow range of values, 0.14 to 0.22, which implies that the radial column density profiles decline in a similar manner, irrespective of Hubble type or galaxy size. Scaling the profiles by their corresponding r_i shows 8 out of 9 discs extending up to $\approx 1.35\ r_i$. In both cases the exception is the galaxy NGC 5194 (M 51) which is obviously interacting with NGC 5195 which explains why this galaxy does not fit the mould.

Definitions to measure the extent of the neutral, atomic gas discs, still lack general consensus, and many are the ones linked with limitations of the instruments or that a surface brightness threshold rather than are based on intrinsic property of the galaxies under study. We believe that the H I extent should be based on a measurement of some characteristic scalelength such as a characteristic radius, r_i found in our Sérsic–type fit. Based on our results we proposed a new definition for a neutral hydrogen radius, R_{HI}, which we set at a level of 5×10^{19} atoms cm^{-2} . Short of doing a Sérsic–type fit to a galaxy and agreeing on, e.g., measuring the extent at $1.2r_i$, this level of 5×10^{19} atoms cm^{-2} will for most galaxies give an extent which is in the range $1.1 - 1.3r_i$. This surface brightness threshold is easily reached by current interferometric arrays.

Finally, we recognised three radial column density regions, an inner region with almost constant H I column density, a transition region around r_i where the H I rapidly decreases, followed by a precipitous drop near $1.3r_i$. As we argued in Chapter 2, the initial decrease beyond r_i is difficult to reconcile with ionisation as the column densities are still high and well above the critical column density introduced by Maloney (1993). If ionized, a column density of $\sim 10^{20}$ atoms cm^{-2} would produce a healthy Hα emission measure (EM) and the required flux of an extragalactic radiation field would far exceed any reasonable value for the extragalactic flux. In addition a relevant question raised by (Oosterloo *et al.* 2007a) whilst studying NGC 891 is why would an isotropic radiation field preferentially act in the plane of the disc of this edge–on galaxies be oblivious of the low density gas in the halo region, since recent and deep H I images did not increase the disc size of this object but only the amount of gas present in its halo. We conjectured that the H I distribution might be set by other factors which are related to how Dark Matter haloes acquired their baryonic components in the first place. If ionisation plays a rôle, it must be restricted to the outermost reaches of galaxies, once the column density has dropped below a few $\times 10^{19}$ atoms cm^{-2} .

Having convinced ourselves that the HI edges are due to a genuine decrease of matter, and not due to a phase transition in this matter, and that they arise as a natural consequence of galaxy formation as a result of baryonic matter accumulating within a dark matter dominated gravitational potential, we decided to put this hypothesis to the test by extending our study to more extreme galaxy types and ask ourselves: What happens to edges in a broader range of disc sizes? Are they still present? Do they decline in a steeper or shallower fashion than the ones seen in spirals? To shed light on this matter we analysed an H I rich giant Low Surface Brightness galaxy. We presented a set of multi–wavelength observations of NGC 765 in Chapter 4.

NGC 765 sports a large H I disc, 240 kpc in diameter for an assumed distance of 72 Mpc. This is one of the largest H I discs reported for a late–type galaxy and makes it unique. Assuming an optical scale length of 7.8 kpc, NGC 765 presents an H I–to–optical ratio of 15. This is considerably larger than what has been found in other giant LSBs such as Malin 1, the prototypical 'crouching giant' galaxy.

We found the H I disc morphology of NGC 765 clearly presented two different regimes: an inner H I disc (< 50 kpc) tracing the spiral structure with the presence of at least three arms, and an outer, lower surface brightness plateau. This latter region is populated by several H I gas clumps of compact morphology. The galaxy has two nearby companions: NGC 765a, a previously uncatalogued companion, towards the Northeast. Towards the South we have UGC 1453, an irregular galaxy. We report the detection of a faint optical counterpart for NGC 765a. The outer disc of NGC 765 is slightly warped. It is populated with compact H I regions with sizes of ~ 10 kpc and H I masses of $\sim 10^8 \mathcal{M}_\odot$. These are possibly remnants of past mergers events.

We also detect 1.4 GHz radio–continuum emission from the NGC 765 optical core. This emission is weak, with a flux density of 2.16 mJy and a luminosity of $L_{1.4\,\mathrm{GHz}} = 1.3 \times 10^{21}$ W Hz^{-1}. No radio continuum emission is found related to the stellar or H I disc. *Chandra* X–ray data reveal emission coincident with the galaxy nucleus. We derive a luminosity of $L_X(0.2\text{–}10\ \mathrm{keV}) \approx 1.7 \times 10^{40}$ erg s^{-1}. The radio and X–ray emission is compatible with the nucleus being powered by a weak AGN, as also suggested by its optical nuclear emission lines.

Star formation activity in NGC 765 is low, with no star formation detected in the outer disc, suggesting the gas is well below the threshold for star formation. The combination of a lopsided H I distribution and the presence of substructure in the disk combined with modest linear resolution precludes us making any strong statements on the shape of the edge of the outer H I disk. However, observing time for higher resolution observations with the VLA has been granted.

After having explored the outer disc of a true giant, Malin 1 cousin, we next turned our attention to dwarfs. We explored the structure of the outer disk of dwarf irregulars. We recognised that dwarf irregulars resemble a small–scale, less organised and thicker version of what constitutes a spiral disc. This implies that any line of sight probes a range of densities and z–scaleheights as it crosses the disc of a dwarf. In a preliminary exploration of the parameter space, we created an ensemble of GALMOD models for NGC 2366 using fairly realistic parameters for the model density and scaleheight distribution of the gas. We found that for inclinations less than 60° the observed density profile closely follows the intrinsic profiles. The Sérsic–like parameterisation fitting results reveal dwarfs to have discs with an average central column density evenly distributed around a range of column densities ($\log_{10}$ NH I $=$ 20.7 atoms cm^{-2}) to $\log_{10}$ NH I $= 21.3$ atoms cm^{-2}, which decline in shallower fashion (slope index peak around $n \approx 0.3$) in relation to spirals. Using both spiral and dwarf sub–sample data, our results also suggest that a higher H I content translates into a more extended disc. There is no correlation of the inflection radius, r_i, with R_{25} but there is between $r_{3.6}$ and r_i, larger stellar scalelengths being linked to more extended H I disks. Although preliminary, we felt compelled to include this analysis since literature work on this matter is fully lacking, and we see this brief approach as a first step towards a better and perhaps more accurate view of neutral gas in the outskirts of dwarf galaxies.

In summary, the neutral hydrogen discs content of a sample of local spiral and dwarf galaxies analysed in this work, exhibit signatures of edges at their outskirts. These edges can be parameterised and are an intrinsic property of galaxies and probably are related to the formation and evolution of this class of objects rather than to ionisation by an external radiation field.

6.2 Future work

The results found in this thesis have clarified several aspects of the edges of H I discs across a sizeable range of objects. In the following we explore different follow–up plans related to the current project.

With respect to the edges of spirals, two major aspects are yet to be explored. The first we would like to emphasize is that the THINGS project has been successful in demonstrating the advantages of a sample of the local Universe observed at a common high resolution. However, the number of isolated spirals is quite modest and any attempt to statistically support some of the results here shown would be of great benefit, e.g. if a larger number of candidates would become available.

The next generation of interferometric arrays such as the Karoo Array Telescope (MeerKAT) or the Square Kilometre Array (SKA) will be able to explore to deeper levels the Universe in the 21–cm emission regime. More specifically the MeerKat H I Observations of Nearby Galactic Objects: Observing Southern Emitters (hereafter, MHONGOOSE; P.I. de Blok), aims to map the neutral hydrogen distribution of a diverse sample of 301 nearby galaxies, over five orders of magnitude in H I mass and column density, within a local volume of D $<$ 20 Mpc. We see in this project a window of opportunity to enlarge the number of local isolated galaxies where the edge analysis could be performed.

Perhaps, more important than to study more objects is to go deeper in observations, exploring the realms of extended outer components of the H I discs of galaxies. We revisited one of the premisses of this thesis: the extent of an H I disc. At the current instrumental limits of our observations ($\log_{10}(\mathrm{NHI}) = 10^{18}$ atoms cm^{-2}) galaxies present edges and present themselves as isolated entities. What remains to be proven is how they relate to the faint and mainly ionised Cosmic Web, since little is known about the transitional column density desert from mainly neutral outskirts of galaxies to mainly ionised gas filaments which build up the Cosmic Web. We do know that deep observations will reveal more of the halo structure of the galaxies, as shown by (Fraternali *et al.* 2001) and (Oosterloo *et al.* 2007a), as well as larger diffuse areas surrounding galaxies (Braun & Thilker 2004; Popping *et al.* 2009). Will the shape of current edges change when pushing towards these lower levels ? Are they sharper, or will they instead decline in a much more shallow fashion blending into the Cosmic

Web? To tackle this matter again we have great expectations of MHONGOOSE. The project aims to obtain very deep observations of a subsample of 30 galaxies probing the edges down to column densities of $\sim 5 \times 10^{17}$ atoms cm^{-2}. This will be deep enough to dive into the faint regime of the gas halos of galaxies, the interlinking structures forming the Cosmic Web and be sensitive enough to trace gas accretion phenomena (cold accretion). Going to lower levels will also shed light on the ionisation mechanism thought to shape the edges of galaxies (Maloney 1993; Dove & Shull 1994a). As shown here, this should only become prominent below $\log_{10}(\mathrm{NHI}) = 10^{18}$ atoms cm^{-2}. Related to this, we would wish to compare the observational results presented here for edges of spiral discs with state–of–the–art cosmological disc simulations which accurately determine the H I properties at z$\sim$ 0. Stellar disc properties are commonly the main focus of a broad range of simulations, whereas little attention has been given to the gaseous component. To tackle this matter we will run the same edge analysis and parameterisation here shown on a small sample of five H I disc simulations created by our collaborators (Sommer–Larsen, priv. comm.).

With respect to the LSB giant, NGC 765, observing time for higher resolution observations with the VLA C–array has been granted and will be used for a follow–up paper. As shown, the D–array data on NGC 765 at the current resolution of $\sim$ 15 kpc is woefully inadequate, leaving the edge unresolved, hence the desired $\sim 5''$ data for 10 times higher resolution, providing valuable insight in to the distribution and interaction of baryonic matter on large scales with a dark matter halo. This eventually will call for B–array observations.

The high resolution data will help answer the following questions: How can such large H I structures be assembled and survive, the H I in the outer disk being far more weakly bound to the optical galaxy than gas closer to the centre? Can we associate the outer highly asymmetric disk with accretion or is it distorted due to tidal interaction, either with its companions or at some time in the past? Or should the outer disk be considered as tidal debris that is re–accreting? Is this enormous disk a reservoir for future star formation? If so, is there an H I column density threshold that explains why there are hardly any stars beyond the central H I depression whereas the H I column density appears to be sufficient for star formation as compared to that found in a range of nearby galaxies taken from THINGS?

In addition to a detailed study of NGC 765 we will also study the dynamics and morphology of the two dwarf galaxies and look for traces of tidal interaction.

We also would like to observe the CO content of this giant disk to make an inventory of the molecular gas thought to be present at the H I –poor centre of the galaxy which is occupied by the bar and to trace a radial profile through the optical disk, to sample the very outer extended H I disk, and to probe the CO content of one of the compact H I regions in the outer disk.

As mentioned in Chapter 4, the inner disk is only slightly underluminous and shows clear spiral arms, where one finds associated star formation, as evidenced in Fig. 4.11 which shows a GALEX UV image of NGC 765. The H I column density lies consistently above the critical threshold for H_2 and star formation of $\sim 3 \times 10^{20}$ atoms cm^{-2} proposed by Schaye (2004). Hence, we again would expect CO to be present. This is also based on our experience in nearby galaxies where Leroy *et al.* (2008) and Bigiel *et al.* (2008) find that in the H_2 dominated inner regions of spirals a single power law with an index of 1.0 ± 0.2 relates the SFR density to the molecular gas surface density and that in turn high molecular gas surface densities are linked to high mass surface densities, provided by the stars in the disk. It is in the outer LSB stellar disk and low surface density H I in the outskirts that it becomes really interesting. H I is in plentiful supply there, but it has to undergo a phase change to molecular gas, H_2, traced by other molecules, such as CO, in order to eventually be turned into stars. Various mechanisms have been proposed (Robertson & Kravtsov 2008; Gnedin *et al.* 2009; Krumholz *et al.* 2009, and references therein) to explain SF in this environment, where it is patchy and restricted in part by stochastic processes, creating locally conditions which fulfil the necessary and sufficient conditions for SF.

The exploratory results obtained for the dwarfs in this thesis will serve as foundation for a follow–up analysis. In this context we propose to create a collection of models based on NGC 2366, using the radial density distribution from model 2. This radial distribution resembles more the intrinsic distribution of such a dwarf and would help to reveal line–of–sight column density measurement biases raised by disc inclination and H I vertical structures. Moreover we also should look at the z–distribution of the gas not only in terms of exploring different densities but also in terms of other vertical layer geometries.

The recently started Local Irregular That Trace Local Extremes (LITTLE) THINGS project (Hunter *et al.* 2007), will boost the amount of H I data available on local dwarf irregular (dIm) galaxies, addressing fundamental questions pertaining to gas dynamics and star formation. Although dwarf galaxies are seen as one of the simplest structures of the Universe, little is known about the process that triggers and regulates star formation in their discs. LITTLE THINGS will compile a multi–wavelength database for a sample of dwarf irregular galaxies in the local Universe. The project focuses on the low mass end of dwarfs and presents a larger mass range which can potentially translate into a more complete study of mass models which are in turn linked to a more diversified sample of rotation curves. LITTLE THINGS H I data are obtained with the VLA both from archive and new observations. Its spatial and velocity resolutions match or in some cases exceed that of the data of the THINGS sample. In this regard, we feel that many of the issues raised in this project could easily migrate to LITTLE THINGS, opening a window of opportunity for a follow–up study on the physical properties of neutral hydrogen at the peripheries of dwarf discs.

Looking deeper and farther, the SKA will hopefully reignite the debate around the presence of an universal extragalactic ionisation agent, as well as addressing the distribution of neutral hydrogen associated with the large-scale structure of the Universe, tackling some of the questions raised at the beginning of the thesis concerning the cosmological filamentary structure of the Cosmic Web.

Bibliography

Bagetakos, I., Brinks, E., de Blok, W. J. G., Usero, A., Leroy, A. Rick, A. K., & Kennicutt, R. C. (2010). *Submitted to The Astronomical Journal.*

Banerjee, A., Bagetakos, I., & Jog, C. B. (2010). *In preparation.*

Banerjee, A. & Jog, C. J. (2008). *The Astrophysical Journal,* **685**, 254–260.

Banerjee, A., Matthews, L. D., & Jog, C. J. (2010). *New Astronomy,* **15**, 89–95.

Barth, A. J. (2007). *The Astronomical Journal,* **133**, 1085–1091.

Becker, R. H., White, R. L., & Helfand, D. J. (1995). *The Astrophysical Journal,* **450**, 559.

Begeman, K. G. (1987). PhD thesis Rijksuniversiteit Groningen, (1987).

Begeman, K. G. (1989). *Astronomy and Astrophysics,* **223**, 47–60.

Bennett, C. L., Bay, M., Halpern, M., Hinshaw, G., Jackson, C., Jarosik, N., Kogut, A., Limon, M., Meyer, S. S., Page, L., Spergel, D. N., Tucker, G. S., Wilkinson, D. T., Wollack, E., & Wright, E. L. (2003). *The Astrophysical Journal,* **583**, 1–23.

Bigiel, F., Leroy, A., Walter, F., Brinks, E., de Blok, W. J. G., Madore, B., & Thornley, M. D. (2008). *The Astronomical Journal,* **136**, 2846–2871.

Bland-Hawthorn, J. & Maloney, P. R. (1999). *The Astrophysical Journal,* **510**, L33–L36.

Boomsma, R., Oosterloo, T. A., Fraternali, F., van der Hulst, J. M., & Sancisi, R. (2008). *Astronomy and Astrophysics,* **490**, 555–570.

Bosma, A. (1981). *The Astronomical Journal,* **86**, 1825–1846.

Bothun, G., Impey, C., & McGaugh, S. (1997). *Publications of the Astronomical Society of the Pacific,* **109**, 745–758.

Bothun, G. D., Impey, C. D., Malin, D. F., & Mould, J. R. (1987). *The Astronomical Journal,* **94**, 23–29.

Bothun, G. D., Schombert, J. M., Impey, C. D., & Schneider, S. E. (1990). *The Astrophysical Journal,* **360**, 427–435.

Bournaud, F., Combes, F., Jog, C. J., & Puerari, I. (2005). *Astronomy and Astrophysics,* **438**, 507–520.

Bournaud, F., Elmegreen, B. G., & Elmegreen, D. M. (2007). *The Astrophysical Journal,* **670**, 237–248.

Braun, R., Thilker, D., & Walterbos, R. A. M. (2003). *Astronomy and Astrophysics,* **406**, 829–846.

Braun, R. & Thilker, D. A. (2004). *Astronomy and Astrophysics,* **417**, 421–435.

Braun, R. & Thilker, D. A. (2005). In: *Extra-Planar Gas*, (ed, Braun, R.). *Astronomical Society of the Pacific Conference Series,* **331**, 121.

Brinks, E. & Shane, W. W. (1984). *Astronomy and Astrophysics Supplement Series,* **55**, 179–251.

Brinks, E., Walter, F., & Ott, J. (2002). In: *Disks of Galaxies: Kinematics, Dynamics and Perturbations*, (ed, E. Athanassoula, A. Bosma, & R. Mujica). *Astronomical Society of the Pacific Conference Series*, **275**, 57–60.

Broeils, A. H. & Rhee, M.-H. (1997). *Astronomy and Astrophysics,* **324**, 877–887.

Chung, A., van Gorkom, J. H., Kenney, J. D. P., & Vollmer, B. (2007). *The Astrophysical Journal,* **659**, L115–L119.

Combes, F. & Pfenniger, D. (1997). *Astronomy and Astrophysics,* **327**, 453–466.

Condon, J. J., Cotton, W. D., Greisen, E. W., Yin, Q. F., Perley, R. A., Taylor, G. B., & Broderick, J. J. (1998). *The Astronomical Journal,* **115**, 1693–1716.

Corbelli, E., Schneider, S. E., & Salpeter, E. E. (1989). *The Astronomical Journal,* **97**, 390–404.

Dalcanton, J. J., Spergel, D. N., & Summers, F. J. (1997). *The Astrophysical Journal,* **482**, 659.

Das, M., Reynolds, C. S., Vogel, S. N., McGaugh, S. S., & Kantharia, N. G. (2009). *The Astrophysical Journal,* **693**, 1300–1305.

Davé, R., Hernquist, L., Katz, N., & Weinberg, D. H. (1999). *The Astrophysical Journal,* **511**, 521–545.

Davies, J. I., Phillipps, S., & Disney, M. J. (1988). *Monthly Notices of the Royal Astronomical Society,* **231**, 69.

de Blok, W. J. G., Walter, F., Brinks, E., Trachternach, C., Oh, S., & Kennicutt, R. C. (2008). *The Astronomical Journal,* **136**, 2648–2719.

de Jong, R. S. (1996). *Astronomy and Astrophysics, Supplement,* **118**, 557–573.

de Jong, R. S. & van der Kruit, P. C. (1994). *Astronomy and Astrophysics Supplement Series,* **106**, 451–504.

de Vaucouleurs, G., de Vaucouleurs, A., Corwin, Jr., H. G., Buta, R. J., Paturel, G., & Fouque, P. (1991). *Third Reference Catalogue of Bright Galaxies.* Springer-Verlag.

Desroches, L.-B. & Ho, L. C. (2009). *The Astrophysical Journal,* **690**, 267–278.

Devereux, N. A., Kenney, J. D., & Young, J. S. (1992). *The Astronomical Journal,* **103**, 784–792.

Disney, M. & Phillipps, S. (1987). *Nature,* **329**, 203.

Dove, J. B. & Shull, J. M. (1994a). *The Astrophysical Journal,* **423**, 196–206.

Dove, J. B. & Shull, J. M. (1994b). *The Astrophysical Journal,* **430**, 222–235.

Elmegreen, D. M., Elmegreen, B. G., Marcus, M. T., Shahinyan, K., Yau, A., & Petersen, M. (2009). *The Astrophysical Journal,* **701**, 306–329.

Erwin, P. (2005). *Monthly Notices of the Royal Astronomical Society,* **364**, 283–302.

Fall, S. M. & Efstathiou, G. (1980). *Monthly Notices of the Royal Astronomical Society,* **193**, 189–206.

Ferrara, A. & Tolstoy, E. (2000). *Monthly Notices of the Royal Astronomical Society,* **313**, 291–309.

Filho, M. E., Barthel, P. D., & Ho, L. C. (2006). *Astronomy and Astrophysics,* **451**, 71–83.

Fraternali, F. & Binney, J. J. (2006). *Monthly Notices of the Royal Astronomical Society,* **366**, 449–466.

Fraternali, F., Oosterloo, T., Sancisi, R., & van Moorsel, G. (2001). *The Astrophysical Journal,* **562**, L47–L50.

Freeman, K. C. (1970). *The Astrophysical Journal,* **160**, 811.

Garcia, A. M. (1993). *Astronomy Astrophysics Supplement,* **100**, 47–90.

Giavalisco, M., Ferguson, H. C., Koekemoer, A. M., Dickinson, M., Alexander, D. M., Bauer, F. E., Bergeron, J., Biagetti, C., Brandt, W. N., Casertano, S., Cesarsky, C., Chatzichristou, E., Conselice, C., Cristiani, S., Da Costa, L., Dahlen, T., de Mello, D., Eisenhardt, P., Erben, T., Fall, S. M., Fassnacht, C., Fosbury, R., Fruchter, A., Gardner, J. P., Grogin, N., Hook, R. N., Hornschemeier, A. E., Idzi, R., Jogee, S., Kretchmer, C., Laidler, V., Lee, K. S., Livio, M., Lucas, R., Madau, P., Mobasher, B., Moustakas, L. A., Nonino, M., Padovani, P., Papovich, C., Park, Y., Ravindranath, S., Renzini, A., Richardson, M., Riess, A., Rosati, P., Schirmer, M., Schreier, E., Somerville, R. S., Spinrad, H., Stern, D., Stiavelli, M., Strolger, L., Urry, C. M., Vandame, B., Williams, R., & Wolf, C. (2004). *The Astrophysical Journal,* **600**, L93–L98.

Giovanelli, R., Myers, S. T., Roth, J., & Haynes, M. P. (1986). *The Astronomical Journal,* **92**, 250–274.

Gnedin, N. Y., Tassis, K., & Kravtsov, A. V. (2009). *The Astrophysical Journal,* **697**, 55–67.

Governato, F., Brook, C., Mayer, L., Brooks, A., Rhee, G., Wadsley, J., Jonsson, P., Willman, B., Stinson, G., Quinn, T., & Madau, P. (2010). *Nature,* **463**, 203–206.

Governato, F., Mayer, L., Wadsley, J., Gardner, J. P., Willman, B., Hayashi, E., Quinn, T., Stadel, J., & Lake, G. (2004). *The Astrophysical Journal,* **607**, 688–696.

Governato, F., Willman, B., Mayer, L., Brooks, A., Stinson, G., Valenzuela, O., Wadsley, J., & Quinn, T. (2007). *Monthly Notices of the Royal Astronomical Society,* **374**, 1479–1494.

Graham, A. W. (2001). *The Astronomical Journal,* **121**, 820–840.

Greisen, E. W., Spekkens, K., & van Moorsel, G. A. (2009). *The Astronomical Journal,* **137**, 4718–4733.

Haynes, M. P., van Zee, L., Hogg, D. E., Roberts, M. S., & Maddalena, R. J. (1998). *The Astronomical Journal,* **115**, 62.

Hess, K. M., Pisano, D. J., Wilcots, E. M., & Chengalur, J. N. (2009). *The Astrophysical Journal,* **699**, 76–88.

Hinshaw, G., Weiland, J. L., Hill, R. S., Odegard, N., Larson, D., Bennett, C. L., Dunkley, J., Gold, B., Greason, M. R., Jarosik, N., Komatsu, E., Nolta, M. R., Page, L., Spergel, D. N., Wollack, E., Halpern, M., Kogut, A., Limon, M., Meyer, S. S., Tucker, G. S., & Wright, E. L. (2009). *The Astrophysical Journal Supplement Series,* **180**, 225–245.

Ho, L. C., Feigelson, E. D., Townsley, L. K., Sambruna, R. M., Garmire, G. P., Brandt, W. N., Filippenko, A. V., Griffiths, R. E., Ptak, A. F., & Sargent, W. L. W. (2001). *The Astrophysical Journal,* **549**, L51–L54.

Ho, L. C., Filippenko, A. V., & Sargent, W. L. W. (1997). *Astrophysical Journal Supplement,* **112**.

Hoffman, Y., Silk, J., & Wyse, R. F. G. (1992). *The Astrophysical Journal,* **388**, L13–L17.

Hunter, D. A., Brinks, E., Elmegreen, B., Rupen, M., Simpson, C., Walter, F., Westpfahl, D., & Young, L. (2007). In: *Bulletin of the American Astronomical Society***38**, 895.

Ibata, R. A., Gilmore, G., & Irwin, M. J. (1994). *Nature,* **370**, 194.

Ibata, R. A. & Razoumov, A. O. (1998). *Astronomy and Astrophysics,* **336**, 130–136.

Impey, C. & Bothun, G. (1989). *The Astrophysical Journal,* **341**, 89–104.

Impey, C. & Bothun, G. (1997). *Annual Review of Astronomy and Astrophysics,* **35**, 267–307.

Kalberla, P. M. W., Burton, W. B., Hartmann, D., Arnal, E. M., Bajaja, E., Morras, R., & Pöppel, W. G. L. (2005). *Astronomy and Astrophysics,* **440**, 775–782.

Kalberla, P. M. W. & Dedes, L. (2008). *Astronomy and Astrophysics,* **487**, 951–963.

Kennicutt, Jr., R. C., Armus, L., Bendo, G., Calzetti, D., Dale, D. A., Draine, B. T., Engelbracht, C. W., Gordon, K. D., Grauer, A. D., Helou, G., Hollenbach, D. J., Jarrett, T. H., Kewley, L. J., Leitherer, C., Li, A., Malhotra, S., Regan, M. W., Rieke, G. H., Rieke, M. J., Roussel, H., Smith, J.-D. T., Thornley, M. D., & Walter, F. (2003). *Publications of the Astronomical Society of the Pacific,* **115**, 928–952.

Krumholz, M. R., McKee, C. F., & Tumlinson, J. (2009). *The Astrophysical Journal,* **699**, 850–856.

Leroy, A. K., Walter, F., Bigiel, F., Usero, A., Weiss, A., Brinks, E., de Blok, W. J. G., Kennicutt, R. C., Schuster, K., Kramer, C., Wiesemeyer, H. W., & Roussel, H. (2009). *The Astronomical Journal,* **137**, 4670–4696.

Leroy, A. K., Walter, F., Brinks, E., Bigiel, F., de Blok, W. J. G., Madore, B., & Thornley, M. D. (2008). *The Astronomical Journal,* **136**, 2782–2845.

Linder, S. M., Gunesch, R., Davies, J. I., Baes, M., Evans, R., Roberts, S., Sabatini, S., & Smith, R. (2003). *Monthly Notice of the Royal Astronomical Society,* **342**, 1093–1101.

Maloney, P. (1993). *The Astrophysical Journal,* **414**, 41–56.

Mapelli, M., Moore, B., Giordano, L., Mayer, L., Colpi, M., Ripamonti, E., & Callegari, S. (2008). *Monthly Notices of the Royal Astronomical Society,* **383**, 230–246.

Martínez-Delgado, D., Aparicio, A., Gómez-Flechoso, M. Á., & Carrera, R. (2001). *The Astrophysical Journal,* **549**, L199–L202.

Mashchenko, S., Wadsley, J., & Couchman, H. M. P. (2008). *Science,* **319**, 174.

McGaugh, S. S. & de Blok, W. J. G. (1997). *The Astrophysical Journal,* **481**, 689.

Mihos, J. C., Spaans, M., & McGaugh, S. S. (1999). *The Astrophysical Journal,* **515**, 89–96.

Morganti, R., Sadler, E. M., Oosterloo, T., Pizzella, A., & Bertola, F. (1997). *The Astronomical Journal,* **113**, 937–949.

Nakanishi, H. & Sofue, Y. (2003). *Publications of the Astronomical Society of Japan,* **55**, 191–202.

Narayan, C. A., Saha, K., & Jog, C. J. (2005). *Astronomy and Astrophysics,* **440**, 523–530.

Navarro, J. F., Frenk, C. S., & White, S. D. M. (1995). *Monthly Notices of the Royal Astronomical Society,* **275**, 56–66.

Noguchi, M. (2001). *Monthly Notices of the Royal Astronomical Society,* **328**, 353–358.

Noordermeer, E., Sparke, L. S., & Levine, S. E. (2001). *Monthly Notice of the Royal Astronomical Society,* **328**, 1064–1080.

Oh, S., de Blok, W. J. G., Walter, F., Brinks, E., & Kennicutt, R. C. (2008). *The Astronomical Journal,* **136**, 2761–2781.

O'Neil, K., Bothun, G., van Driel, W., & Monnier Ragaigne, D. (2004). *Astronomy and Astrophysics,* **428**, 823–835.

Oosterloo, T., Fraternali, F., & Sancisi, R. (2007a). *The Astronomical Journal,* **134**, 1019.

Oosterloo, T. A., Morganti, R., Sadler, E. M., van der Hulst, T., & Serra, P. (2007b). *Astronomy and Astrophysics,* **465**, 787–798.

Peñarrubia, J., McConnachie, A., & Babul, A. (2006). *The Astrophysical Journal,* **650**, L33–L36.

Peterson, C. J., Thonnard, N., Rubin, V. C., & Ford, Jr., W. K. (1976). *The Astrophysical Journal,* **208**, 662–672.

Pickering, T. E., Impey, C. D., van Gorkom, J. H., & Bothun, G. D. (1997). *The Astronomical Journal,* **114**, 1858.

Pisano, D. J. & Wilcots, E. M. (2003). *The Astrophysical Journal,* **584**, 228–238.

Pohlen, M. & Trujillo, I. (2006). *Astronomy and Astrophysics,* **454**, 759–772.

Popping, A., Davé, R., Braun, R., & Oppenheimer, B. D. (2009). *Astronomy and Astrophysics,* **504**, 15–32.

Portinari, L. & Sommer-Larsen, J. (2007). *Monthly Notice of the Royal Astronomical Society,* **375**, 913–924.

Rahman, N., Howell, J. H., Helou, G., Mazzarella, J. M., & Buckalew, B. (2007). *The Astrophysical Journal,* **663**, 908–923.

Richter, O.-G. & Sancisi, R. (1994). *Astronomy and Astrophysics,* **290**, L9–L12.

Roberts, M. S. & Haynes, M. P. (1994). *Annual Review of Astronomy Astrophysics,* **32**, 115–152.

Robertson, B. E. & Kravtsov, A. V. (2008). *The Astrophysical Journal,* **680**, 1083–1111.

Sancisi, R. & Fraternali, F. (2010). In: *The Impact of HST on European Astronomy,* (ed, Macchetto, F. D.), 179–182, Springer Netherlands.

Sancisi, R., Fraternali, F., Oosterloo, T., & van der Hulst, T. (2008). *Astronomy and Astrophysics Reviews,* **15**, 189–223.

Scannapieco, C., Tissera, P. B., White, S. D. M., & Springel, V. (2008). *Monthly Notices of the Royal Astronomical Society,* **389**, 1137–1149.

Schaye, J. (2004). *The Astrophysical Journal,* **609**, 667–682.

Schneider, S. E., Thuan, T. X., Magri, C., & Wadiak, J. E. (1990). *The Astrophysical Journal Supplement Series,* **72**, 245–289.

Schombert, J. (1998). *The Astronomical Journal,* **116**, 1650–1656.

Schulman, E., Bregman, J. N., & Roberts, M. S. (1994). *The Astrophysical Journal,* **423**, 180–189.

Sérsic, J. L. (1968). *Atlas de galaxias australes.* Cordoba, Argentina: Observatorio Astronomico.

Silich, S., Lozinskaya, T., Moiseev, A., Podorvanuk, N., Rosado, M., Borissova, J., & Valdez-Gutierrez, M. (2006). *Astronomy and Astrophysics,* **448**, 123–131.

Sommer-Larsen, J., Gelato, S., & Vedel, H. (1999). *The Astrophysical Journal,* **519**, 501–512.

Sommer-Larsen, J., Götz, M., & Portinari, L. (2003). *The Astrophysical Journal,* **596**, 47–66.

Spergel, D. N., Bean, R., Doré, O., Nolta, M. R., Bennett, C. L., Dunkley, J., Hinshaw, G., Jarosik, N., Komatsu, E., Page, L., Peiris, H. V., Verde, L., Halpern, M., Hill, R. S., Kogut, A., Limon, M., Meyer, S. S., Odegard, N., Tucker, G. S., Weiland, J. L., Wollack, E., & Wright, E. L. (2007). *The Astrophysical Journal Supplement Series,* **170**, 377–408.

Sprayberry, D., Impey, C. D., Bothun, G. D., & Irwin, M. J. (1995). *The Astronomical Journal,* **109**, 558–571.

Sprayberry, D., Impey, C. D., Irwin, M. J., McMahon, R. G., & Bothun, G. D. (1993). *The Astrophysical Journal,* **417**, 114.

Springel, V., White, S. D. M., Jenkins, A., Frenk, C. S., Yoshida, N., Gao, L., Navarro, J., Thacker, R., Croton, D., Helly, J., Peacock, J. A., Cole, S., Thomas, P., Couchman, H., Evrard, A., Colberg, J., & Pearce, F. (2005). *Nature,* **435**, 629–636.

Springob, C. M., Haynes, M. P., Giovanelli, R., & Kent, B. R. (2005). *The Astrophysical Journal Supplement Series,* **160**, 149–162.

Sunyaev, R. A. (1969). *Astrophysical Letters,* **3**, 33.

Tamburro, D., Rix, H., Walter, F., Brinks, E., de Blok, W. J. G., Kennicutt, R. C., & MacLow, M.-M. (2008). *The Astronomical journal,* **136**, 2872–2885.

Telfer, R. C., Kriss, G. A., Zheng, W., Davidsen, A. F., & Tytler, D. (2002). *The Astrophysical Journal,* **579**, 500–516.

Trujillo, I., Graham, A. W., & Caon, N. (2001). *Monthly Notice of the Royal Astronomical Society,* **326**, 869–876.

Usero, A., Brinks, E., de Blok, W. J. G., Leroy, A. Rick, A. K., & Kennicutt, R. C. (2010). *In preparation.*

Uson, J. M. & Matthews, L. D. (2003). *The Astronomical Journal,* **125**, 2455–2472.

van Albada, T. S., Bahcall, J. N., Begeman, K., & Sancisi, R. (1985). *The Astrophysical Journal,* **295**, 305–313.

van der Hulst, J. M. & Sancisi, R. (2005). In: *Extra-Planar Gas*, (ed, Braun, R.). *Astronomical Society of the Pacific Conference Series.* **331**, 139.

van der Hulst, J. M., Terlouw, J. P., Begeman, K. G., Zwitser, W., & Roelfsema, P. R. (1992). In: *Astronomical Data Analysis Software and Systems I*, (D. M. Worrall, C. Biemesderfer, . J. B., ed) volume 25 p. 131, Astronomical Society of the Pacific Conference Series.

van der Kruit, P. C. (2007). *Astronomy and Astrophysics,* **466**, 883–893.

van Gorkom, J. (1991). In: *Atoms, Ions and Molecules: New Results in Spectral Line Astrophysics*, (eds, Haschick, A. D. & Ho, P. T. P.). *Astronomical Society of the Pacific Conference Series 16*, 1.

van Moorsel, G. A. (1982). *Astronomy and Astrophysics,* **107**, 66–74.

Walter, F., Brinks, E., de Blok, W. J. G., Bigiel, F., Kennicutt, R. C., Thornley, M. D., & Leroy, A. (2008). *The Astronomical Journal,* **136**, 2563–2647.

Wilcots, E. M. (2001). In: *Gas and Galaxy Evolution. Astronomical Society of the Pacific Conference Series.*, **240**, 167.

Williams, R. E., Blacker, B., Dickinson, M., Dixon, W. V. D., Ferguson, H. C., Fruchter, A. S., Giavalisco, M., Gilliland, R. L., Heyer, I., Katsanis, R., Levay, Z., Lucas, R. A., McElroy, D. B., Petro, L., Postman, M., Adorf, H., & Hook, R. (1996). *The Astronomical Journal,* **112**, 1335.